UNIVERSITY OF SOUTHAMPTON

Faculty of Physical Sciences and Engineering
School of Electronics and Computer Science

Development of an organ on chip microfluidic platform with real-time viability sensing capabilities

Volume 1 of 1

by

João Ricardo Cabaço Gonçalves Fernandes

ORCiD: 0000-0002-4504-8249

A thesis for the degree of
Doctor of Philosophy

January 2023

University of Southampton

Abstract

Faculty of Physical Sciences and Engineering
School of Electronics and Computer Science

Doctor of Philosophy

Development of an organ on chip microfluidic platform with real-time viability sensing capabilities

by João Ricardo Cabaço Gonçalves Fernandes

Estimated cost per drug is over $1.5 billion, with success rates ranging between 3 and 14%. Current models used in preclinical trials are based in static *in vitro* and animal models, which fail to recapitulate complex environments from the human body. The organ-on-chip model emerged middle way between both aforementioned models, providing high experimental throughput while maintaining a complex environment for drug testing. In this thesis the design, development and fabrication of a compact and easy to use organ-on-chip platform was described. The platform is capable of cell culture with constant cell media perfusion underneath the cell culture, housed in individual microfluidic chips. Continuous epithelial barrier integrity assessment was possible via electrical impedance spectroscopy measurement using electrodes located underneath the cell culture. Fluidics were provided to each microfluidic chip individually, with placement, alignment and replacement possible using magnets in a ”plug-and-play” manner. Transepithelial resistance equivalent and cell barrier capacitance values were extrapolated from impedance spectroscopy data utilising an electrical circuit model. Complex non-linear square fit and Nelder-Mead minimisation algorithms were used to extrapolate cell media resistance, electrode parameters (electrode polarization) and cell barrier resistance (TER) and capacitance from the complex impedance spectroscopy data. Two different types of epithelial cell lines (bronchial and gut) were successfully cultured in the platform, with continuous transepithelial resistance (TER) and cell barrier capacitance measurements throughout the experiments. Both cell lines displayed lower TER comparatively to static models (Transwells), with results matching recent findings in literature regarding TER of cell cultures with and without flow. Additionally, epithelial barrier integrity disruption was measured following Triton X-100 or viral mimetic apical stimulation using human bronchial epithelial cells, with both conditions displaying a decrease in barrier integrity after stimulation.

Lastly, a droplet generator was designed, developed and used to compartmentalise cell media from the organ-on-chip platform, allowing temporal analysis of epithelial barrier molecular permeability and/or excreted analytes. The droplet generator was composed of polydimethylsiloxane (PDMS) and was could generate droplets every 20 minutes in 8 channels simultaneously, with an average droplet volume of 9.47 ± 0.6 μL. Fluorescein diffusion across the porous membrane was assessed, with results similar to simulated data using COMSOL. Fluorescein-Dextran permeability across human bronchial epithelial cells following barrier formation was assessed with and without Triton X-100 apical stimulation. Both permeability and TER data reached the same conclusion, with Triton X-100 cultures displaying a decline in barrier integrity compared to media controls. Interleukin-8 production was assessed using the same cell line following apical stimulation with a viral mimetic, however no conclusions could be inferred due to data variability between repeats.

Contents

List of Figures

List of Tables

List of Additional Material

Data sets associated with the thesis have been deposited in the University of Southampton's institutional repository (Pure) and are accessible via the following DOI: https://doi.org/10.5258/SOTON/D2205

Declaration of Authorship

I declare that this thesis and the work presented in it is my own and has been generated by me as the result of my own original research.

I confirm that:

1. This work was done wholly or mainly while in candidature for a research degree at this University;
2. Where any part of this thesis has previously been submitted for a degree or any other qualification at this University or any other institution, this has been clearly stated;
3. Where I have consulted the published work of others, this is always clearly attributed;
4. Where I have quoted from the work of others, the source is always given. With the exception of such quotations, this thesis is entirely my own work;
5. I have acknowledged all main sources of help;
6. Where the thesis is based on work done by myself jointly with others, I have made clear exactly what was done by others and what I have contributed myself;
7. Parts of this work have been published as: Fernandes et al. (2022)

Signed:.. Date:..................

Acknowledgements

I would like to Prof. Hywel Morgan and Dr. Emily Swindle for providing me the opportunity of starting this PhD project at the University of Southampton and for their continued guidance and support. To Wendy Rowan and Theresa J. Pell for the continuous support, interest and insights into the project from an industry perspective. To Prof. Donna Davies for her continuous help in understanding the biological intricacies in the project. To all members of the CHB lab for the help and companionship, with a special thanks to Nikita Karra for working alongside me on the Lung-on-Chip project, without whom this PhD would not have been possible. To GlaxosmithKline for funding and support on the project.

I would also like to thank my family, specially my parents and brother for the continuous support, advices and help throughout these years. My evening friends, Diogo Albuquerque, Gonçalo Horta and André Malafaia who were always available to talk and relax after work regardless of the distance between us. To Ana Beaumont and Daniela Magalhães, both of which are and always will be there to hangout and explore the world with.

List of Publications

Joao Fernandes, Nikita Karra, Joel Bowring, Riccardo Reale, Jonathan James, Cornelia Blume, Theresa J Pell,Wendy C Rowan, Donna E Davis, Emily J Swindle, and Hywel Morgan. Real-Time Monitoring of Epithelial Barrier Function by Impedance Spectroscopy in a Microfluidic Platform. Lab on a Chip, 1, 2022. ISSN 1473-0197;

Joao Fernandes, Nikita Karra, Emily J Swindle, and Hywel Morgan. Droplet fluidics for time-dependent analysis of barrier permeability in an epithelial barrier on chip system, Lab on a Chip, Under Review;

Definitions and Abbreviations

ALI	Air-Liquid Interface
Caco-2	Human Gut Epithelial Cell Line (Cancer Coli-2)
DMEM	Dulbecco's Modified Eagle Medium
ECIS	Electric cell-substrate impedance sensing
EGTA	Egtazic Acid
EIS	Electrical Impedance Spectroscopy
EVOM	Epithelial Voltohmmeter
FBS	Foetal Bovine Serum
FEM	Finite Element Method
FITC	Fluorescein
HBSS	Hanks Buffered Saline Solution
IA	Immunoassay
IL-8	Interleukin-8
LLI	Liquid-Liquid Interface
LOD	Limit of Detection
PBEC	Primary Bronchial Epithelial Cells
PDMS	polydimethylsiloxane
PEEK	polyarylethe-retherketone
PET	polyethylene terephthalate
PMMA	Poly(methyl methacrylate)
Poly I:C	Polyinosinic-polycytidylic acid
PTFE	Polytetrafluoroethylene
OoC	Organ-on-Chip
MEM	Minimum Essential Medium
NEAA	Non-essential Amino Acids
TER	Transepithelial Resistance
TX-100	Triton X-100
UoS	University of Southampton
16HBE14o-	Human Bronchial Epithelial Cell Line

Chapter 1

Introduction

This chapter will provide an overview of the current challenges facing the drug discovery field, along with the most commonly used cell types and their importance in such studies. Current models used to study said cells will be explained and an in-depth explanation of the recent emergence of Organ-on-Chip models will be provided. Additionally, several examples of commercially available Organ-on-Chip platforms will be presented, as well as the platform previously developed at the University of Southampton.

1.1 Drug Discovery Landscape

The high costs and large timescales required to produce successful treatments are, in part, a consequence of the failure of current models to mimic human specific diseases. For each successful drug candidate there are several unsuccessful ones which are accounted in the total cost required to develop the drug. This phenomenon has led to a recent estimated cost per drug of over $1.5 billion, with success rates ranging from 3 to 14 % for respiratory and HIV/AIDS specific drugs Barnes et al. (2015). Costs of capital and failure past preclinical stages account for 93 % of the total development cost (Figure 1.1) van der Schans et al. (2021). Therefore, an effective way to reduce the overall cost and time of drug development would be to increase fidelity of models used in preclinical studies to recapitulate the human body and mimic human specific diseases and interactions.

Models used in preclinical studies consist of simplified *in vitro* models or *in vivo* animal models. While *in vitro* models study cells, either cell lines or primary cells, cultured in simplified environments and provide high experimental throughput but fail to recapitulate the complex environments from the human body Miller and Spence (2017). *In vivo* animal models provide more dynamic conditions for drug testing but have low throughput, are expensive and labour intensive. Additionally, cell composition differences between humans and animal models increases difficulty when testing for human specific diseases Mullane and Williams (2014); Graham and Prescott (2015).

Organ-on-Chip (OoC) emerged middle way between *in vitro* and *in vivo* animal models, providing both high experimental throughput while maintaining a dynamic environment in which drug candidates can be tested. Devices are usually sub-millimetre in size and can provide more physiologically relevant conditions such as interstitial flow, chemical stimuli or mechanical stress Huh et al. (2010). Yet to be integrated into the drug development industry, the recent commercialization of several OoC platforms has increased interest in their use, with efficacy and physiological relevance currently being tested globally Hagiwara et al. (2022); Tsamandouras et al. (2017); Maass et al. (2017); Hughes et al. (2017); Pediaditakis et al. (2021); Kerns et al. (2021); Si et al. (2021); El-Dairi and House (2019); Apostolou et al. (2021); Junaid et al. (2021); Dourson et al. (2021); Geyer and Queiroz (2021); Chen et al. (2017); Maass et al. (2018).

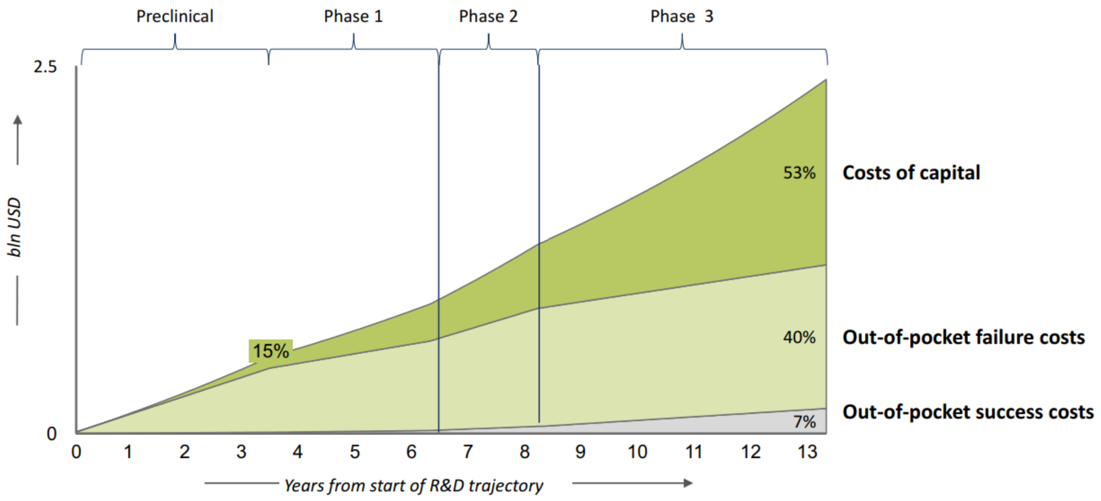

FIGURE 1.1: Drug discovery process displaying the extensive time and money required for the release of a single drug to the market. Incorrect approval of drug candidates in the preclinical stages leads to increase rate of failure in subsequent stages, increasing the cost of the entire process. From van der Schans et al. (2021)

1.2 Epithelial Cell Barrier

Epithelial cell barriers are the most used tissue in drug development studies, as it is the first barrier which the human body has against the external environment and drugs being tested need to be able to pass through said barriers to become effective. These consist of a physical barrier, through which paracellular transport of ions and molecules occur (ionic and macromolecular permeability), an immunological barrier, with the release of cytokines and chemokines for immune cell recruitment and function, and a chemical barrier, through production and release of mucus (respiratory, intestinal and corneal epithelia). Barriers compose the interfaces between human body and external (skin, respiratory and gastrointestinal tracts) (Figure 1.2) or internal environments (liver, kidneys and blood vessels) and prevent invasion of environmental particulates (e.g. microorganisms), while allowing important body functions to occur, such as gas exchange in the lungs and digestion through the gastrointestinal tract Moens and Veldhoen (2012a); Diamond (1977).

Epithelial barriers have two well-defined regions: the apical region, which is in con- tact with the external environment, and the basolateral region, which is in contact with the internal environment (including endothelial cells of blood vessels). These regions are formed by the different junctional complexes which maintain the epithelial barrier tight (Figure 1.3), such as desmosome, focal adhesions, gap junctions, adheren junctions and tight junctions Moens and Veldhoen (2012a). Desmosomes are electron-dense discs that are arranged symmetrically at cell-cell interfaces. Intermediate filaments extend from the interior of cells and attach to the desmosome structure. Due to the mediation of both cell- cell adhesion and cytoskeletal connections, desmosomes are typically found in physically stressed tissues, such as the skin and heart, and can be present in the form of hesmidesmossome, when only half of the structure is present Kowalczyk and Green (2013); Todorović et al. (2013). Focal adhesions are regions of close proximity to the which mediate cell adhesion to the extracellular matrix (ECM) located underneath and are composed of links between integrins and ends of actin filaments Romer et al. (2006). Gap junctions are intercellular channels that allow direct diffusion of ions and small molecules between adjacent cells. These channels are formed by tetraspan integral membrane proteins Churko and Laird (2011). Adheren junctions, composed of nectins and E-cadherin proteins, hold epithelial cells together just below tight junctions, link to the actin cytoskeleton network across cell-cell junctions and are responsible for initial- ising and stabilising cell-cell adhesion, regulating the actin cytoskeleton, intracellular signalling and transcriptional regulation Hartsock and Nelson (2008).

Tight junctions are the most apical member of the junctional complex and form close focal points between the plasma membranes of neighbouring cells, resulting in a continuous intercellular region where adjacent plasma membranes are juxtaposed Zihni et al. (2016). Their main protein components are tetraspan proteins of the claudin family, MARVEL domain proteins (occludin, tricellullin and MARVELD3), junctional adhesion molecules (JAMs), crumbs homologue 3 (CRB3) and blood vessel epicardial substances (BVES). These proteins are responsible for the regulation of several cell-cell adhesion processes and characteristics such as paracellular ion conductance (claudin family), cell transformation and junction dissociation (occludin), F-actin organization (tricellullin), angiogenic signalling, endothelial and immune cell migration (JAMs), gene expression and stress response (MARVELD3) Zihni et al. (2016); Moens and Veldhoen (2012a); Hartsock and Nelson (2008). These junctions form intramembrane and

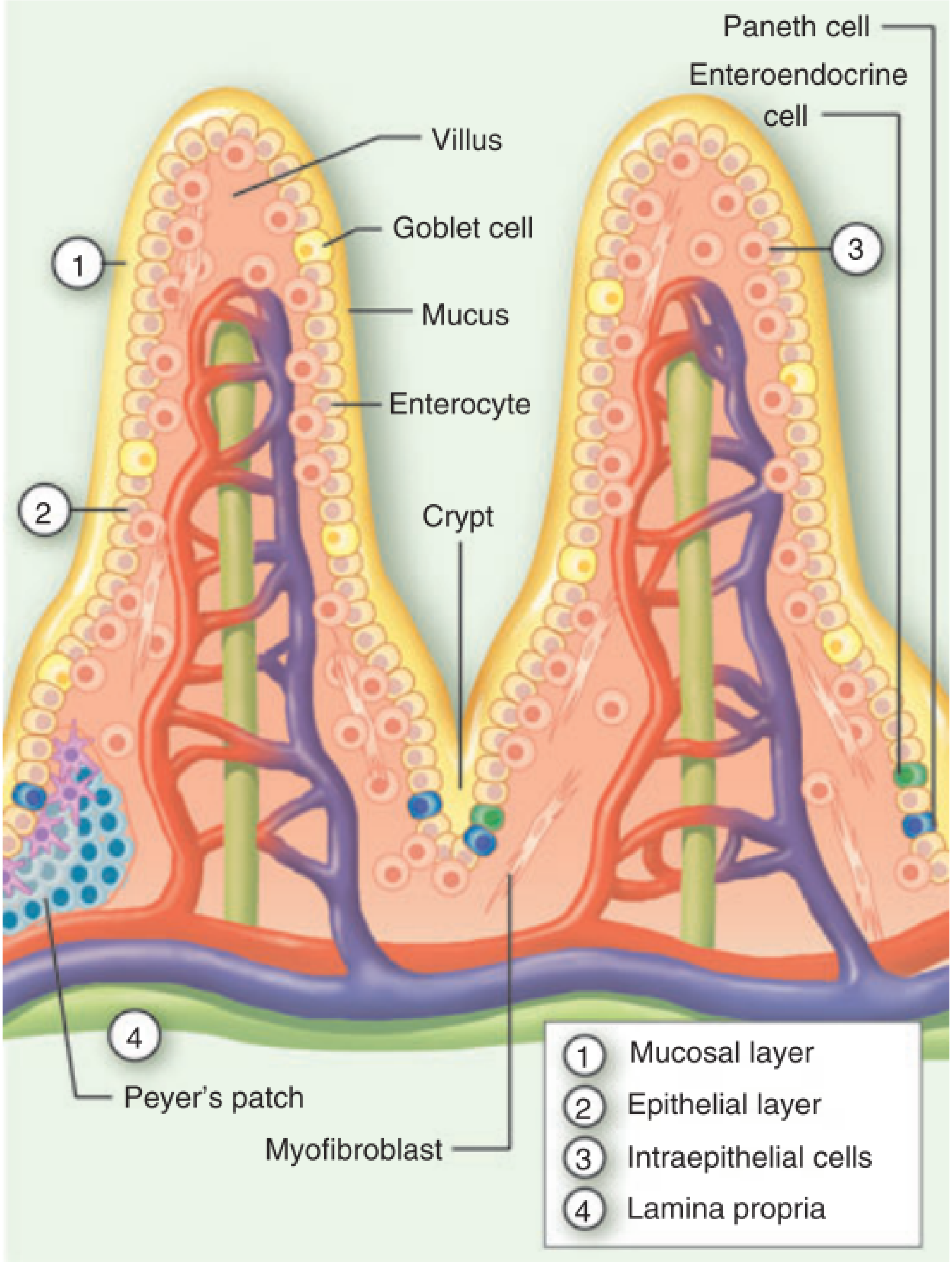

FIGURE 1.2: Schematic representing the small intestinal barrier. From Moens and Veldhoen (2012a)

paracellular barriers. The in- tramembrane barrier restricts exchange of apical and basolateral lipid diffusion in the plasma membrane, regulating the composition of cell's apical and basolateral regions, maintaining cell polarity. The paracellular barrier maintains the homeostasis of organs and tissues, regulating the diffusion of solutes through the barrier based on size and charge Zihni et al. (2016). Tight junctions are commonly associated with epithelial barrier tightness and integrity, often studied by electrical means due to their ionic paracel- lular barrier nature. When a potential difference is applied across a tissue, movement of ions through tight junctions lead to an increase of electrical resistance, commonly denominated by transepithelial resistance (TER).

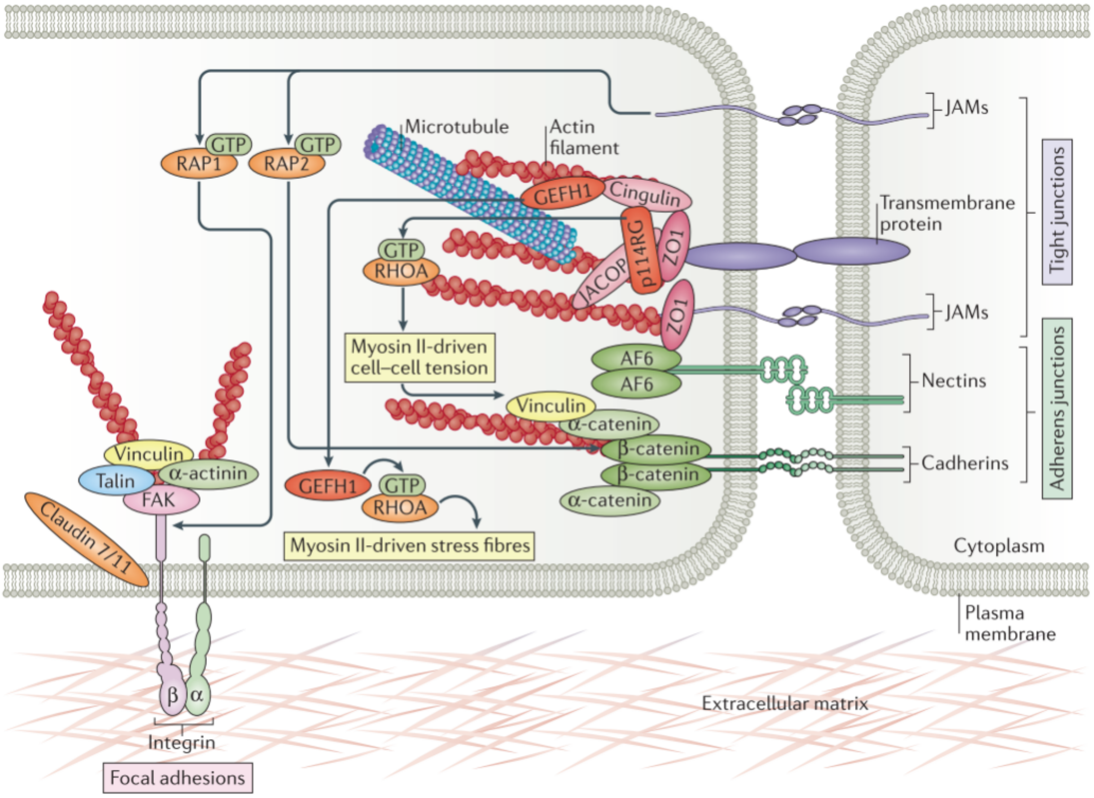

FIGURE 1.3: Representation of the tight junction, adherens junction and focal adhesions placement in the epithelial barrier and proteins which comprise each junctional complex. From Zihni et al. (2016)

Transport across epithelial cell barriers occurs by paracellular transport, transcellular transport or endocytosis/transcytosis Brune et al. (2015); Taylor et al. (1999); Dorrington and Boyd (1995); Shachar-Hill and Hill (1997). Paracellular transport refers to the transport of molecules through the space between adjacent epithelial cells and is mediated by the tight junction complex. Structures through which this transport takes place consist of a system of charge selective pores of small size, discriminating molecules based on their size and charge. Transcellular transport through the epithelial cell barrier defines the passage of compounds through the barrier by entering and exiting a cell's cytoplasm. This type of transport relies on standard passive (simple or facilitated diffusion) and/or active transport (primary or secondary) mechanisms. Endocytosis/-transcytosis describes the transport of compounds through individual cells using vesicles, not involving access to the cell's cytosol. The transport of compounds through the epithelial cell barrier plays a crucial part in drug development studies, as drugs are required to transpose these barriers before entering the human body. Methods to assess epithelial cell barrier permeability in static *in vitro* studies include TER, for ionic permeability, and molecular assays, for molecular permeability. Both methodologies will be explored in subsequent chapters.

Epithelial barrier dysfunction is linked to pathogenesis in several diseases in both the respiratory and gastrointestinal tract ranging from asthma, chronic obstructive pulmonary disease (COPD) and allergic rhinitis on the airway epithelium to inflammatory bowel disease and eosinophilic oesophagitis on the gastrointestinal epithelium. Evidence has shown that industrialization and urbanization are linked with chronic inflammatory conditions, consequence of the increased use of epithelial barrier damaging substances, such as detergents, and air pollution Clayburgh et al. (2004); Moens and Veldhoen (2012b); Schleimer and Berdnikovs (2017); Faber et al. (2020). Additionally, the disruption of airway and gut epithelial barriers can lead to an increase of permeability of other barriers, such as the blood-brain barrier and other vascular endothelial barriers, which may lead to the development of several metabolic and autoimmune disorders Akdis (2021).

1.3 Standard Pre-Clinical Models

Current models used in the preclinical stage of drug development for epithelial barrier function studies consist of *in vivo* and *in vitro* models. *In vivo* animal models use complete representations of biological systems, where the effectiveness of drug candidates is governed by its absorption, distribution, metabolism and excretion (ADME), processes relevant for human physiology Li et al. (2004). Although capable of providing a dynamic environment for drug testing, these models usually have low throughput, are expensive and labour intensive. The composition of the epithelial cell population in the human epithelium and its overall structure varies between humans and most animal models, leading to failure when trying to recapitulate physiological structural changes that occur in human organs or tissues with human-specific diseases Mullane and Williams (2014); Garattini and Grignaschi (2017). Additionally, it is difficult to infer data obtained from animal models, many times leading to the incorrect approval of compounds in pre-clinical trials Graham and Prescott (2015); Miller and Spence (2017).

Standard 2D *in vitro* models rely on cell cultures, either immortalised or primary cells obtained from humans, grown in simplified environments. Immortalised cell lines are cells that, due to mutations or viral transfections, are not affected with cellular senescence and keep undergoing division, allowing their proliferation *in vitro* for prolonged periods of time. Changes to the genetic profile of cells can occur naturally or be induced and can lead to the incorrect modelling of the normal epithelial barrier physiology Miller and Spence (2017). Primary cells obtained from patients can provide a more reflective result of the patient's reaction to a certain compound, but the data obtained cannot be easily extrapolated or generalised, due to genetic and lifestyle variations

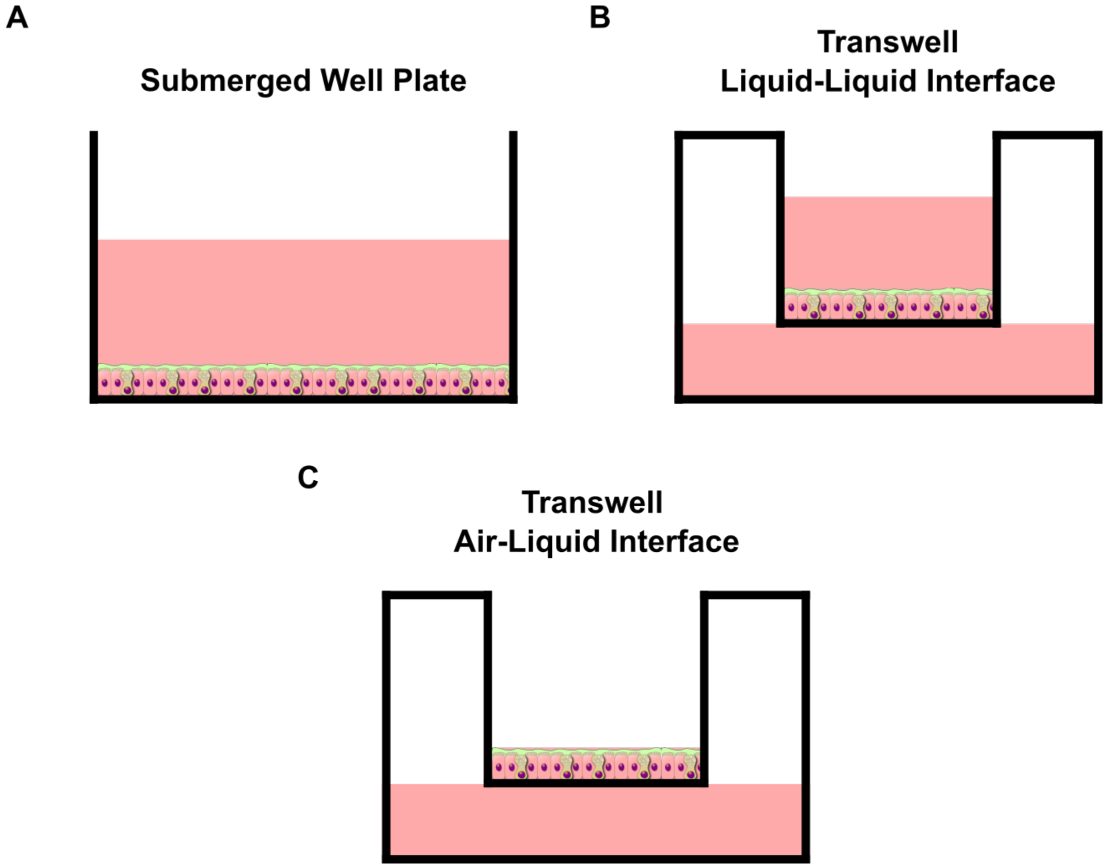

FIGURE 1.4: Different static models used to grow cell lines, which include submerged cell cultures in cell plates (A) and Transwells with cells under LLI (B) or ALI (C).

between donors, and are harder to obtain while having limited proliferation capacity Huang et al. (2011). Cells can be cultured on the surface of a well plate or on top of a nanoporous support membrane (Transwells), whereby cell media can be present just above cells in the well plate (submerged), above and below the cell culture (liquid-liquid interface LLI) or just below cells in the nanoporous support (air-liquid interface ALI) , as shown in Figure 1.4. These different conditions allow for cells to differentiate depending on their usual environment in the human body, with cells from the human lung epithelium being able to polarise and differentiate when cultured at ALI for example Miller and Spence (2017).

Current *in vitro* and *in vivo* models are unable to predict and recapitulate important key factors of human physiology. The organ-on-chip model emerged as a midpoint between these two, as a way to address the lack of physiologically relevant models for drug development. This model aims to simulate the activities, mechanics and physiological responses of entire organs or tissues inside a microfluidic device.

1.4 Organ-on-Chip Models

Organ-on-chips are biomimetic microfluidic devices used to grow and study cells in a continuously perfused and sub-millimetre environment. These devices can be as simple as a single perfused microfluidic chamber, containing one or more cell types, in an attempt to correctly recreate the interfaces between different tissues Zhang et al. (2017). Traditional two-dimensional cell cultures cannot support tissue-specific and differentiated functions of many cell types or accurately predict *in vivo* tissue functions and drug reactions. Due to this fact, there has been an increased interest in organ-on-chip models, which provide better representation of the spatial and chemical complexity of living tissues Huh et al. (2011). Therefore, organ- on-chips devices aim to recreate complex organ-level physiological functions, clinically relevant disease phenotypes and pharmacological responses that arise from structural and functional integration of multiple tissues or interfaces Blume et al. (2015).

Devices are usually made of transparent polymers, for example polydimethylsiloxane (PDMS) or poly (methyl methacrylate) (PMMA), which provide an advantage over animal models, as the biological processes occurring within the cell culture can be more easily visualized and quantified, directly, in real-time. Due to their micrometer-sized environment, the cost of reagents such as cells, culture media or drug compounds is greatly reduced when compared to standard *in vitro* studies. Thus, organ-on-chips have the potential to serve as a model that sits between *in vitro* and *in vivo* animal models, becoming a new enabling platform to identify and validate the efficacy and safety of potential drugs in the preclinical studies, increasing the likelihood of success in clinical trials Skardal et al. (2016); Esch et al. (2015). This potential is especially important when drug screening for respiratory diseases, where neither the *in vitro* nor the animal models used today can mimic the cell environment of the human lungs Huh et al. (2010).

Organ-on-chip devices used to study epithelial cell barriers are often compared to Transwells and typically consist of two channels separated by a thin and porous membrane, on which epithelial and endothelial cells can be cultures on the respective apical and basolateral sides of said membrane. The culture of endothelial cells in conjunction with the epithelial layer provides a more physiologically relevant environment since both cell populations coexist within the human body. Unlike *in vitro* models, the medium is continuously perfused below and/or above the membrane, mimicking the interstitial flow, transport of fluid through the extracellular matrix, of the human body Blume et al. (2015).

The most recognizable OoC system to date is the one developed at Harvard's Wyss Institute, and later commercialised by Emulate, reported by Huh et al. (2010). The device (Fig 1.5) reconstituted the critical functional alveolar-capillary interface of the human lung, mimicking mechanical stress, caused by cyclic breathing in the alveoli. It

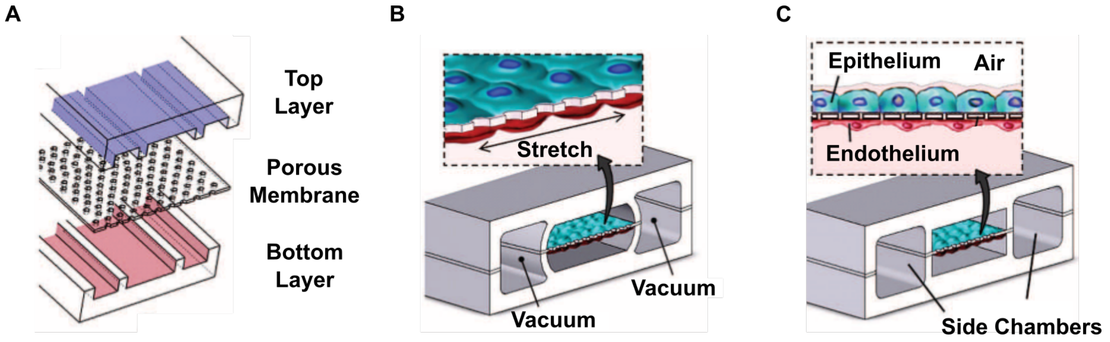

FIGURE 1.5: Lung-on-Chip device developed at Harvard's Wyss Institute. Composed of two patterned PDMS layers covalently bonded together with a porous membrane in-between (A). The side chambers are used to provide vacuum and stretch the membrane while the channels enable the cell culture on both sides of the porous membrane,(B) and (C). From Huh et al. (2010).

is composed of two PDMS slabs with patterned channels and one porous PDMS membrane sandwiched in-between. All three components are irreversibly bonded and cyclic stretching is generated by applying vacuum to chambers on the sides of the medium channel. Epithelial cells are cultured inside the top channel while the cell medium is continuously perfused underneath. It was shown that human alveolar epithelial cells and microvascular endothelial cells were successfully cultured in the device, reconstituting multiple physiological functions seen in human lungs, such as the alveolar-capillary unit microarchitecture, ALI cell culture and analysis of various physiological and pathological lung functions, such as the interaction with immune cells and pathogens. Although the device was successful in culturing and differentiating human lung cells, the material of choice (PDMS) is problematic. PDMS is known for the absorption of small hydrophobic molecules, such as biomolecules, into its porous structure and the adsorption of small molecules onto its surface. This interaction between PDMS and cell medium is especially undesirable when pathogens or cell pathways are being tested (dsRNA, viruses, cytokines) since PDMS adsorption can lead to incorrect concentrations of compounds in flow, resulting in incorrect data analysis. Additionally, the lack of a real-time cell culture viability tool integration, such as the assessment of TER, in organ-on-chip devices can lead to the loss of crucial data regarding epithelial cell barrier integrity.

1.4.1 Air-Liquid Interface

The use of ALI in cell culture is crucial for the correct polarisation and differentiation of certain epithelia, such as the skin Tavares et al. (2020); Sriram et al. (2018); Wufuer et al. (2016) and lung Huh et al. (2010); Ghaemmaghami et al. (2012); Nguyen et al. (2019); Song et al. (2018); Humayun et al. (2018); Doryab et al. (2016); Blume et al. (2015). As previously stated, Huh et al. (2010) reported a device that was able to culture alveolar cells at an ALI. Cells grown at an ALI displayed culture-induced cellular differentiation

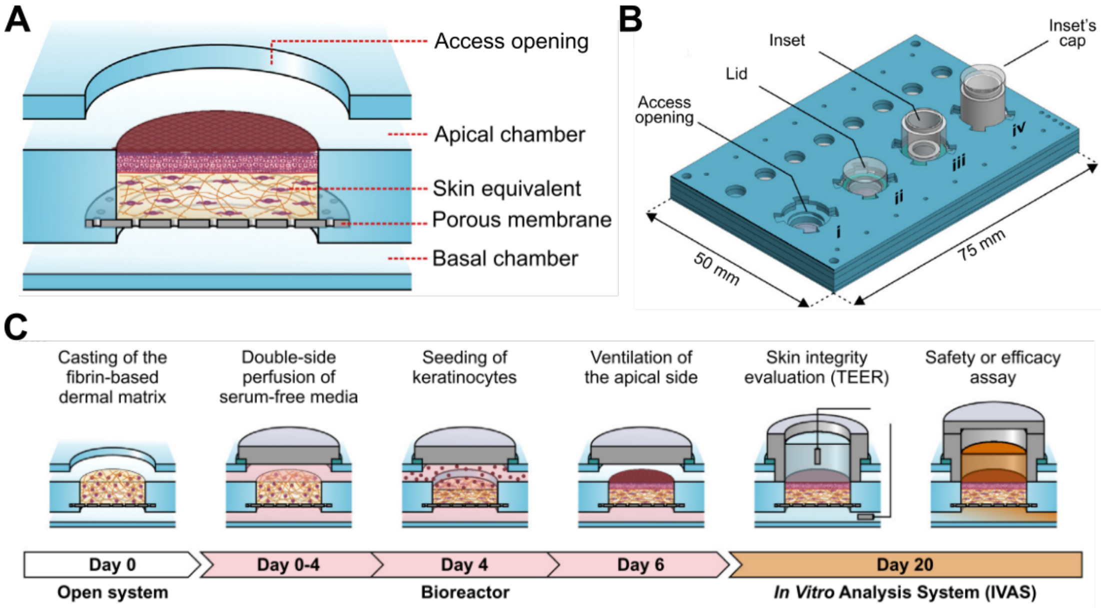

FIGURE 1.6: Schematic of the OoC device developed by Sriram et al. (2018). Each cell chamber (A) is composed of the apical and basal chambers, with skin equivalents cultured on top of a porous membrane. The platform is capable of providing flow both apically and basolateraly (B) with the insertion of a lid the access opening. A custom inset was fabricated for TER measurements of the formed skin equivalent. (C) displays the cell culture protocol used throughout the 20 days

that strengthened the monolayer integrity via the formation of desmosomes and tight junctions. It was also hypothesized that the production of secretory proteins initiated and maintained by ALI culture could serve to protect cells against external mechanical stresses, such as liquid plugs. Nalayanda et al. (2009) fabricated a device that allowed the study of pulmonary cells in an ALI microenvironment. These devices, made of two layers of PDMS covalently sealed to a glass slide, allowed the creation of an air-liquid interface with an alveolar epithelial cell line (A549). These cells were supported for up to two weeks without loss in cell function and provided a more physiologically relevant response when compared to cells cultured in static media at both LLI and ALI. Alexander et al. (2018b) developed a skin-on-chip device with continuous flow in the basolateral and automatic acquisition of TER. The device was comprised of a modified IMOLA BioChip-D Alexander et al. (2018a); Weiss et al. (2013), with a 3D printed encasing of polyactic acid (PLA). The device successfully monitored metabolic rates and barrier integrity of L929 cells for 24 hours. Sriram et al. (2018) developed a microfluidic device of PMMA and 3D printed inserts and lids for the culture of full-thickness human skin equivalents, shown in Figure 1.6. After 6 days of apical and basolateral perfusion, the cell cultures in the device were maintained at ALI for 14 days, with epithelial barrier integrity and sample thickness being assessed at day 20, demonstrating the positive effect on epidermal morphogenesis due to the dynamic perfusion and controlled ventilation.

1.4.2 Mechanical Stress

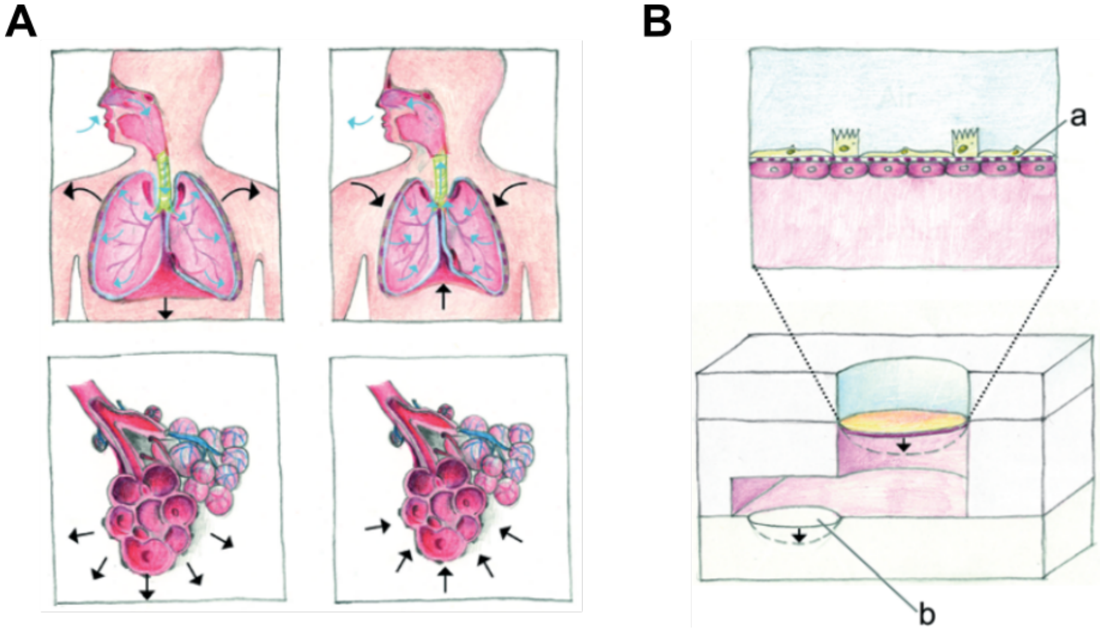

FIGURE 1.7: OoC device with bio-inspired respiration mechanism reported by Stucki et al. (2015). To recapitulate the contraction and relaxation of the human diaphragm during breathing motions (A), a micro-diaphragm (b) in the OoC device is pneumatically actuated, indirectly expanding and contracting the thin, porous and stretchable membrane onto which cells are cultured (a) (B).

Human epithelial barriers are continuously subjected to mechanical stress, originating solely from the existence of interstitial flow or external motions, such as breathing, in the lungs, or peristalsis, in the gastrointestinal tract. To develop a useful organ surrogate device for *in vitro* analysis of the complex human physiology, it is necessary to recreate all the tissue-tissue interfaces and the complex physiological microenvironment in which cells reside *in vivo* Karra et al. (2019). Huh et al. (2010) demonstrated that the induction of mechanical strain in endothelial cells resulted in their alignment in the basolateral compartment, mimicking physiological responses previously observed Thodeti et al. (2009). Stucki et al. (2015), also incorporated mechanical stress in their lung-on-chip device, in which the membrane housing the cell culture is deflected indirectly by the deflection of an actuation membrane (Figure 1.7). The induction of mechanical stress in the growing cell culture led to the increase in stiffness of the porous membrane, as the epithelial barrier integrity increased with time.

1.4.3 Commercial Organ-on-Chip Systems

While organ-on-chip technologies still have not been integrated into drug development workflows, the commercialisation of lab-scale products is already present in the current market space, providing different ways to perform cell and tissue culture. These products still require extensive testing in known ADME & Toxicology (ADMET) effects on tissues and the additional cost of this technology needs to be balanced with their predictive validity when compared to traditional cell culture techniques before their full use in drug development workflows becomes a reality. Additionally, quantification of physiological relevance between these devices and the targeted organ function is required before result correlation Zhang and Radisic (2017). Below are some examples of commercially available OoC platforms emulating epithelial barriers.

1.4.3.1 Emulate

Expanding the work first presented by Huh et al. (2010), Emulate OoC platforms (figure 1.8 (A)) allow users to culture several types of epithelia in an automated and controlled manner, offering OoC kits specific for the growth of brain, intestine, kidney, liver and lung. Devices are made of PDMS and contain two fluidic microchannels separated by a porous support membrane. Chambers in the sides can provide mechanical movement to the culture. Up to 12 devices can be cultured in parallel using their Zoe-CM2 culture module. Devices are optically clear, allowing easy access to the cell culture chamber through microscopy, and benchtop immunoassays can be performed with collected effluent.

1.4.3.2 MIMETAS

First reported by Trietsch et al. (2013), MIMETAS offers OoC solutions which fit in conventional 384 microtiter plates, with the possibility of culturing 40, 64 or 96 chambers in parallel depending on microfluidic channel architecture. Devices are made of glass with patterned dry film resist microchannels. Perfusion is performed passively when plates are placed into a microtiter plate shaker, as the reservoirs connected to the inlet and outlet have different liquid heights at each stage of the process, inducing hydrostatic pressure and flow between reservoirs. Therefore, cell media is not renewed, and any cell excretions are present in the cell media throughout experiments, requiring manual refreshments of cell media every 2-3 days Nicolas et al. (2021). Additionally, the more recent Graft platform allows the user to have direct access to the apical and basal chambers of the device for addition of cells, compounds and stimuli. MIMETAS also offers the possibility of real-time continuous TER measurements of each culture with the OrganoTEER platform. As detailed by Nicolas et al. (2021), TER is measured with electrodes placed in the inlet and outlet media reservoirs, allowing epithelial barrier integrity assessment of up to 40 samples in under one minute without disturbing the cell culture.

1.4.3.3 Alveolix

With their ^{AX}Lung-on-Chip system (figure 1.8 (B)), Alveolix allows the user to culture up to 12 independent cultures in a 96 well plate format. Each culture can be accessed and has perfusion provided by a peristaltic pump. 3D cyclic mechanical strain can be applied on cells by applying vacuum to the actuation chamber and deflecting the membrane located above. This will then indirectly deflect the membrane in which cells are cultured Stucki et al. (2015, 2018). Additionally, TER can be measured using standard techniques used in static cultures, such as the use of EVOM chopstick electrodes. Mermoud et al. (2018) reported in the integration of TER electrodes with the device, but no commercial version is available at the time of writing.

1.4.3.4 CNBio

CNBio offers their PhysioMimix OoC platforms (Figure 1.8 (C)) for 12 single or 6 multi-organ cultures in parallel. Based on the work presented by Domansky et al. (2010), each cell culture chamber is separated into the reactor well and the reservoir well, with cells cultured on top of a porous membrane. Perfusion is achieved through an inbuilt peristaltic pump located underneath and connecting both chambers, recirculating cell media in the device Inman et al. (2007). Both chambers are sealed with a removable lid, allowing easy access to the area in which cells are cultured.

1.4.3.5 Draper

The PREDITC96 OoC system (Figure 1.8 (D)) combines a microfluidic device design similar to the one seen in Emulate products with the TER capabilities of MIMETAS. Each cell culture chamber is composed of two microfluidic channels with a porous membrane in-between. Perfusion can be applied in both channels with recirculating media controlled via peristaltic pumps. TER is measured using four electrodes located in the 4 available cell media inlets and outlets. Although hypothetically possible to measure during an experiment in real-time inside an incubator, Azizgolshani et al. (2021) only displayed the device's TER capabilities outside the incubator.

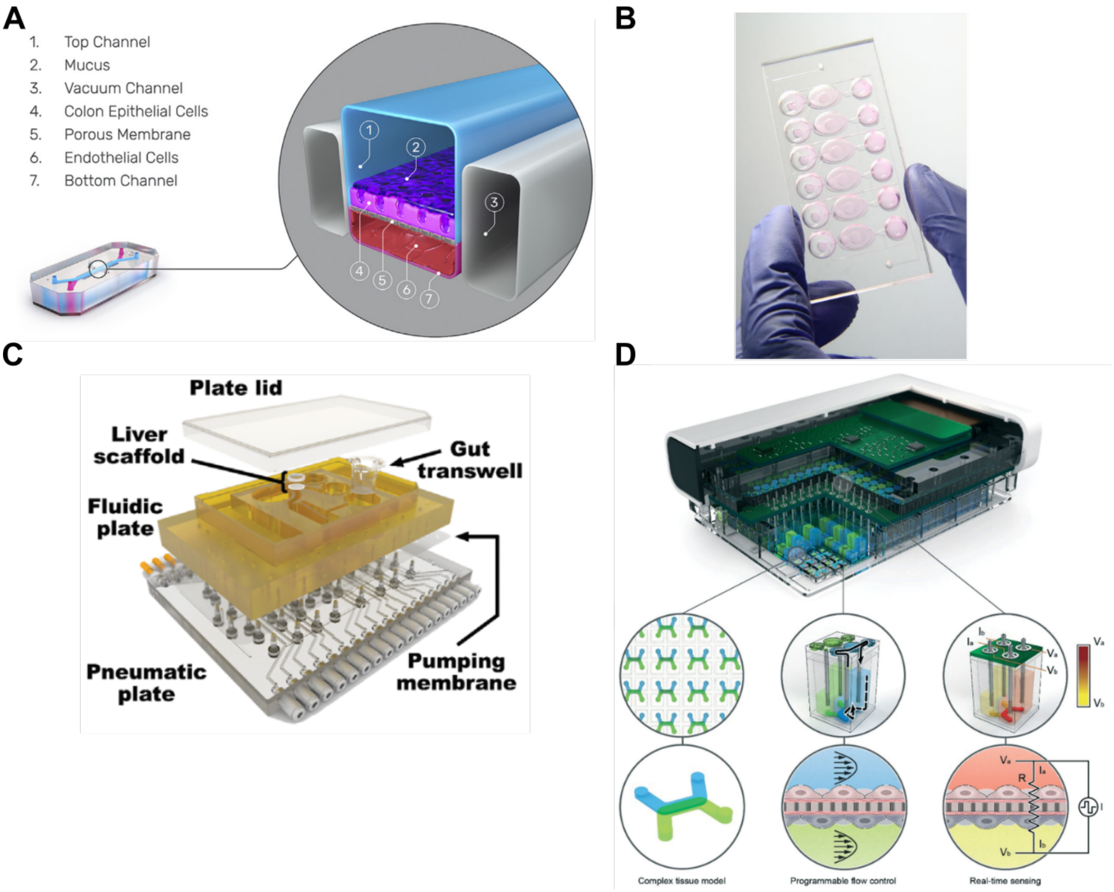

FIGURE 1.8: Emulate's OoC device (A), with two microfluidic channels, separated by a porous membrane, and two vacuum chambers which provide mechanical motion to the cell culture. MIMETAS OrganoPlate 2-Lane (B), which allows for 96 cell cultures in parallel. CNBio PhysioMimix Multi-Organ system (C) used for simultaneous culture of liver and gut cells with recirculation of cell media through both chambers. AlevoliX ^{AX}Lung-on-Chip device (D), which recapitulates respiration mechanism through the deflection of the porous membrane in which cells are cultured. Draper's PREDITC96 platform, which allows for the culture of 96 parallel with perfusion provided by micro-peristaltic pumps and TER measurements with inbuilt electrodes. (A) from Apostolou et al. (2021), (B) from Stucki et al. (2018),(C) from Chen et al. (2017) and (D) from Azizgolshani et al. (2021)

1.5 Organ-on-chip at University of Southampton

With an overview of the current commercial landscape of available OoC systems, there is a lack of a scalable system in which epithelial cell barrier can be analysed in real-time while providing fresh cell media to the cell cultures. The only platform close to that goal is provided by MIMETAS, in which there is no cell media renewal (apart from manual interventions from the user). Additionally, no platform is capable of providing temporal analysis of biological analytes, which can be of crucial importance when analysing how drugs affect the epithelial cell barrier. For this purpose, work started with the goal of providing a system with all these characteristics: real-time assessment of epithelial cell barrier integrity, cell media renewal and temporal analysis of biological analytes without user interventions. Additionally, the developed system should be capable of supporting cell cultures which require ALI conditions.

The development of an OoC platform at the university of Southampton started with the work presented by Sun et al. (2010b), with the design and fabrication of a bio-impedance chip for real-time monitoring of transepithelial resistance in static models (Figure 1.9A). Human bronchial epithelial cells (16HBE14o-) were cultured in Transwell supports, with TER measured using circle-dot shaped electrodes placed underneath the cell culture. Electrical impedance spectroscopy measurements over a frequency range between 100 Hz to 1 MHz were used to assess epithelial barrier formation. The platform was able to distinguish between Transwells with and without a confluent cell layer (Figure 1.9B). Additionally, epithelial barrier disruption following Triton X-100 or EGTA stimulation was continuously monitored for one hour in one minute intervals, displaying a concentration dependent barrier disruption for both compounds (Figure 1.9C).

Blume et al. (2015)) reported the design and fabrication of a microfluidic culture system (Figure 1.10A). Following differentiation, Transwell supports containing primary bronchial epithelial cells (PBEC) were placed in the microfluidic system, with perfusion of cell media at 30 μL/hour underneath the cells throughout the basolateral compartment. Transwells without flow (static) were used as controls. After 1 hour of flow equilibration, cells were apically stimulated with grass pollen extract and interleukin-8 (IL-8) concentration was measured in basolateral media. Addition of grass pollen leads to epithelial barrier disruption and increased IL-8 release, a pro-inflammatory cytokine. Basolateral media in the microfluidic system was automatically dispensed into reservoirs every 2 hours using an automated fraction collector, with static Transwell cultures basolateral medium manually collected at matching time points. Microfluidic and static cultures displayed a peak IL-8 release at 4-6 hours post stimulation (Figure 1.10B), with a significant difference comparatively to control cultures (Figure 1.10C). Also, the microfluidic system was able to detect IL-8 release faster (2-4 hour increase), displaying higher detection sensitivity comparatively to static cultures.

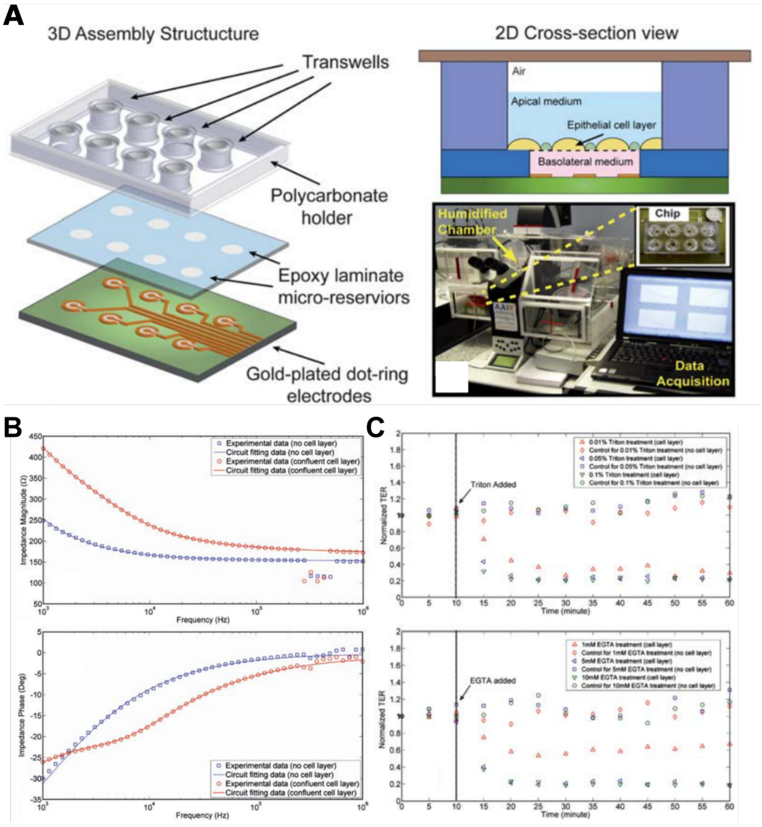

FIGURE 1.9: (A) 3D and 2D schematic of device developed by Sun et al. (2010b), in which ring shaped electrodes beneath a Transwell support were used for continuous EIS measurements and epithelial barrier integrity assessment. (B) Electrical impedance spectroscopy data obtained from Transwell supports with and without a confluent cell layer, with an increase of magnitude of impedance (top) and decrease of phase angle (bottom). (C) Epithelial barrier disruption following Triton (top) and EGTA (bottom) apical stimulation. A decrease of normalised TER is seen for all conditions, with a concentration dependent response.

The same system was subsequently used for epithelial/endothelial co-culture studies Blume et al. (2017) (Figure 1.11A). Transwell supports were used to culture endothelial (human umbilical vein) and epithelial (16HBE14o-) cells separately and in co-culture. TER was assessed using EVOM chopstick electrodes. An increase in TER was visible for Transwells with epithelial cells and co-culture, both peaking at day 3 and with the co-culture displaying a 2-fold increase in TER at day 6 compared to epithelial cells mono-cultures. Endothelial cells did not show an increase of TER over the 6 days of culture. Following 6 days of culture, Transwell supports were placed in the microfluidic system and each culture was apically stimulated with a viral mimetic (Poly I:C). A decrease

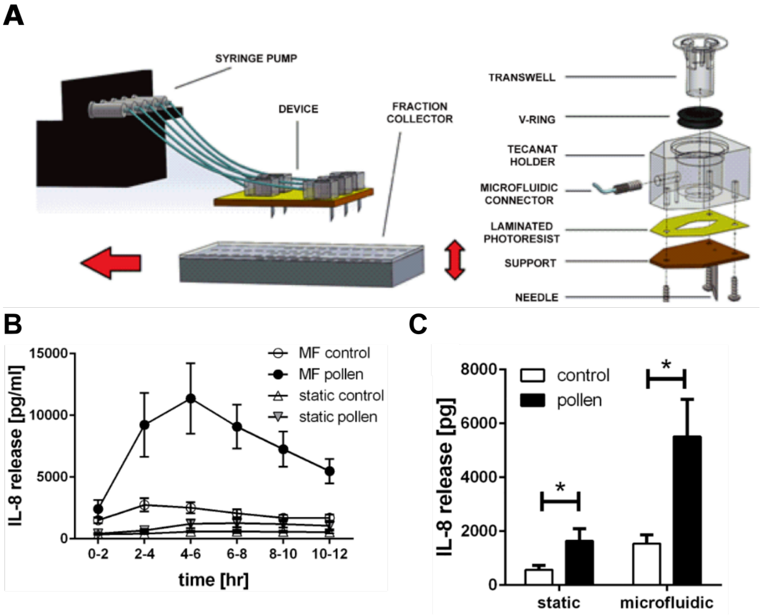

FIGURE 1.10: (A) Adaptation of microfluidics to Transwell supports, reported by Blume et al. (2015), in which a standard Transwell support is placed in the device and basolateral flow is provided via syringe pump. The system was placed in an automated fraction collector for time-dependent analysis of cell released analyte present in basolateral medium. (B) IL-8 release over 12 hours post grass pollen extract stimulation of PBEC cultured with and without microfluidic flow (MF). (C) Differences in IL-8 release between stimulated and unstimulated for cultures with and without flow.

in barrier integrity was observed for both epithelial and co-cultures, with a decrease in TER 3 hours post stimulation (Figure 1.11B). Additionally, Poly I:C stimulation lead to the increase of barrier permeability for epithelial and co-cultures to FITC-Dextran 4 kDa (Figure 1.11C). Peaks of TNF-α and CX_3 CL1 release were visible at 4 and 8 hours post stimulation respectively, with co-cultures and epithelial cells releasing higher amounts of TNF-α and CX_3 CL1 respectively (Figure 1.11D and E).

Further work on a microfluidic platform was developed at UoS since, combining the work presented by Sun et al. (2010b) and Blume et al. (2015), with the possibility of real-time TER measurements while providing a programmable interstitial flow, both of which are not visible together in any commercial platform at the time of writing. Although a full explanation on this system is present in 4, the system was neither compact nor user-friendly, with several changes required to it's design and functionality before it would be robust enough for reliable use.

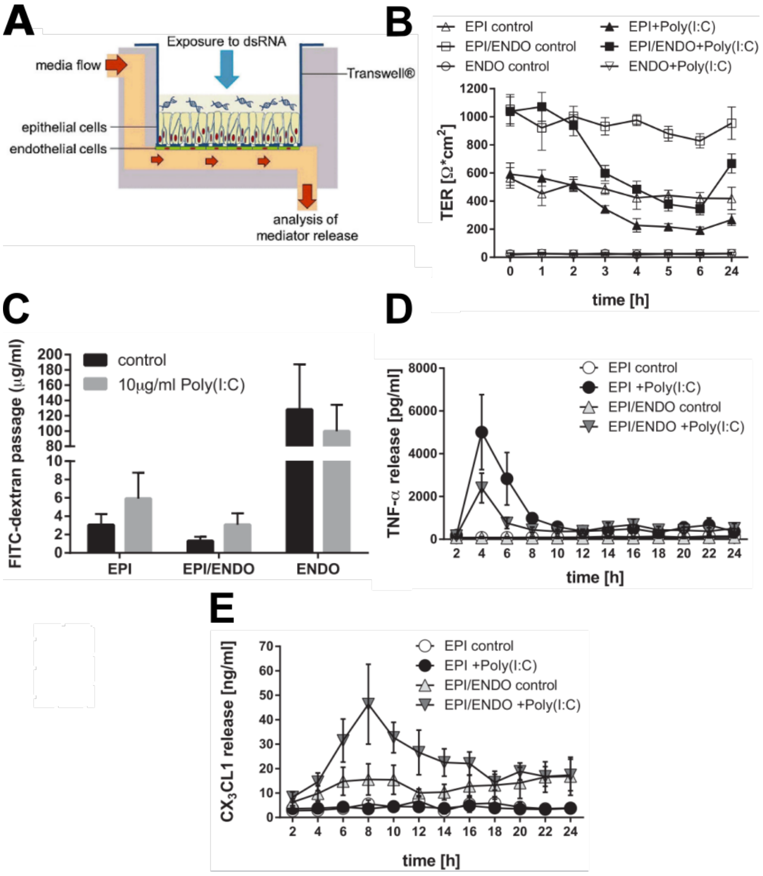

FIGURE 1.11: (A) Device used to deliver basolateral flow to a Transwell support following epithelial barrier formation. (B) TER of epithelial, endothelial and co-culture Transwell supports with and without apical stimulation with a viral mimetic (Poly I:C) over the course of 24 hours. (C) Barrier permeability assessment with FITC-Dextran 4 kDa following stimulation for each Transwell culture. (D) and (E) TNF-α and CX_3CL1 release over 24 hours after apical stimulation with Poly I:C.

1.6 Aims and Objectives

High costs and time spent in the drug development industry are a consequence of inadequate models used in pre-clinical stages. The organ-on-chip model aims to revolutionise the industry, with platforms that provide users high experimental throughput while recapitulating key factors of human physiology. Devices currently commercially available already provide important parameters required for cell differentiation, such as interstitial flow, mechanical stress and air-liquid interfaces, for tissues which require it such as the lung and the skin. Unfortunately, a gap still exists in systems capable of assessing epithelial barrier integrity continuously in real-time with minimum disruption of the cell culture. At this time, only the PREDICT96 platform has inbuilt electrodes for TER measurements, but these can only be performed in submerged cells cultures and are not suitable for ALI cultures. We aim to develop a platform capable of providing human representative interstitial flow and cell media renewal, while allowing data acquisition regarding epithelial cell barrier integrity in real time. Lastly, the platform will have inbuilt electrodes which allow for ALI cultures to be used in the platform with ease.

The first aim of this project is to develop a scalable platform into which microfluidic OoC devices can be easily placed and replaced in a ”plug-and-play” manner. This platform will be built upon the work previously done at the University of Southampton by Dr. Riccardo Reale (Reale (2017)), Dr. Summit Kalsi and Dr. Sofia Johansson and will have the requirements listed below. These were discussed with key members of GlaxoSmithKline (Wendy Rowan and Theresa J. Pell) and the final system always had the end user in mind.

- Allow cell culture of different epithelial barriers, such as respiratory and intestinal.
- Perform epithelial cell barrier integrity assessments through TER measurements. Such measurements have to be possible inside the incubator in an automated manner, without user interaction or cell culture disruption.
- Platform has to be low weight and compact, allowing the use of multiple platforms in a standard incubator,increasing possible scalability and commercial potential of the final platform.
- Microfluidic chips in which cells are cultured need to be small and easy to insert/remove from the platform.

The second aim of this project involves development of an attachment to the platform which allows for the temporal analysis of biological analytes released by the cells in culture. At the time of writing, there is no available commercial platform capable of providing the user with such data without manual interventions from an experienced user. This problem will be addressed by employing droplet microfluidics for analyte compartmentalisation in a small microfluidic device. Similarly, to TER measurements, analyte compartmentalisation will be performed inside the incubator in an automated manner without user interaction. Compartmentalised analyte will be stored in standard fluidic tubing for post analysis using standard bench-top techniques.

The finalised platform will encompass the work presented in the two aims as a joined product, combining the ease of use, reliability and data acquisition through electrical impedance spectroscopy to the added acquisition of temporal analysis of biological analytes.

Chapter 2

Fundamentals of Microfluidics

This chapter will provide an introduction to the various aspects of microfluidics and particle diffusion used in work present in subsequent sections.

2.1 Fluid Dynamics

A fluid deforms continuously under external forces, it does not have a general shape and its properties are not affected by the rearrangement of its parts. Liquids in microfluidic environments are continuous flows and are described by the continuity equation (equation 2.1), which states that mass is conserved within a system. Flow rates in these environments are considerably slower than the speed of sound and, therefore, liquids can be treated as incompressible with a fixed viscosity in space and time. Mass conservation in microfluidics leads to adjustment of the liquid shape, adjusting to the channel dimensions, and change of speed, without increasing or decreasing volume.

$$\nabla \cdot v = 0 \tag{2.1}$$

The movement of an incompressible Newtownian fluid in a microfluidic channel is described by the Navier-Stokes equation (equation 2.2), which is Newton's second law ($F = ma$) applied to fluid movement. Here V is the velocity field, which is affected by the spatial coordinates and time, P the pressure field, ρ_0 and μ_0 the fluid density and dynamic viscosity respectively Ostadfar (2016).

$$\rho_0 \left(\frac{\partial V}{\partial t} + V \cdot \nabla V \right) = -\nabla P + \mu_0 \nabla^2 V \tag{2.2}$$

While equation 2.2 is dependent on spatial dimensions, it is possible to obtain a dimensionless equation by rearranging the existing constant terms. Dimensionless equations provide quantitative comparisons irrespective of a system's scale. The rearranged equation is in equation 2.3, where Re, St and Ru are dimensionless numbers, L_0, V_0, T_0 and P_0 the system's characteristic length, speed, timescale and pressure respectively Bruus (2008).

$$Re\left(St\frac{\partial V^*}{\partial t^*}V^* \cdot \nabla^* V^*\right) = -\frac{Re}{Ru}\nabla^* P^* + \nabla^{2^*} V^* \tag{2.3}$$

$$St = \frac{L_0}{T_0 V_0} \tag{2.4}$$

$$Ru = \frac{\rho_0 V_0^2}{P_0} \tag{2.5}$$

$$Re = \frac{\rho V d}{\mu} \tag{2.6}$$

The Strouhal number (St; equation 2.4) represents the ratio between advection and external time. If a system is in a steady state, $T_0 = \infty$ and $St = 0$, resulting in a time dependent velocity.

The Ruark number (Ru; equation 2.5) expresses the relation between advection forces and the system's characteristic pressure.

The Reynold's number (Re; equation 2.6) is the ratio between the inertial and viscous forces of a liquid in motion. It can be used to predict the state of flow (turbulent or laminar, figure 2.1) within a microfluidic channel and is of importance in microfluidic system analysis. While laminar flows ($Re < 100$) are represented by movement of fluid in a parallel and organized manner, turbulent flow ($Re > 10000$) leads to chaotic fluid flow across a microfluidic channel and vortex formation (figure 2.1). If $10 < Re < 10000$ the flow can be both turbulent and laminar, with transitions between both flow states. Re is dependent on the fluid density (ρ), velocity (V) and viscosity (μ) and the channel length (L), Reynolds (1883).

On the micrometer scale the Reynold's number is usually low (< 10), meaning that flow is laminar inside microfluidic channels. The flow along a cylindrical channel due to pressure drop can be calculated using the Hagen-Poiseuille equation Sutera and Skalak (1993). Assuming a steady flow along the channel and rigid walls, the flow velocity (with $0 < r < R$) is defined by:

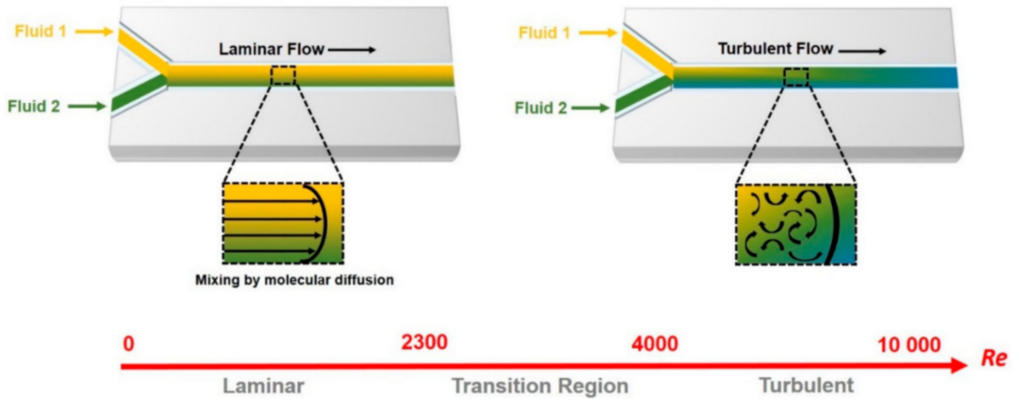

FIGURE 2.1: Differences between laminar and turbulent flow regimes and their dependency on low and high Reynold numbers respectively. From Saliba et al. (2018)

$$v_z = \frac{\nabla p R^2}{4\mu L}\left(1 - \frac{r^2}{R^2}\right) \tag{2.7}$$

Laminar flow has a parabolic profile as a result of the *no slip* boundary condition at the wall (figure 2.2). With a viscous liquid, the fluid velocity at a *no slip* boundary is equal to that of the solid boundary ($V_{InterfacingFluid} = V_{Solid} = 0$), as fluid particles "stick" to solid surfaces. This leads to a minimum fluid velocity close to the boundary and a maximum velocity (equation 2.8) at the centre of the microfluidic channel, Ostadfar (2016).

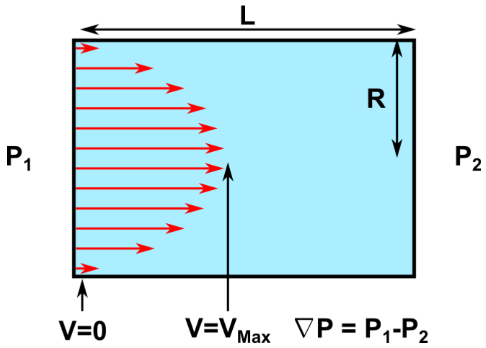

FIGURE 2.2: Schematic of laminar microfluidic flow of a liquid along a circular channel due to a differential pressure applied from left to right.

$$V_{Max} = \frac{\nabla P R^2}{4\mu L} \tag{2.8}$$

The volumetric flow-rate (Q) through a microfluidic channel can be obtained by multiplying the fluid average speed ($V_{Average} = 0.5V_{Max}$) by the channel cross sectional area. Thus, the relation between pressure difference (∇P) and volumetric flow-rate across a circular channel is given by equation 2.9, with μ the fluid's viscosity, L the channel's length and R the radius, Bruus (2008).

$$\nabla P = \frac{8\mu L Q}{\pi R^4} \tag{2.9}$$

The same principle can be applied to rectangular channels, with the relation between applied pressure and flow-rate given by equation 2.10. Here w and h are the channel width and height respectively Bruus (2008).

$$\nabla P = \frac{12\mu L Q}{wh^3\left(1 - 0.63 \times h/w\right)} \tag{2.10}$$

2.2 Diffusion

Diffusion refers to the passive movement of molecules or particles from higher to lower concentration and occurs in both liquids and gases. Fick's laws of diffusion (Fick (1995)) demonstrates how the flux of particles or molecules between two areas is proportional to the concentration gradient (figure 2.3). This can be calculated using Fick's first law (equation 2.11), in which J is the diffusion flux, D the diffusion coefficient, ϕ the concentration and x the distance between areas. The diffusion coefficient is specific for each pair of substances and relates to how fast the pair of substances diffuses into each other, with higher diffusion coefficients leading to faster diffusion Fick (1995).

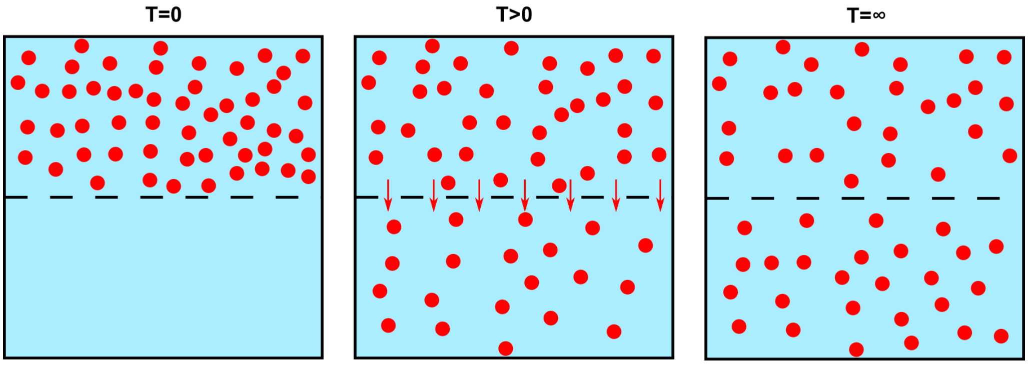

FIGURE 2.3: Diffusion of a substance in a fluid through a porous membrane. At T=0 there is a concentration gradient between top and bottom compartments, with diffusion across the membrane occurring over time. For long times, the concentrations will become equal between top and bottom compartments.

$$J = -D\frac{d\phi}{dx} \tag{2.11}$$

Fick's second law of diffusion is used to calculate how the concentration of a substance will change over time when diffusion occurs (equation 2.12).

$$\frac{\partial \phi}{\partial t} = D\frac{\partial^2 \phi}{\partial x^2} \tag{2.12}$$

In a microfluidic channel, substances in a flow are subject to both diffusion and advection. The effective diffusion through a microchannel in a flowing fluid is known as Taylor-Aris dispersion. This encompasses the effects of both diffusion and advection and is given by equation 2.13 Taylor (1953); Aris (1999). Due to the difference in fluid velocity between the centre and edges of the microchannel, solutes travelling at the centre will travel longer distances comparatively to solutes closer to the edges (figure 2.4). Thus, solute travelling faster will diffuse quicker to surrounding fluid and dispersion occurs due to advection. The Péclet (Pe) number defines the ratio between advection and diffusion effects on a substance flowing in a microchannel (equation 2.14), with $\tau_{diffusion} = \frac{L^2}{D}$, $\tau_{convection} = \frac{L}{V}$, L the microchannel length, V the fluid speed and D the diffusion coefficient between substances. This number conveys the relative importance of both effects, with a low Pe correlating to high diffusion and negligible convection effects, and vice-versa, Fan et al. (2018).

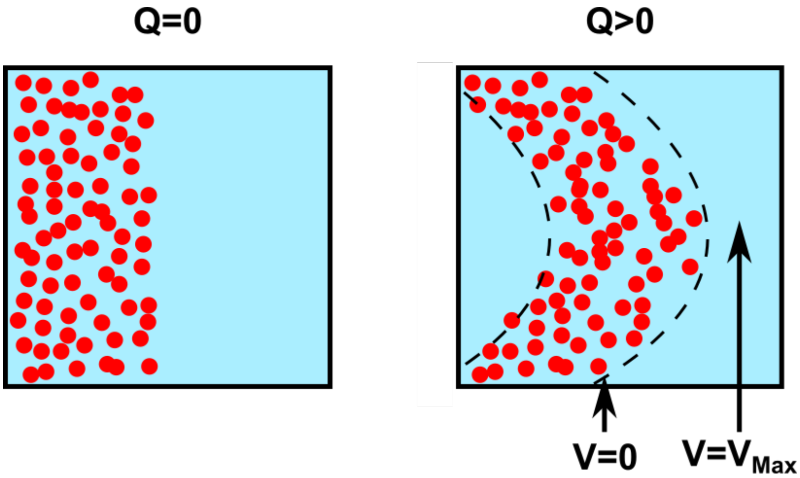

FIGURE 2.4: Schematic showing dispersion inside a microfluidic channel subjected to fluid flow. Substances located at the centre of the channel will move faster and travel longer distances comparatively to substances located near the walls.

$$D_{Effective} = D\left(1 + \frac{Pe^2}{192}\right) \tag{2.13}$$

$$Pe = \frac{\tau_{diffusion}}{\tau_{convection}} \tag{2.14}$$

Chapter 3

Impedance Modelling

In this chapter, an introduction of measurement techniques for electrical assessment of epithelial cell barrier integrity will be provided. Following this, the proposed electrical setup and circuit model will be described. Lastly, experiments validating said circuit model will be presented, with and without the presence of cells in the system.

3.1 Electrical Measurement of Epithelial Cell Barrier Integrity

Epithelial cell barrier integrity is commonly assessed through transepithelial electric resistance (TER) in static cell cultures and, more recently, in organ-on-chip devices. In a typical experiment, cells are cultured above a porous support and electrodes are placed in the apical and basolateral compartments (trans configuration) as seen in Figure 3.1A. An electrical signal is applied between electrodes and the resulting resistance can be measured. Cell growth, polarization and formation of tight junctions (which maintain barrier tightness, integrity and are selectively permeable to ions) between cells leads to an increase of resistance Benson et al. (2013); Yeste et al. (2018); Gerasimenko et al. (2020a). Additionally, the technique can be used to assess cell's ability to polarise with a differential protein expression at the apical-to-basolateral surface Zihni et al. (2016); Barrier (1981); Srinivasan et al. (2015). In a TER measurement, the electrical current can take two different paths; the paracellular or transcellular route (Figure 3.1B). In the paracellular route, current preferentially travels in space available between cells and it occurs at low frequency measurements ($< 1kHz$). At these lower frequencies, cell's lipid bilayer capacitance acts as an open circuit and the measured signal is predominantly related to tight junction formation and barrier tightness. At higher frequencies ($> 1kHz$), the current flows through cell's cytoplasm (transcellular route), with measured resistance correlated to surrounding cell medium resistance Yeste et al. (2018); Gerasimenko et al. (2020b); Benson et al. (2013).

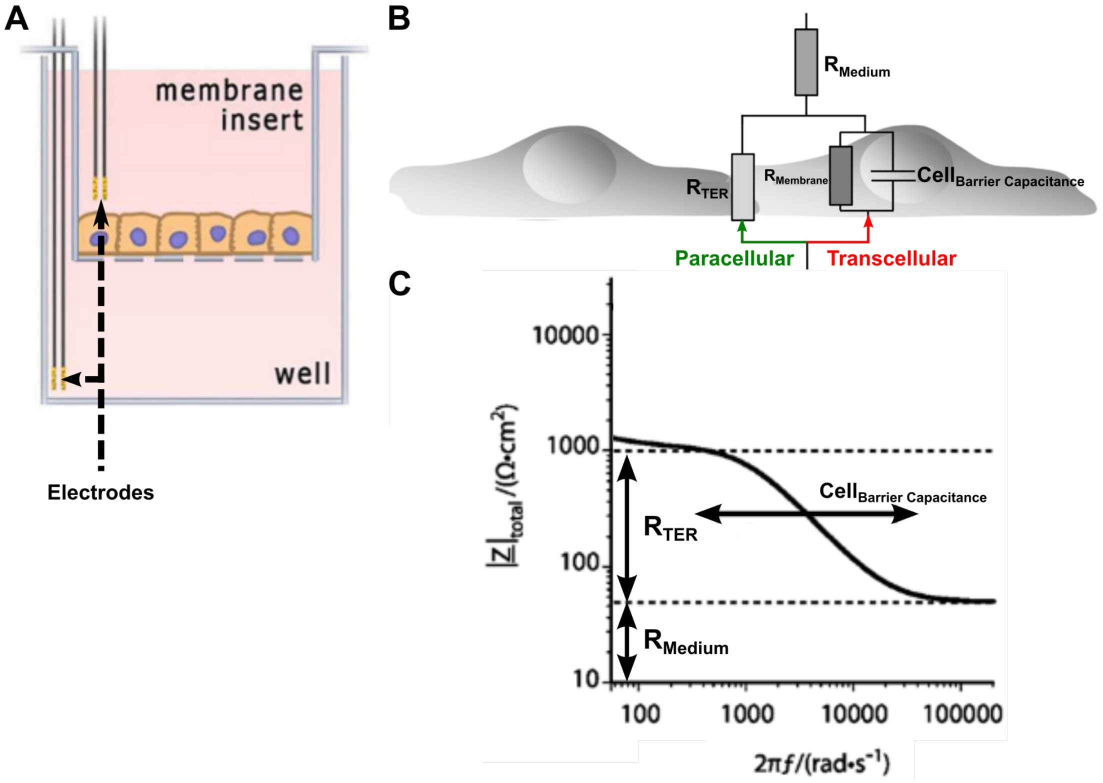

FIGURE 3.1: (A) Typical electrode placement for TER measurements, with electrodes in a *trans* configuration (above and below cell culture). (B) Display of signal routes when measuring TER, with paracellular route between adjacent cells and transcellular route through cells cytoplasm. (C) Magnitude of impedance over a range of frequencies (100 to 100000 Hz) when measuring TER with setup from (A), with lower frequencies characterized by TER (R_{TER}), higher frequencies by cell medium resistance (R_{Medium}). Cell barrier resistance defines at which frequency the electrical signal route changes from paracellular to transcellular. (A) from Gerasimenko et al. (2020a), (B) and (C) from Benson et al. (2013).

Standard methodologies for TER acquisition typically use single frequency measurements at low frequencies (12.5 Hz), higher frequencies measurements can provide important information about cells barrier capacitance over time Benson et al. (2013); Gerasimenko et al. (2020a). Alternatively, both TER and cell barrier capacitance can be assessed using electrical impedance spectroscopy, in which an electrical signal is applied between electrodes in a range of frequencies, providing more information regarding cell barrier integrity and morphology (Figure 3.2A) Gerasimenko et al. (2020a); Arlk et al. (2018); Odijk et al. (2015); Yeste et al. (2018).

Electrode placement during impedance measurements will affect the electric signal pathway, depending if these are placed in a *cis* or *trans* configuration (figure 3.2BC). Electrodes in a *trans* configuration are placed above and below the cell culture, while electrodes in a *cis* configuration are placed parallel to each other below the cell culture. TER values vary depending on the type of epithelial tissue being measured, where intestinal epithelia have a low TER value, due to the high nutrient absorption rate and leaky structure in intestinal epithelia, while airway epithelia have a high TER value, due to the exposure of this cell layer to components from the inhaled environment (e.g air dust and pathogens), Diamond (1977).

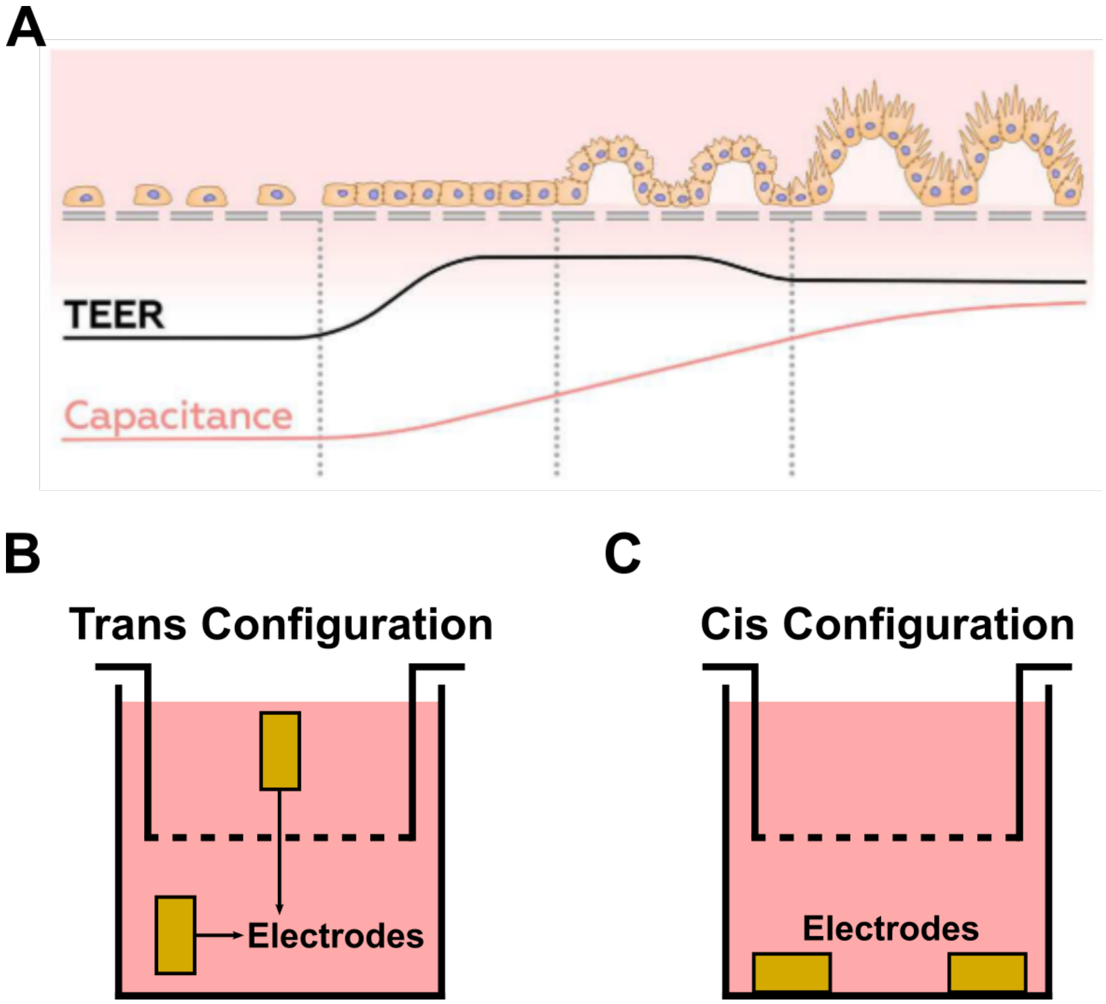

FIGURE 3.2: (A) TER and cell barrier capacitance values dependency on cell barrier formation and morphology, with increased barrier tightness resulting in a sharp TER increase while formation of 3D structures such as microvilli (gut epithelial cells) lead to an increase of capacitance. (B) and (C) Schematics for electrode placement configuration during TER measurements, with *trans* configuration having electrodes in the apical and basolateral compartments while *cis* configuration has two coplanar electrodes located underneath the cell culture. (A) from Gerasimenko et al. (2020a).

Measurements of TER involves the submersion of electrodes in conductive liquids.Although the submersion of electrodes into an electrolyte solution always creates an ionic double layer, the application of an electrical signal between submerged electrodes leads to the rapid movement of dissolved free ions towards the interfacial regions between the electrode surface and surrounding liquid (Figure 3.3A). The resulting ionic double layer, which is more pronounced comparatively to the absence of electrical signal, formation at these regions affects the electrical measurement, with the capacitance, and impedance, of this layer capable of dominating the signal and masking the sample at lower frequencies (Figure 3.3B). Formation of this layer can depend on the sample conductivity, temperature, electrode structure, composition and surface area Ishai et al.

(2013b); Schwan (1968); Hoffmann et al. (2006). Additionally, electrochemical reactions occurring at the electrode's surface can either inhibit or exacerbate this effect. One such example are the commonly used silver/silver-chloride ($Ag/AgCl$) electrodes, in which a silver electrode is coated with its chloride salt. When an electrical potential is applied between $Ag/AgCl$ electrodes, a redox reaction takes place at the interface between electrodes surface and surrounding solution (equation 3.1).

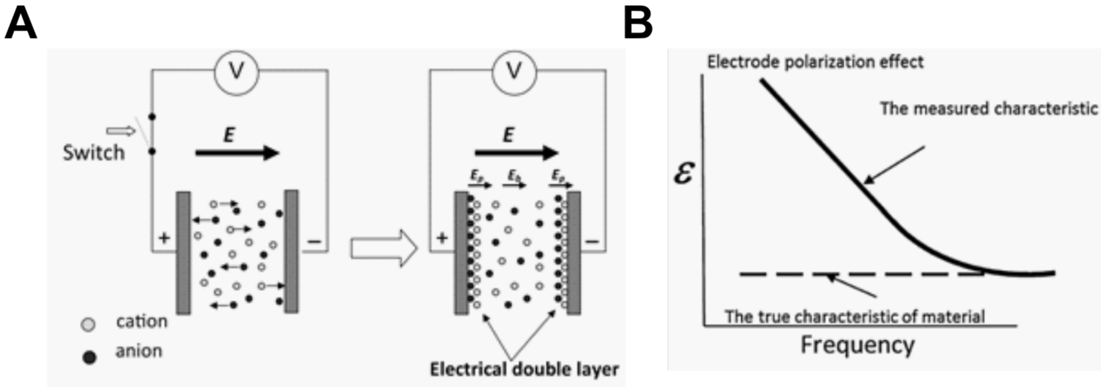

FIGURE 3.3: Electrode polarization schematic displaying the formation of an electrical double layer on the electrode's surface (A) and it's effect in the measured impedance throughout a frequency range (B). From Ishai et al. (2013b)

$$AgCl(s) + e^{-} = Ag(s) + Cl^{-} \tag{3.1}$$

Due to fast reaction kinetics, there is no accumulation of charge at the interfacial region and no formation of an ionic double layer, since electrical charges reaching the electrodes surface are quickly transferred to the conductive solution as chloride ions (Cl^{-}). In addition, silver ions are also release to the surrounding solution as a reaction product, which are cytotoxic to biological samples. Therefore, although Ag/Cl are close to ideal non-polarisable electrodes, these cannot be used for long term measurements of biological samples due to cytotoxicity.

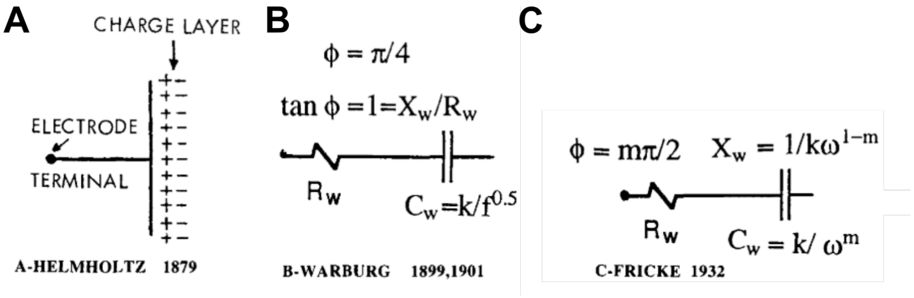

FIGURE 3.4: (A) Helmholtz's model of physical phenomenon occurring at the electrode-electrolyte interfaces with the formation of a double layer of charge at these regions. (B) and (C) represent Warburg's and Fricke's proposed electrical circuit models for double layer capacitance and resistance at low current densities with application of alternating current. From Geddes (1997)

The first model of electrode-electrolyte interface was proposed by Helmholtz, in which the ionic double layer was modelled as a double layer of charge at the interface region (Helmholtz layer; Figure 3.4A). Due to its similarity to a charged capacitor, it became evident that any future model would need to include this capacitive behavior. Additionally, the increased resistance of this layer to electrical current was also required in subsequent models Helmholtz (1879). The Warburg electrical circuit model (Figure 3.4B) was derived from these assumptions, as the impedance of this interfacing layer would arise from the unrestricted diffusion of ions to a large planar electrode surface, with capacitance inversely proportional to the square root of frequency and a constant phase angle at 45 ∘. In this model the polarization layer reactance is equal to its resistance, with the same dependency to the square root of frequency. This model was only valid at infinitely low current density measurements and was not capable of modelling direct-current behaviors Warburg (1899, 1901). Due to these limitations, Fricke proposed another circuit model (Figure 3.4C) for low current density and measurements between the frequencies of 100 and 3500 Hz. With this model and conditions, the electrode capacitance (C_w) and signal phase angle (ϕ) were given by $C_w = k/\omega^m$ and $\phi = m\pi/2$ respectively, with k and m values characteristic of the electrode material Geddes (1997). Lastly, constant phase elements (CPE) have been used to model both capacitive and resistive behaviours of polarized electrodes, in which the double layer impedance is characterized as being an imperfect capacitor. CPE impedance (equation 3.2) is defined by the CPE magnitude (Q) and exponent ($0 < \alpha < 1$), with Q being the electrodes capacitance magnitude and α it's level of deviation from a perfect capacitor. While the CPE is not described by discrete elements such as resistors, capacitor or inductors, specific values of α simplify the component to discrete elements. For instance, if $\alpha = 1$ the CPE is a capacitor with Q capacitance and if $\alpha = 0$ the CPE is a resistor with a resistance of Q^{-1} Láng and Heusler (1998).

$$Z_{CPE} = \frac{1}{Q} \times (j\omega)^{-\alpha} \tag{3.2}$$

Electrode surface coatings and four-terminal/three-terminal sensing can be used to minimise the effect of electrode polarization on electrical impedance measurements. During an electrical measurement, current from the electrode is converted into an ion flowing in solution and vice-versa, with electrochemical reactions occurring at this interface highly dependent on the electrode's material and surface area. As previously seen with Ag/Cl, coating a polarizable electrode with a cation containing salt leads to redox reactions at the interfacing regions, minimising electrode polarization at low frequencies Hoffmann et al. (2006). Additionally, increasing the electrode-electrolyte interface area, either by mechanical roughening or porous/fractal structure creation at the surface, minimises electrode polarization. Due to the ionic double layer capacitive behavior, increasing the electrodes capacitance leads to the decrease of capacitance of the electrode + interfacing region capacitance, which is in series with the sample. Covering the surface of platinum electrodes with platinum black leads to an extremely rough electrode surface, shifting electrode polarisation to lower frequencies comparatively to bare platinum electrodes Ishai et al. (2013a); Schwan (1968). Similar characteristics have been observed by Mingels et al. (2019) when covering platinum electrodes with ruthenium oxide, while it's deposition onto platinum electrodes is performed through sputtering instead of electroplating (as the case of platinum black). Additionally, four-terminal sensing uses two pairs of electrodes to measure the impedance across a substance. While one pair of electrodes supply a known value of current, the inner electrodes measure the resulting voltage differential. By separating the current and voltage electrodes and providing a high entrance impedance between the voltmeter and the electrodes, the contact resistance and capacitance can be ignored from the measurement, providing high-precision measurements of minute impedances when compared to simpler two-terminal sensing setups Chandra et al. (2017). Lastly, three-terminal sensing could also be used to measure the impedance across a substance. This setup consists of a working electrode, a counter electrode and a reference electrode. A signal is applied between the working and counter electrodes and an impedance signal can be obtained. The reference electrode is maintained in stable solution and acts as a reference when measuring and/or controlling the working electrode potential. The use of the reference electrode can facilitate the attenuation of polarization effects in the acquired data, but requires a more complicated setup to be used in a stable and robust manner comparatively to a two-electrode setup Onor et al. (2017).

Commercial systems capable of measuring TER in static cultures are available, such as the Epithelial Voltohmmeter (EVOM) and CellZscope systems for Transwell cultures and the Electric Cell-Substrate Impedance Sensing (ECIS) for cell coverage experiments. The EVOM (figure 3.5A) uses two pairs of electrodes housed in a "chopstick" handler and positions one pair of electrodes in the apical compartment and the other pair in the basal compartment, therefore measuring the cell culture TER in a *trans* configuration. The CellZscope (figure 3.5B) uses the same concept as the EVOM but both pairs of electrodes are in a fixed position, minimizing user interaction and human induced error in measurements due to placement or electrode movement during measurements. Additionally, electrical impedance spectroscopy measurements are recorded over a range of frequencies, providing information regarding TER and cell barrier capacitance. Unfortunately, both these systems suffer from the same limitation when measuring TER cell cultures requiring an ALI environment (such as lung or skin cells), as TER can only be measured after submerging the apical compartment. Lastly, the ECIS system (figure 3.5C) uses electrodes in a *cis* configuration and is used to assess cell growth, directly on top of the electrodes, and electrode coverage, thus is not suitable for epithelium cell experiments which require the use of a porous support, necessary for cell polarisation and differentiation Anwer and Szászi (2020).

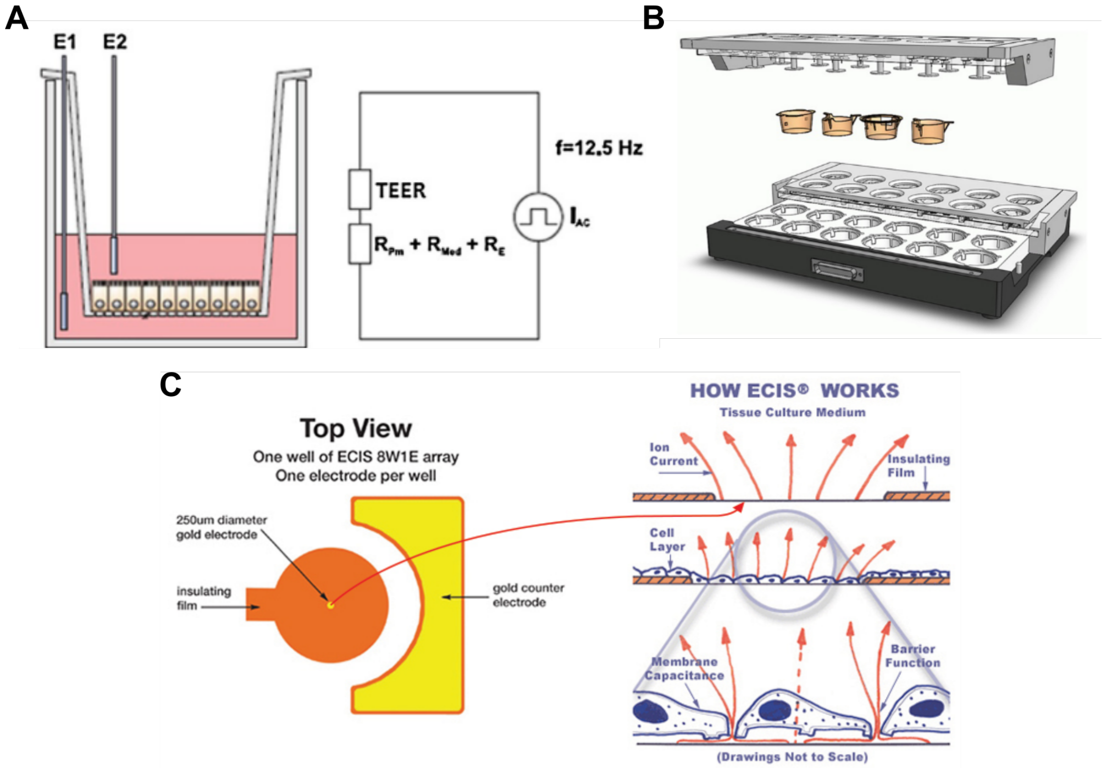

FIGURE 3.5: (A) EVOM chopstick electrodes are placed in a *trans* configuration for cell barrier integrity assessment through TER measurements. Two pairs of electrodes are located in each chopstick, with one pair applying an alternating current at 12.5 Hz and the other pair measuring the resulting resistance. (B) The CellZscope system utilises fixed electrodes in a *trans* configuration similarly to the EVOM system. (C) The ECIS system uses electrodes in a *cis* configuration and cells are directly cultured on top of the electrodes. It is mainly used for cell growth and coverage assessment. (A) and (B) from Benson et al. (2013), (C) from Applied BioPhysics.

Integration of EIS into OoC platforms has been used to analyse barrier integrity, not only providing data regarding epithelia barrier resistance but also epithelial barrier capacitance, which correlates to the cell membrane surface area and provides information regarding cell stacking or even development of complex membrane structures such as microvilli van der Helm et al. (2019); Tavares et al. (2020); Sriram et al. (2018); Wufuer et al. (2016); Ashammakhi et al. (2020); Huh et al. (2010); Ghaemmaghami et al. (2012); Nguyen et al. (2019); Song et al. (2018); Humayun et al. (2018); Doryab et al. (2016). Electrodes built into OoC devices allow for continuous data collection of cell barrier characteristics but usually require specific electrode positioning and conditions Zhang et al. (2018); Arlk et al. (2018); Odijk et al. (2015); Gerasimenko et al. (2020a); Ferrari et al. (2020). Typically, electrodes are placed on both sides of the epithelial barrier (*trans* configuration) and require submerged conditions to endure electrical connection between electrodes. In this case, the cell culture requires ALI conditions to grow and differentiate, the apical side of the culture will momentarily be submerged during TER measurements, similar to standard static cultures. Henry et al. (2017) utilised a four-terminal EIS configuration to assess airway epithelial barrier formation (Figure 3.6 A and B). The device has two pairs electrodes placed above and below the cell culture and measurements were taken periodically over a period of 65 days (56 days in ALI). Before ALI, the TER values taken averaged 200 Ω on day 4 and 500 Ω on day 6, confirming the growth of a tight monolayer. Once the cell culture was taken to ALI and differentiation medium used, the TEER values increased steadily from 500 Ω to 1700 Ω on day 62. During ALI cell culture, warm cell medium was introduced apically for 10 minutes to perform the TER measurement. Alexander et al. (2018a) cultured fibroblasts and EpiDermTM reconstructed human epidermis in an OoC device ALI, for each TER measurement, the apical layer was temporarily submerged in PBS using an automated pumping system (Figure 3.6 C).

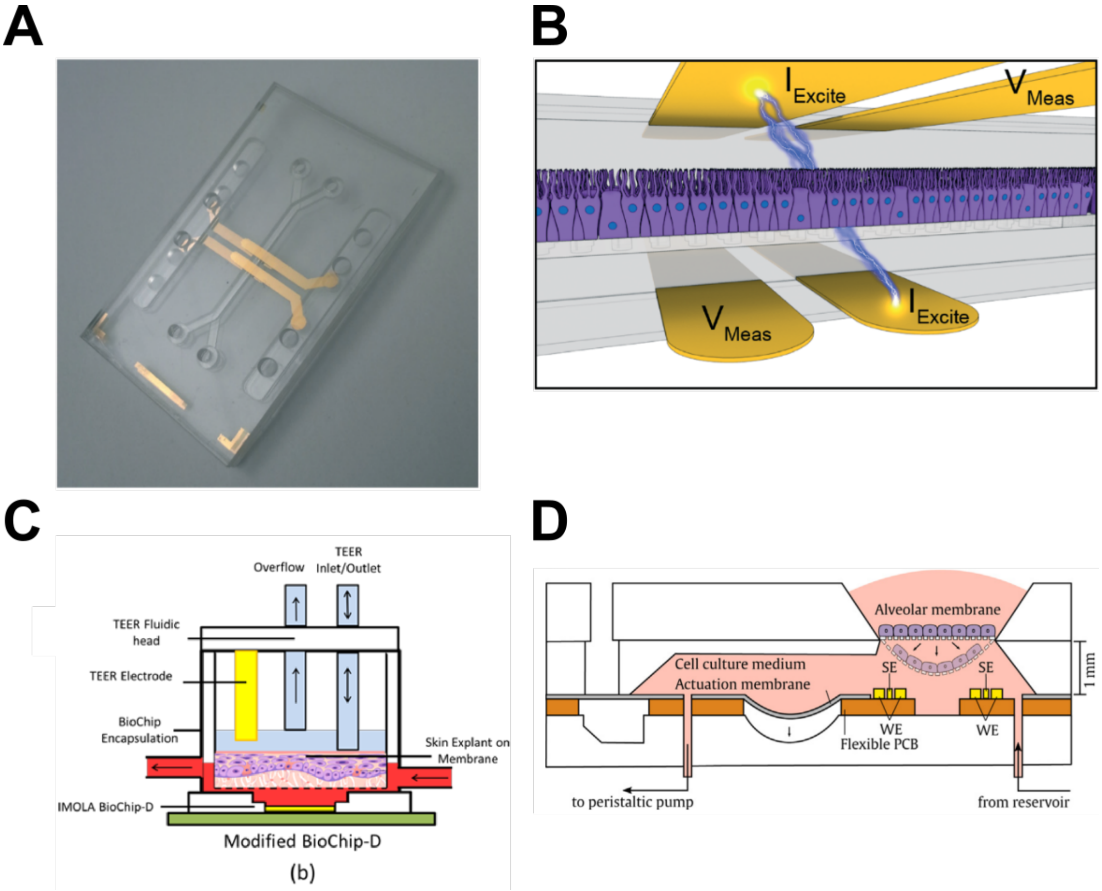

FIGURE 3.6: OoC device reported by Henry et al. (2017) (A), with two pairs of electrodes located above and below the cell culture for EIS measurements (B). The setup uses four-terminal sensing and allows for continuous measurements while the cell culture is submerged. The automated setup proposed by Alexander et al. (2018a) used to periodically measure the TER of ALI cell cultures under perfusion (C), where PBS is automatically dispensed and retrieved for measurements. Mermoud et al. (2018) device with the two pairs of electrodes located underneath the cell culture (D), allowing EIS measurements of ALI cell cultures

A system capable of recording TER without submerging the cell culture was demonstrated by Sun et al. (2010a) using dot and ring electrodes below Transwells. Airway epithelial cells were challenged using Triton X-100 or EGTA after a polarised monolayer was formed. Both challenges resulted in a decrease of the TER value, with a concentration dependent response. Mermoud et al. (2018), proposed a tetrapolar electrode design for TER measurement of airway epithelial cells (Figure 3.6 D). Electrodes were positioned 1 mm below the cell culture chamber parallel to each other. Human lung epithelial cells were cultured and challenged with Triton X-100 and impedance measurements displayed a decrease in TER following challenge.

The Organ-on-Chip platform used in UoS, previous iteration and work described in Chapter1 and improved version to be explained in Chapter4, uses electrodes in a *cis* configuration to perform regular electrical impedance measurements of the growing cell culture. Unfortunately, the data from said measurements encompasses all components which the signal travels through including the growing cell culture, cell medium, porous membrane (onto which the cells are grown) and the inherent electrode polarization. Post processing is required before the data acquired from the platform can be correlated to TER values stated in the literature, obtained from commercial systems such as the EVOM. To that goal a custom-made Python script was written which fits the acquired impedance data into an electrical circuit model, allowing the extraction of cell barrier resistance as a separate parameter and its conversion to a comparable value of TER.

3.2 Electrical Circuit Model

Impedance measurements carried out in the UoS Organ-on-Chip platform are possible due to two pairs of electrodes patterned on the surface of the glass chip component of the microfluidic chip, Figure 3.7. Detailed explanation on components, assembly and dimensions of the developed Organ-on-Chip platform is present in Chapter 4, with fabrication methods in A.2.2.2. The patterned electrodes are made onto glass with an adhesion layer of titanium, covered with platinum and finalised with a surface layer of ruthenium oxide, increase electrode's surface area and reducing existing polarisation effects in the interface between the electrode surface and cell medium. Sensitivity studies using different electrode geometries, regarding the cell electrodes, were previously performed by Reale et al,. Reale (2017) , in which the use of two circular parallel electrodes underneath the cell culture chamber resulted in the highest sensitivity of all electrode designs tested. Since there is a space between each electrode, this design has the added benefit of allowing visual inspection of the cell culture in real-time during experiments, assuming that the system can be placed into an appropriate optical setup. The media electrodes are composed of two parallel rectangular sections, which are larger than the microfluidic channel which sits above them. This is to account for any manual error while assembling the chip and maintaining maximum sensitivity and uniformity between these electrodes. While the glass chip has 5 total connection pads originating from the electrodes, only 4 of those pads are used for electrical connection, with the middle pad not having any function.

The fitting algorithm aims to utilise fitted variables from the media electrode as strict boundaries on most of the variables regarding cell electrode data fitting, with the final objective of obtaining a TER equivalent, which can be correlated to TER values measured in standard Transwell supports and other OoC platforms.

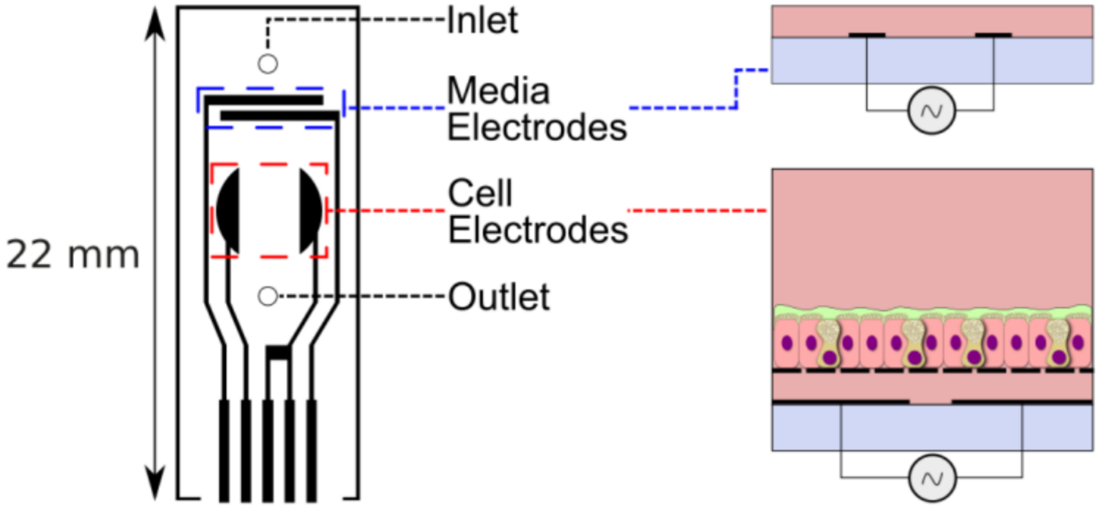

FIGURE 3.7: Schematic of the two pairs of electrodes present in the microfluidic chip and representation of it's cross-section during cell culture, with the red line pointing to the cell electrodes and the blue line to the media electrodes. Circles in the chip represent the fluidic inlet and outlets

3.2.1 Media Electrode

The media electrode is responsible for impedance measurements upstream of the cell chamber, obtaining parameters regarding electrode characteristics and cell medium. The use of two-terminal sensing entails the existence of polarization in the interface between electrodes and surrounding cell media, leading to the formation of an electrical double layer. This effect was modelled as a CPE (equation 3.2). Surrounding cell media is an electrically conducting solution which was modelled as a resistor ($R_{CellMedia}$), with it's capacitance being negligible in the overall system. The final electrical circuit model for the media electrodes is shown in equation 3.3 and Figure 3.8.

$$Z_{MediaElectrode} = Z_{CPE} + R_{CellMedia} \tag{3.3}$$

3.2.2 Cell Electrode

The cell electrodes are located directly underneath the cell culture chamber and assess cell media resistance ($R_{CellMedia}$), electrode characteristics (CPE) and cell barrier resistance ($CB_{Resistance}$) and capacitance ($CB_{Capacitance}$) through impedance spectroscopy. The

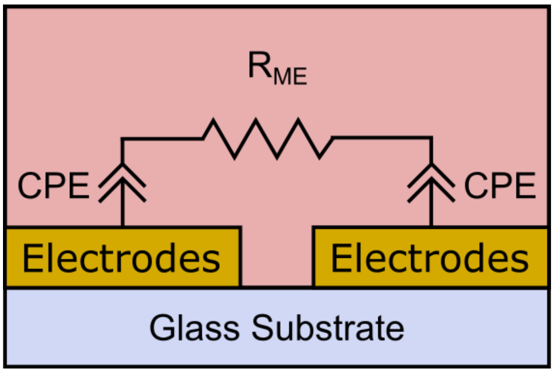

FIGURE 3.8: Equivalent electrical circuit model for the media electrodes in which R_ME represents the medium resistance and CPE the constant phase element for the electrode double layer capacitance.

cell chamber is divided by the high porous membrane into two separate compartments; the basolateral compartment, where cell medium provided flows underneath the cells at 30 μL/hour, and the apical compartment, where epithelial cell barrier formation occurs, with presence of cell medium (100 µL) for LLI cultures or absence of cell medium for ALI cultures.

Similarly to the media electrode, electrode characteristics can be modelled using a CPE element, extracting both the CPE magnitude and exponent, and cell media can be modelled as a resistor. Information regarding cell media resistance needs to be separated between existing compartments in case of the existence of cell medium in the apical compartment of the microfluidic chip. Thus, the resistance given by cell medium located in the basolateral and apical compartments were denominated as basolateral resistance (R_B) and apical resistance (R_A) respectively. Cell barrier impedance (Z_{CB}) grown in the microfluidic chip was modelled as a resistor (R_{CB}) (equation 3.4), modelling the ohmic resistance given by tight junctions when current travels the paracellular route, and capacitor (C_{CB}) (equation 3.5), due to the lipid bilayer capacitive characteristics, in parallel (equation 3.6). Additionally, citosolic resistance was ignored in the final equation due to it's negligible value when compared to other components in the circuit.

$$ZR_{CB} = R_{CB} \tag{3.4}$$

$$ZC_{CB} = \frac{1}{j\omega C_{CB}} \tag{3.5}$$

$$Z_{CB} = ZC_{CB}||ZR_{CB} = \frac{ZR_{CB} \times ZR_{CB}}{ZR_{CB} + ZR_{CB}} \tag{3.6}$$

Lastly the resistance of the nanoporous support membrane onto which cells are seeded was modelled following Hall (1975), where pores were modelled as cylindrical channels (equation 3.7) with fixed conductivity defined by their geometry (L being the pore lenght and r its internal radius) and media conductivity (σ) in conjunction with a pore access resistance (equation 3.8). The total resistance per pore was the subsequent sum of the pore resistance and corresponding access resistance, as seen in equation 3.9. The total resistance of the nanoporous membrane is then calculated as a parallel resistor of all pores through which the electric field passes (equation 3.10). The nanoporous membrane used in the OoC platform contains pores with 200 nm radius, 10 μm in length and a pore density of 10^8 pores/cm^2. Assuming that the cell media has a conductivity of 1.5 S/m and the surface onto which cells are cultured has a total area of 0.2 cm^2, the resulting nanoporous membrane resistance is 13.3 Ω. Since this value is much smaller than and in series with R_A, the two were assigned to a single variable in the final electrical circuit model.

$$R_{Pore} = \frac{L}{\sigma \pi r^2} \tag{3.7}$$

$$R_{Access} = \frac{1}{4\sigma r} \tag{3.8}$$

$$R_{PoreTotal} = R_{Pore} + R_{Access} = \frac{1}{\sigma r}\left(\frac{L}{\pi r} + \frac{1}{4}\right) \tag{3.9}$$

$$R_{NanoporousMembrane} = \frac{4 \times R_{PoreTotal}}{PoreDensity \times SurfaceArea} \tag{3.10}$$

The complete electrical circuit model equation for the cell electrodes is described by equation 3.11 and can be seen in figure 3.9.

$$Z_{CellElectrode} = Z_{CPE} + \left[\left(2 \times \frac{R_{CB}}{j\omega C_{CB} R_{CB} + 1} + R_A\right)^{-1} + \frac{1}{R_B}\right]^{-1} \tag{3.11}$$

3.2.3 Mathematical Algorithm for TER Extraction

Using the defined electrical circuit models for both the media and cell electrodes, the workflow (figure 3.10) for cell barrier resistance and capacitance extrapolation worked as follows:

1. Data from EIS measurements (magnitude of impedance (A) and phase angle(θ)) was converted into real and imaginary values using equation3.12.

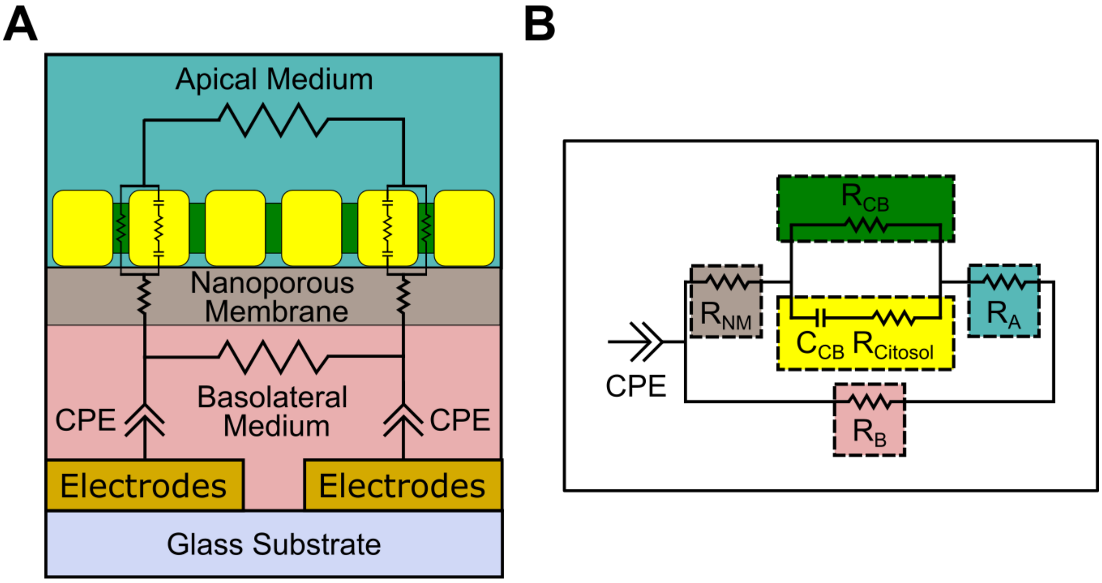

FIGURE 3.9: Electrical circuit model for the cell electrodes (A). Simplified version is shown in (B), with R_A and R_B the basolateral and apical medium resistance respectively, R_{NM} the nanoporous membrane resistance and R_CB the cell barrier resistance and C_CB the cell barrier capacitance respectively.

2. Media electrode data was fitted to the electrical circuit model, extracting values of CPE magnitude, CPE exponent and cell media resistance.
3. Extracted values are used to determine upper and lower boundaries for variables used in the cell electrode data fitting.
4. Cell barrier resistance was multiplied by the total surface area onto which the epithelial cell barrier was cultured, resulting in a TER equivalent.

$$Real = A \times cos(\theta); Imaginary = A \times 1j \times sin(\theta) \tag{3.12}$$

For the purpose of using the values obtained through the media electrode data fitting as boundaries and starting points for the cell electrode fitting process, differences between chamber geometries and electrode surface characteristics and area need to be considered.

The CPE exponent (α) defines how capacitive or resistive the electrode polarized surface is. Since both electrode pairs undergo the same ruthenium oxide deposition, it can be assumed that both electrode pairs would have similar values of CPE exponent. Thus, the CPE exponent obtained from the reference electrode can be directly used to set boundaries for the fitting of the CPE exponent of the cell chamber electrode without adjustments (equation 3.13).

$$\alpha_{CellElectrode} = \alpha_{MediaElectrode} \tag{3.13}$$

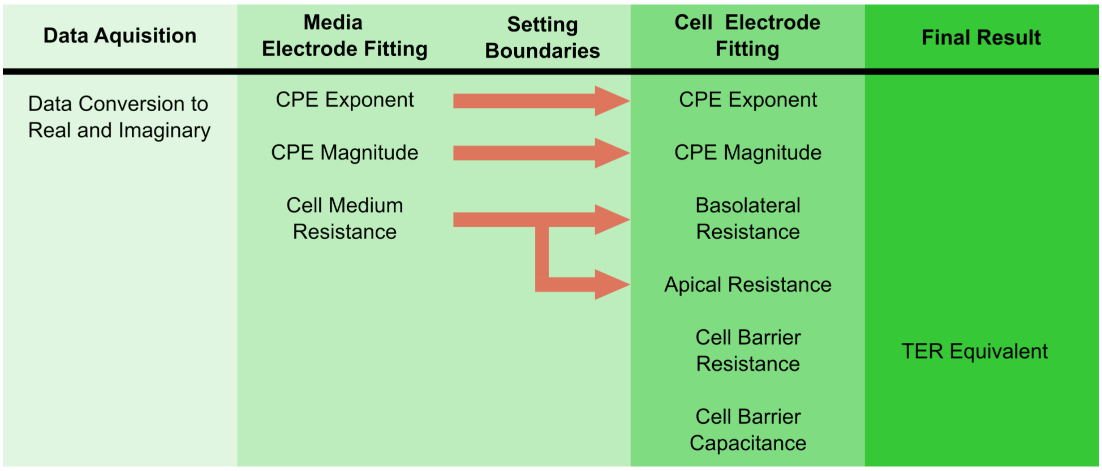

FIGURE 3.10: Schematic showing the workflow of the fitting algorithm. Data is first converted from magnitude of impedance and phase angle into real and imaginary components. Following this, the media electrode variables are fitted to the electrical circuit model. These variables are then used to set the boundaries required for the cell electrode fitting, which extracts the cell barrier resistance and capacitance.

The CPE magnitude (Q) defines the magnitude of how resistive/capacitive the electrode polarized surface is during measurements. Thus, the different electrode surface areas need to be considered when setting boundaries for the cell chamber electrodes, with the cell electrode having approximately 2.3 times more surface area comparatively to the media electrode (equation 3.14).

$$Q_{CellElectrode} = Q_{MediaElectrode} \times 2.3 \tag{3.14}$$

Adjustment of the cell media resistance values obtained from the media electrodes for cell electrode data fitting was performed using the respective measured chambers geometrical cell constants. The cell constant is a geometrical constant defined by the electrode areas, the gap between the electrodes and resulting electrical field pattern. Resistance of an electrolyte with conductivity σ and contained in a chamber with a cell constant of k is given by:

$$R = \frac{1}{\sigma \times k} \tag{3.15}$$

Cell constant values were obtained using conformal mapping and finite element method (FEM) simulations. Reference electrodes are coplanar and rectangular, with a width and length of 2.8 and 0.5 mm respectively, with a gap of 0.2 mm between the pair and a microfluidic channel height of 0.3 mm. The cell electrodes are coplanar and have a half-circle shape, with a maximum length of 1.1 mm, width of 2.07 mm and a gap between electrodes of 2.8 mm. The basolateral and apical height are 0.3 and 5.3 mm respectively, assuming a total volume of 100 μL present in the apical compartment of the microfluidic chip. Both electrode pairs are represented in the figure below, with the microfluidic channel outline represented by the dashed blue line.

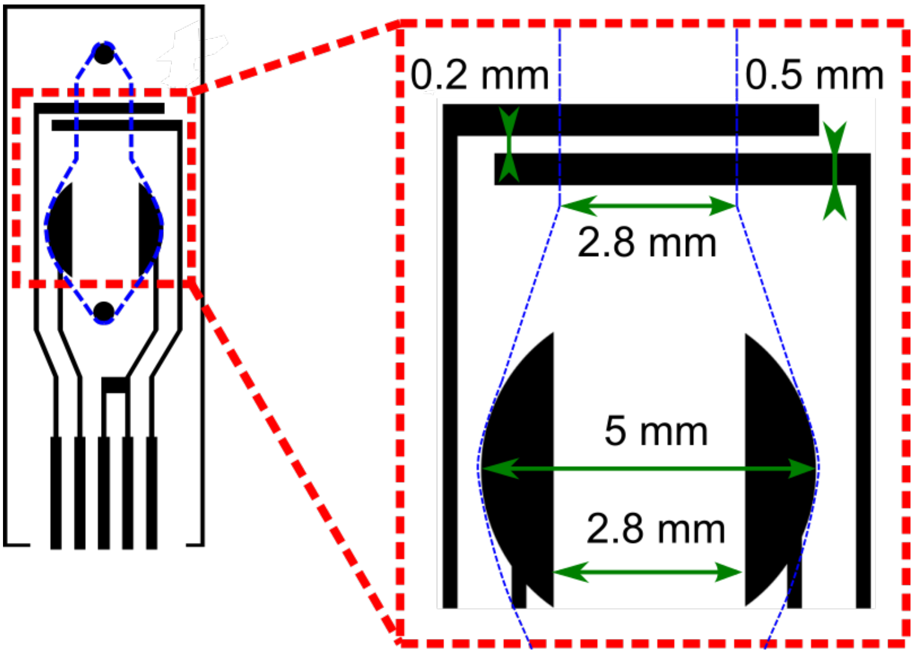

FIGURE 3.11: Schematic detailing each dimension of the electrodes in the microfluidic chip. These dimensions were used to calculate the geometrical cell constants of each compartment in the chip by conformal mapping and FEM simulations.

Conformal mapping is an angle-preserving transformation, allowing complex physical problems, due to inconvenient geometries, to be transformed into a problem with more convenient geometry, while preserving the original complex angles and shapes. This method can be used to transform complex non-uniform electrical fields into simpler linear electrical fields. Sun et al. (2007) proposed the use of Schwarz-Christoffel mapping (SCM) method for electrical field distributions between co-planar electrodes. Using SCM, a nonuniform two-dimensional field with a polygonal shape was altered into an equivalent rectangular region, in which the electric field distribution was uniform. Using this method, the electrical cell constant (k) of the electrical field generated by co-planar electrodes is given by the equations below, in which L and w represents the electrode length and width respectively, g the gap between electrodes and h the height of the chamber which houses the electrodes. T_A, T_B, T_C and T_D represent geometrical points used in the SCM process and K the complete elliptic integral of the first kind. While equation 3.22 can be directly applied to the media electrodes, the cell electrodes are not rectangular. Each half circle electrode was divided into numerous smaller rectangular shaped electrodes. The total geometrical cell constant equated to the sum of the cell constant computed from each smaller rectangular electrode. An example of the cell electrode simplification is shown in Figure 3.12. Using this approach, the cell constant values calculated using conformal mapping for the media electrode chamber and cell electrode basolateral and apical chambers were $1.8 \times 10^{-3} m^{-1}$, $3.8 \times 10^{-4} m^{-1}$ and $1.5 \times 10^{-3} m^{-1}$ respectively.

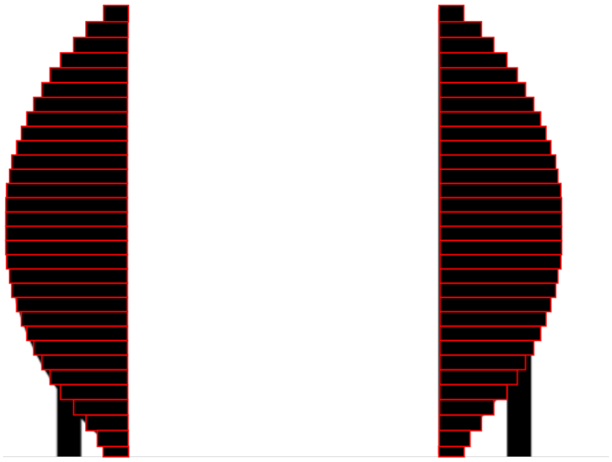

FIGURE 3.12: Approach taken to extrapolate the geometrical cell constant from the half-circle shaped electrodes with conformal mapping. The half-circle shape was split into numerous rectangles, for which the conformal mapping calculations are possible. Results from all the rectangles are then added together to obtain an approximation to cell constant of the original electrode.

$$T_A = \left[cosh\left(\frac{\pi \times (g + 2 \times L)}{4 \times h}\right)\right]^2 \tag{3.16}$$

$$T_B = \left[cosh\left(\frac{\pi \times g}{4 \times h}\right)\right]^2 \tag{3.17}$$

$$T_C = 1 \tag{3.18}$$

$$T_D = 0 \tag{3.19}$$

$$k_b = \sqrt{\frac{(T_A - T_D) \times (T_B - T_C)}{(T_A - T_C) \times (T_B - T_D)}} \tag{3.20}$$

$$k_{b2} = \sqrt{1 - k_b^2} \tag{3.21}$$

$$k = \frac{K(k_{b2})}{K(k_b) \times 2} \tag{3.22}$$

Finite element methods are used to solve partial differential equations in two or three dimensional spaces. This is achieved by subdividing the overall system into smaller and simpler parts, denominated finite elements, through space discretization. The simpler equations which model each of the smaller finite elements are assembled into a larger system of equations, modelling the behavior of the larger system. COMSOL was used as the FEM software for cell constant extraction, using the Electric Currents physics module. Reference and cell electrode chambers were designed according to the specifications shown in 3.11 (detailed geometries in appendix A.1.1). The electrodes and surrounding electrolyte conductivity (σ) was set to 1 S/m and a potential difference (V) of 1 V was applied between the electrodes. Resulting current (I) was measured in a static study and cell constants for each chamber were calculated by resolving equation 3.15, as seen below. Figure 3.13 displays the potential difference (colortable) and current density (streamlined arrows) in the COMSOL simulations for each pair of electrodes. Thus, cell constants for the media electrodes, basolateral and apical compartments have a value of $1.87 \times 10^{-3} m^{-1}$, $2.64 \times 10^{-4} m^{-1}$ and $1.46 \times 10^{-3} m^{-1}$ respectively. Additionally, calculated geometrical cell constants already account for variations in electric field distribution across the chamber. This is especially important at the porous membrane, where the applied electric field ranges from 200 to 400 V/m depending on distance to electrodes (Figure 3.14)

$$k = \frac{1}{\sigma \times R} = \frac{1}{1 \times \frac{V}{I}} = \frac{I}{V} = I \tag{3.23}$$

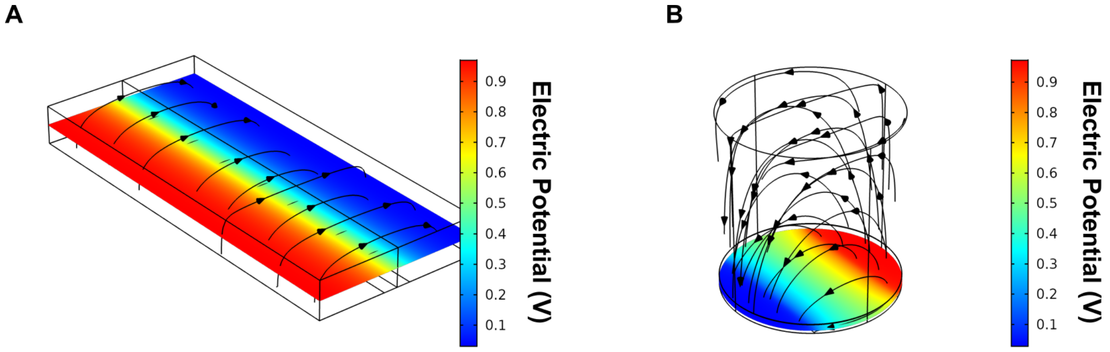

FIGURE 3.13: COMSOL simulations of electrical field distributions in the microfluidic chip for geometrical cell constant extraction for the media (A) and cell (B) electrodes compartments. An electric potential difference of 1 V was established between electrodes. Current density at the electrode's surface was average to their surface area and used to calculate the geometrical cell constants

Due to the similar values obtained via conformal mapping and COMSOL simulations, geometrical cell constants gathered via COMSOL simulation were used, with a value of $1.87 \times 10^{-3} m^{-1}$, $2.64 \times 10^{-4} m^{-1}$ and $1.46 \times 10^{-3} m^{-1}$ for the media electrodes compartment and cell electrodes basolateral and apical compartments respectively. Therefore, cell media resistances for the basolateral and apical compartments of the cell culture chamber were calculated using equations 3.24 and 3.25 respectively. Calculations are based on the assumption that cell media conductivity does not vary between media and cell electrodes, allowing cell media resistance correlation between chambers using equation 3.15.

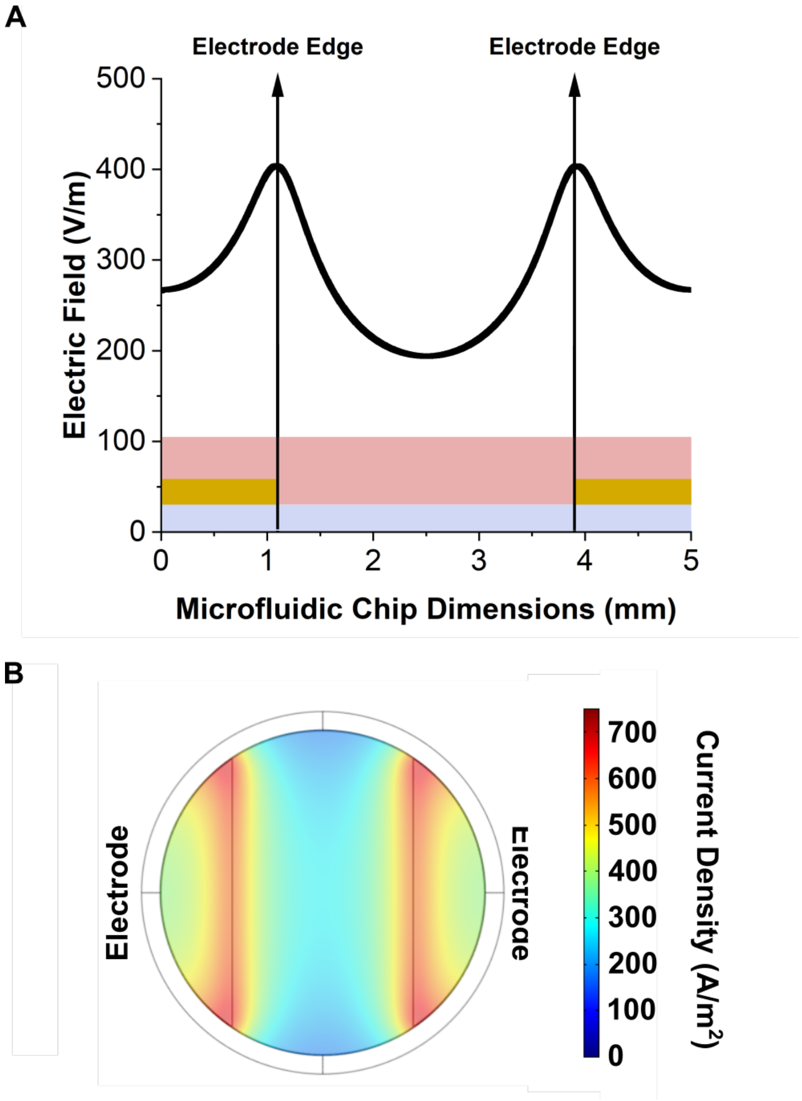

FIGURE 3.14: (A) COMSOL simulation of electric field magnitude across the porous membrane. (B) Current density across the porous membrane surface.

$$R_B = R_{CellMedia} \times \frac{MediaElectrode_{CellConstant}}{Basolateral_{CellConstant}} \tag{3.24}$$

$$R_A = R_B \times \frac{Basolateral_{CellConstant}}{Apical_{CellConstant}} \tag{3.25}$$

To fit the complex data acquired from the impedance analyser, parameters need to be extracted from two sets of data, real and imaginary, simultaneously. For this purpose, complex non-linear least squares function was used to define the objective function as the weighed sum of squared residuals from both real and imaginary data components (equation 3.26). The Nelder-Mead algorithm was then used to minimise the objective function and extract the required values from the complex set of data. The algorithm maps each variable of interest as vertices of a simplex and sequentially minimises its size as new minimum values for each variable are found. The best fitted values correspond to the ones that resulted in the smallest sized simplex.

$$Obj = \sum_{i=1}^{f_N} \sqrt{\frac{\left(Real_{Data_i} - Real_{Model_i}\right)^2]}{Real_{Data_i}} + \frac{\left(Imaginary_{Data_i} - Imaginary_{Model_i}\right)^2}{Imaginary_{Data_i}}} \tag{3.26}$$

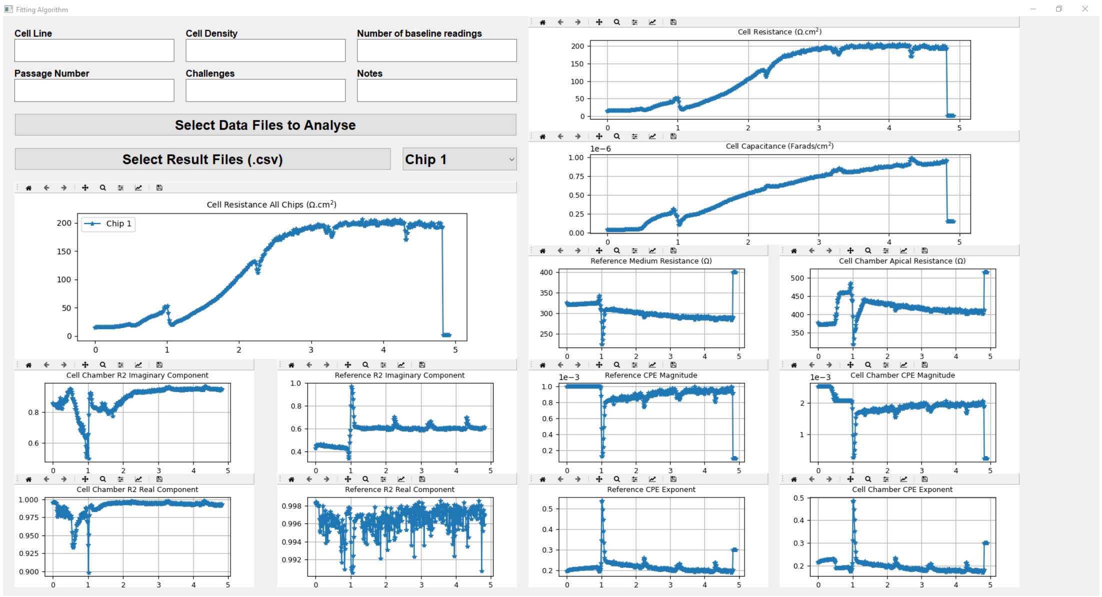

FIGURE 3.15: Graphical user interface created for EIS data modelling software. Experimental details can be included in appropriate text boxes. Once files are analysed, media and cell electrodes parameters are displayed in respective plots and the user can visualise detailed data for one specific chip at a time. Detailed use instructions for software present at appendix A.1.2

The complete fitting algorithm was programmed in Python (code in Appendix A.1.2) and was programmed with a graphical user interface (GUI) seen in Figure 3.15, increasing it's ease of use for future users. The program displays the values of each fitted variable over the required time range and provides a measurement of accuracy, by computing the R^2 for both the real and imaginary components of the original data. Instructions on how to use the software are present in Appendix A.1.2.

3.3 Calibration Experiments

To validate the model, two experiments were initially performed before computing cell growth data. The first experiment tested the model accuracy at determining the numerous variables without the presence of cells in the microfluidic chip. For this purpose, Minimal Essential Medium (MEM) was perfused basolaterally (at 30 μL/hour) through 8 microfluidic chips in parallel for 12 hours, with 100 μL of MEM placed in the apical chamber of each chip. Information regarding the microfluidic chip structure, materials and fabrication is found in Chapter4. EIS data was collected from each chip every 17 minutes during the experiment. Data was fitted to equations 3.3 and 3.11 for the media and cell electrodes respectively, with the removal of cell components ($R_{CB} = 0$ and $C_{CB} = 0$) from the cell electrodes fitting. Mean values and standard deviation for medium resistance and electrode CPE are summarised in tables 3.1.

Media electrodes

	Culture Medium Resistance (Ω)	CPE Magnitude	CPE Exponent
Average	376	4.2×10^{-5}	0.6
Standard Deviation	14.0 (3.7%)	1.1×10^{5} (28.3%)	0.04 (6.7%)

Cell electrodes

	Apical Resistance (Ω)	CPE Magnitude	CPE Exponent
Average	467	9.2×10^{5}	0.64
Standard Deviation	18.8 (4%)	3.1×10^{5} (34 %)	0.44 (6.25 %)

TABLE 3.1: Electrical parameters for the media and cell electrodes determined from EIS measurements over 12 hours. Average and standard deviation for culture medium resistance (apical resistance in the cell electrodes), CPE magnitude and CPE exponent collected from 8 microfluidic chips running in parallel in the OoC platform with MEM cell medium basolateral perfusion

Both cell culture medium resistance and CPE exponent have low standard deviation, while the CPE magnitude proved to be more variable between microfluidic chips. This increased deviation may be due to variations in the electrode surface area arising from the manual assembly of each microfluidic chip and variability in the metal oxide deposition onto the electrodes.

Cell culture medium resistance values were converted to conductivity using equation 3.15, resulting in a cell culture medium conductivity of 1.41 and 1.46 S/m for the media and cell electrodes respectively. Using a commercially available conductivity meter (YSI Conductivity Meter 3200), a value of 1.456 S/m was obtained for the cell medium conductivity, closely matching the value obtained with the fitting algorithm. Additionally EIS measurements with two microfluidic chips with and without the nanoporous support membrane were performed and resulted in a difference of approximately 14 Ω of magnitude of impedance at 1000 Hz between them. This value is similar to the nanoporous support electrical resistance previously calculated and negligible compared to the culture medium resistances. Additionally, due to the small standard deviation regarding cell culture medium resistance over the 12 hours, it can be concluded that the electrode surface is not being adversely affected by electrolyte flow on it's surface over this period of time.

The second experiment tested the model's accuracy at detecting cell barrier resistance. For this purpose, a non-conductive PMMA disk was placed on top of the nanoporous membrane in 1 microfluidic chip and 1 Transwell support. The disks had 1 mm in height and covered approximately 70% of the surface area of both the microfluidic chip and Transwell support. Cell culture medium was placed on the basolateral (500 μL) and apical (100 μL) compartments of Transwells and the disk was located in the apical compartment on top of the support membrane. Resistance measurements were taken with chopstick electrodes connected to an EVOM before and after placing the PMMA disk in the apical compartment. In the microfluidic chip, cell culture medium was perfused basolaterally and 100 μL placed in the apical compartment. EIS measurements were taken between 1 and 100 kHz before and after placing the PMMA disk in the apical compartment. Data obtained through EIS was then fitted using equations 3.3 and 3.11 for the media and cell electrodes respectively, with the removal of cell barrier capacitance ($C_{CB} = 0$) from the cell electrodes fitting. Resistance values were multiplied by the Transwell (0.33 cm^2) and microfluidic chip (0.2 cm^2) membrane surface area for data normalisation and comparisons.

	Transwell		**Microfluidic Chip**	
PMMA Disk	No	Yes	No	Yes
Measured Resistance (Ω)	200	262	20.3	140.3
Normalised disk Resistance ($\Omega.cm^2$)	20.5		24.0	

TABLE 3.2: Resistance data from Transwell and microfluidic chip with and without a PMMA disk in the apical compartment. Data was normalised by multiplying resistance values by the respective membrane surface area (0.33 cm^2 for Transwell supports and 0.2 cm^2 for microfluidic chips).

Results are shown in table 3.2 and confirm the accuracy of the proposed fitting algorithm, with a disk resistance measured in the Transwell and microfluidic chip of 20.5 and 24 $\Omega.cm^2$ respectively. The small difference in value can be attributed to human error in the manual measurements of Transwells with the EVOM and fabrication variation between PMMA disks due to their small size.

3.4 Human Bronchial Epithelial Cell Growth

Human bronchial epithelial cells were used to test the modelling algorithm with cell barrier formation data. Bronchial epithelial cells (16HBE14o-) were cultured in the apical compartment of 8 microfluidic chips inside a humidified incubator at 37 ○C and 5 %

CO_2 for 4 days. Minimal Essential Medium (MEM) supplemented with 1X Glutamax, 10 % foetal bovine serum (FBS) and 1 % penicillin/streptavidin (P/S) was perfused through the basolateral compartment of each microfluidic chip at 30 μL/hour for the experiment duration. EIS measurements were performed every 34 minutes for all microfluidic chips throughout the experiment, daily examples of the measured magnitude of impedance and phase angle are shown in Figure 3.16AB , with a Nyquist plot of the data shown in 3.16C.

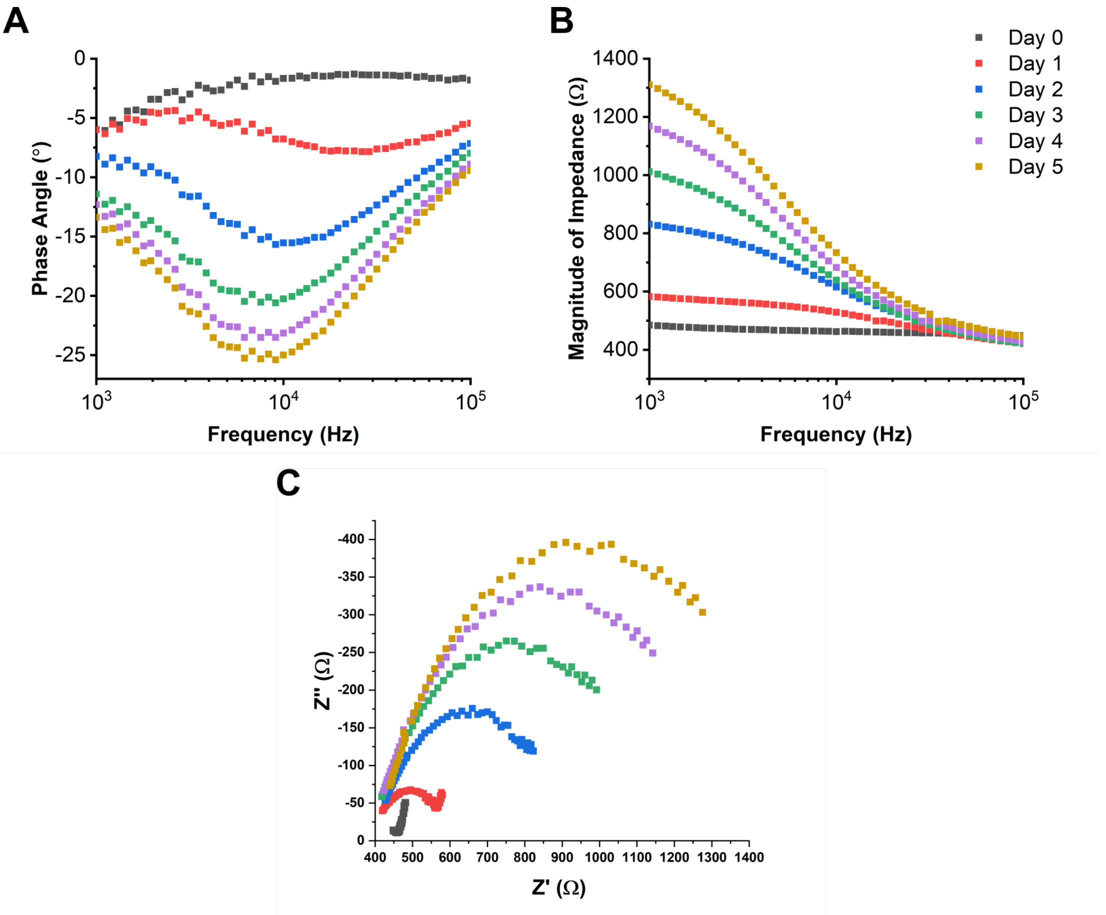

FIGURE 3.16: Daily electrical impedance spectra showing changes in phase (A) and magnitude (B) throughout the experiment, as the 16HBE14o- cells polarise and create an electrically insulating barrier. The Nyquist plot visible in (C) displays the same trend, with both Real and Imaginary components of the signal increasing over the course of 5 days. Data is from a single microfluidic chip and is representative of 8 microfluidic chips in parallel. Each coloured line represents a different day.

Data from EIS measurements was fitted with the algorithm to determine electrode CPE parameters, medium resistance and cell barrier resistance and capacitance (Figure 3.17, 3.18 and 3.19). Similar to previous experiments, the values for cell medium resistance and CPE exponent displayed small variation and increased variation is seen in the CPE magnitude between microfluidic chips, in both the media and cell chambers. The existence of high discrepancy in the CPE magnitude while maintaining a low R^2 error signifies that the modelling is correctly extrapolating the required variables from the dataset, but that there is a possible variation between microfluidic chip electrode coating across the used chips. Cell barrier resistance and capacitance increased over the course of 4 days, reaching an average of 450 ± 149 $\Omega.cm^2$ and 0.14 ± 0.02 $\mu F/cm^2$ respectively. Cell barrier resistance variation are result of manual microfluidic chip assembly. Cell reached cell barrier resistance values similar to the previously reported for the 16HBE14o- cell line, with TER values between 330-2500 $\Omega.cm^2$ considered as a well established epithelial cell barrier. Additionally, Blume et al. (2017) reported on 16HBE14o- culture in Transwell supports with flow reaching 560 $\Omega.cm^2$ after 5 days of culture. Calculations of r-squared values between measured data from the platform and measured data using fitted variables displays accuracy and reliability of the fitting algorithm, with both media and cell electrode values being above 0.9 for the majority of the experiment.

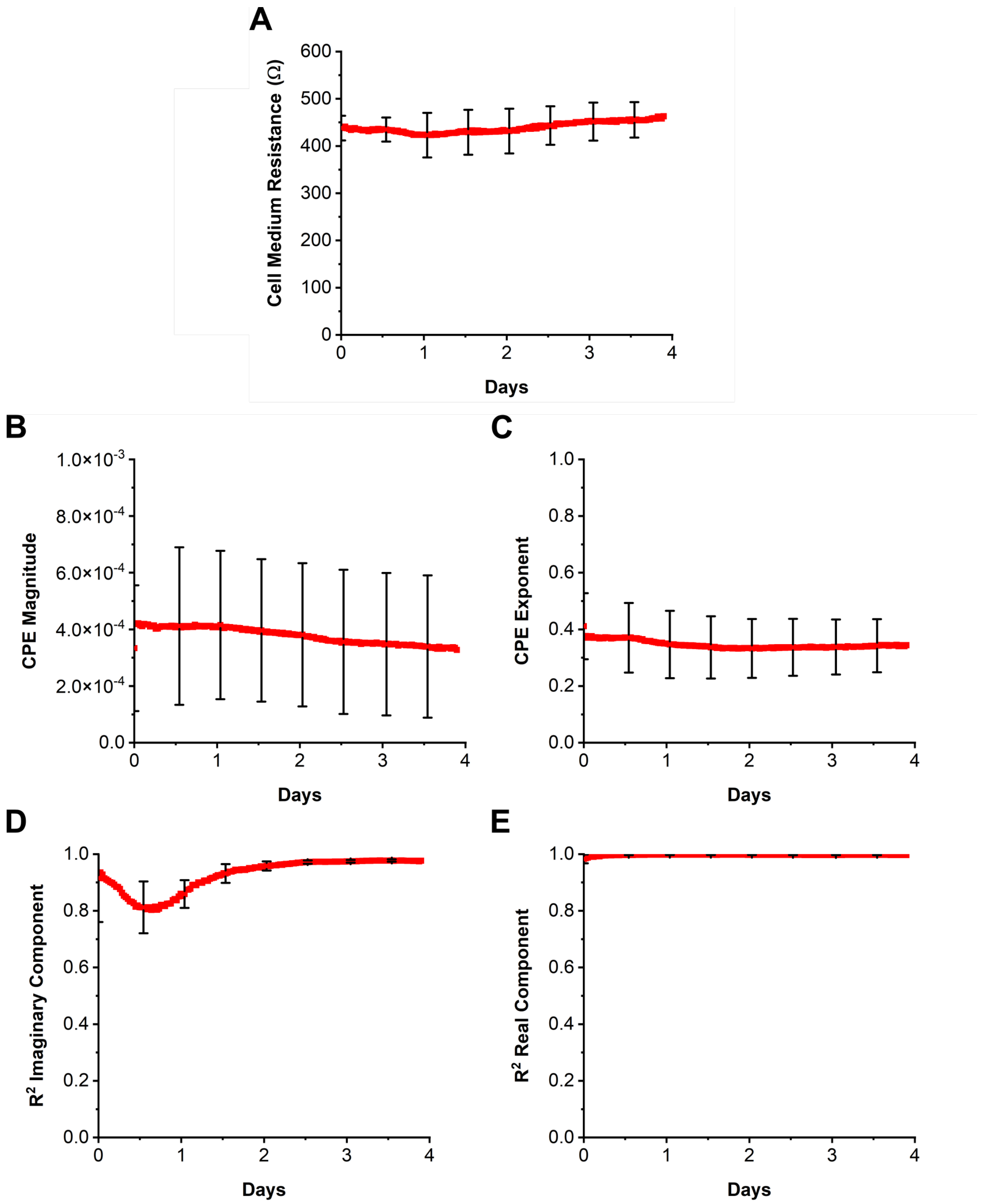

FIGURE 3.17: Modelled data for the cell medium resistance (A), electrode's CPE magnitude (B) and CPE exponent (C) from the media electrodes throughout the experiment. R-squared data for imaginary (D) and real (E) components of EIS data provides an estimate on fitting accuracy. Red line represents the average of 8 microfluidic chips running in parallel and the error bars the standard deviation between chips every 0.5 days.

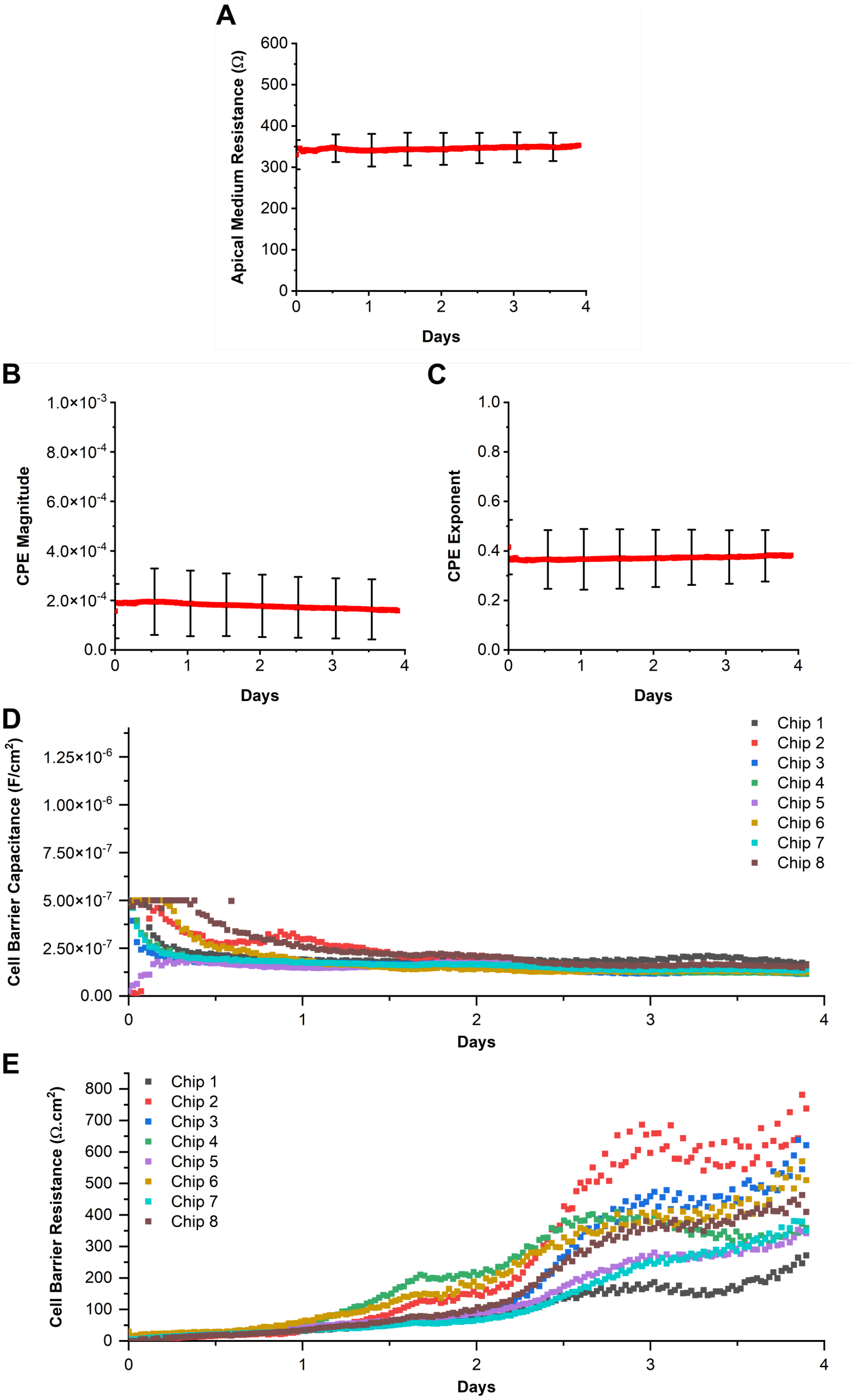

FIGURE 3.18: 16HBE14o- growth cell electrode modelled data, with apical medium resistance (A), CPE magnitude (B), CPE exponent (C), cell barrier capacitance (D), cell barrier resistance in the microfluidic chips (E). Red line in (A), (B) and (C) represents the average of 8 microfluidic chips for the respective variable, with standard deviation displayed every 0.5 days. Data in (D) and (E) is from 8 individual microfluidic chips.

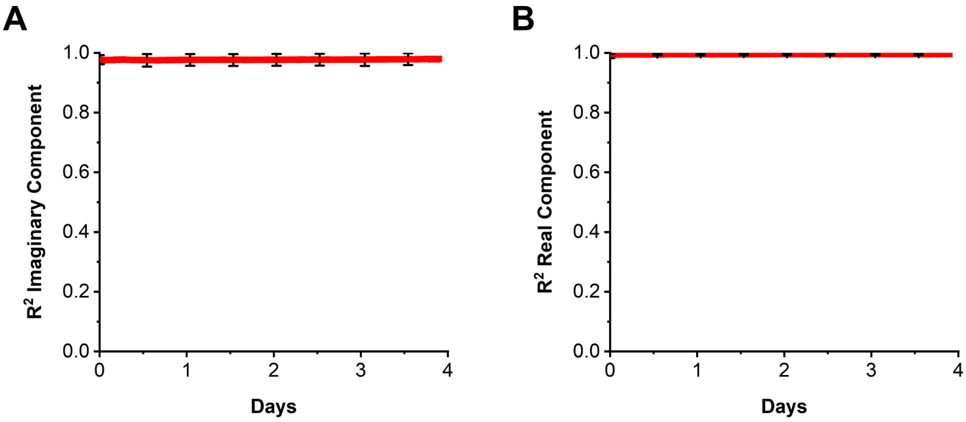

FIGURE 3.19: R-squared values calculated with fitted variables from the electrical circuit model for the imaginary (A) and real (B) components of the EIS data for the cell electrodes.

3.5 Summary

In this chapter, methods of epithelial barrier integrity assessment via electrical measurements was explored and the methodology for the extraction of TER from EIS data obtained with the OoC platform was developed. Current methods used in standard *in vitro* models mainly use single-point resistance measurements using EVOM chopstick electrodes. Integration of EIS in OoC systems allows for an increased data temporal resolution. Additionally, use of EIS measurements in a wider range of frequencies allows for assessment of cell barrier capacitance, as this parameter is more pronounced at higher frequencies. The impact of electrode polarization in EIS capable systems was explained, in which measurements of biological systems can lead to an increase of measuring electrode capacitance and mask data from the sample due to double-ionic layer formation at the interfacial region between electrode and electrolyte. This effect was minimized in the UoS system using ruthenium oxide covered platinum electrodes (which have a larger surface area) and modelled as a constant phase angle in subsequent work.

Epithelial barrier integrity in the UoS platform was assessed with EIS spectroscopy measurements between 1 and 100 kHz every 17 minutes using a custom-made impedance analyser. An equivalent electrical circuit diagram was used to model the EIS data and obtain a TER equivalent, enabling comparison to standardized data collection methods in Transwell supports and other work in literature. The electrical circuit model was used to first model cell media resistance and electrode polarization effects using one pair of electrodes upstream of the cell culture. The resulting data was then used to provide boundaries for EIS data modelling from the pair of electrodes located underneath the cell culture, allowing extraction of both TER and cell barrier capacitance values. Modelling of data was performed using complex non-linear square fitting and Nelder-Mead minimization algorithm. COMSOL simulations were used to visualize signal distribution across the porous membrane support in the microfluidic chip and obtain geometrical cell constants, with geometrical cell constant values confirmed using numerical calculation using conformal mapping. Modelling was performed via Python, in which a user-friendly graphical user interface was created, allowing future use of the software.

The electrical circuit model was first tested with cell media, allowing modelling and calculation of cell media conductivity over the course of 12 hours. Following this, a PMMA disk was placed above the porous support and used to assess the model capabilities at detecting small differences in resistance, generating modelled resistance values similar to those obtained via EVOM measurements in Transwell supports. Lastly, data collected from human bronchial epithelial cells cultured in the OoC system over 5 days was modelled, in which an increase of TER is visible throughout the 5 days.

Additionally, every parameter used in the electrical circuit model was plotted throughout the duration of the experiment, providing valuable data regarding system stability and chip-to-chip variation, with the values of CPE possible to use to assess chip-to-chip coating and electrode quality and cell media resistance being an indicator of proper cell medium balance in the system.

Chapter 4

Organ-on-Chip System

In this chapter, an introduction will be given regarding the system already present at UoS at the start of the project. Following this, the improved system will be described and it's use for cell culture optimization experiments will be presented using two different epithelial cell lines (gut and bronchial epithelial cells). Data presented in this chapter regarding TER obtained using the OoC platform was obtained using the modelling work presented in Chapter 3.

4.1 Existing System

The 1st generation OoC platform fabricated at the UoS combined key pieces of the work presented by Sun et al. (2010b) and Blume et al. (2015), with a microfluidic platform for culture of epithelial cells. This had basolateral perfusion, along with continuous measurement of TER, via inbuilt electrodes placed beneath the cell culture chamber. This platform was developed by Dr. Riccardo Reale, Dr. Summit Kalsi and Dr. Sofia Johansson, and comprised two main components, the plastic fluidic manifold and the biochip.

The plastic fluidic manifold (Figure 4.1A) was composed of 6 layers of machined poly (methyl methacrylate) (PMMA) and provided an interface between the syringe pump and biochip. All the PMMA layers were bonded together using double-sided adhesive (3M 467). A bubble trap was integrated into the manifold design, trapping any air present in the perfused liquid before it reached the cell culture in the biochip. Two Lee solenoid 2-way valves were screwed onto the manifolds and used to direct the flow, enabling the removal of air from the system before experiments.

The biochip consisted of 5 layers of machined PMMA (Figure 4.1B), a glass chip with patterned electrodes, a high porosity polyethylene terephthalate (PET) membrane and

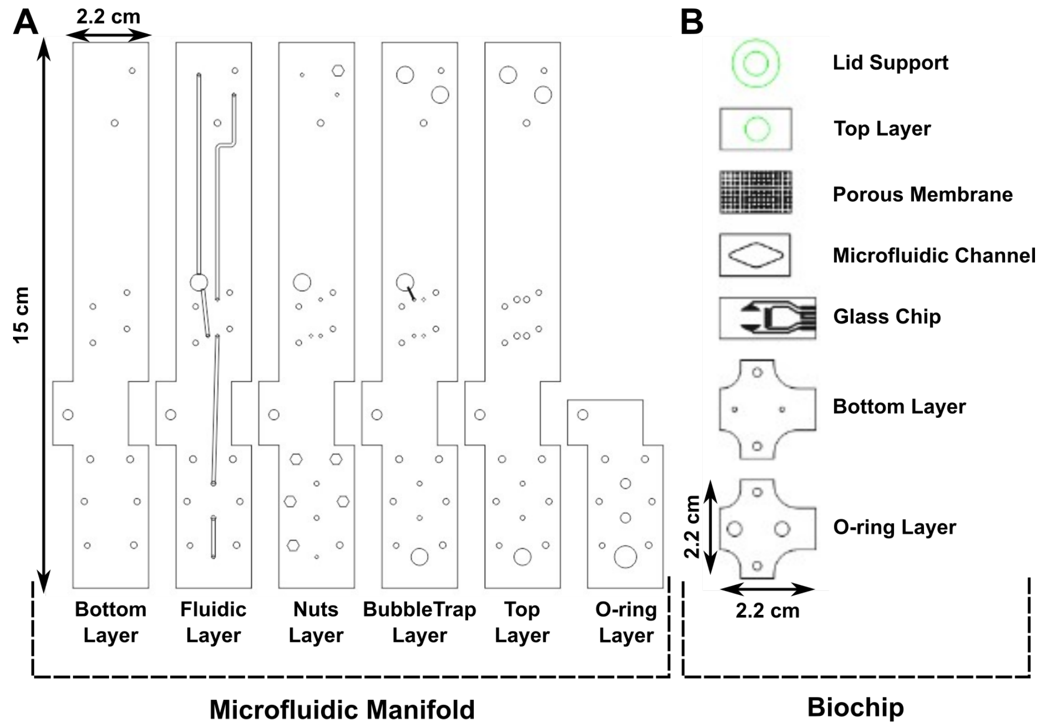

FIGURE 4.1: Diagram of the existent OoC platform at UoS at the start of the PhD project, developed by Dr. Riccardo Reale, Dr. Summit Kalsi and Dr. Sofia Johansson, composed of microfluidic manifold (A) and chip (B)

polydimethylsiloxane (PDMS) lid. The PDMS lid maintains sterility of the microfluidic apical chamber while allowing gas exchange and CO_2 equilibration. All layers were held together using double-sided tape. Two pairs of platinum electrodes were used for measurements of electrical impedance, gathering data about the growing cell culture and basolateral perfused cell media. Measurements were performed using a commercial impedance analyser (C60 impedance analyser from Cypher Instruments) controlled with a graphical user interface in MATLAB. Platinum black was deposited onto each electrode in the microfluidic chip by electroplating. This leads to the formation of porous structures at the surface of each electrode, increasing its surface area and reducing the effects of electrode polarization. Inlet and outlet holes in the glass chip were machined using a laser cutter. Chips were manually aligned onto the fluidic manifold, with seals between both components created with two nitrile O-rings clamped using screws.

This platform could house 8 microfluidic chips in parallel with real-time monitoring of electrical impedance. However, it was neither compact nor user-friendly. Further issues were encountered with the solenoid valves used for flow control. The valves were not suitable for continuous use at 37 °C and high humidity, the typical environment inside a cell culture incubator. The valves would overheat, decreasing their expected lifetime and eventually stop working. Valves would close the fluidic connections between syringes and chips and stall the syringe pump, leading to experimental failure during cell culture over 5 days. Also, due to the large surface area of the fluidic manifolds, double-sided adhesive did not provide an even surface across the entire manifold, leading to microchannel blockage, delamination and leaks. Therefore, the platform was redesigned to be more compact, robust and user friendly.

4.2 Improved System

Design and fabrication changes and all work regarding the use of 16HBE14o- cells discussed in this section were performed in conjunction with PhD student Nikita Karra, as both PhD projects required the design, fabrication and testing of a functional and reliable organ-on-chip platform. Additionally, the work involving Caco-2 cells pertained to this PhD project alone, not both. Materials, reagents and protocols for manifold and biochip fabrication, cell culture of gut (caco-2) and bronchial (16HBE14o-) cells, cell staining and cell fixing protocols are in appendix A.2.2.1, A.2.2.2, A.2.3.2, A.2.3.1, A.2.6 and A.2.5 respectively. Additionally, a full Standard Operating Protocol written together with Nikita Karra is present at appendixA.2.1.

The chip (Figure 4.2) is comprised of 2 layers of micromachined PMMA, a glass chip with patterned electrodes and a high porosity PET membrane. All layers were bonded using double-sided tape; inlet and outlet holes were made by powder blasting. Platinum electrodes on the glass chip were covered with ruthenium oxide, which is biocompatible and increases the electrode surface area similarly to platinum black, but more stable, Mingels et al. (2019). Deposition of ruthenium oxide was performed in the clean-room during chip fabrication. The microfluidic channel is approximately 375 μm in height, with the entire chip assembly having a width, length and height of 22 x 22 x 12 mm respectively. Commercially available PDMS adhesive seals are placed on top of the apical chamber after cell seeding, allowing gas exchange while maintaining sterility. The cell culture compartment is circular with a diameter of 5 mm, equating to a cell culture surface area of approximately 0.2 cm^2. Inlet and outlet holes are 1 mm diameter and are located 10.5 mm apart, with the microfluidic channel connecting the inlet to the cell culture area and outlet. One magnet is located in each side of the biochip so that when the chip is placed onto the microfluidic manifold, both components are magnetically aligned and pushed together. This provides an easy and robust way to insert, remove and replace chips. Each layer is shown in Figure 4.3A.

Fluidic manifolds (Figure 4.3B) were redesigned to be more compact. These were machined from individual 10 mm high layers of polyarylethe-retherketone (PEEK) with an additional alignment layer of 3D printed VeroClear placed above for O-ring alignment. A commercial bubble trap (Darwin Microfluidics, LVF-KBT-S) is located between the manifolds and the syringe pump. The bubble trap has an internal volume of 44 μL and removes air bubbles present in the liquid flow via the PTFE membrane. Vacuum can be applied to the bubble trap, increasing air removal efficiency. One magnet is located

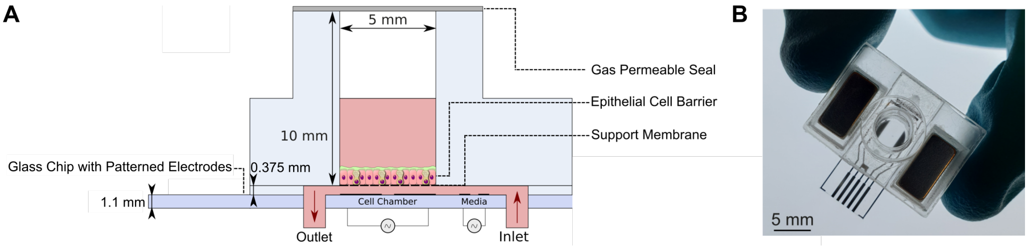

FIGURE 4.2: (A) Cross-section of the microfluidic chip, showing the cell and media electrodes. (B) Photograph of a microfluidic chip, in which magnets can be seen on either side.

in each side of the manifold and is responsible for the placement and alignment of the chip onto the manifold. The seal between manifold and chip is done with use of nitrile O-rings located concentrically with the chip inlet and outlet holes. The alignment layer allows for O-ring placement onto manifolds before chip placement.

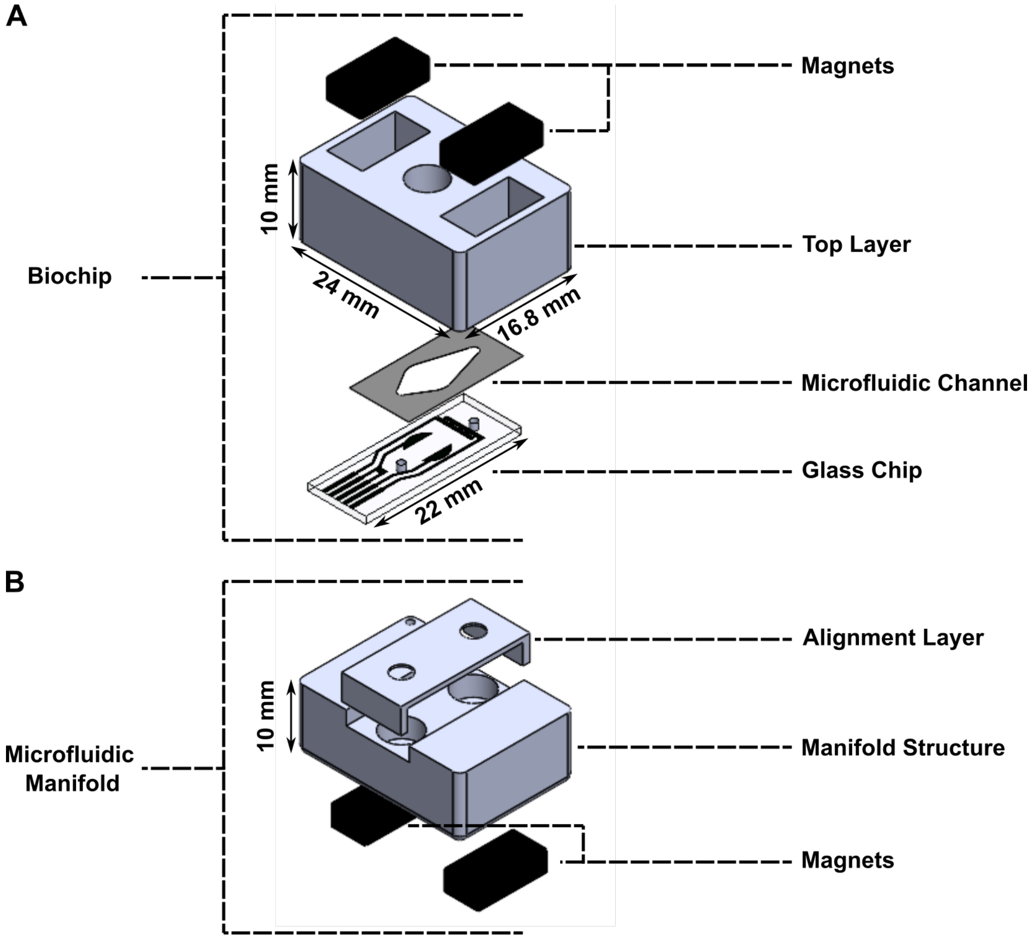

FIGURE 4.3: Diagram of chip (A) and microfluidic manifold (B) showing each separate layer. Chip layers are held together using double-sided adhesive and the chip-manifold assembly is aligned and sealed using 2 pairs of magnets.

Impedance spectroscopy measurements were performed using a home-made impedance analyser developed and fabricated by project student Joel Bowring. The analyser is mounted on top of a raspberry pi and is based on the AD5933 network analyser IC from Analog Devices. It is capable of electrical impedance spectroscopy measurements between 1 and 100 kHz, providing data in logarithmic or linear scales. The analyser can connect up to 4 separate PCB breakout boards via ethernet cables, with each breakout board capable of connecting to 8 different chips. Thus each analyser board can connect up to 32 biochips in parallel. It is possible to stack up to 4 analyser boards in one raspberry pi. Operation of the analyser is handled with custom software written in Python, with a graphical user interface in which measurement parameters can be defined (Figure 4.4). Magnitude of impedance (Ω) and phase angle data (°) is exported to .csv files for each chip and electrode pair (media and cell electrodes). For results presented in this chapter, impedance measurements were recorded every 17 minutes on a logarithmic scale between 1 and 100 kHz, with a total of 50 points. Impedance data was modelled after each experiment to extract cell barrier resistance (TER equivalent) and capacitance according to the methodology demonstrated in Chapter 3.

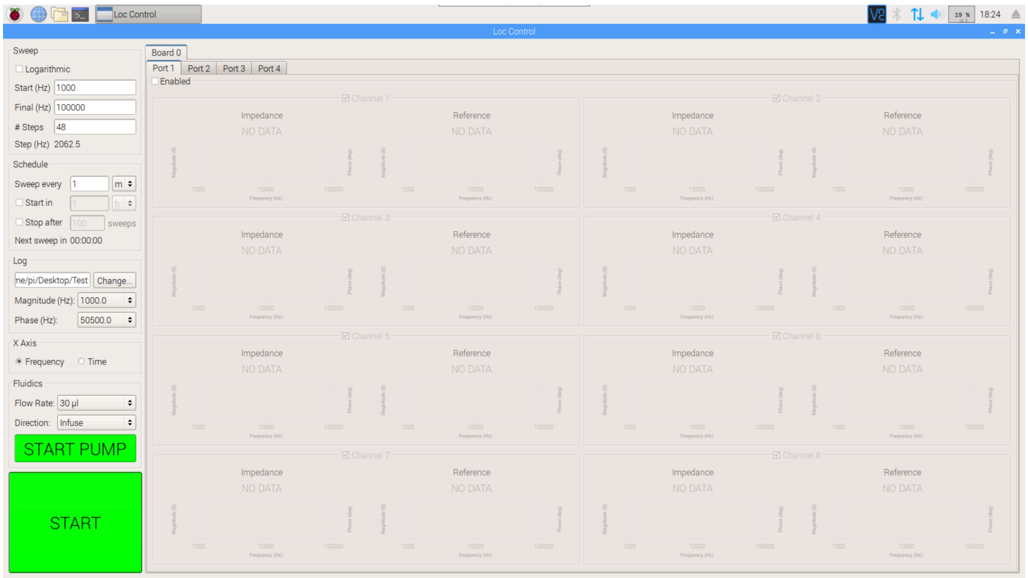

☐ Logarithmic

Start (Hz) 1000

Final (Hz) 100000

Steps 48

Step (Hz) 2062.5

Sweep every 1 m

☐ Start in 1 h

☐ Stop after 100 sweeps

Next sweep in 00:00:00

ne/pi/Desktop/Test

Magnitude (Hz): 1000.0

Phase (Hz): 50500.0

● Frequency ○ Time

Flow Rate: 30 µl

Direction: Infuse

FIGURE 4.4: Interface used to control the homemade impedance analyser. The user determines the start and end frequencies for the EIS spectra, and the number of points in the range. Data is displayed in real-time as it is collected, either as individual spectra or the complex impedance at a specific frequency. Additionally, the syringe pumps (controlled by an Arduino microcontroller) are operated through the interface.

Manifold-chip assemblies were placed onto a platform machined from PMMA, with each platform housing a total of 8 biochips (Figure 4.5). Due to the decreased size of the new platform, it is possible to place 2 platforms (16 biochips) side-by-side in a standard incubator shelf. While performing cell culture experiments with the OoC platform inside a humidified incubator at 37 °C and 5 % CO_2, the syringe pump and impedance analyser are placed outside the incubator. Fluidic tubing and electrical cables were connected to the platform (fluidic manifolds and breakout PCB board) through appropriate holes in the incubator.

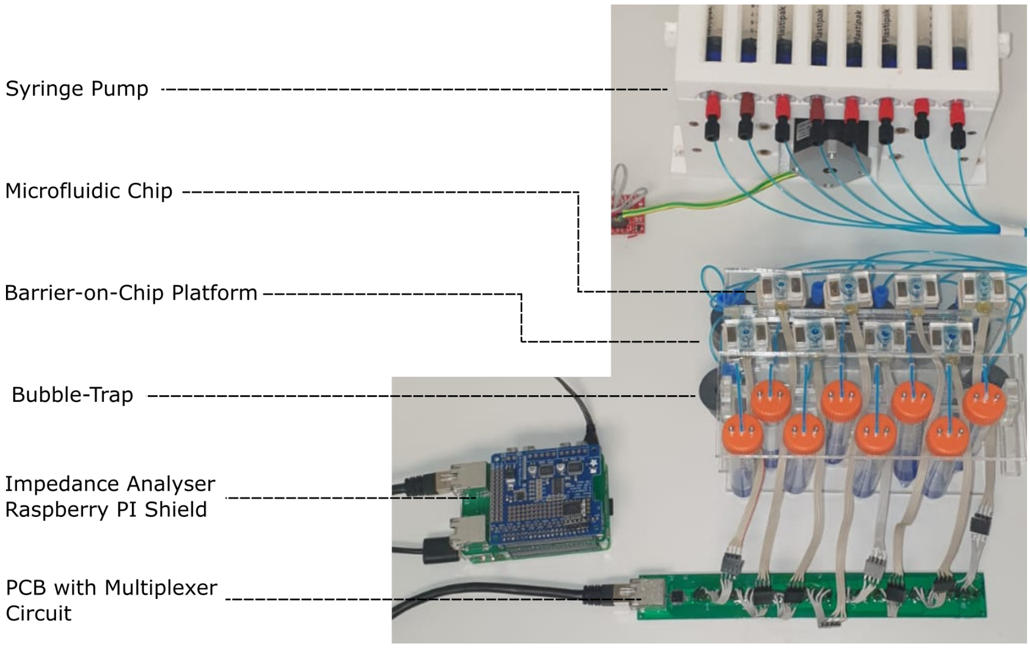

FIGURE 4.5: Photograph of the Barrier-on-Chip platform with syringe pump and impedance analyser. The eight separate chips are individually connected to a header board.

4.3 Cell Culture Optimisation

Cell culture optimization in the new platform was performed using two different cell lines, a human bronchial epithelia (16HBE14o-) and a gut epithelial (Caco-2) cell line, based on parameters used in previous work by Dr. Riccardo Reale Reale (2017). Protocols for continuous culture of both Caco-2 and 16HBE14o- cell lines are present in appendix A.2.3.2 and A.2.3.1.

The 16HBE14o- cell line is an immortalized human bronchial epithelial cell line derived from a 1 year old heart-lung transplant patient Cozens et al. (1994). This cell line retains polarised epithelial morphology and functions, such as presence of tight junctions and cilia, being used as a model for studies into respiratory diseases (COPD, asthma, lung cancer) Callaghan et al. (2020b). When cultured without flow (static models), 16HBE14o- cell tight junction formation leads to a gradual increase of epithelial barrier TER over time, with reported values for a confluent barrier in the range between 330-2500 $\Omega.cm^2$ Callaghan et al. (2020a); Blume et al. (2015); Linz et al. (2020).

The Caco-2 (cancer coli-2) cell line is widely used as a gut epithelial barrier model and was derived from a colon adenocarcinoma, Fogh et al. (1977). Culture of these cells without flow results in the formation of an adherent monolayer of epithelial cells. Proteins normally present in the gastrointestinal tract are expressed by Caco-2 cells. Cell polarisation leads to formation of tight junctions between cells, leading to increased electrical resistance, with a confluent cell layer having between 475-1500 $\Omega.cm^2$ Verhoeckx et al. (2015); Srinivasan et al. (2015).

In previous work by Reale (2017), 16HBE14o- cells were cultured on a porous support with basolateral flow using the microfluidic chip shown in Figure 4.1B. Before cell seeding, porous membranes were coated with 30 μg/mL of collagen I for 1 hour. Following polymerisation, the collagen solution was removed and Minimum Essential Medium (MEM) containing 16HBE14o- cells (9×10^5 cells/mL) was added to the apical compartment of the device (100 μL volume per chip). Cells were left undisturbed for 1 hour, allowing attachment to the porous membrane. Basolateral perfusion was set to 30 μL/hour and devices were placed inside a humidified incubator at 37 °C and 5 % CO_2. Based on these parameters, protocols for cell culture of Caco-2 and 16HBE14o- cells in the optimized platform were tested.

4.3.1 Caco-2 Growth Optimisation

The following protocol for culture of caco-2 cells was used throughout the section. Caco-2 cells were maintained within collagen coated flasks (30 μg/mL) in Dulbecco's Modified Eagle Medium (DMEM) with 1X Glutamax, 10 % foetal bovine serum (FBS), 1 % penicilin/streptomycin (P/S), 1 % sodium pyruvate and 1 % non-essential amino acid solution (NEAA). To extract cells from the flask, cells were first incubated with Ca^{2+}/Mg^{2+} free hanks buffered saline solution (HBSS) (Life Technologies, 15400) for 10 minutes, followed by a second incubation of 5 minutes in 1 mL of HBSS with 1x trypsin. Following cell detachment from the flask, 10 mL of DMEM were used to neutralise the existing trypsin and the entire cell solution centrifuged at 300 x *g* for 5 minutes at 20 ºC. After centrifugation, the cell pellet was resuspended in DMEM. Prior to introducing cells into the chips, the apical side of the support membrane was coated with collagen I (30 μg/mL) for 30 minutes inside an incubator at 37 °C and 5 % CO_2. Collagen solution was removed and cells were then seeded (cell density was tested) in 100 μL of DMEM and the chip left undisturbed in the incubator for approximately 20 hours (overnight). Following adhesion of cells to the porous membrane, DMEM was perfused through the basolateral compartment at 30 μL/hour. Cells were cultured over 5 days, with electrical impedance spectroscopy measurements recorded every 17 minutes for each chip. Cell barrier resistance (TER equivalent) and capacitance were obtained through mathematical modelling, described in Chapter 3.

Cell densities of 3×10^5 (3 chips), 2×10^5 (3 chips) and 1×10^5 (2 chips) cells/mL were tested in the microfluidic platform with a total of 8 chips (100 μL are added to each chip). Transwell supports were cultured in parallel with the same densities (2 per density). Results are shown in Figure 4.6.

Cell barrier resistance increased over the 5 days of culture, with average values of 48.4 ± 30.35, 151.3 ± 28.9 and 147.4 ± 6.9 $\Omega.cm^2$ for cell densities of 1×10^5, 2×10^5 and 3×10^5 cells/mL respectively (Figure 4.6A). Similarly, cell barrier capacitance increased throughout the experiment, averaging at 4.2E-7 ± 3.3E-8, 1.3E-6 ± 6.6E-8 and 1.1E-6 ±

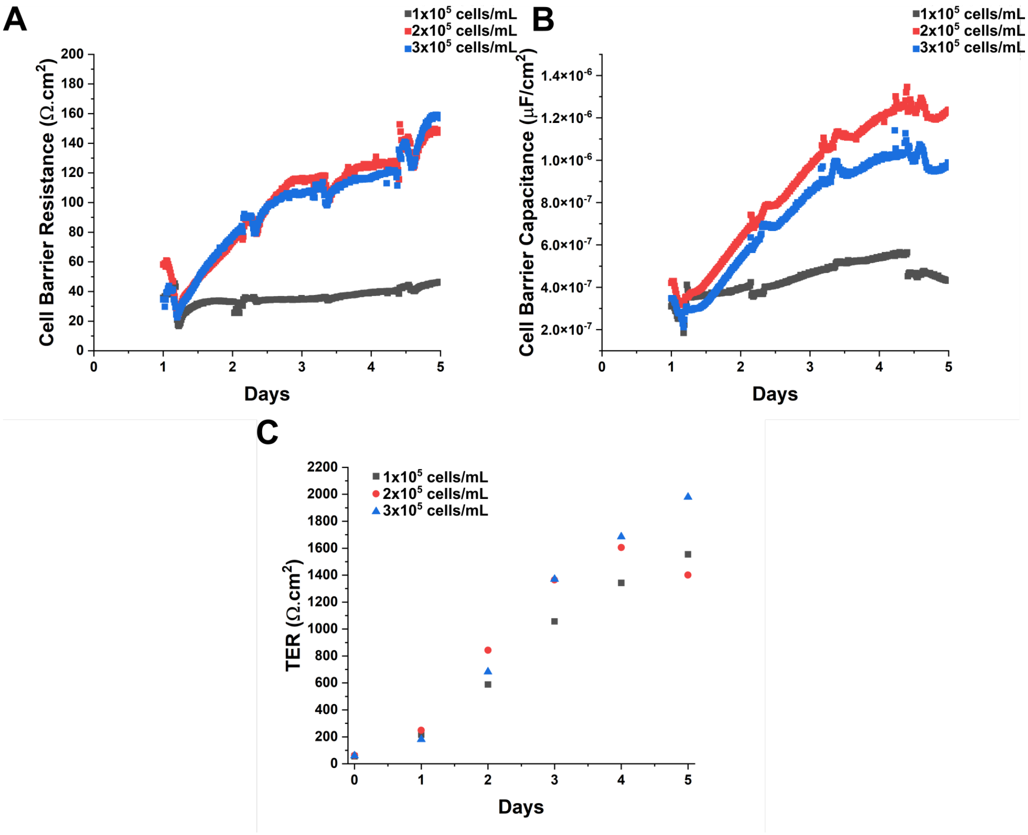

FIGURE 4.6: Epithelial cell layer capacitance (A) and resistance (B) for Caco-2 cells grown in the microfluidic chip using different cell seeding densities. Epithelial cell layer capacitance and resistance (B) were calculated assuming a support membrane surface area of 0.2 cm^2. Data are from 6 individual microfluidic chips run in parallel, with 3 chips per higher densities density and 2 chips with lower density, and the average TER of 2 individual Transwell® static cultures (C).

4.0E-8 $\mu F/cm^2$ for cell densities of 1×10^5, 2×10^5 and 3×10^5 cells/mL respectively (Figure 4.6B). A perturbation in both cell barrier characteristics was visible at day 1, which coincides with, and was caused by, the start of basolateral perfusion. Smaller perturbations were seen on a daily cycle, caused by the opening and closing of the incubator for Transwell measurements. A clear difference in both resistance and capacitance is seen with the use of 1×10^5 cells/mL, with lower values of both cell barrier resistance and capacitance comparatively to other conditions used. This could be explained by a lack of cell layer confluency on top of the porous membrane, as there were not enough cells to properly cover and expand throughout the entire surface area of the porous support in the 5 days of culture. It is possible that, by increasing the experiment duration, the use of 1×10^5 cells/mL would result in similar values of cell barrier resistance and capacitance over time comparatively to higher cell densities. Use of higher cell densities resulted in similar values for both cell barrier resistance and capacitance. Transwell supports cultured in parallel with the microfluidic chips had average TER values of 1554 ± 3, 1401 ± 294 and 1979 ± 229 $\Omega.cm^2$ with cell densities of 1×10^5, 2×10^5 and 3×10^5 cells/mL respectively (figure 4.6C). TER measured in static cultures was higher than measured with cells cultured under flow. Differences in TER between flow and no-flow conditions for Caco-2 culture were recently reported in the literature, with Azizgolshani et al. (2021) obtaining a TER of approximately 200 $\Omega.cm^2$ and van der Helm et al. (2019) a TER of 200 $\Omega.cm^2$ and cell barrier capacitance of 2 $\mu F/cm^2$. Results obtained with the OoC with higher cell densities are similar to values reported in both studies, for both cell barrier resistance and capacitance. Use of lower cell density in Transwells resulted in a slower increase of TER, possibly linked with lack of cell layer confluency.

Following the cell density experiment, the OoC platform was used to assess chip-to-chip variation during Caco-2 cell growth over 5 days. Based on previous results, a cell density of 3×10^5 cells/mL was used, due to the decreased cell barrier resistance variation. Eight microfluidic chips were used alongside two Transwell supports and cells were introduced in the OoC platform and cultured using the previously detailed protocol (also available at appendixA.2.1). Additionally, the effect of TER measurements on cell barrier formation was assessed, with EIS measurements in 4 microfluidic chips starting after cell seeding (chips 1,2,3 and 4) and the remaining chips after 20 hours (chips 5,6,7 and 8), coinciding with the start of basolateral perfusion. Results are shown in Figure 4.7.

Cell barrier resistance and capacitance increased over the 5 days of cell culture, culminating in an average of 207 ± 59 $\Omega.cm^2$ and 2.0 ± 0.13 $\mu F/cm^2$ respectively. The perturbation seen at day 1 coincides, with the start of basolateral perfusion. Epithelial cell barrier resistance and capacitance reached values similar to the previous experiment by day 5. Transwell supports cultured in parallel had a TER of 1258 ± 40 $\Omega.cm^2$. As previously seen, a clear difference in TER is visible between flow and no-flow conditions, which is consistent to recent findings by van der Helm et al. (2019); Azizgolshani et al. (2021), as previously discussed.

4.3.2 16HBE14o-

To compare the response of epithelial cells from a different tissue, human bronchial epithelial cells were cultured in the system for 5 days following the protocol detailed by Reale (2017). Electrical impedance spectroscopy measurements were taken every 17 minutes in the frequency range between 1-100 kHz. Transwell supports were used in parallel. Modelled data for cell barrier resistance and capacitance in the platform and TER data from Transwells over 5 days of culture are shown in figure 4.8. Following 5 days of culture, cells were fixed on the porous membranes immunofluorescently stained and imaged by PhD student Nikita Karra.

For 16HBE14o- growth, cell barrier resistance and capacitance reached average values of 418 ± 121 $\Omega.cm^2$ and 0.13 ± 0.02 $\mu F/cm^2$ respectively (Figure 4.8). Unlike the Caco-2

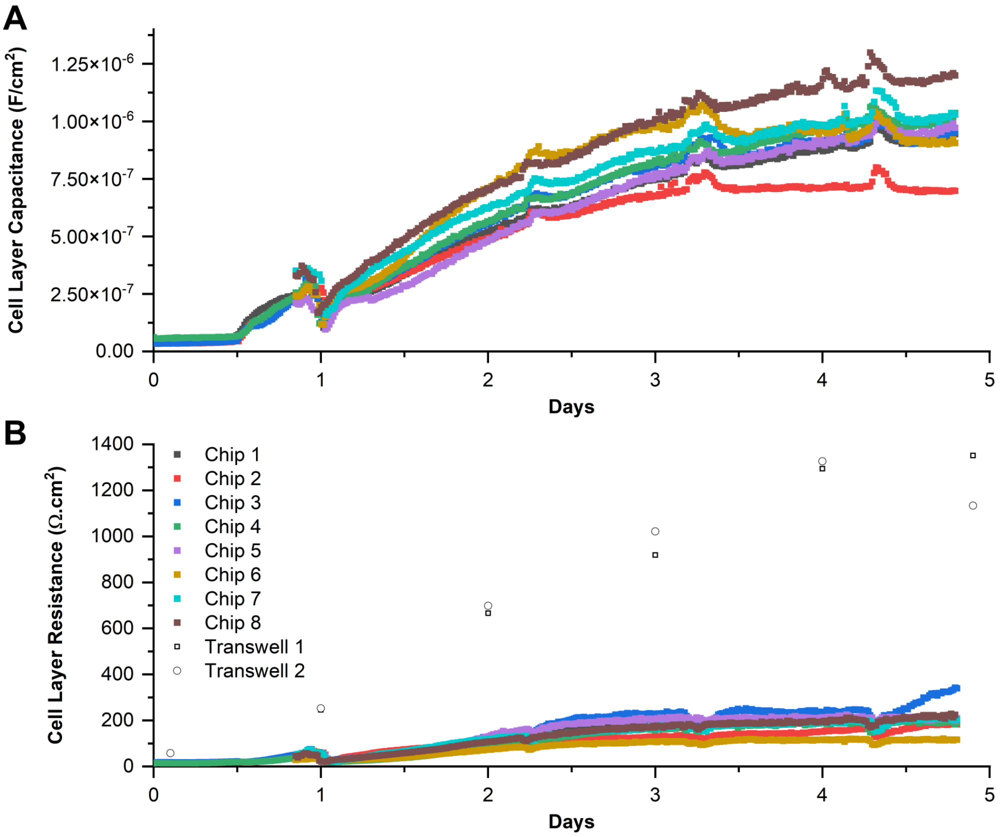

FIGURE 4.7: Epithelial cell layer capacitance (A) and resistance (B) for Caco-2 cells grown in the microfluidic chip. Epithelial cell layer capacitance and resistance (B) were calculated assuming a support membrane surface area of 0.2 cm^2. Data are from 8 individual microfluidic chips run in parallel and the average TER of 2 individual Transwell® static cultures, with error bars representing the standard deviation.

cells, the cell capacitance quickly stabilised (0.5 days) after initial seeding, most probably since cells were seeded at confluency. Also, the capacitance for the 16HBE14o- was lower compared to other reported cell layers, which are typically between 1-4 $\mu F/cm^2$ Odijk et al. (2015); Sun et al. (2010b); Linz et al. (2020). This could be due to cell stacking, as seen in Figure 4.9, which would result in a lower value of capacitance. Cell barrier resistance for 16HBE14o- cells was double the Caco-2 values. Cells cultured in Transwells reached an average TER of 803 $\pm$ 34 $\Omega.cm^2$, consistent with values reported without flow (330-2500 $\Omega.cm^2$ Callaghan et al. (2020a); Blume et al. (2015); Papazian et al. (2016)). Similar to the findings with Caco-2 cells, 16HBE14o- cells had lower values of TER when cultured with basolateral perfusion. This is supported by previous studies by Blume et al. (2017) with 16HBE14o- cells, in which Transwell supports with flow reached an average TER of 560 $\Omega.cm^2$ after 5 days of culture, and in cells perfused in Ussing chambers, with a TER of 105 $\Omega.cm^2$. Additionally, values are consistent to the ones presented in Chapter 3, where 16HBE14o- cells cultured in the OoC reached an average cell barrier resistance and capacitance of 450 $\pm$ 149 $\Omega.cm^2$ and 0.14 $\pm$ 0.02 $\mu F/cm^2$ respectively (Figure 3.18).

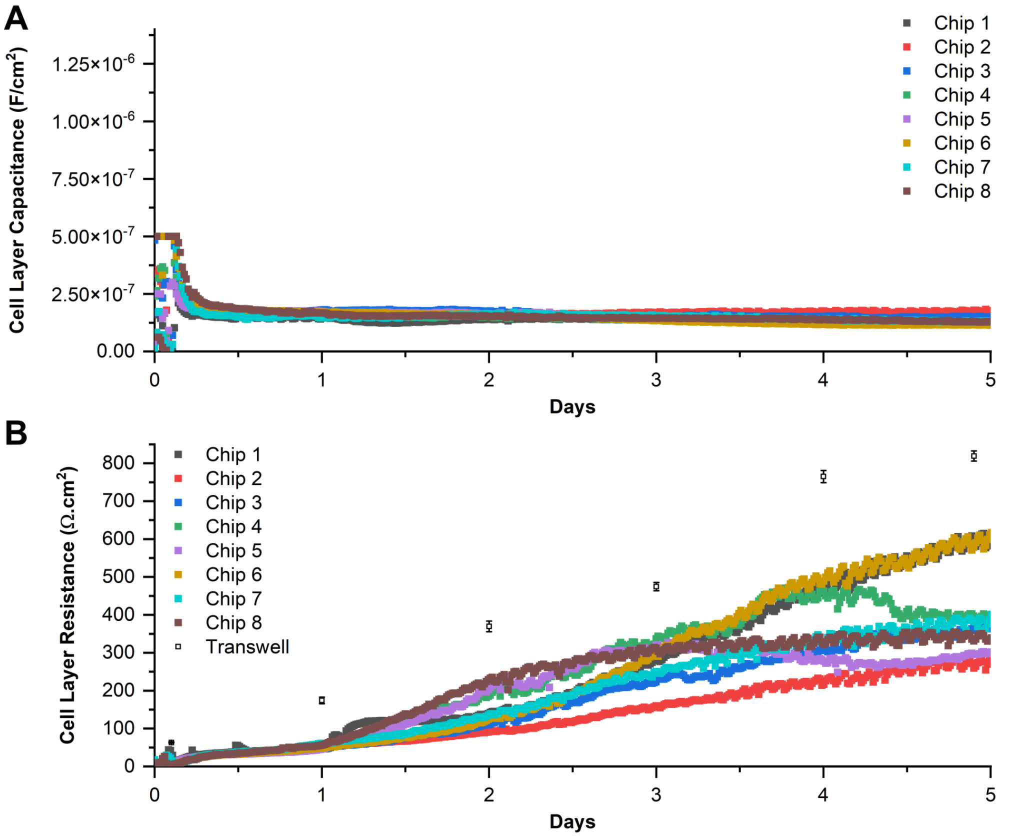

FIGURE 4.8: 16HBE14-o barrier formation cell electrode modelled data, with cell barrier capacitance (A) and cell barrier resistance in the microfluidic chips and TER in Transwell static cultures (B). Data in (A) and (B) is from 8 individual microfluidic chips and 4 Transwells ran in parallel.

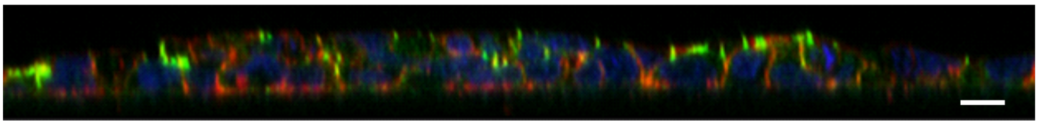

FIGURE 4.9: Examples of cell stacking of 16HBE14o- cells grown in the microfluidic chip (A). Z projection stack captured by Nikita Karra using confocal imaging at 63X at wavelengths 405 (DAPI), 561 (Actin) and 488 (Occludin) (Leica TCS laser scanning microscope). White scale line indicates 10 μm.

4.3.3 16HBE14o- Challenge experiment

To assess the ability to detect epithelial barrier disruption, 16HBE14o- cells were apically stimulated with two different compounds, Triton X-100 and Poly I:C. Triton X-100 (TX-100) is a mild detergent commonly used to solubilize proteins while Poly I:C is a dsRNA viral analogue. dsRNA is produced when viruses replicate RNA and is a pathogen associated molecular pattern, detectable by receptors within infected cells.

Addition of dsRNA triggers an antiviral and inflammatory response, disassembly of tight junctions and cytoskeletal reorganisation without cell apoptosis. This reorganisation leads to an increased barrier permeability, culminating in a decrease of TER Rezaee et al. (2011). The methodology related to reagent preparation and solution introduction to the apical compartment of each microfluidic chip is presented in appendix A.2.7.1 and A.2.7.2.

16HBE14o- cells were cultured in 8 microfluidic chips for 5 days. Cells were then apically exposed to 1 % TX-100 in MEM. Results are shown in Figure 4.10A. Addition of TX-100 leads to an immediate disruption of the epithelial barrier, with a decrease of normalised TER from 100 to 0 %. This effect was not visible in microfluidic chips not apically stimulated with TX-100, in which the normalised TER was stable at approximately 100 %.

16HBE14o- cells were apically exposed to 25 μg/mL of Poly I:C after 5 days of culture in the platform (Figure 4.10B-G). Addition of cell medium to the apical compartment caused an initial perturbation in the cell barrier, irrespective of whether the cell medium contained Poly I:C or not. This may be due to small mechanical perturbations when puncturing the gas permeable seal and/or temperature fluctuations during introduction of challenge solutions to the entire platform. This effect was not seen in the TX-100 experiment, since the incubator was open for less time during stimulation, minimising the temperature drop. Addition of cell medium with Poly I:C lead to a fast decrease in normalised TER, reaching a minimum 20-25 hours post-stimulation, with an average normalised TER of approximately 14 % between experimental repeats. When only cell medium was added there was minimal effect on barrier integrity, with normalised TER values of approximately 100 % after 24 hours (Figure 4.10B-D). The same effect was visible in Transwell supports used in parallel with the platform, as seen in figure (Figure 4.10E-G). The experiment was repeated 3 times, with each repeat giving similar results.

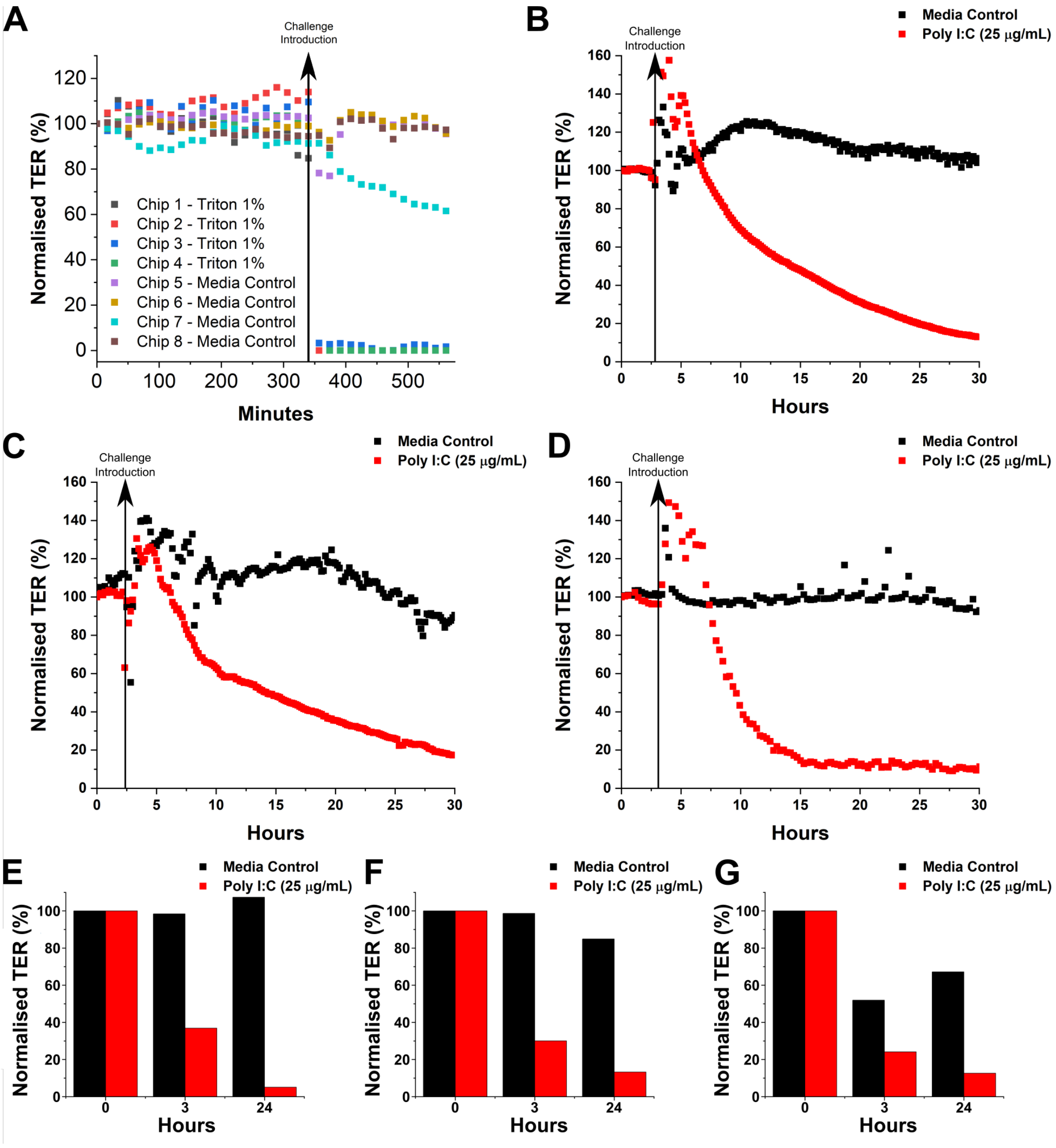

FIGURE 4.10: Effects of TX-100 or Poly I:C challenge on 16HBE14o- cells grown on microfluidic chips. Plots of TER for two separate apical stimuli experiments extracted from the impedance spectrum for the microfluidic chip. (A) Normalised TER data for TX-100 apical stimulation, with each coloured line representing a different chip. (B)-(D) Normalised TER data for Poly I:C apical stimulation, with average of two chips per condition for Poly I:C (red) or media controls (black). The vertical black line represents the time point of apical stimulation for each experiment. Each graph represents one biological repeat. (E)-(F) Normalised TER of Transwell supports used in parallel with microfluidic chips for Poly I:C apical stimulation

4.4 Summary

In this chapter previous work and advancements in the project were discussed, including a detailed description of the early iterations of the OoC platform at the start of the project. Previous work entailed the use of electrodes placed underneath of Transwell supports for continuous EIS measurements and epithelial barrier integrity assessment. Following this, a microfluidic system was used to provide interstitial flow to cell cultures in Transwell supports, enabling cell culture in a more physiologically relevant environment. The first iteration of the combined platform encompassed elements from both pieces of work, with a microfluidic chip with inbuilt EIS electrodes in which cells were cultured with a microfluidic flow in the basolateral compartment.

Improvements were made to the OoC platform in order to reduce its footprint, making it more compact, lightweight and easy to use. The platform was composed of 2 main components, the microfluidic chip, with patterned electrodes for EIS measurements and TER extraction in which cells were cultured on top of a porous support with basolateral flow underneath, and the manifold, which supplied a constant flow of cell media from a syringe pump. Fluidic connection between both components was performed with nitrile o-rings and magnets, allowing easy insertion, alignment and replacement of microfluidic chips in the system in a plug-and-play manner.

Human bronchial (16HBE14o-) and gut (Caco-2) epithelial cell lines were successfully cultured in the platform over 5 days, reaching TER values similar to the ones reported in literature for cells cultured under flow. Additionally, epithelial barrier disruption of 16HBE14o- cells following Triton X-100 or dsRNA apical stimulation was detected at higher temporal resolution comparatively to Transwell supports.

Chapter 5

Droplet Generating System

In this chapter, an explanation on the importance of molecular permeability and immunoassays in the current clinical and drug discovery landscape will be provided. The use of droplet microfluidics to facilitate data acquirement in those two fields will be explained and the proposed droplets microfluidic system will be presented. Results regarding each component of this system will be conferred, including flow-rate, droplet generation and substance diffusion through a nanoporous membrane. Lastly, diffusion of FITC-Dextran through an intact or destroyed epithelial cell barrier will be assessed using this system and bronchial epithelial cells cultured in the OoC system developed at UoS (shown in 3 and 4).

5.1 Analysis of Biological Material

As previously explained in Chapter 1, drugs need to cross epithelial cell barriers in the human body before reaching their target. Transport through the epithelium can be performed by passive and active absorption. Epithelial barrier macromolecular permeability studies are commonly performed with fluorescently labelled compounds, such as dextran or mannitol, with diffusion rates through the epithelium providing crucial information regarding barrier tightness and affinity to compounds Li et al. (2018); Zhu et al. (2021).

Analysis of biological material from human sources plays a critical role in the clinical and drug development industries. Material originating from fluids, tissues and single cells provide a unique insight into cell metabolic procedures and signalling pathways Kellogg (2017). Several techniques can be employed to measure different compounds originating from human sources, with most of these relying on immunoassays, which use specific antibody-antigen interactions for detection of relevant analytes.

Both molecular permeability studies and immunoassays are commonly performed as an end point measurement in both standard *in vitro* and OoC models Hagiwara et al. (2022); Tsamandouras et al. (2017); Maass et al. (2017); Hughes et al. (2017); Pediaditakis et al. (2021); Kerns et al. (2021); Si et al. (2021); El-Dairi and House (2019); Apostolou et al. (2021); Junaid et al. (2021); Dourson et al. (2021); Geyer and Queiroz (2021); Chen et al. (2017); Maass et al. (2018). Time-dependent analysis in both fields is possible with collection of cell media at set intervals or, in the case of OoC models, with large fraction collectors Blume et al. (2015); Nawroth et al. (2020). Alternatively, OoC models can be designed with micro-electrodes for electrochemical detection of biological analytes Mahato et al. (2018). Lastly, small microfluidic devices for analyte compartmentalisation (allowing temporal analysis of said analytes) are possible using droplet microfluidics, although their application in OoC models is currently scarce Cedillo-Alcantar et al. (2019).

5.2 Molecular Permeability

Epithelial barrier macromolecular permeability refers to the diffusion of compounds across epithelial barriers, either due to passive or active transport methods. This is a crucial aspect of drug development studies, as orally administered drugs are required to cross epithelial cell barriers to reach the systemic circulation and therefore the target organ or tissue LeCluyse et al. (2012). Studies on molecular permeability are typically performed with fluorescently labelled compounds of specific size and/or molecular weight, such as dextran, mannitol, inulin or bovine serum albumin (BSA). Rao et al. (1997) studied oxidant induced barrier disruption of gut epithelial cells (Caco-2) cultured in Transwells supports. Cells cultured for different periods of time, ranging from 10 to 15 days of culture, were apically stimulated with H_2O_2. Cell barrier integrity was evaluated through TER and mannitol permeability studies. Introduction of H_2O_2 caused disruption of paracellular junctional complexes, leading to an increase of mannitol flux through the epithelial barrier with a decrease in TER (Figure 5.1A). Forbes et al. (2003) reported the molecular permeability of human bronchial epithelial cells (16HBE14o-) cultured at ALI conditions for 6 days. As cells polarized the barrier got tighter, due to tight junction formation, with a simultaneous increase of TER and decrease of mannitol permeability, similarly to the data gathered from the gut epithelial cell line.

Molecular permeability assays in OoC models typically rely on endpoint measurements, similarly to static models. These can be performed on-chip, if the device is optically clear and can be placed in a fluorescent microscope stage. Chrobak et al. (2006) described the formation and maturation of microvascular tubes cultured inside a PDMS device. Molecular permeability was assessed using Alexa-Fluor-488 labeled

3kDa dextran and Alexa-Fluor-488 labeled BSA, with images of the cell culture captured every minute for 20 minutes inside an environmental chamber at 37 °C with a fluorescent microscope. Treatment of the tubes with histamine resulted in an increase of barrier permeability to the fluorescent BSA, while addition of histamine + pyrilamine (histamine receptor antagonist) led to a decrease of permeability. Villenave et al. (2017) studied molecular permeability of human gut epithelial cells (Caco-2) cultured in an Emulate platform, as shown in Figure 5.1B. Inulin-FITC was perfused through the apical channel at 60 μL/hour for 24 hours and permeability was measured based on fluorescent intensity of the liquid collected at the apical and basolateral outlets of the device. An immediate decrease in apparent permeability (Papp, a measure of compound permeation across cells over a given area) was visible after cell seeding, when compared to an exposed porous membrane. Unfortunately, no data was presented regarding the effect of viral infection on inulin permeability in this study.

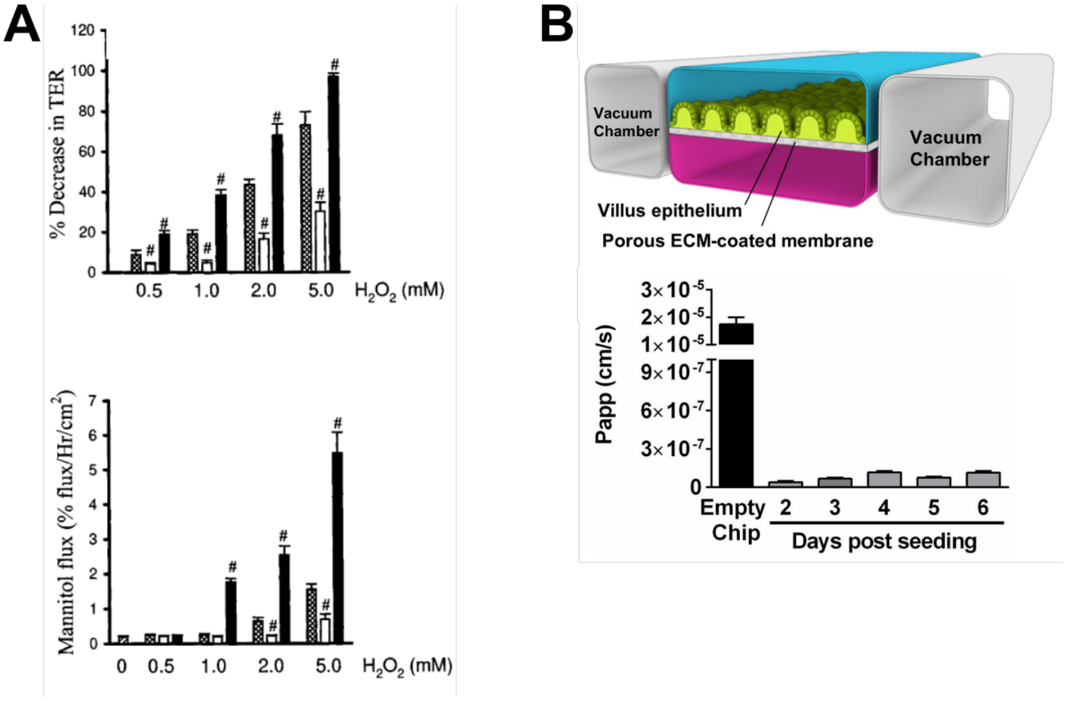

FIGURE 5.1: Gut epithelial barrier TER and molecular permeability following apical addition of H_2O_2 at several concentrations (A) reported by Rao et al. (1997). Decreasing molecular permeability throughout gut epithelial barrier formation (B), from Villenave et al. (2017).

5.3 Immunoassays

Immunoassays (IA) provide quantitative, semi-quantitative or qualitative detection of biological analytes. They are an effective monitoring tool for the quality of biopharmaceutical drugs, foods and the environment Vashist and Luong (2018); Kellogg (2017); Wu and Ju (2012). The assays rely on the interaction between an antigen and antibody, giving methods with high specificity and sensitivity. Antigens are molecules with antigenic sites (epitopes) and vary in size, while antibodies are generated in response to antigens and can be assembled to recognize a large number of epitopes. Alternatively, short single stranded oligonucleotides, denominated aptamers, can be used in replacement of antibodies while providing the same degree of antigen affinity and specificity Lakhin et al. (2013). Several types of IAs have been developed since the inception of the first radioimmunoassay Yalow and Berson (1960), with classification based on molecular labels, bound/free separation requirements and signal detection technology. IAs are critical in numerous settings, such as: clinical, where detection, monitoring and management of certain diseases is linked to determination of disease specific biomarker concentrations; industrial, routinely used in the biopharmaceutical industry; environment, for detection of polluting substances, toxins or biowarfare chemicals; food, for detection of adulterants, toxins and other harmful substances Vashist and Luong (2018).

Organ-on-chip devices typically employ IAs methods as an endpoint measurement of cellular or epithelial barrier viability Zhu et al. (2021). Šuligoj et al. (2020) used the Emulate organ-on-chip platform to study the effects of human milk in the gut epithelium. Analysis of interleukin-8 and interleukin-6 (pro-inflammatory cytokines) was performed on collected basolateral medium using standard ELISA kits. To provide some degree of analyte time-resolution, organ-on-chip devices can be connected to fraction collectors, which dispense cell medium to separate reservoirs in a timely manner, or to droplet generating devices, which use droplet microfluidics to compartmentalize flowing cell medium in micrometric droplets surrounded by a continuous immiscible phase of oil. Blume et al. (2015) reported an organ-on-chip platform which allowed cell culture of PBEC in standard Transwells with microfluidic flow. This platform was coupled with an automated fraction collector and allowed time-dependent analysis of interleukin-8 release over a period of 24 hours, with eluate being collected approximately every 2 hours. More recently, Nawroth et al. (2020) used a custom-made fraction collector for temporal profiling of IFN-I1, CXCL10 and IL-6 secretions following HRV infection of co-cultures of primary airway epithelial cells with either human microvasculature endothelial cells or human umbilical vein endothelial cells. The fraction collector dispensed basolateral cell media into a 96 well plate in two hour intervals over 72 hours, with an increase of analyte concentration for HRV infected cultures. Additionally, use of integrated electrodes in OoC models allows for biomarker detection utilising electrochemical IAs Zhu et al. (2021). Shin et al. (2017) developed a self-regenerating electrochemical biosensor for continuous measurement of albumin and GST-α (Figure 5.2A), with an LOD of 0.023 and 0.01 ng/mL respectively. Electrodes were covered with antigen-specific byotinylated antibodies and analyte detection was possible due to the change of interfacial electron-transfer kinetics of the redox probe upon antigen-antibody binding. The sensor was integrated into a liver-on-chip platform and allowed the automatic and continuous monitoring of cell-secreted biomarkers of human liver organoids in culture for 7 days. Lastly, droplet microfluidics can be utilised in conjunction with OoC platforms, allowing temporal analysis of biological analytes. Cedillo-Alcantar et al. (2019) developed a pneumatic device capable of droplet generation in oil and *in situ* glucose, bile acids and lactate dehydrogenase assays separately (Figure 5.2C). Detection of each analyte was possible in small volumes, down to 3 μL. The platform was directly connected to the outlet of an organ-on-chip device (used for culture of spheroids), streamlining sample collection and analysis. Droplet generation and reagent dispensing was controlled via pneumatic valves, allowing precise and automated fluid handling.

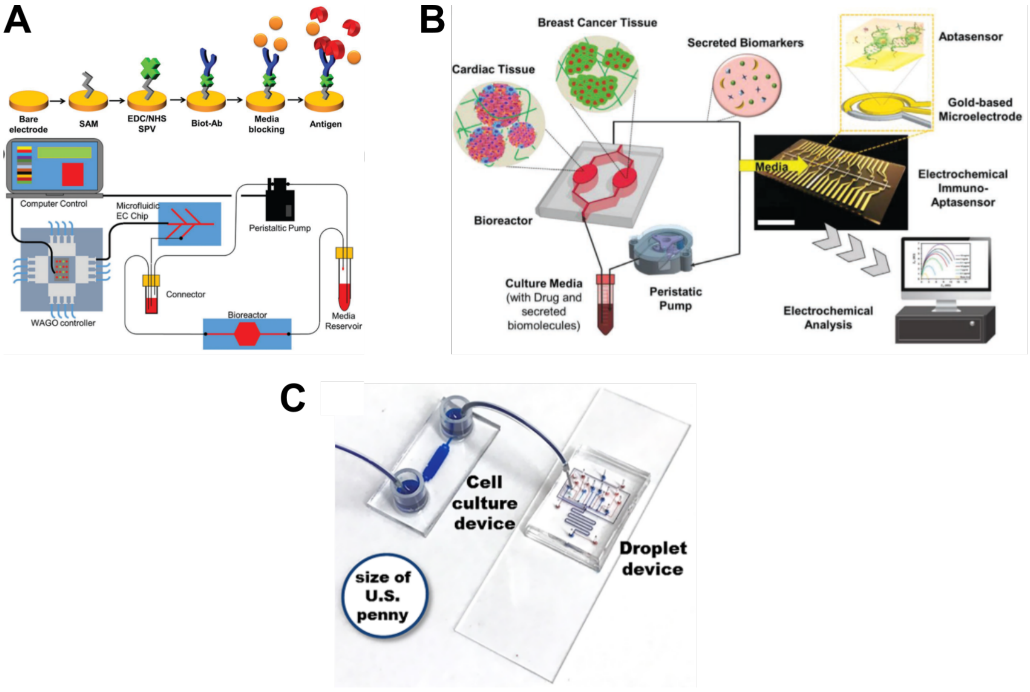

FIGURE 5.2: Electrochemical immunoassays used in conjunction with OoC platforms, using antibody (A) or aptamer (B) covered electrodes for analyte detection. Use of droplet microfluidics for sample compartmentalisation and in-droplet assay development (C). (A) from Shin et al. (2017), (B) from Lee et al. (2021) and (C) from Cedillo-Alcantar et al. (2019).

5.4 Droplet Microfluidics

Droplet microfluidics defines the manipulation of discrete volumes of fluid in immiscible phases. These volumes/droplets are water droplets dispersed in oil or vice-versa. This methodology has become a reliable tool for analyte encapsulation, sampling, metering, dilution, reaction and detection, crucial procedures required in immunoassays. Selection of immiscible phases, surfactants, substrate materials and channel surface coating greatly affects droplet generation, requiring varying high degree of personalization depending on device application Niu and DeMello (2012). Devices used for biological assays preferably use oil as the continuous phase, due to the inability of biological samples to dissolve or diffuse from aqueous solutions to oil and that the majority of biological fluids have a high composition of water. Surfactants are used to stabilize droplet surface interface and control biocompatibility, with choice of surfactant type and concentration being influenced by the type of oil phase being used Teh et al. (2008).

Droplet generation and manipulation in microfluidic devices is related to channel architecture, with generation usually performed using T-junction or flow focusing microchannels. Combined effects of interfacial tension, flow rates and channel geometry determine droplet size and generation frequency Hassan et al. (2017). Additionally, droplet manipulation such as splitting, merging and mixing allows for full laboratory benchtop assays to be performed inside small microfluidic devices in an automated manner, with each droplet analysed separately Jamalabadi et al. (2017); Sohrabi et al. (2020); Teh et al. (2008).

Due to their time-dependent generation, when used in conjunction with biological assays, droplet microfluidic devices are able to provide a quasi real-time analysis of analytes, providing invaluable resolution when compared to standardized end-point analysis methodologies. Use of droplet microfluidics has been shown to allow for continuous sampling and analysis of sample originating from human tissue, with the use of biomarker specific reagents encased in droplets and enabling the monitoring of specific biomarkers in real-time *in vivo* Nightingale et al. (2019); Leong et al. (2019); Kennedy (2013); Niu et al. (2007). Evans et al. (2021) reported a portable droplet microfluidic device capable of collecting samples (*ex vivo*), producing droplets, perform a magnetic bead-based ELISA assay and provide colorimetric readouts in an automated manner (Figure 5.3A). The device was capable of detecting cortisol present in 350 nL of sample in 10 minutes, with a detection range between 3.175 and 100 ng/mL. Nightingale et al. (2019) demonstrated a wearable device capable of analysing glucose and lactate autonomously (Figure 5.3B). The device consisted of a peristaltic pump, an optical flow cell, electronics, fluids reservoir and the microfluidic chip. A microdialysis probe is connected to the peristaltic pump, allowing sample encapsulation into nanolitre sized droplets. Assay reagents are then mixed with sample inside each droplet and, following incubation, are optically measured with an LED and photodetector. It was shown that use of droplet microfluidics allowed for an earlier and more accurate detection of analytes when compared with continuous flow.

5.5 System Design

The aim of this chapter is to develop a device which, when attached to the OoC platform, will compartmentalise cell media originating from the platform's outlet into single and separate droplets. Droplets are to be stored for post processing via standard

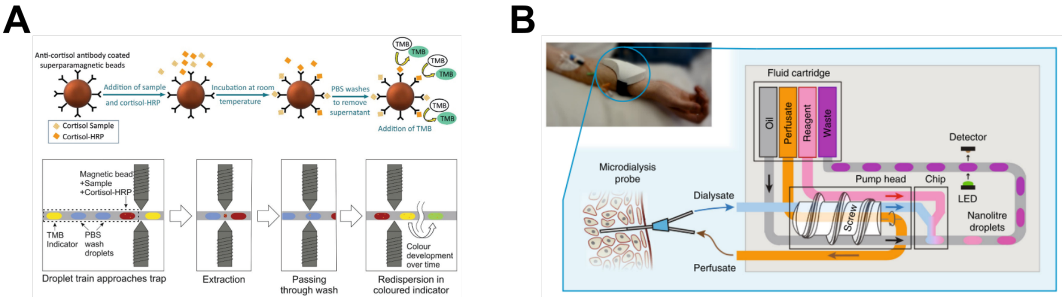

FIGURE 5.3: Use of droplet microfluidics for continuous detection of cortisol using a magnetic bead-based ELISA assay (A) and a wearable device for glucose and lactate analysis in an automated manner (B). (A) from Evans et al. (2021) and (B) from Nightingale et al. (2019).

benchtop methodologies. The following constraints were followed:

- Cell media will enter the device at a set flow-rate of 30 μL/hour. This value is the flow-rate originating from the OoC platform, previously described in Chapter4
- Attachment of the device to the OoC platform will not negatively impact cells in culture or the equipment used for TER measurements.
- The device needs to operate in an automated manner inside the incubator without user interaction for long periods of time (24-48 hours).

Due to the slow flow rate used in the OoC platform, the device will produce 10 μL droplets every 20 minutes, providing good trade-off between time-resolution and sample volume. The device will be activated every 20 minutes and start the flow of oil into the outlet tubing. This will break the continuous flow of cell media and create a droplet at the T-junction. Once the droplet is formed, the device will enter ”standby” mode, in which cell media from the OoC platform can freely flow into the outlet tubing. This cycle will repeat until the end of the experiment, with droplets being stored in the outlet tubing. A schematic of the workflow is shown in Figure 5.4. All fabrication protocols used throughout this chapter are present at appendix A.3.

5.5.1 Peristaltic Pump

Peristaltic pumping was chosen for the oil flow in the device due to scalability, as a minimum of 8 separate microchannels need to be actuated simultaneously. Peristaltic pumps work by sequentially compressing and uncompressing a microfluidic channel. Flow rate is determined by the shape, speed and design of the used roller head and microchannel dimensions (Figure 5.5A) Nightingale et al. (2017). Alternatively, pumps using PDMS Quake valves as actuation platforms to induce a peristaltic motion have been used replace traditional systems (Lai and Folch (2011); Nakahara et al. (2011);

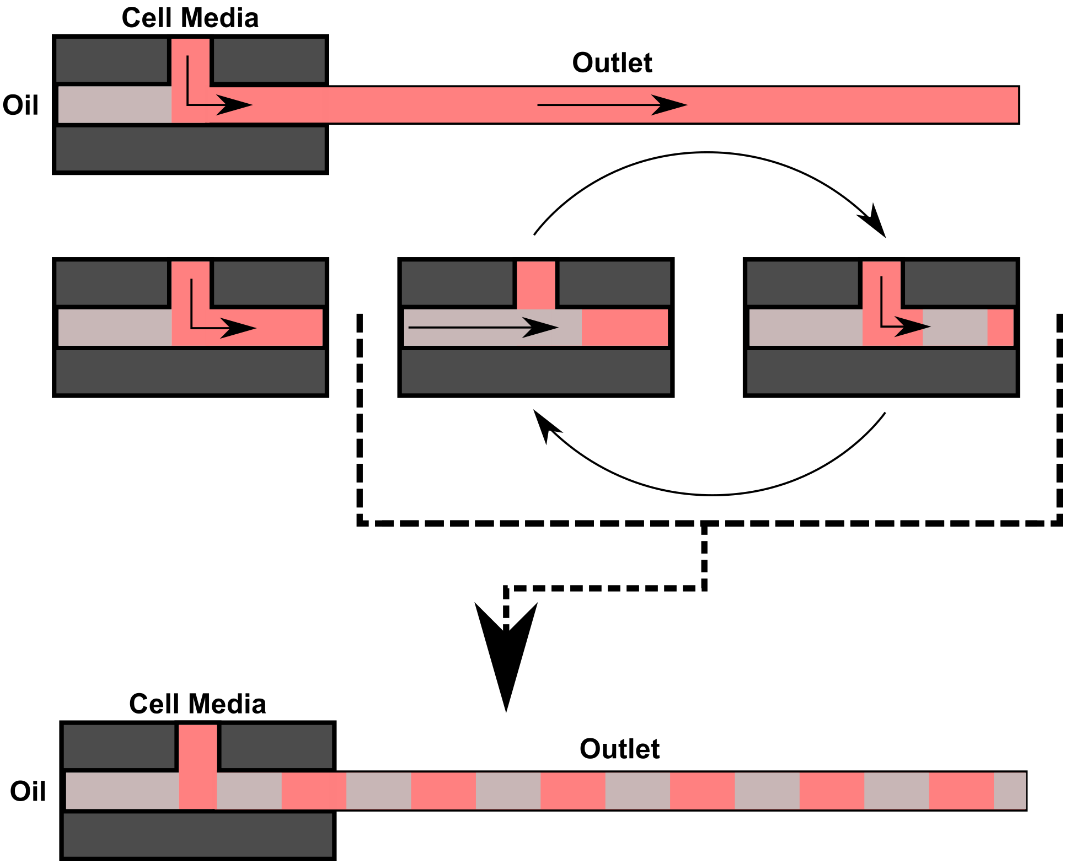

FIGURE 5.4: Schematic of the droplet generation approach deployed in the project. Cell media flows to the outlet. When the droplet generator is activated, oil is pushed to the outlet every 20 minutes, breaking the flow of cell media and creating a droplet. Droplets are then stored in the outlet tubing.

Gerasimenko et al. (2017); Wang et al. (2017)). The valves are composed of two layers of PDMS, with patterned microchannels for air pressure (above) and fluids (below), with a thin flexible PDMS membrane in-between. Air pressure in the PDMS layer above leads to deflection of the intermediate membrane into or out of the PDMS layer below Au et al. (2011). Placement and actuation of valves in succession leads to a peristaltic motion, which is translated into fluid flow (Figure 5.5B). Kimura et al. (2008) demonstrated a micro cell culture platform that maintained stable medium delivery (between 3.6 μL/h and 439.0 μL/h) through the use of a five-step, three actuators, integrated pneumatic micropumps fabricated with PDMS. Lai and Folch (2011) developed a ”single-stroke” peristaltic PDMS micropump, which relies on the relation between actuation time and membrane area. Increasing the area of the actuation membrane downstream, produced peristaltic motion with a single pressure channel connecting all the membranes in series, achieving a maximum flow rate of 5.87 μL/min operating at 15 Hz with a pressure of 12 psi. Recently, Azizgolshani et al. (2021) demonstrated the PREDITC96 OoC platform, in which perfusion through each cell culture chamber is achieved by regulating the height difference between inlet and outlet reservoirs. This regulation is performed via a peristaltic pump located between inlets and outlets. Flow-rate was programmable and directly correlated to cell chamber hydrodynamic resistance; a flow-rate of 60 μL/hour was maintained throughout cell culture.

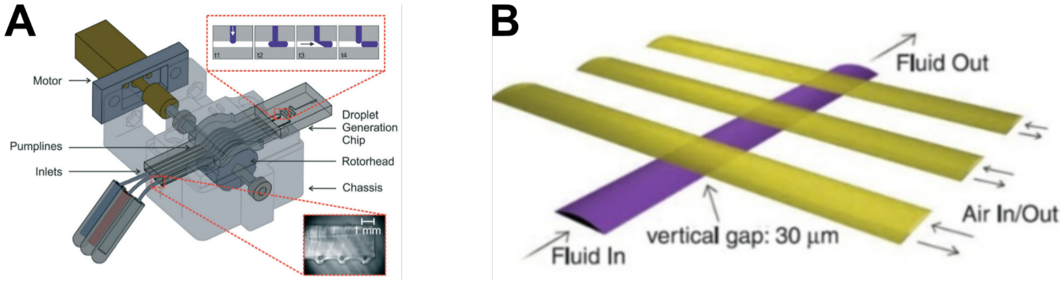

FIGURE 5.5: Different types of peristaltic pumps, with a roller pump developed by Nightingale et al. (2017) (A) and a PDMS Quake valve pump reported by Au et al. (2011) in (B).

The single channel peristaltic pump for the droplet microfluidic system was made of PDMS. The peristaltic pump has 3 PDMS Quake valves sequentially placed above the microfluidic channel, as shown in Figure 5.6. PDMS Quake valves were chosen over other types of peristaltic pumps due to it's ease of prototyping and fabrication. It is composed of 3 PDMS layers, with air pressure channels located in the top layer, fluid channels present in the bottom layer and a 0.2 mm thin PDMS membrane located in between (Figure 5.6A). Top and bottom layers are 3 mm thick and cast from 3D printed moulds made of Veroclear. All three layers were bonded using oxygen plasma. Fluidic and air pressure channels have a semi-circular and rectangular shape respectively, with both channels having a height of 0.1 mm and width of 1.5 mm. Fully detailed methods for device fabrication are present in appendix A.3.2. The pump works as follows (figure 5.6B):

1. All 3 channels are closed.
2. When activated, the left and middle channel open, pulling 0.9 μL from the reservoir connected to the inlet.
3. Left channel closes, pushing a volume of 0.45 μL back to the inlet.
4. Right channel opens and middle channel closes, moving the oil further through the pump.
5. All channels close, finally pushing a volume 0.45 μL to the outlet.
6. Cycle returns to step 2 and repeats, with each cycle pushing a volume of 0.45 μL to the outlet.

Opening and closing the channels is done with the application of positive and negative pressures respectively. The rectangular shape of the air pressure channel allows for

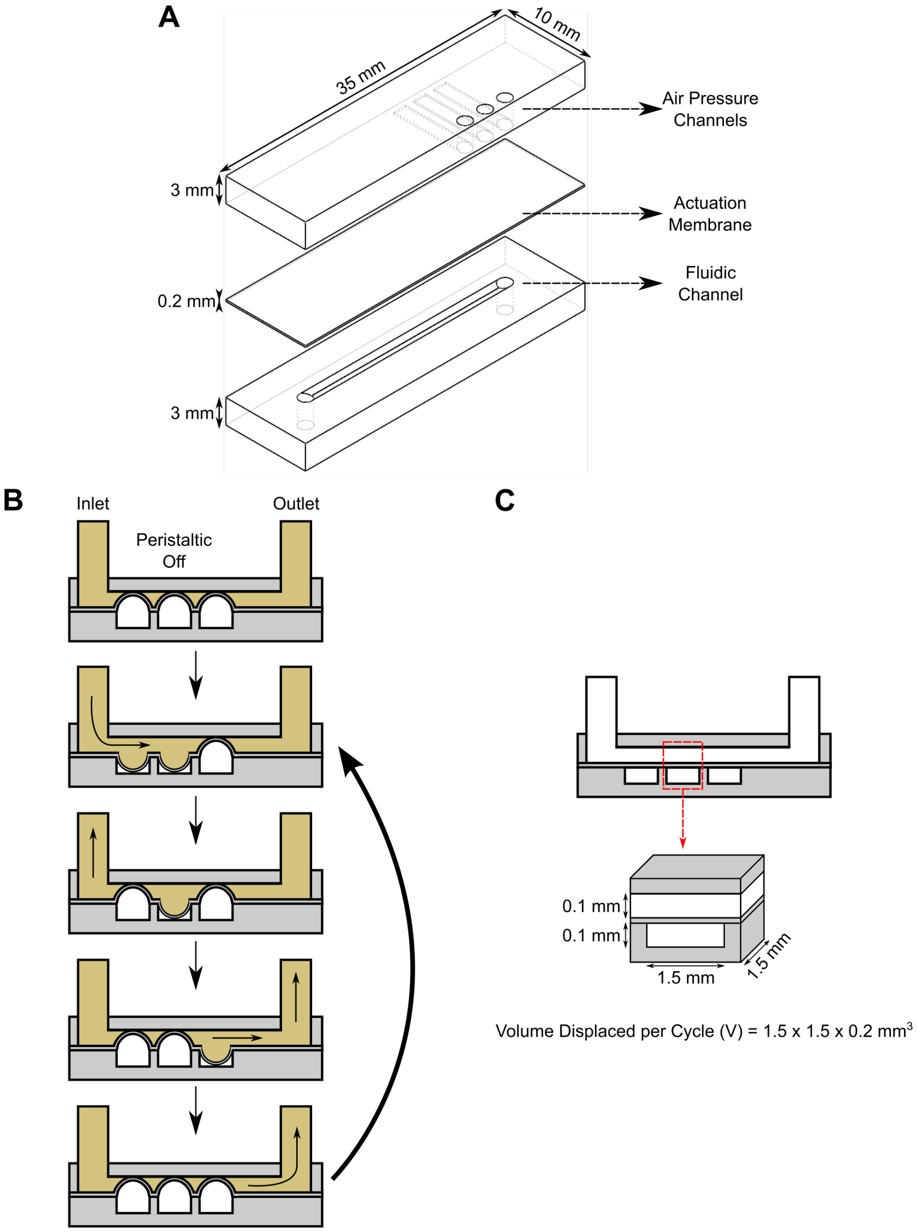

FIGURE 5.6: 3D schematic of the peristaltic pump (A) and pump workflow (B). Calculation of volume pushed in each peristaltic cycle is seen in (C).

pressure to be applied to multiple channels without obstruction, as the PDMS membrane takes a semi-circular shape when deflected into the channel. This design aspect will be crucial in future steps regarding device scalability. Theoretical flow rate (Q) provided by the pump equates to the volume (V) pushed into the outlet after each cycle per time spent (T_{Cycle}), shown in equation 5.1. Figure 5.6C shows how V is calculated from the peristaltic pump dimensions.

$$Q = \frac{V}{T_{Cycle}} \tag{5.1}$$

To control the application of positive and negative pressures in the peristaltic pump, a homemade pressure controller was developed. It was composed of 3 PMMA layers (Figure 5.7A). Top and bottom layers provide structural integrity to the controller while the middle layer has microchannels laser cut from thin PMMA (275 μm). All layers are held together using double sided adhesive. Detailed fabrication methodology is in appendix A.3.1. Two pressure inlets are located in the top layer, which maintain constant levels of positive and negative pressure respectively. Three outlets are present in the bottom layer, which are connected to each of the separate PDMS valves in the peristaltic pump. Application of positive or negative pressures at outlets leads to the closing or opening of specific microvalves in the peristaltic pump. Routing of air pressure between inlets and outlets is done with Lee solenoid valves placed in the top layer, electrically actuated using transistors and an Arduino microcontroller. A schematic showing connections between pressure controller and peristaltic pump is shown in Figure 5.7B. The minimum positive pressure required to fully close the microfluidic channel was tested by manually pushing liquid with a syringe through the channel while increasing the pressure applied to the peristaltic pump. At 500 mBar, channels were fully closed and liquid could not be pushed through. Thus, working positive and negative pressures were set to ± 500 mBar respectively.

5.5.1.1 Flow-rate

To test the peristaltic pump flow rate for water and mineral oil, 2 mL microtubes were connected to the inlet and outlet of the pump (Arduino script used for continuous flow in appendix A.3.1.1). The inlet reservoir was filled with 1 mL of either water or mineral oil. The pump was powered on at select frequencies and the amount of time needed for the inlet reservoir to empty was measured. The outlet microtube weight was measured before and after pump activation, with liquid volumes calculated based on density. Frequencies were based on solenoid valves maximum response time of 20 ms. With each solenoid valve requiring activation three times per peristaltic cycle, the maximum peristaltic pump frequency is set to 16.67 Hz. Frequencies of 6.67, 3.33 and 1.67 Hz were tested as to not overload the solenoid valves, as the device will need to work over long periods of time when connected to the OoC platform. Results are shown in figure 5.8 and correspond to the average and standard deviation of three different devices.

Theoretical flow rate was calculated with equation 5.1, with $V = 4.5 * 10^{-4} mL$ and $T_{Cycle} = \frac{Frequency^{-1}}{3600}$, in milliliter per hour. While the flow rate with water followed the same trend as the theoretical line, there is a slight increase in the volume pushed in each cycle. Calculations for flow rate assume that the membrane only deflects in a 1.5x1.5 mm square, where the top and bottom channels cross. If the membrane is deflected over a larger area, the volume of liquid pushed in each cycle will be higher than expected. The decrease in flow rate when using mineral oil can be explained by its

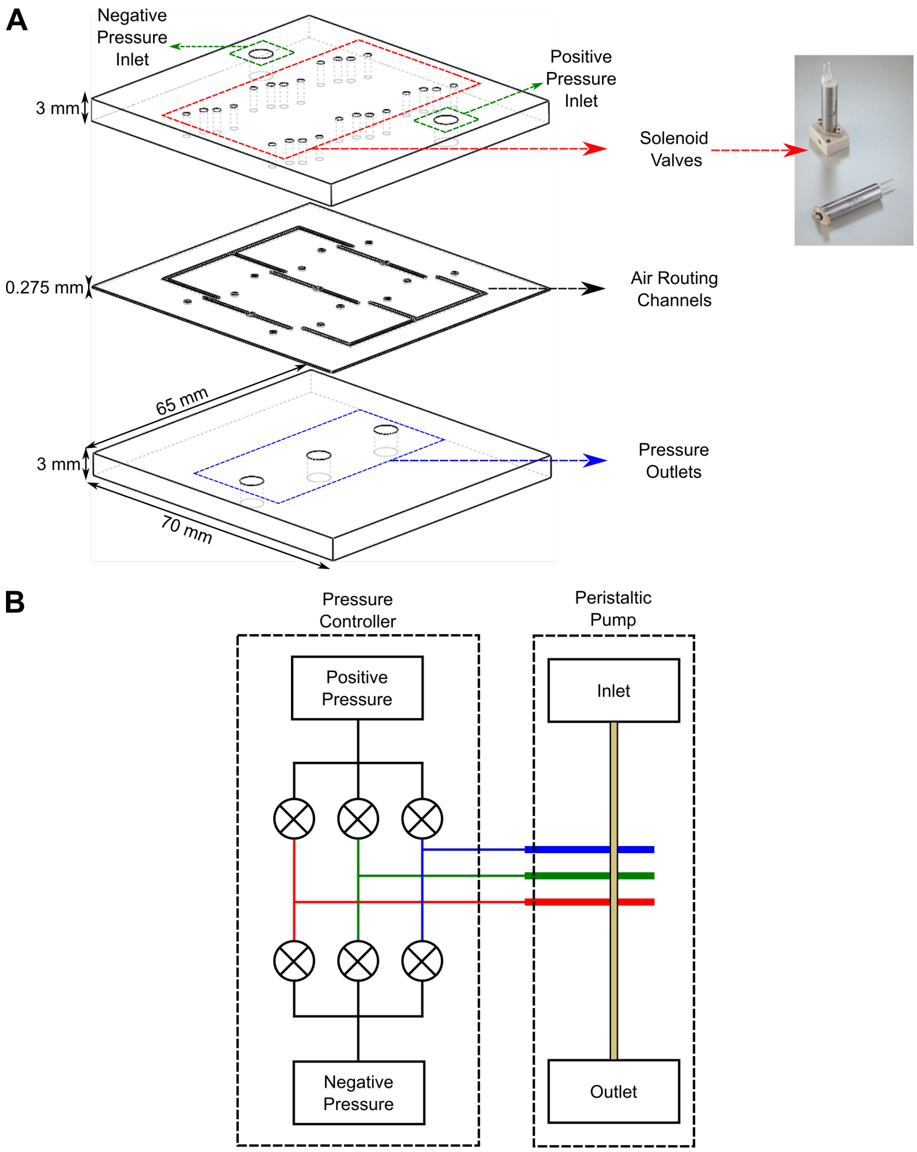

FIGURE 5.7: Pressure controller schematic (A) showing the 3 layers that comprise the pressure inlets in the top layers, air routing channels in the middle layer and pressure outlets in the bottom layer. Connections between the pressure controller and peristaltic pump are shown in (B). Lee solenoid valve from LFN

higher viscosity. Mineral oil has a viscosity of 14.2-17.0 cP at 40 °C, 14 to 17 times higher than water, which affects the PDMS membrane effectiveness in pushing/pulling the oil from the inlet to the outlet of the pump, as more pressure is required. If the membrane is unable to push or pull oil before the peristaltic cycle restarts, the overall flow-rate will decrease as observed. For this reason, FC-40 oil was chosen for droplet experiments. This oil is utilised in biological assays Evans et al. (2021); Leong et al. (2019); Hassan et al. (2017); Lyu et al. (2018); Nightingale et al. (2017), with a low viscosity of 4.1 cP at 25 °C. This value sits in-between viscosity of mineral oil and water and should provide flow-rates more closely resembling the calculated values.

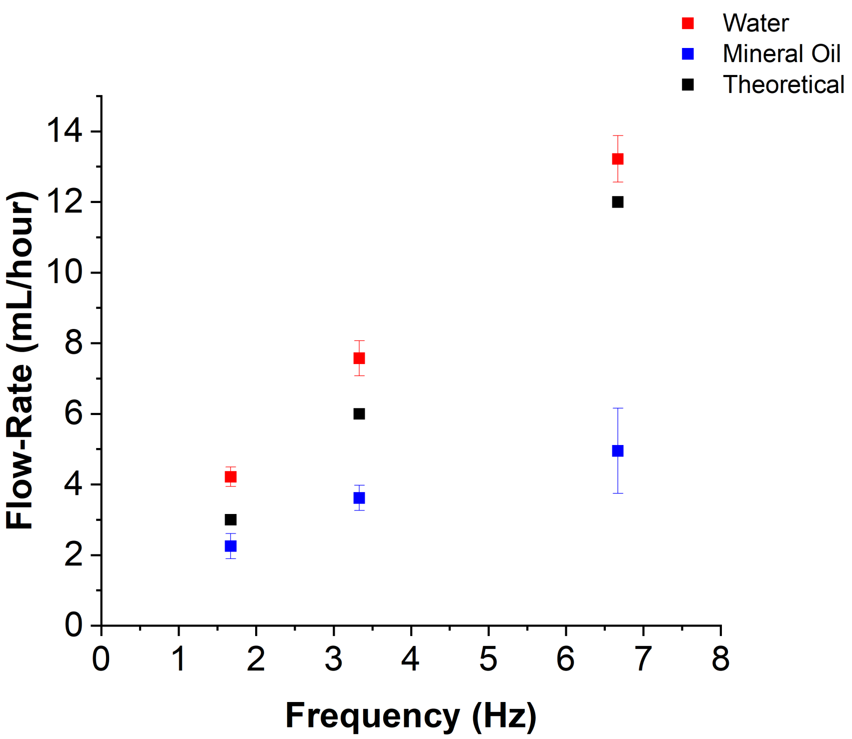

FIGURE 5.8: Flow-rate data obtained with the developed peristaltic pump for perfusion of water (red) and mineral oil (blue). Theoretical values for optimal flow-rate is represented in black.

5.5.2 Droplet Generation

For droplet generation, the PDMS pump was modified to include one more inlet, through which cell media enters the device; Figure 5.9A. An additional PDMS microvalve was placed between the cell media inlet and the device's outlet, as to stop the flow of cell media into the device while oil is being pumped. To actuate the extra PDMS microvalve, the pressure controller was redesigned with the addition of two more solenoid valves and 1 pressure routing channel, as seen in Figure 5.9B. This new droplet generator works as follows (Figure 5.9C):

1. Cell media flows into the device at 30 μL/hour.
2. PDMS microvalve between cell media inlet and device outlet is actuated, preventing flow of cell media into the device and backflow of oil into the OoC chips.
3. Peristaltic pump is activated for a total of 22 cycles at a frequency of 6.67 Hz (7 seconds total), leading to an oil displacement of 10 μL from the reservoir to the outlet. 10 μL was chosen for the droplet size as it provides a good trade-off between sample size and time-resolution. This value can be changed by altering how often the pump is activated if sample size can be diminished for a specific workflow or assay.

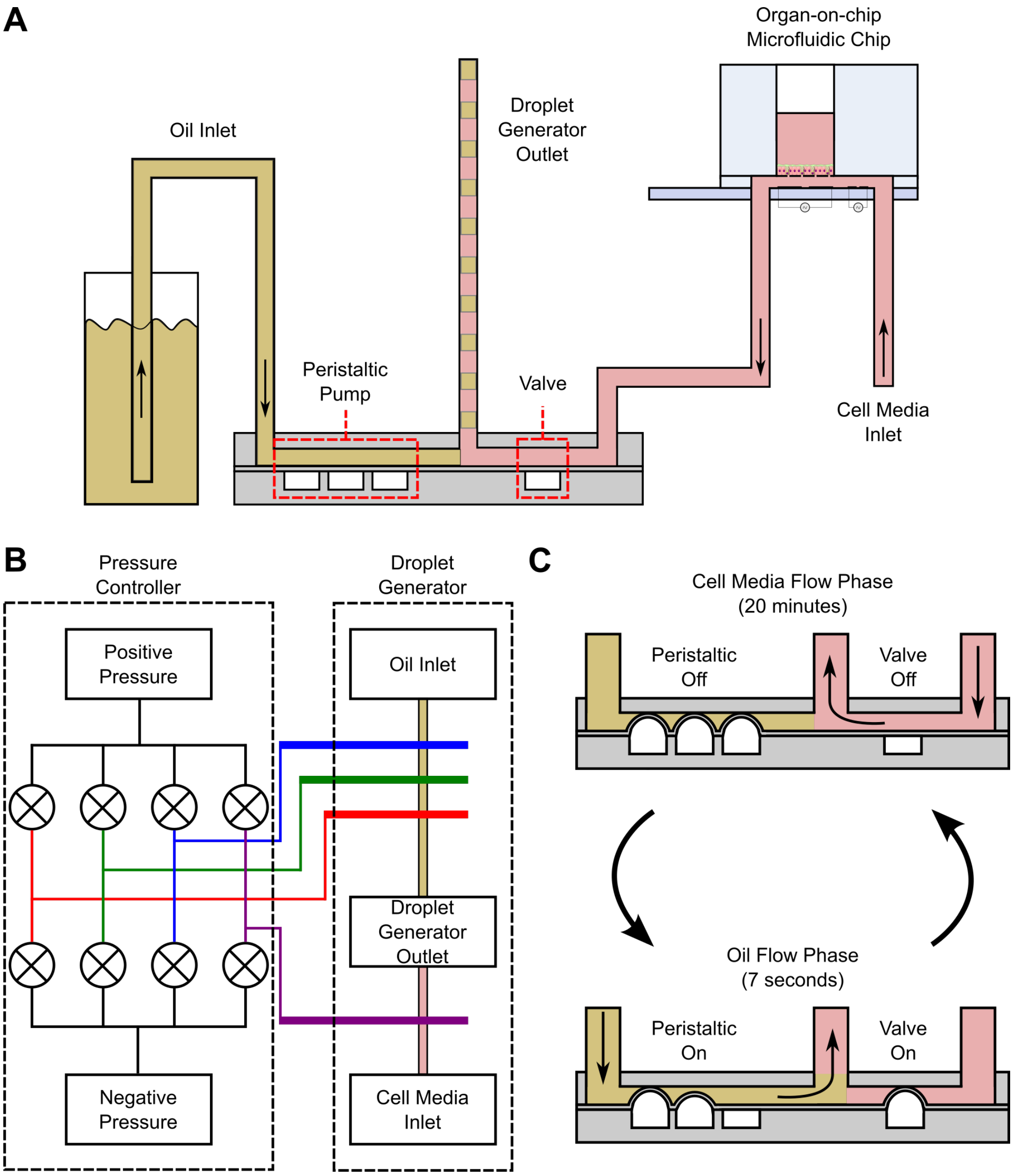

FIGURE 5.9: (A) Cross-section schematic view of the droplet generator, displaying the fluidic inlets (to the oil reservoir and OoC platform) and outlets, the peristaltic pump and the PDMS valve. (B) Diagram showing the connections between the peristaltic controller and droplet generator. Each coloured line represents a different pressure connection between the 2 devices. The pressure controller has 2 extra solenoid valves and 1 extra pressure channel for valve actuation in the droplet generator. (B) Droplet generation workflow schematic, which entails the use of the cell media flow phase for 20 minutes, followed by the oil flow phase for 7 seconds. The 2 processes sequentially switch with one another for the duration of the experiment.

4. Flow of oil breaks the continuous flow of cell media, leading to generation of a droplet of cell media with 10 μL volume.
5. All valves from the peristaltic pump are actuated and the pump is stopped. The PDMS microvalve inhibiting cell media flow is turned off. Cell media perfuses into the generator for 20 minutes, at 30 μL/hour, before the cycle repeats.

Repeating the cycle generates sequential droplets of oil and cell media with 10 μL each at the outlet tubing (Arduino script used for droplet generation in appendix A.3.1.2). Droplets contained inside the tubing can then be manually dispensed into microtiter plates for further analysis. The outlet tubing is made of PTFE, with an internal diameter of 1 mm and 2 m in length, equating to a volume of 1570 μL and back-pressure of 0.108 mBar (for water at 20 °C), calculated using equation 2.9 assuming a flow-rate of 30 μL/hour originating from the OoC platform. This length of tubing stores 24 hours of continuous droplet generation. The OoC perfuses 720 μL and an additional 720 μL of oil is pushed by the peristaltic pump during droplet generation over the course of 24 hours, equating to a total volume of 1440 μL.

To assess variation in droplet generation, the setup was attached to the OoC outlet. Water was perfused through the basolateral compartment of the chip at 30 μL/hour. The droplet generator was activated to produce droplets every 20 minutes. Sequential 10 μL droplets were generated in the outlet tubing over 33.3 hours, leading to a total of 100 droplets. A camera was placed above the outlet tubing, with pictures automatically taken every 20 minutes. The size and volume of each droplet was determined with image analysis software (ImageJ). Experiment was repeated with 3 different devices and the results are shown in Figure 5.10.

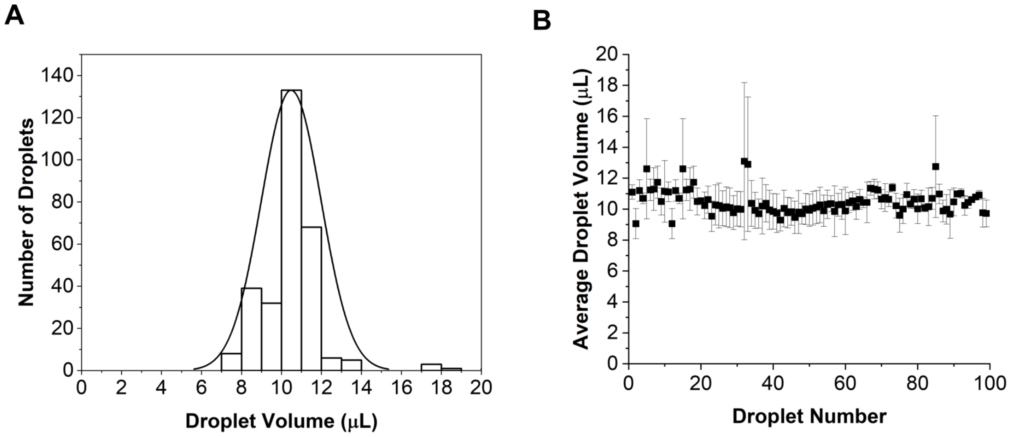

FIGURE 5.10: Droplet volume distribution following 34 hours of continuous droplet generation (A), with droplet volume stability throughout the experiment shown in (B). Data in (A) is for droplets collected from 3 different devices. Data in (B) represents the average droplet volume per droplet generation, with error bars showing the standard deviation.

Droplets were generated with an average volume of 10.34 ± 0.9 μL between devices. Two of the three devices showed good droplet generation stability throughout the entire experiment and droplet sizes slightly above 10 μL. The third device had more variation at the start and a smaller droplet volume. Variation between devices could be caused by human error when inserting connection tubes between the droplet generator and the oil reservoir and/or OoC platform. Droplet sizes were determined by measuring how many pixels each droplet occupies in each picture, which is an additional source of error in the entire set of data. Each pixel in the dataset equates to approximately 0.2 mm, which results in an error of 2% by mistakenly measure the incorrect pixel-length of each droplet by one pixel.

The droplet generator was redesigned to simultaneously generate droplets from all 8 microfluidic chips. To achieve this scalability, 8 of the single-channel droplet generators were placed alongside each other, with 4 air pressure channels located above all of them (Figure 5.11). Therefore, simultaneous actuation of all single-channel droplet generators is possible with the pressure controller and 4 air pressure channels.

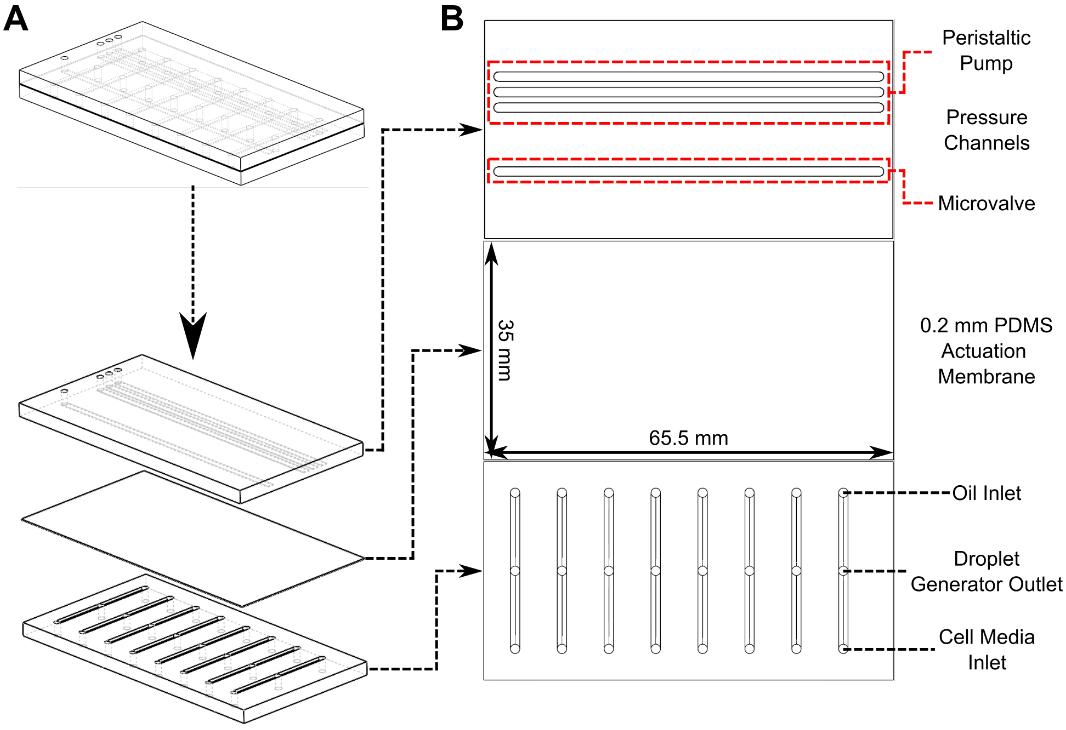

FIGURE 5.11: 3D Schematic of the scaled droplet generator (A) and top-down view of each layer (B).

Droplet generation variation of the 8-channel droplet generator device was measured as previously described. The droplet generator was connected to 8 microfluidic chips, with water perfused through the basolateral compartment at 30 μL/hour and droplets generated every 20 minutes. Droplets were expected to have 10 μL of volume and the experiment ran for 33.3 hours, resulting in 100 droplets generated per channel. A camera was used to photograph the outlet tubing every 20 minutes and pictures were analysed with ImageJ to extract the droplet size and volume. Results are shown in Figure 5.12 correspond to 1 device.

Results show that droplet volume follows a Gaussian distribution, with a mean volume of 9.47 ± 0.6 μL. Droplet generation remained stable across all 8 channels throughout the experiment.

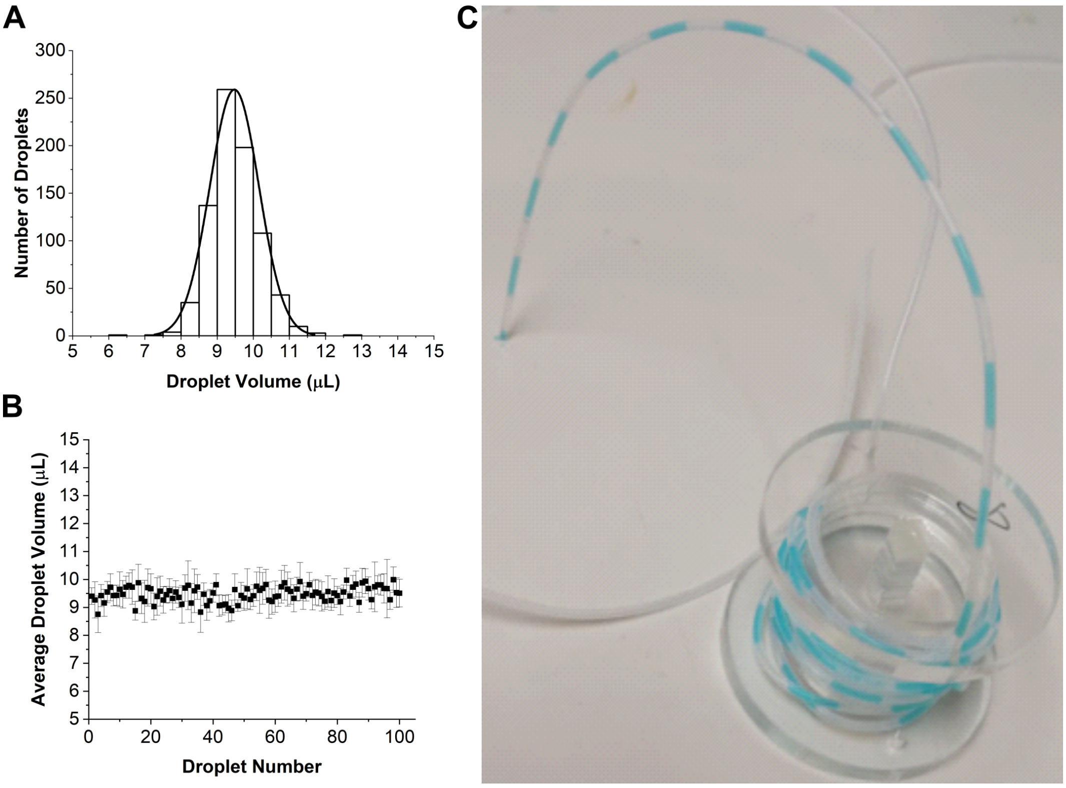

FIGURE 5.12: Droplet volume distribution (A) and average droplet volume (B) after 34 hours of continuous droplet generation with 8 microfluidic chips in parallel. Example of droplets stored in tubing (C). Data is from 1 device.

5.5.3 Diffusion through porous supports

The solutes expelled by cells need to diffuse through the porous support, on which cells are cultured, and reach the basolateral compartment. In static models (Transwells) this diffusion can be modelled using Fick's law, where the concentrations reach equilibrium where both apical and basolateral compartments have equal concentration of solutes. Diffusion through the porous support in a chip with flow is defined by the convection-diffusion equation, where mass transport due to convection from flow of liquid must be considered.

Comsol simulations of diffusion of fluorescein (FITC) in static and OoC models over time are shown in Figures 5.13 A,B,C and D. For both simulations, solute concentration in the apical and basolateral compartments was initially set to 1 mM and 0 mM respectively. Geometry and studies specifications found in appendix A.3.3. The diffusion coefficient of the solute was set to $0.4 \times 10^{-9}\ m^2/s$, which corresponds to the diffusion constant for FITC in water at 20 °C Casalini et al. (2011). The porous support was modelled as a porous matrix, with a porosity of 0.5 and 12.6 % for Transwells and OoC respectively. Porosity was calculated from physical properties of membranes used in Transwells and the OoC platform and equation 5.2. Transwells have a porous membrane area of 0.33 cm^2, with pore sizes of 0.4 μm and pore density of $4 \times 10^6\ pores/cm^2$

respectively. The OoC model has a porous membrane area of 0.2 cm^2, with pore sizes of 0.4 μm and pore density of 10^8 $pores/cm^2$ respectively. The Transwell was modelled as two separate liquid volumes of 200 and 500 μL for the apical and basolateral compartments respectively, with the porous matrix in-between. The OoC model has a fixed apical volume of 100 μL and basolateral flow-rate of 30 μL/hour. Flow in the microfluidic chip was modelled by solving the Navier-Stokes equations for incompressible non-Newtonian fluids. Diffusion of solutes in Transwells was determined using Fick's second law, while for the OoC the convection-diffusion equation was used. Concentrations of solute in the apical and basolateral compartments were measured over time for a period of 48 hours. Simulations show an equilibrium between basolateral and apical solute concentration in Transwells after 43 hours, while the OoC has a continuous exponential decay of apical concentration, followed by a decrease of basolateral concentration as perfusion removes solute from the microfluidic chip. After 48 hours, the microfluidic chip has negligible amounts of solute left in solution.

$$Porosity(\%) = \frac{EmptyVolume}{Membrane_{TotalVolume}} = \frac{Pore_{Volume} \times Pore_{Density}}{Membrane_{TotalVolume}} \tag{5.2}$$

Repeating the OoC Comsol simulation and calculating solute concentration over time at the end of a 10 cm outlet tubing (Figure 5.14A), gives the same exponential decay with a 6-7 hour offset (Figure 5.14B). The offset is caused by time required for liquid leaving the microfluidic chip to reach the end of the outlet tubing. Taylor-dispersion increases the effective diffusion of solutes along the outlet tubing, before liquid is compartmentalised in droplets. This is expected, as solute dispersion in the OoC outlet tubing is predominantly due to convection. For a length of tubing of 10 cm, with a flow-rate of 30 μL/hour, an internal diameter of 1 mm and diffusion coefficient of $0.4 \times 10^{-9} m^2/s$ the Peclet number is 26500. The Peclet number indicates the relative balance between diffusion and convection of solutes in a microfluidic channel, and a high Peclet numbers indicates predominance of convection of solutes.

To experimentally measure the diffusion of solutes through the porous membrane in the OoC, water was perfused through 6 microfluidic chips for 24 hours at 30 μL/hour. A 100 μL volume of FITC solution (0.05 mg/mL) was added to the apical compartment of each chip. The droplet generator was attached to the outlet of each chip and droplets were generated every 20 minutes. After 24 hours, droplets stored in the droplet generator outlet tubing were manually dispensed into 384 well plates for analysis. This dispensing was performed by attaching the tubing to a syringe pump and pushing water through the tube at 0.1 mL/min while manually dispensing each droplet into the appropriate well. The experiment was repeated 2 times, with results shown in Figure 5.14C. The data correlates with the simulated results, showing FITC diffusion through the porous membrane with a 4-5 hour delay before appearing in the droplets, followed by a peak in concentration at 6-8 hours. After the peak, the concentration decays over time as the solute in the apical compartment of the microfluidic chip diffuses out. Chip-to-chip and experimental variation can be mainly attributed to human error, associated with the manual dispensing of droplets into the 384 well plates.

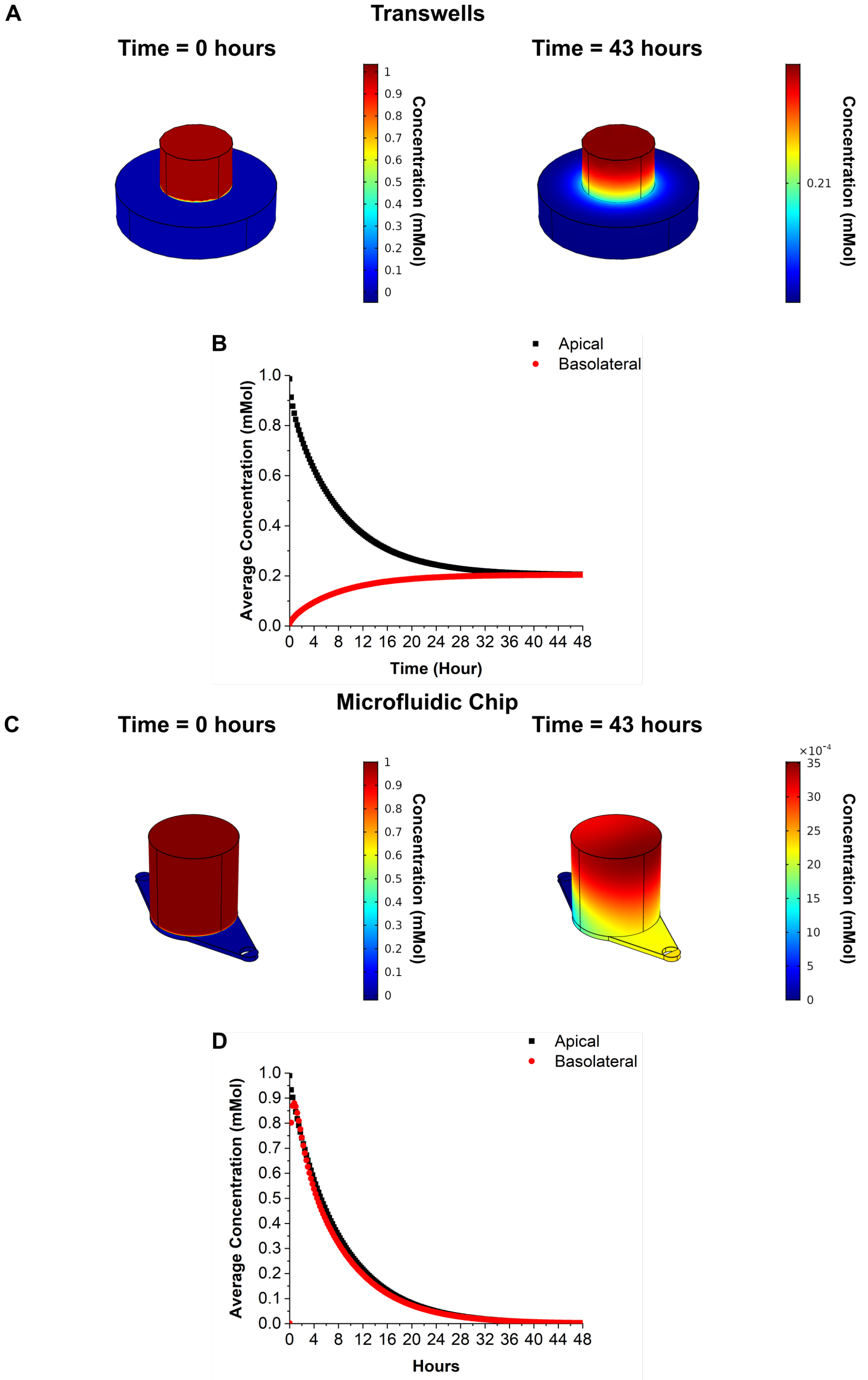

FIGURE 5.13: COMSOL simulations of solute diffusion through the porous support present in a Transwell support (A) and a microfluidic chip (C). Initial solute concentration was set in apical compartments to 1 mMol, with a diffusion coefficient of $0.4 \times 10^{-9}\ m^2/s$. Porous support membranes were modelled as a porous matrix, with a porosity of 0.5 and 12.6 % for Transwell supports and microfluidic chip respectively. Apical and basolateral concentrations of solute were measured over the course of 48 hours, in which Transwell supports reach a concentration equilibrium between basolateral and apical compartments (B), and the microfluidic chip is depleted of solute (D), due to existence of basolateral perfusion.

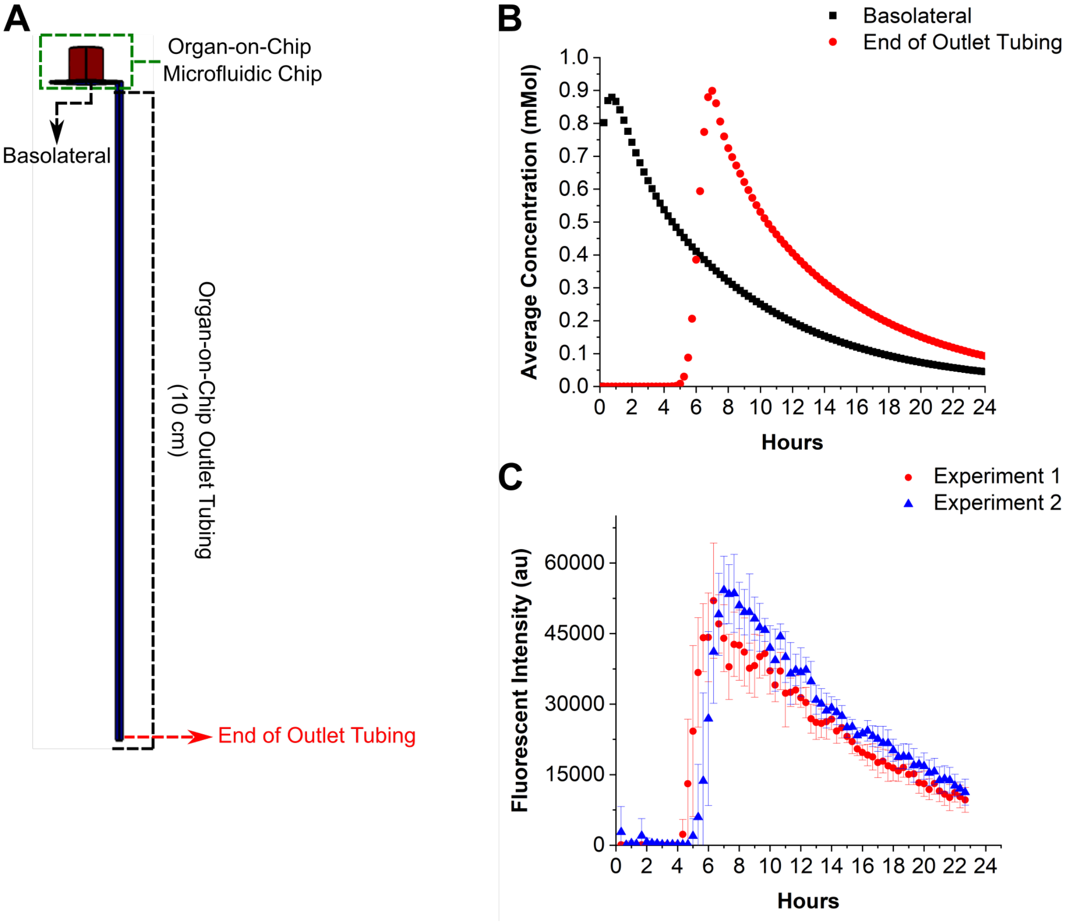

FIGURE 5.14: COMSOL diagram (A) displaying the microfluidic chip and locations were solute concentration was measured and compared. Simulated data of average solute concentration present in the basolateral compartment and at the end of the outlet tubing of the OoC platform (B), to which the droplet generator will be attached. Diffusion of FITC through the OoC porous support using the droplet generator over the course of 24 hours (C), where each data point represents a different collected droplet and each coloured line a different experimental repeat. Error bars in C correspond to the standard deviation across all 6 microfluidic chips, while each point relates to the average.

5.5.4 Cell Experiments

The same setup was used to assess macromolecular permeability and Interleukin-8 (IL-8) production of human bronchial epithelial cells (16HBE14o-) to chemical stimuli (TX-100 or Poly I:C) in two separate experimental sets.

5.5.4.1 FITC-Dextran Permeability

In the first set of experiments, the droplet generator was used to assess 16HBE14o- cells permeability to FITC-Dextran following apical stimulation with TX-100. For each experiment, cells were cultured in the chips for 4 days, and barrier formation measured by TER. Following barrier formation, FITC-Dextran was added to the apical compartment of each chip, to a final concentration of 2 mg/mL. TX-100 solution was added to 3 of 6 chips, at an apical concentration of 1 % v/v. Protocols for TX-100 and FITC-Dextran reagent preparation in appendix A.3.4 and A.2.7.1. After addition of Triton, the droplet generator was attached to each chip and droplets were generated every 20 minutes for 24 hours. Transwells were used alongside the OoC platform and stimulated after 4 days of culture. At the end of the experiment, droplets and 10 μL of the apical and basolateral solution of each Transwell were dispensed into 384 well plates and fluorescence analysed. The experiment was repeated 3 times, with results shown in Figure 5.15.

Basolateral florescence in microfluidic chips without Triton showed constant diffusion of FITC-Dextran across the barrier, with fluorescence increasing above the baseline at 3-4 hours post treatment and remaining stable throughout the following 24 hours. This indicates slow diffusion of FITC-Dextran across the intact epithelial cell barrier, confirmed by TER measurements. Additionally, use of the droplet generator did not negatively impact cells in chip, as controls remained with normalized TER values close to 1 in the three experimental repeats. Treatment with Triton lead to rapid cell barrier disruption, as indicated by the sharp decrease in TER and increase in basolateral fluorescence, peaking at 3-4 hours post treatment. Following the peak, FITC-Dextran concentration slowly decays over 24 hours, as it diffuses through the exposed porous support in a similar manner as seen in Figure 5.14. This data correlates with the Transwell endpoint measurements. Transwells without Triton had limited FITC-Dextran diffusion between basolateral and apical compartments, due to the presence of an intact cell barrier. Cell barrier disruption with Triton resulted in equal FITC-Dextran concentration between apical and basolateral sides, as diffusion drives the system to equilibrium.

5.5.4.2 Interleukin-8 Production

The second set of experiments measured 16HBE14o- interleukin-8 (IL-8) production following apical stimulation with Poly I:C. IL-8 is a pro-inflammatory cytokine produced by several cell types. Poly I:C is a dsRNA viral analogue which triggers an anti-viral and proinflammatory response, actin cytoskeletal reorganization and disassembly of tight junctional complexes. Apical stimulation of cells with Poly I:C induces epithelial barrier disruption and an increase of IL-8 production Heijink et al. (2016). To assess barrier disruption and IL-8 production over time in the OoC, cells were grown in 6 chips for 4 days, with continuous monitoring of TER. After formation of an intact epithelial barrier, 3 of 6 chips were apically treated with Poly I:C, to an apical concentration of 25 μg/mL. Droplets were generated, for each chip, every 20 minutes over 20 hours. Transwells were used in parallel with cells cultured for 4 days followed by apical stimulation with Poly I:C. At the end of the experiment, the 10 µL droplets were merged into 30 µL volumes (by dispensing 3 droplets per well) and dispensed into 96 well plates, and the apical solution of each chip dispensed into centrifuge tubes for analysis. Transwell apical and basolateral solutions were transferred to centrifuge tubes. IL-8 production was measured using a standard ELISA kit for two microfluidic chips, one per condition. IL-8 production and TER results for two individual experiments are shown in Figure 5.16.

A decrease of TER was visible in the OoC following Poly I:C addition (figure 5.16A), although the two repeats were not similar. Droplet generation did not negatively impact cells cultured in chips, as both media controls retained normalized TER values above between 1 and 1.5. Basolateral IL-8 production (Figure 5.16C) was extremely variable in the OoC, with and without addition of Poly I:C, whilst an increase in apical IL-8 was measured in apical cell media from chips stimulated with Poly I:C (Figure 5.16D). Results show low variability in the Transwells of both TER (Figure 5.16B) and IL-8 concentration (Figure 5.16D). Addition of Poly I:C leads to barrier disruption, as seen by the decrease of TER compared to media control, and increase of IL-8 production, in the apical and basolateral compartments, for both experimental repeats. The exact causes of the variability in the OoC for IL-8 concentration is unknown and could be related to variability in microfluidic chip fabrication or uncharacterised biological processes occurring under flow.

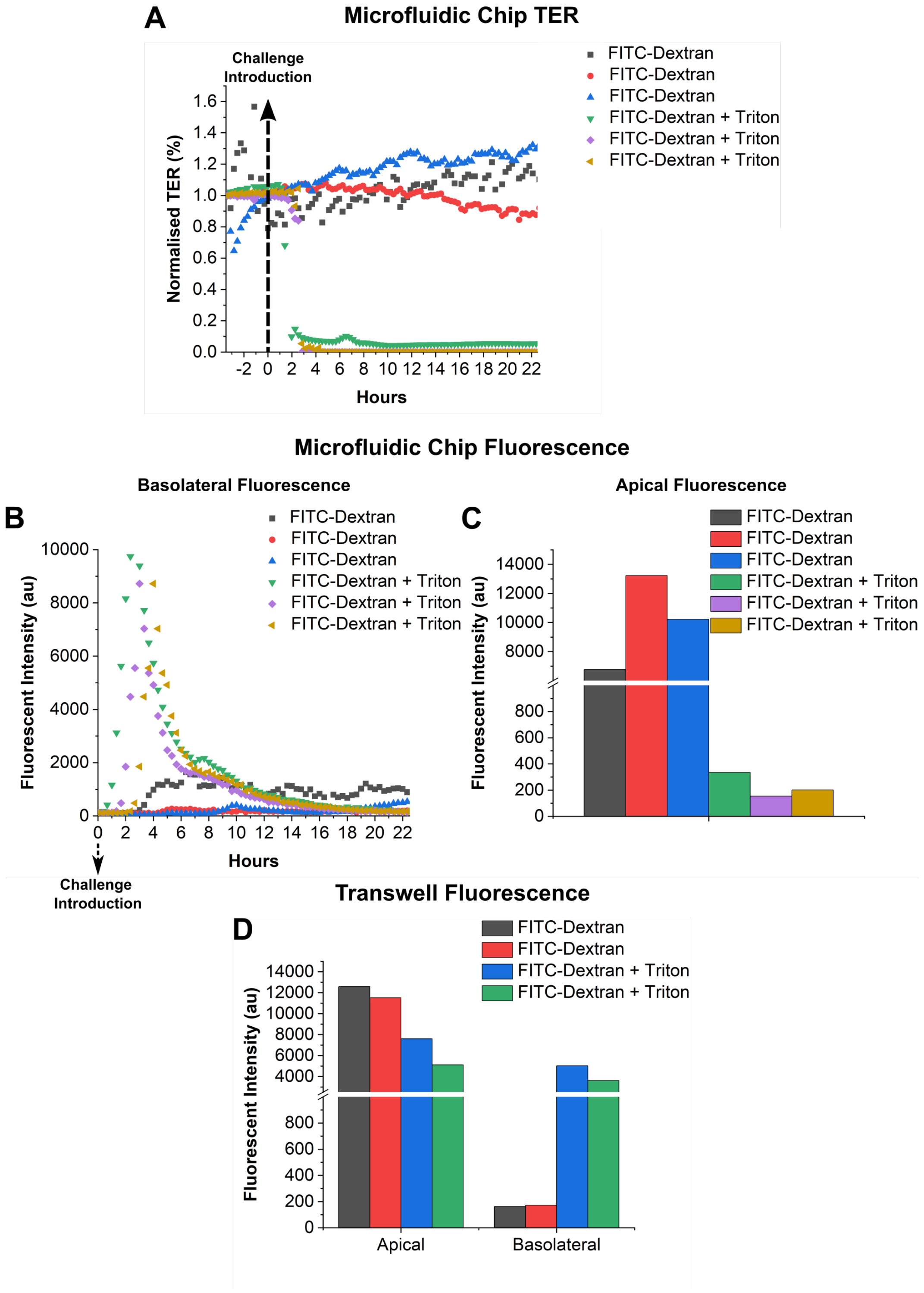

FIGURE 5.15: 16HBE14o- Triton (1%) and FITC-Dextran (2mg/mL) apical stimulation data. Cells cultured in the OoC platform displaying a sharp decline in TER post addition of Triton + FITC-Dextran, while addition of only FITC-Dextran did not affect cell barrier integrity (A). Molecular permeability data collected obtained from basolateral (B) and apical (C) samples correlate with TER results, with Triton treated cells displaying low high levels of basolateral and low levels of apical FITC-Dextran. Data obtained from Transwells cultured in parallel agrees with the OoC data, with Triton treated cells displaying equal levels of FITC-Dextran in apical and basolateral compartments. Data is from one microfluidic chip per condition, from 3 experimental repeats.

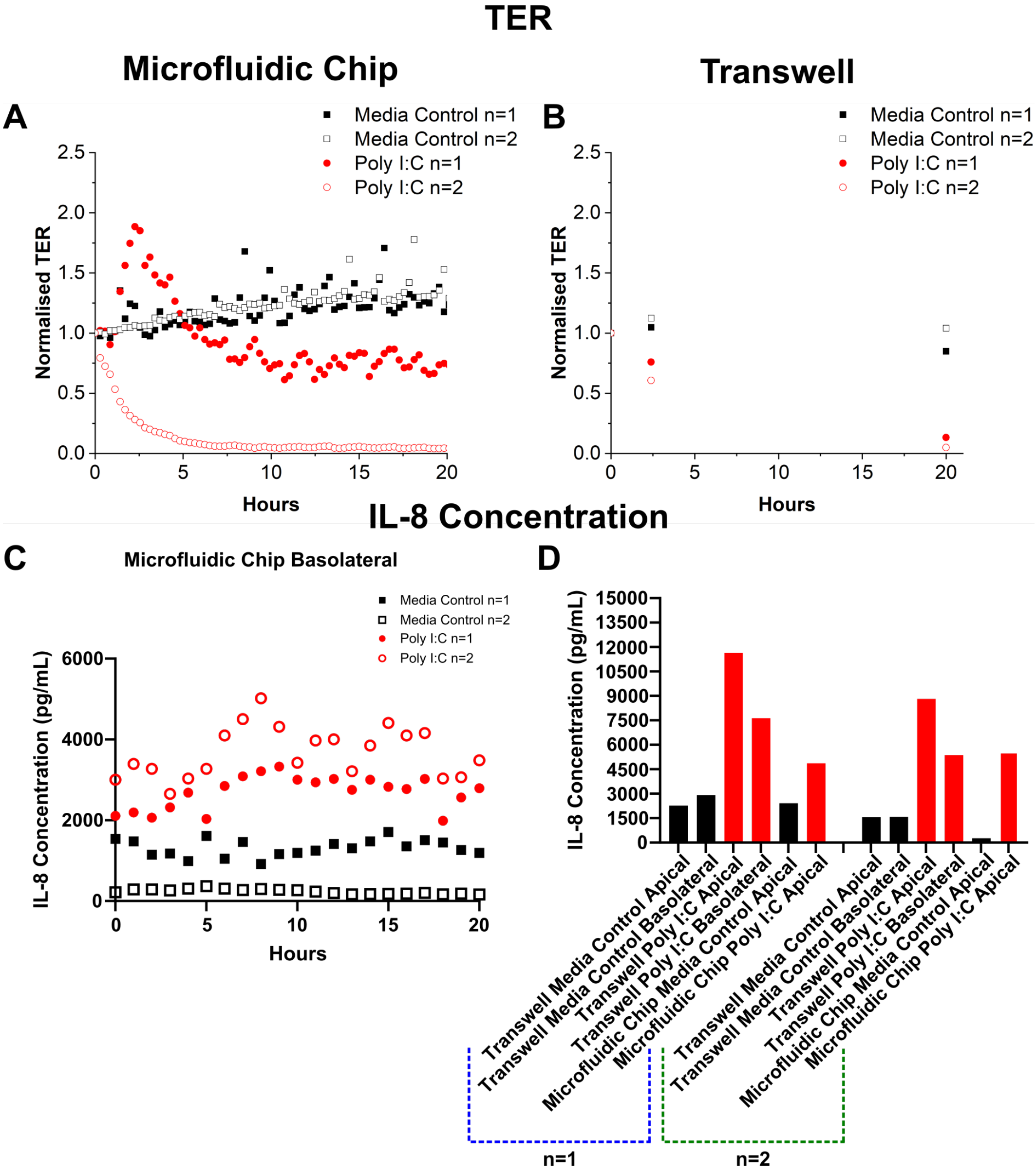

FIGURE 5.16: Normalised TER data for microfluidic chips (A) and Transwell supports (B) following addition of Poly I:C (25 μg/mL). Microfluidic chips basolateral IL-8 concentration over the course of 20 hours post Poly I:C stimulation (C). IL-8 concentration present in the apical compartments of each microfluidic chip and in the apical and basolateral compartments of each Transwell (D). Data is from 1 microfluidic chip and transwell support for each condition, from two different experimental repeats.

5.6 Summary

In this chapter methodologies for epithelial barrier permeability assessment and immunoassays were provided, for both static and OoC models. Molecular permeability is usually based on diffusion of molecular compounds across the epithelial cell barrier, while immunoassays in cell models typically rely in ELISA or ELISA based approaches for cytokine detection. Use of OoC platforms for molecular permeability or immunoassay studies provided higher temporal resolution and improved data analysis comparatively to static models. An explanation was provided regarding droplet microfluidics, and it's use for analyte compartmentalization in OoC platforms.

An attachment to the UoS OoC platform was developed which employs droplet microfluidics for analyte compartmentalization. The attachment was composed of 2 main blocks; the droplet generator, in which a PDMS peristaltic pump pushed and generated 10 µL droplets of cell media and oil sequentially, and the pressure controller, used to control the actuation of PDMS valves present in the droplet generator. Tests were performed regarding flow rate and droplet generation throughout the attachment development, starting as a single channel peristaltic pump and ending as an 8-channel droplet generator, with all 8 channels actuated in parallel using a single pressure input, providing an average droplet size of 9.47 ± 0.6 μL over the course of 33.3 hours.

The droplet generator was used to assess fluorescein diffusion across the porous support membrane in the microfluidic chip, with experimental results showing a similar diffusion trend as the one seen with COMSOL simulations. Diffusion of FITC-Dextran across a formed human bronchial epithelial barrier was tested following triton apical stimulation, with microfluidic chips treated with triton displaying the expected peak in fluorescence 4-5 hours post stimulation (similar to COMSOL simulation) while media controls maintained low diffusion of FITC-Dextran across the intact epithelial barrier. Further, analysis of the media control normalised TER when connected to the droplet generator indicated that there were no adverse effects to the barrier integrity, with a maintained TER of 1. Comparatively to Cedillo-Alcantar et al. (2019), the platform is able to store the droplets over prolonged periods of time for a variety of benchtop assays, not being constrained by assays which can be done in-chip. Additionally, the droplet generator was able to reliably be used while connected to 8 parallel microfluidic chips, demonstrating high degree of scalability.

Lastly, 16HBE14o- cells were apically stimulated with dsRNA and basolateral IL-8 released was assessed using the droplet generator over time. However data did not show any trends and displayed high variability between experimental repeats, with no conclusions possible. While further work is required to understand the biological effects of culturing cells with flow, the droplet generator provided an easy and robust tool to obtain a temporal resolution for molecular permeability and/or immunoassays using the OoC platform.

Chapter 6

Conclusions and Future Work

The design, fabrication and experimental characterization of a compact organ-on-chip platform with a plug-and-play functionality was described. The platform was composed of two main components, the microfluidic chip and the fluidic manifold. The microfluidic chip has several structural PMMA layers, one porous support membrane (on which cells are seeded and cultured) and a glass chip (with patterned platinum electrodes coated with ruthenium oxide). Electrodes located in the glass chip were responsible for electrical impedance spectroscopy measurements, used to assess epithelial barrier formation and integrity. Two pairs of electrodes were present in each microfluidic chip, with one pair responsible for measurements of cell medium resistance and electrode characteristics and the second pair located underneath the cell culture for cell barrier parameter measurement. The manifold was responsible for fluidic routing from the syringe pump to the microfluidic chip. A fluidic seal between both components was achieved using nitrile o-rings and magnets, allowing placement, alignment and replacement of microfluidic chips in the platform in a ”plug-and-play” manner. The platform was capable of running 8 cell cultures in parallel and two platforms could fit on a standard incubator shelf. Both human bronchial and gut epithelial cell lines were successfully cultured in the platform independently, generating similar TER and cell barrier capacitance values to those reported in literature. Additionally, epithelial barrier integrity disruption was recorded with high temporal resolution in the platform following apical stimulation of 16HBE14o- cells with either a detergent (Triton X-100) or a viral mimetic (Poly I:C).

Cell barrier parameters were extrapolated from electrical impedance spectroscopy data using electrical circuit modelling. Each parameter (cell media resistance, electrode characteristics and cell barrier characteristics) was modelled as an equivalent electrical component and data was fitted to the circuit utilising complex non-linear square fitting and the Nelder-Mead minimisation algorithm. Geometrical cell constants required for the electrical circuit modelling were obtained via COMSOL simulation and numerical calculations (conformal mapping). Software was written in Python and a graphical user interface was created for ease of use. Using the model, cell media conductivity and electrode parameters were calculated over 12 hours, with minimal difference when compared to values recorded using a commercial conductivity meter. Additionally, the model was capable of detecting small differences in resistance after placing a small PMMA disk onto the porous membrane within the apical compartment of chips. Lastly, it was possible to extrapolate a TER equivalent of human bronchial cells cultured in the system over 5 days, allowing comparisons to standardized methods of epithelial barrier integrity assessment in static models or to reported results in literature.

A droplet generator which attached to the organ-on-chip platform was designed, developed and fabricated, which allowed analyte compartmentalisation originating from cells cultured in the platform through droplet microfluidics. The droplet generator was able to generate droplets in 8 separate channels simultaneously while utilising only 1 pressure input per actuation channel (4 in total). Droplets generated over 33.3 hours in 8 channels reached an average volume of 9.47 ± 0.6 μL, similar to the expected 10 μL droplet volume. The droplet generator was used to study fluorescein diffusion through the porous support membrane in the microfluidic chip, with results showing similar fluorescein diffusion when compared to COMSOL simulations. Following this, diffusion of FITC-Dextran through an epithelial cell barrier (16HBE14o- cells) was tested with and without apical stimulation with triton, with a clear difference between conditions visible in both TER and basolateral fluorescence data. Lastly, IL-8 production of 16HBE14o- cells following viral mimetic (Poly I:C) apical stimulation was tested, but no conclusions could be inferred from the data due to chip-to-chip and experimental variation between different repeats.

6.1 Improvements

In this section, improvements to the various aspects of this project will be discussed. These improvements will increase the platform, software and droplet generator robustness and reliability for future users and experiments.

6.1.1 Software and Modelling

The current Python software analyses data from each chip sequentially. While functional, the sequential analysis was responsible for the bulk of the time required for analysis and parameter extraction from EIS data. Implementation of threading in the software would significantly decrease time needed for analysis, as each chip could be analysed in parallel.

Additionally, the electrical circuit diagram assumes that there are 100 μL of cell media placed in the apical compartment throughout the entire experiment, which may not always be representative of experimental conditions as apical volume fluctuations are common due to outlet tubing placement and Laplace pressure fluctuations by droplet detachment from the tubing. Therefore, the electrical circuit model should extrapolate the cell media conductivity, via media electrodes modelling, and model the volume in the apical compartment of each microfluidic chip, providing the user with more information regarding experimental conditions. This value is most crucial for apical stimulation experiments, in which a specific final concentration is desired.

6.1.2 Droplet Generator

The current droplet generator design relies on a T-junction architecture to break the flow of cell media and create a droplet. During cell experiments, an increased droplet size variation was visible, most likely attributed to inability of oil flow to completely separate the cell media flow. This could be improved by changing the microfluidic architecture and employing a flow-focusing channel between oil and cell media flows, which would ensure complete droplet formation. The addition of surfactant to the oil phase would also enable better stabilisation of the interface between both phases, improving droplet stability over time while being stored. Additionally, the current droplet generator is composed of PDMS for ease of prototyping. This material is known to adsorb small molecules and should be replaced. Thermoplastics, such as PMMA, provide similar optical properties as PDMS without molecule adsorption and could be used as the droplet generator structure. While the PDMS actuation membrane is unlikely to adsorb significant quantities of molecules, due to small time interfacing with cell media, this membrane could be replaced with Viton or Nitrile membranes, which are inert and provide similar actuation motion using air pressure.

6.1.3 OoC Platform

Cell experiments demonstrated large chip-to-chip variation in TER and electrode parameters. Improvements in microfluidic chip fabrication are required to decrease said variation. One major cause for variation in TER data is due to the tautness of the porous membrane onto which cells are seeded and cultured. Since the chip is manually assembled, variation is visible in the tautness of this membrane, which greatly impacts cell culture surface area and membrane movement with basolateral flow. Additionally, each microfluidic chip is manually assembled, with assembly taking approximately 15 minutes per chip. To increased tautness of the porous membrane and reduce both time and variation in the assembly process, the microfluidic chips should be injected moulded as a single piece. If possible, the porous membrane should be mechanically stretched in the injection moulding mould, as to be integrated in the microfluidic chip following material injection.

Once fabrication and assembly of the OoC platform is improved and chip-to-chip variation decreased, several biological focused experiments should be performed to assess the effects of different types of apical/basolateral stimuli in cells used in this project (Caco-2 and 16HBE14o-). Additionally, other types of epithelial cell lines could be cultured using the platform, as to further validate its use as a valid option to existent cell models.

6.2 Final Remarks

Comparatively to other platforms in the current commercial landscape, the developed OoC platform provides an easy, robust and cheap manner to develop and use more physiologically representative models for drug discovery. At the time of writing, the only commercially available platform providing real-time TER measurement while inside a standard incubator is the one provided by MIMETAS, although the platform itself is lacking cell media renewal or constant basolateral flow-rate. The developed platform allows for control of the flow-rate, which can be of great importance when mimicking interstitial flow. Additionally, no commercial platform allows for continuous collection of basolateral cell media, lacking time-resolution when measuring for molecular permeability or detecting biological analytes, and require manual collection from said platforms (if possible). Therefore, the developed platform has an important edge when delivering crucial data to users working in the drug development field, being able to correlate epithelial cell barrier integrity through TER with the increase/decrease of biological analyte and/or molecular permeability.

Appendix A

Appendix

A.1 Impedance Modelling

A.1.1 COMSOL Electrical Field Simulation

Electrical field simulations were performed using the Electric Currents physics module in COMSOL Multiphysics.

A.1.1.1 Geometry

Media electrodes were created as blocks with 0.5 mm, 2.8 mm and 500 nm width, length and height respectively. There is a spacing of 0.2 mm between electrodes. Media electrode compartment was created as a block above the electrodes with 1.2, 2.8 and 0.275 mm of width, length and height respectively.

Cell electrodes were created as single cylinder with a radius of 2.5 mm and height of 500 nm. Spacing of 2.8 mm between electrodes was generated by subtracting the initial cylinder with a block with 2.8 mm width. Basolateral and apical compartments were created as cylinders above the electrodes with a radius of 2.5 mm and heights of 0.275 and 5 mm respectively.

A fine mesh was applied to the geometries.

A.1.1.2 Materials

Electrodes and compartments were set as Platinum and water respectively. For geometrical cell constant calculation, electrical conductivity for both materials was changed to 1 S/m.

A.1.1.3 Conditions

Current conservation was applied to all domains and electrical insulation to all external facing surfaces. An electric potential of 1 V was attributed to one electrode, while the other was set to ground.

Stationary studies were computed for geometrical cell constant calculations.

A.1.2 Python Code and Instructions

Code for modelling of electrical impedance spectroscopy data was written in Python 3.7 using Microsoft VSCode IDE. The following packages need to be installed before using the code:

- PyQt5
- numpy
- pandas
- scipy
- matplotlib

Package installation can be performed via pip using the command *pip install PyQt5 numpy pandas scipy matplotlib*, *pip3 install PyQt5 numpy pandas scipy matplotlib* or *python -m pip install PyQt5 numpy pandas scipy matplotlib*.

When starting the program, an user interface will appear, in which experimental details can be written in the appropriately labelled boxes. If the number of baseline readings (readings performed before cell seeding) is not specified in the interface, it will be assumed to be zero. Once all details are specified, press "Select Data Files to Analyse" button. This will open a new window in which the data files to be analysed can be selected. Navigate to the appropriate folder and select the files required for data analysis, selecting both the cell and media electrodes impedance files for each microfluidic chip used. Data in files need to have the same number of data points (same number of lines in both files) and should be in the following format:

Time initiated	Frequency (Hz)	Magnitude (Ω)	Phase (°)
15/05/2021 14:33	112160	1476.8	-5.12

Once files are selected, the program will analyse the data for each microfluidic chip. This process will take time and the interface will appear to have frozen. Progress is printed to the console after each modelled data point for monitoring. When the program finishes the analysis, the interface will unfreeze and modelled data will be plotted throughout the window. A folder named ”Results” will have been created with 3 files inside, a ”CellResults.csv”, ”RefResults.csv” and ”Experimental details.txt” which have the data regarding cell electrodes, media electrodes and experimental notes respectively.

If an user only wants to open previously analysed data in the program, press the ”Select Result Files (.csv)” button. This will create a new window in which the modelled data files can be selected. Select both files (”CellResults.csv” and ”RefResults.csv”) and click open. Plots for the data contained in these files will be displayed throughout the interface.

The following code is used to generate the graphical user interface and perform data analysis:

```python
from sys import argv,exit
from PyQt5.QtWidgets import QLabel, QMainWindow, QApplication, QPushButton,
    QLineEdit, QFileDialog, QComboBox
from PyQt5 import QtGui
from matplotlib.backends.backend_qt5agg import NavigationToolbar2QT as
    NavigationToolbar
from matplotlib.backends.backend_qt5agg import FigureCanvasQTAgg as
    FigureCanvas
import matplotlib.pyplot as plt
import numpy as np
import pandas as pd
from scipy.optimize import minimize
import os

###### Experiment Constants ######
CELLCONSTANT_CELLCHAMBER_BASO = 4.1174e-4
#CELLCONSTANT_CELLCHAMBER_BASO_calculated = 3.8553e-4
CELLCONSTANT_CELLCHAMBER_APICAL = 1.4622e-3
CELLCONSTANT_REFERENCE= 1.8856e-3
TIME_PER_MEASUREMENT=17
BOUNDARIES_PERCENTAGE=0.1
ELECTRODE_AREA_RATIO=2.3
CELL_GROWTH_AREA=0.2

###### Initial Guesses ######
X0REF_Resistance=400
X0REF_CPE_MAGNITUDE=1e-4
X0REF_CPE_EXPONENT=0.3
X0CELL_RESISTANCE=10
X0CELL_CAPACITANCE=3e-8

###### Lower Boundary ######
LBREF_RESISTANCE=0
LBREF_CPE_MAGNITUDE=1e-6
```

```
LBREF_CPE_EXPONENT=0
LBCELL_RESISTANCE=0
LBCELL_CAPACITANCE=1e-9

###### Upper Boundary ######
UBREF_RESISTANCE=2000
UBREF_CPE_MAGNITUDE=1e-3
UBREF_CPE_EXPONENT=1
UBCELL_RESISTANCE=100000
UBCELL_CAPACITANCE=1e-5

class Params(object):
    def __init__(self,x,LB,UB,fun,n,xsize,y,z):
        self.args=x
        self.LB=LB
        self.UB=UB
        self.fun=fun
        self.n=n
        self.xsize=xsize
        self.OutputFcn=y
        self.BoundClass=z
    pass

def MinimizationAlg(RealData,ImagData,value):
    obj=0
    for k in range(0,len(RealData)):
        obj=obj + ((value.real[k]-RealData[k])**2)/RealData[k] + ((value.imag[k]-ImagData[k])**2)/abs(ImagData[k])
    return obj

def ReferenceModel(x,y):

    Zcpe = (1/(x[1]))*((1j*omega)**(-x[2]))
    value=Zcpe+x[0]

    if y==1:
        return MinimizationAlg(RealRef,ImagRef,value)
    else:
        return value

def CellChamberModel(x,y):

    if valuenumber < (BaselineValues-1):

        Zcpe = (1/(x[1]))*((1j*omega)**(-x[2]))
        RbCellChamber=FitRef[0]*(CELLCONSTANT_REFERENCE/CELLCONSTANT_CELLCHAMBER_BASO)
        Zm=0
        value = Zcpe + (((x[0])+Zm)*RbCellChamber)/((x[0]+Zm)+RbCellChamber)

    else:
```

```

        Zcpe = (1/(x[1]))*((1j*omega)**(-x[2]))
        RbCellChamber=FitRef[0]*(CELLCONSTANT_REFERENCE/CELLCONSTANT_CELLCHAMBER_BASO)
        Cm=(1/(1j*omega*x[3]))
        Zm = np.divide((x[4]*Cm),(x[4]+Cm))
        value1=np.divide(((x[0]+(2*Zm))*RbCellChamber),((x[0]+(2*Zm))+RbCellChamber))
        value =  np.add(Zcpe,value1)

    if y==1:
        return MinimizationAlg(RealCell,ImagCell,value)
    else:
        return value

def CellChamberMin(x):

    return CellChamberModel(x,1)

def RefMin(x):

    return ReferenceModel(x,1)

def Nelder_Mead_Bounds(fun,x0,LB,UB):
    ## Nelder Mead is usually only applicable to unconstrained functions. sin(x) variable transformation is used to allow constraints in the model ##########
    ## More information at "John D'Errico (2020). fminsearchbnd, fminsearchcon (https://www.mathworks.com/matlabcentral/fileexchange/8277-fminsearchbnd-fminsearchcon), MATLAB Central File Exchange. Retrieved October 2, 2020." #######
    ## The available MATLAB code was translated into Python and only the required components of the original code were kept ##

    def intrafun(x):
        xtrans=xtransform(x,params)
        fval=eval(params.fun)(np.reshape(xtrans,params.xsize))
        return(fval)

    def xtransform(x,params):
        xtrans=np.zeros(params.xsize[0])
        for i in range (params.n):
            xtrans[i]=(np.sin(x[i])+1)/2
            xtrans[i]=xtrans[i]*(params.UB[i]-params.LB[i])+params.LB[i]
            xtrans[i]=max(params.LB[i],min(params.UB[i],xtrans[i]))
        return(xtrans)

    x0=np.array(x0)
    xsize=x0.shape
    n=len(x0)
    global params
```

```
    params=Params([],LB,UB,fun,n,xsize,[],np.zeros(n))

    x0u=x0
    for i in range(n):
        x0u[i]=2*(x0[i]-LB[i])/(UB[i]-LB[i])-1
        x0u[i]=2*np.pi+np.arcsin(max(-1,min(1,x0u[i])))

    results=minimize(intrafun,x0u,method='Nelder-Mead')
    x=xtransform(results.x,params)
    x=np.reshape(x,xsize)
    return(x)

def ObtainData(filename):
    filenamenew=(filename+'_new')
    with open(filename,'r') as f:
        dataraw=f.readlines()
    datatruncated=dataraw[5:len(dataraw)]
    newfile=open(filenamenew,'w')
    with open(filenamenew, 'w') as newfile:
        for item in datatruncated:
            newfile.write("%s" % item)
    Data=pd.read_csv(filenamenew,sep='\t',lineterminator='\n')
    data = pd.DataFrame(Data)
    os.remove(filenamenew)
    data.columns=["Time Initiated","Frequency","Magnitude","Phase"]
    Magni=np.array(data['Magnitude'])
    Phase=np.deg2rad(np.array(data['Phase']))
    Complex=np.multiply(Magni,(np.cos(Phase)+1j*np.sin(Phase)))
    Frequency = data['Frequency']
    return Complex,Frequency

class LabelTextbox(QMainWindow):

    def __init__(self,parent=None, labeltext=None,xposition=None,yposition=None, width=None, height=None):
        super(LabelTextbox,self).__init__()
        self.Label = QLabel(parent)
        self.Label.setText(labeltext)
        self.Label.move(xposition,yposition)
        self.Label.resize(width,height)
        self.Label.setFont((QtGui.QFont("Arial",12,QtGui.QFont.Bold)))
        self.Text = QLineEdit(parent)
        self.Text.move(xposition, yposition+30)
        self.Text.resize(width,height)
        self.Text.setFont((QtGui.QFont("Arial",12)))

class figure_maker(QMainWindow):

    def __init__(self,parent=None,xposition=None,yposition=None, width=None, height=None):
        super(figure_maker,self).__init__()
```

```python

        self.figure=plt.figure()
        self.canvas=FigureCanvas(self.figure)
        self.canvas.setParent(parent)
        self.canvas.move(xposition,yposition)
        self.canvas.resize(width,height)
        self.toolbar=NavigationToolbar(self.canvas,parent)
        self.toolbar.move(xposition,yposition-20)
        self.toolbar.resize(width ,20)

    def plot_data(self,xdata=[1,2],ydata=[2,1],mode="plain",title=""):

        self.figure.clear()
        ax = self.figure.add_subplot(111)
        ax.plot(xdata,ydata, '*-')
        ax.set_title(title,fontsize=9)
        ax.tick_params(axis="both",which="major",labelsize=9)
        ax.ticklabel_format(axis='y',style=mode, scilimits=(0,0))
        ax.grid()
        self.canvas.draw()

    def plot_allChips(self,xdata=[1,2],ydata=[2,1],numberofchips=0,mode="plain",title=""):
        self.figure.clear()
        ax = self.figure.add_subplot(111)
        for i in range(numberofchips):
            ax.plot(xdata,ydata[:,i] , '*-',label=f"Chip {i+1}")
        ax.legend()
        ax.ticklabel_format(axis='y',style=mode, scilimits=(0,0),)
        ax.set_title(title,fontsize=10)
        self.canvas.draw()

class App(QMainWindow):

    def __init__(self):
        super(App, self).__init__()
        self.title = 'Fitting Algorithm'
        self.left = 10
        self.top = 10
        self.width = 1780
        self.height = 1000
        self.initUI()

    def initUI(self):

        self.setWindowTitle(self.title)
        self.setGeometry(self.left, self.top, self.width, self.height)

        self.CellLineText=LabelTextbox(self, "Cell Line", 20,10,280,40)
        self.PassageNumberText = LabelTextbox(self, "Passage Number", 20,80,280,40)
```

```
        self.CellDensityText = LabelTextbox(self, "Cell Density", 320,10,280,40)
        self.ChallengesText = LabelTextbox(self, "Challenges", 320,80,280,40)
        self.NotesText = LabelTextbox(self, "Notes", 620,80,280,40)
        self.BaselineReadingsText = LabelTextbox(self, "Number of baseline readings", 620,10,280,40)

        self.CellResistanceAll=figure_maker(self,20,310, 880, 290)

        self.CellR2Imag=figure_maker(self,20,620,420,180)
        self.CellR2Real=figure_maker(self,20,820,420,180)
        self.RefR2Imag=figure_maker(self,480,620,420,180)
        self.RefR2Real=figure_maker(self,480,820,420,180)

        self.CellResistance=figure_maker(self,920,20,860,180)
        self.CellCapacitance=figure_maker(self,920,220,860,180)
        self.CellApicalResistance=figure_maker(self,1360,420,420,180)
        self.RefMediumResistance=figure_maker(self,920,420,420,180)
        self.CellCPEMagnitude=figure_maker(self,1360,620,420,180)
        self.RefCPEMagnitude=figure_maker(self,920,620,420,180)
        self.CellCPEExponent=figure_maker(self,1360,820,420,180)
        self.RefCPEExponent=figure_maker(self,920,820,420,180)

        self.ImpedanceAnalyserData = QPushButton('Select Data Files to Analyse', self)
        self.ImpedanceAnalyserData.setFont((QtGui.QFont("Arial",18,QtGui.QFont.Bold)))
        self.ImpedanceAnalyserData.move(20,170)
        self.ImpedanceAnalyserData.resize(880,40)

        self.ResultData = QPushButton('Select Result Files (.csv)', self)
        self.ResultData.setFont((QtGui.QFont("Arial",18,QtGui.QFont.Bold)))
        self.ResultData.move(20,230)
        self.ResultData.resize(660,40)

        self.QComboBox=QComboBox(self)
        self.QComboBox.move(700,230)
        self.QComboBox.setFont((QtGui.QFont("Arial",18,QtGui.QFont.Bold)))
        self.QComboBox.resize(200,40)
        self.QComboBox.setDisabled(True)

        self.ImpedanceAnalyserData.clicked.connect(self.on_click_ImpedanceAnalyserData)
        self.ResultData.clicked.connect(self.on_click_ResultsButton)

        self.QComboBox.activated.connect(lambda: self.CellResistance.plot_data(self.days,self.FittingCell[:,self.QComboBox.currentIndex()],"plain","Cell Resistance (\u03A9.cm$^2$)"))
        self.QComboBox.activated.connect(lambda: self.CellCapacitance.plot_data(self.days,self.FittingCell[:,self.numberofchips+self.QComboBox.currentIndex()],"sci", "Cell Capacitance (Farads/cm$^2$)"))
```

```
        self.QComboBox.activated.connect(lambda: self.CellApicalResistance.plot_data(self.days, self.FittingCell[:, self.QComboBox.currentIndex()+((self.numberofchips-1)*2+2)],"plain","Cell Chamber Apical Resistance (\u03A9)"))
        self.QComboBox.activated.connect(lambda: self.CellCPEMagnitude.plot_data(self.days, self.FittingCell[:, self.QComboBox.currentIndex()+((self.numberofchips-1)*3+3)],"sci","Cell Chamber CPE Magnitude"))
        self.QComboBox.activated.connect(lambda: self.CellCPEExponent.plot_data(self.days, self.FittingCell[:, self.QComboBox.currentIndex()+((self.numberofchips-1)*4+4)],"plain", "Cell Chamber CPE Exponent"))
        self.QComboBox.activated.connect(lambda: self.CellR2Imag.plot_data(self.days, self.FittingCell[:, self.QComboBox.currentIndex()+((self.numberofchips-1)*6+6)],"plain","Cell Chamber R2 Imaginary Component"))
        self.QComboBox.activated.connect(lambda: self.CellR2Real.plot_data(self.days, self.FittingCell[:, self.QComboBox.currentIndex()+((self.numberofchips-1)*5+5)],"plain", "Cell Chamber R2 Real Component"))

        self.QComboBox.activated.connect(lambda: self.RefMediumResistance.plot_data(self.days, self.FittingRef[:, self.QComboBox.currentIndex()],"plain", "Reference Medium Resistance (\u03A9)"))
        self.QComboBox.activated.connect(lambda: self.RefCPEMagnitude.plot_data(self.days, self.FittingRef[:, self.numberofchips+self.QComboBox.currentIndex()],"sci","Reference CPE Magnitude"))
        self.QComboBox.activated.connect(lambda: self.RefCPEExponent.plot_data(self.days, self.FittingRef[:, self.QComboBox.currentIndex()+((self.numberofchips-1)*2+2)],"plain","Reference CPE Exponent"))
        self.QComboBox.activated.connect(lambda: self.RefR2Imag.plot_data(self.days, self.FittingRef[:, self.QComboBox.currentIndex()+((self.numberofchips-1)*4+4)],"plain","Reference R2 Imaginary Component"))
        self.QComboBox.activated.connect(lambda: self.RefR2Real.plot_data(self.days, self.FittingRef[:, self.QComboBox.currentIndex()+((self.numberofchips-1)*3+3)],"plain","Reference R2 Real Component"))

        self.show()

    def on_click_ImpedanceAnalyserData(self):

        global BaselineValues
        global omega
        global valuenumber
        global RealCell
        global RealRef
        global ImagCell
        global ImagRef
        global FitRef


        self.enableUI_Elements(False)
        path=sorted(QFileDialog.getOpenFileNames(self)[0])
        if not self.BaselineReadingsText.Text.text().isdigit():
            BaselineValues=0
```

```
    else:
        BaselineValues=int(self.BaselineReadingsText.Text.text())
    if path == [] or len(path)%2 !=0:
        self.enableUI_Elements(True)
        return None

    ExperimentalNotes=pd.DataFrame([self.CellLineText.Text.text(),self.PassageNumberText.Text.text(),self.CellDensityText.Text.text(),self.ChallengesText.Text.text(),self.NotesText.Text.text()])
    NumberofChips=int(len(path)/2)

    ColumnNameCell=[None]*(NumberofChips*7)
    VariablesCell=[","]*(NumberofChips*7)
    ColumnNameRef= [None]*(NumberofChips*5)
    VariablesRef=[","]*(NumberofChips*5)

    days=[]
    Combolist=[]

    for k in range(NumberofChips):

    ### Opening each data file and extracting data

        filenameref= path[(k * 2) + 1]
        ComplexRef, Frequency = ObtainData(filenameref)

        filenameCell= path[k * 2]
        ComplexCell, _ = ObtainData(filenameCell)

        POINTS_PER_MEASUREMENT=-1
        num=0
        for i in Frequency:
            if i == Frequency[0]:
                num+=1
            if num==2:
                break
            POINTS_PER_MEASUREMENT+=1

        pos1=0
        pos2=POINTS_PER_MEASUREMENT

        TotalValues=int(len(ComplexRef)/(POINTS_PER_MEASUREMENT))

        ColumnNameCell[k]=ColumnNameCell[k+NumberofChips]=ColumnNameCell[k+((NumberofChips-1)*2)+2]=ColumnNameCell[k+((NumberofChips-1)*3)+3]=ColumnNameCell[k+((NumberofChips-1)*4)+4]=ColumnNameCell[k+((NumberofChips-1)*5)+5]=ColumnNameCell[k+((NumberofChips-1)*6)+6]=f"Chip{k+1},"
        ColumnNameRef[k]=ColumnNameRef[k+NumberofChips]=ColumnNameRef[k+((NumberofChips-1)*2)+2]=ColumnNameRef[k+((NumberofChips-1)*3)+3]=ColumnNameRef[k+((NumberofChips-1)*4)+4]=f"Chip{k+1},"
```

```
        Combolist.append(f"Chip {k+1}")

        if k==0:
            FittingRef=np.zeros((TotalValues,NumberofChips+((NumberofChips-1)*4)+4))
            FittingCell=np.zeros((TotalValues,NumberofChips+((NumberofChips-1)*6)+6))

        VariablesCell[k]="CellBarrierResistance,"
        VariablesCell[k+NumberofChips]= "CellBarrierCapacitance,"
        VariablesCell[k+((NumberofChips-1)*2)+2]="ApicalResistance,"
        VariablesCell[k+((NumberofChips-1)*3)+3]="CPEMagnitude,"
        VariablesCell[k+((NumberofChips-1)*4)+4]="CPEExponent,"
        VariablesCell[k+((NumberofChips-1)*5)+5]="R2Real,"
        VariablesCell[k+((NumberofChips-1)*6)+6]="R2Imaginary,"

        VariablesRef[k]="CellMediumResistance,"
        VariablesRef[k+NumberofChips]= "CPEMagnitude,"
        VariablesRef[k+((NumberofChips-1)*2)+2]="CPEExponent,"
        VariablesRef[k+((NumberofChips-1)*3)+3]="R2Real,"
        VariablesRef[k+((NumberofChips-1)*4)+4]="R2Imaginary,"

        for valuenumber in range (TotalValues):
            ImagRef=ComplexRef[pos1:pos2].imag
            RealRef=ComplexRef[pos1:pos2].real
            ImagCell=ComplexCell[pos1:pos2].imag
            RealCell=ComplexCell[pos1:pos2].real
            omega=np.array(Frequency[pos1:pos2]*2*np.pi)

    ####    Reference Electrode Fitting

            x0ref=[X0REF_Resistance,X0REF_CPE_MAGNITUDE,X0REF_CPE_EXPONENT]

            LB=[LBREF_RESISTANCE,LBREF_CPE_MAGNITUDE,LBREF_CPE_EXPONENT]
            UB=[UBREF_RESISTANCE,UBREF_CPE_MAGNITUDE,UBREF_CPE_EXPONENT]

            FitRef=Nelder_Mead_Bounds('RefMin',x0ref,LB,UB)

            valueRef=ReferenceModel(FitRef,2)

            R2RealRef = np.corrcoef(RealRef,valueRef.real)[0, 1]**2
            R2ImagRef = np.corrcoef(ImagRef,valueRef.imag)[0, 1]**2

            FittingRef[valuenumber,k]=FitRef[0]
            FittingRef[valuenumber,k+NumberofChips]=FitRef[1]
            FittingRef[valuenumber,k+((NumberofChips-1)*2)+2]=FitRef[2]
            FittingRef[valuenumber,k+((NumberofChips-1)*3)+3]=R2RealRef
            FittingRef[valuenumber,k+((NumberofChips-1)*4)+4]=R2ImagRef

    ####    Cell Chamber Electrode Fitting
```

```

            RbCellChamber=FitRef[0]*(CELLCONSTANT_REFERENCE/CELLCONSTANT_CELLCHAMBER_BASO)
            CellChamberRatio = CELLCONSTANT_CELLCHAMBER_APICAL/CELLCONSTANT_CELLCHAMBER_BASO
            TeorRA=RbCellChamber/CellChamberRatio

            x0cell=[TeorRA,ELECTRODE_AREA_RATIO*FitRef[1],FitRef[2],X0CELL_CAPACITANCE,X0CELL_RESISTANCE]

            LB=[TeorRA-(TeorRA*BOUNDARIES_PERCENTAGE),(ELECTRODE_AREA_RATIO*FitRef[1])-((ELECTRODE_AREA_RATIO*FitRef[1])*BOUNDARIES_PERCENTAGE),FitRef[2]-(FitRef[2]*BOUNDARIES_PERCENTAGE),LBCELL_CAPACITANCE,LBCELL_RESISTANCE]
            UB=[TeorRA+(TeorRA*BOUNDARIES_PERCENTAGE),(ELECTRODE_AREA_RATIO*FitRef[1])+((ELECTRODE_AREA_RATIO*FitRef[1])*BOUNDARIES_PERCENTAGE),FitRef[2]+(FitRef[2]*BOUNDARIES_PERCENTAGE),UBCELL_CAPACITANCE,UBCELL_RESISTANCE]
            FitCell=Nelder_Mead_Bounds('CellChamberMin',x0cell,LB,UB)

            valueCell=CellChamberModel(FitCell,2)

            R2RealCell = np.corrcoef(RealCell,valueCell.real)[0, 1]**2
            R2ImagCell = np.corrcoef(ImagCell,valueCell.imag)[0, 1]**2

            FittingCell[valuenumber,k+((NumberofChips-1)*2)+2]=FitCell[0]
            FittingCell[valuenumber,k+((NumberofChips-1)*3)+3]=FitCell[1]
            FittingCell[valuenumber,k+((NumberofChips-1)*4)+4]=FitCell[2]
            if valuenumber < BaselineValues:
                FittingCell[valuenumber,k+NumberofChips]=0
                FittingCell[valuenumber,k]=0
            else:
                FittingCell[valuenumber,k+NumberofChips]=FitCell[3]/CELL_GROWTH_AREA
                FittingCell[valuenumber,k]=FitCell[4]*CELL_GROWTH_AREA
            FittingCell[valuenumber,k+((NumberofChips-1)*5)+5]=R2RealCell
            FittingCell[valuenumber,k+((NumberofChips-1)*6)+6]=R2ImagCell

            if k==0:
                days.append((valuenumber-BaselineValues)*(TIME_PER_MEASUREMENT/60/24))

            #### Data from Impedance analyser has one empty row after the frequency sweep #####
            pos1+=POINTS_PER_MEASUREMENT+1
            pos2+=POINTS_PER_MEASUREMENT+1
            print(((valuenumber+1)/TotalValues*100),k+1)

    NewPath=os.path.dirname(filenameCell) + os.sep + "Results" + os.sep
    try:
        os.mkdir(NewPath)
```

```
        except:
            pass

        FittingCellResults = pd.DataFrame(FittingCell,index=days)
        FittingRefResults = pd.DataFrame(FittingRef,index=days)
        with open(NewPath+'CellResults.csv','w',newline='\n') as f:
            f.write(","+"".join(VariablesCell)+'\n')
            f.write("Days,"+"".join(ColumnNameCell)+'\n')
            FittingCellResults.to_csv(f, header=False,index=True)

        with open(NewPath+'RefResults.csv','w',newline='\n') as f:
            f.write(","+"".join(VariablesRef)+'\n')
            f.write("Days,"+"".join(ColumnNameRef)+'\n')
            FittingRefResults.to_csv(f,header=False,index=True)

        with open(NewPath + 'Experimental Details.txt', 'w' , newline='\n')
    as f:
            ExperimentalNotes.to_csv(f,header=False, index=False)

        self.days=days
        self.FittingCell=FittingCell
        self.FittingRef=FittingRef
        self.numberofchips=NumberofChips

        self.QComboBox.clear()
        self.QComboBox.addItems(Combolist)
        self.refreshtextbox("")
        self.enableUI_Elements(True)
        self.refreshfigures([],[])
        self.plotAllResistances()

    def on_click_ResultsButton(self):

        self.enableUI_Elements(False)
        path=sorted(QFileDialog.getOpenFileNames(self)[0])
        if path == [] or len(path)%2 !=0:
            self.enableUI_Elements(True)
            return None
        RefData=pd.read_csv(path[1],header=None,index_col=None,skiprows=2)
        CellData=pd.read_csv(path[0],header=None,index_col=None,skiprows=2)
        self.FittingRef=np.array(RefData)[:,1:(RefData.shape[1])]
        self.FittingCell=np.array(CellData)[:,1:(CellData.shape[1])]
        self.days=np.array(RefData)[:,0]
        self.numberofchips=int((RefData.shape[1]-1)/5)

        Combolist=[f"Chip {i+1}" for i in range (self.numberofchips)]

        self.QComboBox.clear()
        self.QComboBox.addItems(Combolist)
        self.enableUI_Elements(True)
        self.refreshfigures([],[])
```

```
        self.plotAllResistances()

    def enableUI_Elements(self,command=True):
        self.ChallengesText.Text.setEnabled(command)
        self.PassageNumberText.Text.setEnabled(command)
        self.CellDensityText.Text.setEnabled(command)
        self.CellLineText.Text.setEnabled(command)
        self.NotesText.Text.setEnabled(command)
        self.BaselineReadingsText.Text.setEnabled(command)
        self.ImpedanceAnalyserData.setEnabled(command)
        self.QComboBox.setEnabled(command)
        self.ResultData.setEnabled(command)

    def refreshtextbox(self,text=""):
        self.ChallengesText.Text.setText(text)
        self.PassageNumberText.Text.setText(text)
        self.CellDensityText.Text.setText(text)
        self.CellLineText.Text.setText(text)
        self.NotesText.Text.setText(text)
        self.BaselineReadingsText.Text.setText(text)

    def refreshfigures(self,xdata=[],ydata=[]):
        self.CellResistance.plot_data(xdata,ydata)
        self.CellCapacitance.plot_data(xdata,ydata)
        self.CellApicalResistance.plot_data(xdata,ydata)
        self.RefMediumResistance.plot_data(xdata,ydata)
        self.CellCPEMagnitude.plot_data(xdata,ydata)
        self.RefCPEMagnitude.plot_data(xdata,ydata)
        self.CellCPEExponent.plot_data(xdata,ydata)
        self.RefCPEExponent.plot_data(xdata,ydata)
        self.RefR2Imag.plot_data(xdata, ydata)
        self.RefR2Real.plot_data(xdata, ydata)
        self.CellR2Imag.plot_data(xdata, ydata)
        self.CellR2Real.plot_data(xdata, ydata)

    def plotAllResistances(self):
        self.CellResistanceAll.plot_allChips(self.days,self.FittingCell[:,0:self.numberofchips],self.numberofchips,"plain","Cell Resistance All Chips (\u03A9.cm$^2$)")

if __name__ == '__main__':
    app = QApplication(argv)
    ex = App()
    exit(app.exec_())
```

Data_Modelling.py

A.2 UoS Organ-on-Chip

A.2.1 Standard Operating Protocol

This standard operating protocol was written together with Dr. Nikita Karra and involves fabrication, assembly and use of the OoC system developed at UoS.

Lung on Chip:
Standard Operating Procedure.

Written by **Nikita Karra and João Fernandes 18/02/2020**
Updated on **29/06/2020**

Contents

The Set-Up

The Set-Up Contents

- A Syringe Pump that can house 8 x 10mL syringes (Luer Lock)
- 8 Bubble Traps commercially available from Darwin Microfluidics (LVF-3526 – 44µL)
- 8 Manifolds that are micro-milled out of 5mm PEEK connected to the bubble traps by microfluidic ‘screw-in’ connectors and 1/16” tubing and metal ferrules.
- 8 Bio-Chips that are affixed onto the manifolds (contacts facing outwards) using magnets. Alignment is provided by the O-ring 3D printed alignment layer and the O-rings are used to provide a tight fluidic seal.
- Raspberry Pi: Responsible for the pump commands (direction and speed) and for the impedance analysis (frequency, steps, time and display) in person or remotely. Both functions are controlled by custom made scripts (written by Joel Bowring) entitled 'LoC Control’. Files can also be renamed, organised and downloaded through the Raspberry Pi.
- Three PCB’s are used
  - The microcontroller PCB (small green PCB): Allows the pump direction and speed to be controlled. It must be connected to the 12V power cable and the Big Easy Driver (small red PCB), via a 4 pin connector, in addition it receives commands from the Raspberry Pi via USB.
  - The impedance PCB must be connected to the Raspberry Pi by an Ethernet cable. The impedance PCB connects to each of the chips via appropriate pins.

- 8 Micro tubes are sealed with a prepared lid (hole for tubing and air) and placed in the micro tube holder. The exposed air hole is covered with a PDMS seal.

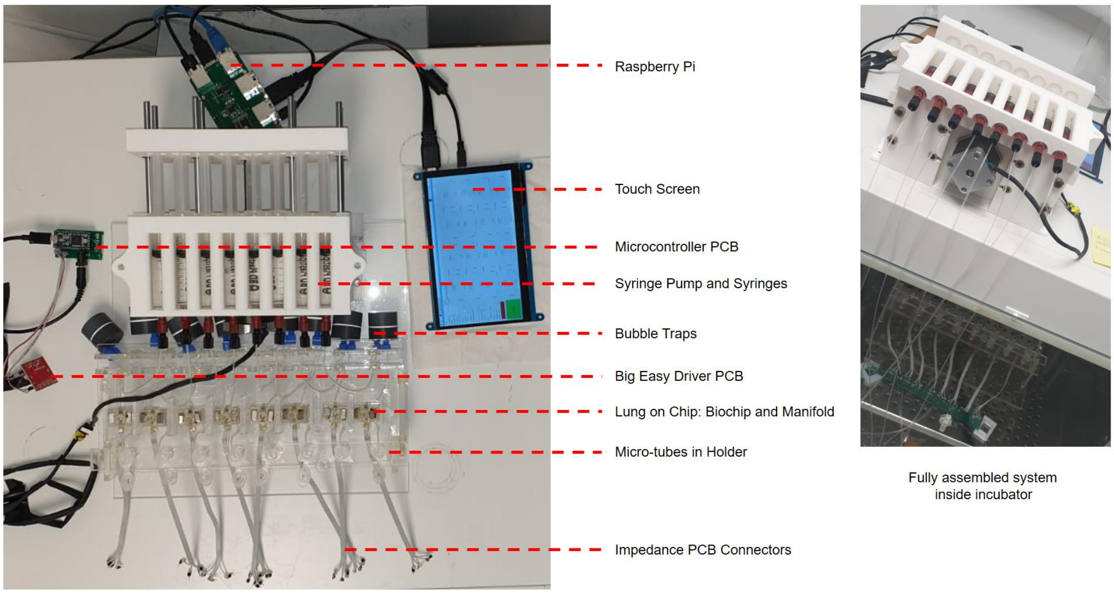

Fully assembled system
inside incubator

Figure 1: Fully Assembled System Components

Fabricating and Assembling: Biochip and Manifold Sub-Assembly

Note: To maximise sterility ensure that the system components (particularly the Biochip) are handled with clean gloves on a clean surface (sprayed with 70% Ethanol or IPA).

Biochip Fabrication and Assembly

1. Biochip cell chamber components (top and bottom) were prepared by applying 50 µm double sided adhesive tape (467 200MP 3M) to 5mm PMMA (TechSoft UK Ltd) followed by machining using a Laser cutter (Epilog Laser) as required.

2. Glass chips with electrodes are fabricated in the cleanroom (please check specific protocol).

3. Inlet and outlet holes in the glass chips were machined using a Powder Blaster and a specifically designed rig for alignment purposes. Other Biochip components include: 12 µm thick, nanoporous (0.4 µm pores), high pore density (1x108 cm-2), polyester (PET) membrane layer (Inpore Track Etched Membrane, it4ip). The channel was fabricated using 50µm (3M) in conjunction with 175 µm PMMA (Goodfellows), the channel was designed on Corel Draw and machined using the laser cutter (Epilog Laser).

4. The multiple components of the biochip were assembled using the intermediary 50 µm double sided tape (3M) layers using manual alignment. When the chip was fully assembled it was sealed using an Epoxy based adhesive (Araldite Rapid).

System Assembly

1. Connect tubing from syringe to bubble trap with microfluidic ‘screw-in’ connectors and 1/16” tubing, the bubble trap can then be joined to the Lung on Chip inlet by threading the tubing through the stand and manifold. The tube is held in place within the manifold using metallic ferrules. On the Lung on chip outlet the tubing is threaded the same way and is inserted into a micro-tube.

2. O-rings are then placed onto the appropriate location on the manifolds (concentric with the metallic ferrules and inlet/outlet holes).

3. The O-ring alignment layer can then be placed on top of the assembly above and pressed down to secure the O-rings in place.

4. The Biochip can then be placed on top and held in location with magnets.

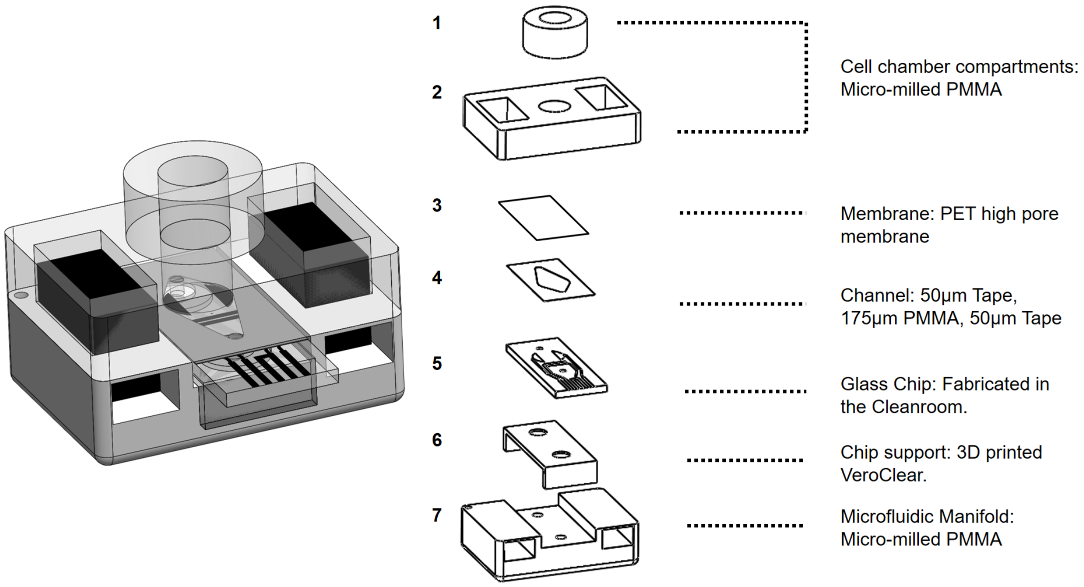

Figure 2: Lung on Chip Biochip and Manifold Components

Cleaning the System

Note: This must be performed inside a class II microbiological safety cabinet (MSC) and the system must be enclosed fluidically (no tubes, syringes or chambers open to air) from syringe to micro-tubes.

Solutions and Materials Required
1:60 thin bleach (diluted with DI autoclaved water)
DI autoclaved water
2 X 10 mL Luer Lock syringes
4 X 50 mL Centrifuge Tubes
8 X 2 mL Micro-Tubes
Box of 1 mL Pipette Tips
Box of 200 µL Pipette Tips
96 Well Plate PDMS Gas-Permeable Adhesive Seals Cut to Individual Sizes
70% Ethanol or IPA
Absorbent Tissue

Protocol

1. Wipe the outside of the assembled system with 70% ethanol or IPA and place only the stand and associated components inside the MSC.
2. Fill 2 of the Centrifuge tubes with 70% Ethanol or IPA, 1 with autoclaved DI water and 1 with 1:60 bleach.
3. Remove syringes from pump, disconnect connectors and spray with 70% Ethanol or IPA and place inside one of the centrifuge tubes containing 70% Ethanol or IPA.

Note: Ensure that any tubing entering the MSC has also been sprayed to maintain aseptic technique.

4. Replace micro-tubes with autoclaved ones.
5. Fill 1 syringe with 1:60 bleach solution and manually flush each chip with 2 mL of solution.

Note: Refill syringe if required. Ensure that the connectors and syringe are sprayed with 70% Ethanol or IPA before connecting together.

6. Remove any apical liquid from the Biochip and replace with 200 µL of 1:60 bleach solution. Cover the apical chamber with a PDMS seal if no seal has been applied yet.

Note: Try to keep apical chamber covered with PDMS seal when not in use.

7. Wait 20 minutes.
8. Fill 1 syringe with autoclaved DI water and manually flush each chip with 2 mL of solution.

Note: Refill syringe if required. Ensure that the connectors and syringe are sprayed with 70% Ethanol or IPA before connecting together.

9. Remove apical liquid from the Biochip and rinse with 200 µL of autoclaved DI water. Repeat this step at least 3 times to ensure complete bleach removal.

Note: Try to keep apical chamber covered with PDMS seal when not in use. Pipette water up and down during washing steps and change tip between each step for each chip.

10. Prepare PDMS seals by cutting to appropriate size and spraying with 70% ethanol or IPA before placing inside MSC.
11. Replace PDMS seal (when dry) and micro-tubes with new ones.
12. If setting up cell experiment follow associated protocol.

Assembling System: Connecting Electronics

Note: If system is being run with PBS only this occurs outside the incubator on the benchtop. If the system is being run with media only (baseline) or with cells this will be in respect to the incubator.

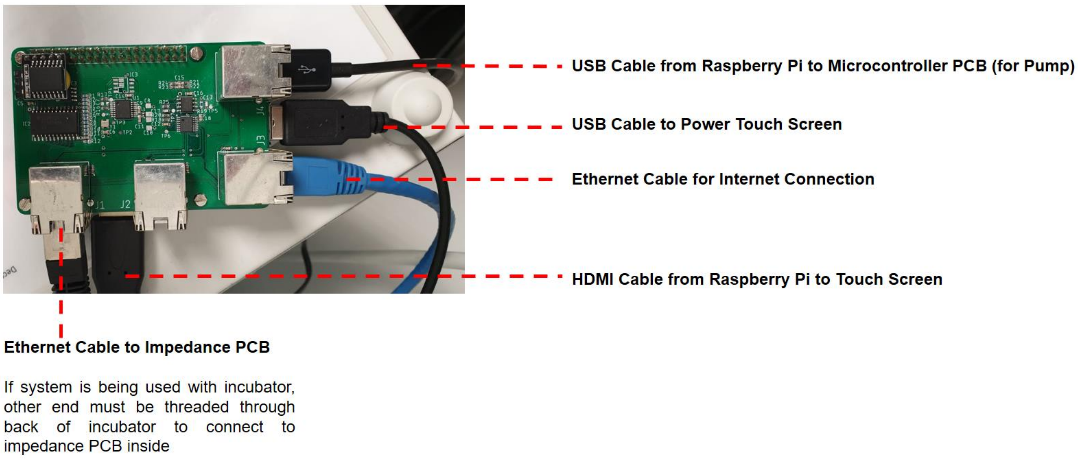

USB Cable from Raspberry Pi to Microcontroller PCB (for Pump)

USB Cable to Power Touch Screen

Ethernet Cable for Internet Connection

HDMI Cable from Raspberry Pi to Touch Screen

Ethernet Cable to Impedance PCB

If system is being used with incubator, other end must be threaded through back of incubator to connect to impedance PCB inside

Figure 3: Overview of connections from the Raspberry Pi to other components of the Lung on Chip. Ensure that the ***Raspberry Pi is not on a bare metal/conductive surface!***

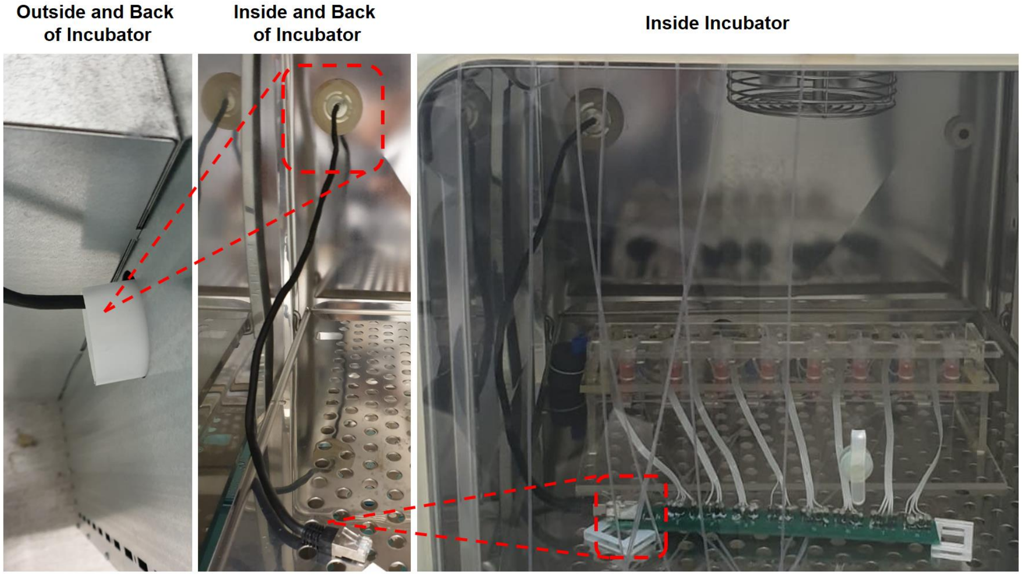

Outside and Back of Incubator

Inside and Back of Incubator

Inside Incubator

Figure 4: Connecting the impedance PCB when the system is ***INSIDE*** *the incubator. The Ethernet cable must be carefully pushed through the back of the incubator allow the greatest possible sealing to avoid infections and leaks. The cable when connected to the* ***PCB must not be placed upon the bare metal/conductive surface****, blocks of PMMA can be used to facilitate this. Ensure that there is a 'click' sound when the Ethernet cable is pushed into the socket on the impedance PCB.*

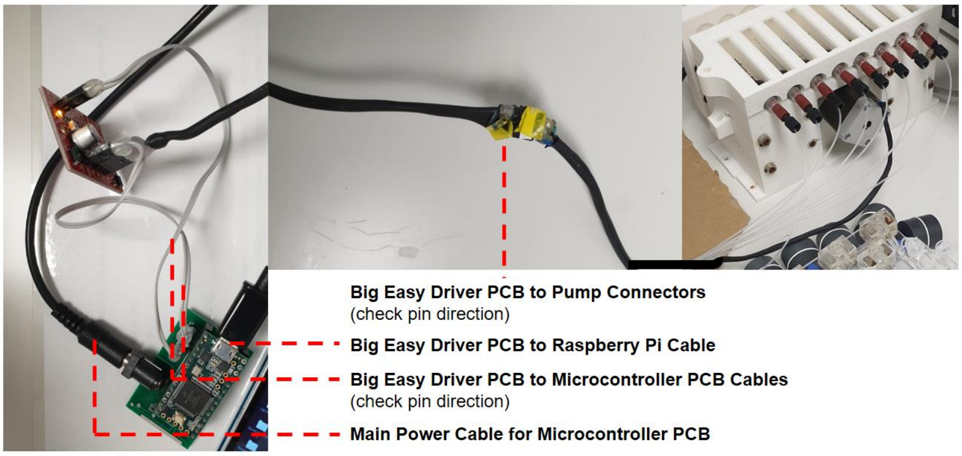

Big Easy Driver PCB to Pump Connectors
(check pin direction)

Big Easy Driver PCB to Raspberry Pi Cable

Big Easy Driver PCB to Microcontroller PCB Cables
(check pin direction)

Main Power Cable for Microcontroller PCB

Figure 5: Overview of Pump control electronic connections. The green microcontroller PCB and the Big Easy Driver red PCB must not be on a bare metal/ conductive surface. The orientation of the cables between these PCBs must be carefully considered to ensure that the pins are matching/correct. Similarly the pin direction between the Big Easy Driver PCB and the Pump Motor should also be the same otherwise the commands will be opposite. Also ensure that all pins are inside their respective sockets and pushed in fully.

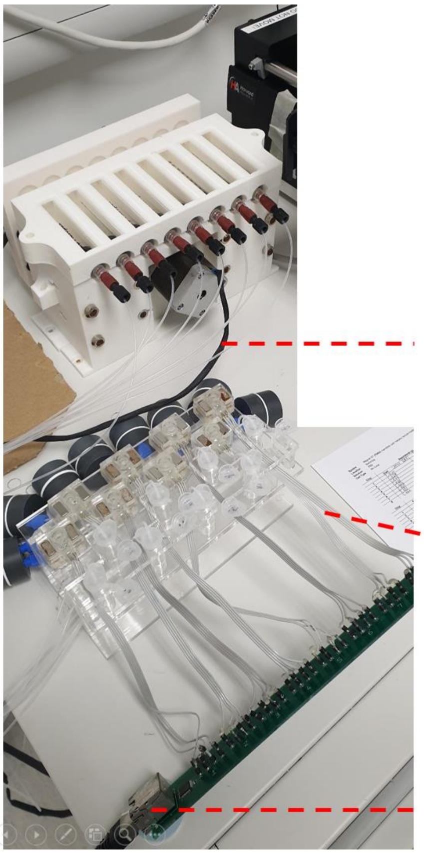

Big Easy Driver PCB to Pump Connector

LoC Biochip to Impedance PCB Cables
Ensure that the cables match the order
‘ref imp imp ref’ and that they are fully pushed in

Ethernet Cable from Raspberry Pi to Impedance PCB
Double check that the port number on the Raspberry Pi matches
the port number enabled on the software

Figure 6: Overview of connections between the Lung on Chip Biochip and Impedance PCB and Raspberry Pi. Also showing the location of the pump motor cable which is connected to the Big Easy Driver. Ensure that the order of the

pins on the impedance PCB matches the pins on the Biochip (outer pins – reference electrodes, inner pins – cell chamber electrodes).

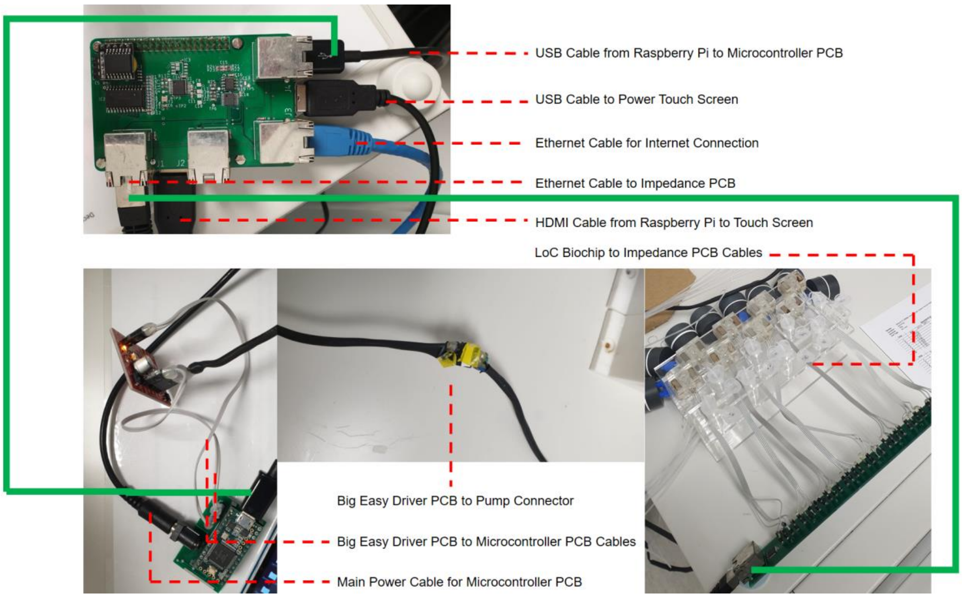

Figure 7: Summary check of all the different electrical connections. Green indicates that it is two ends of the same cable in both images.

Running the System

Switching On

Note: Ensure that the system is connected as indicated in the previous section.

1. Switch on Raspberry Pi and Microcontroller PCB from the switches on the wall. If everything is connected properly, the Raspberry Pi will show a red (power) and green (internet access) light and the Big Easy Driver PCB (Red PCB) will show an orange light.

2. Wait until the following page is displayed on the screen connected to the Raspberry Pi.

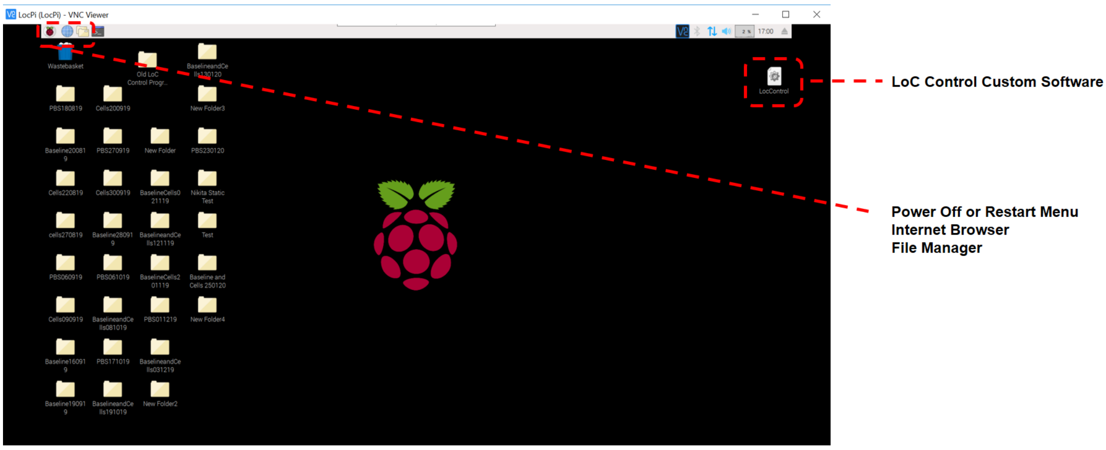

Figure 8: Home screen display when the Raspberry Pi is first switched on.

3. Double-click on the 'LocControl' icon to load the custom programme, the percentage in the top right corner (next to the time display) will increase if it is loading.

4. When the programme has opened it will display the following (Figure 9) as it initialises

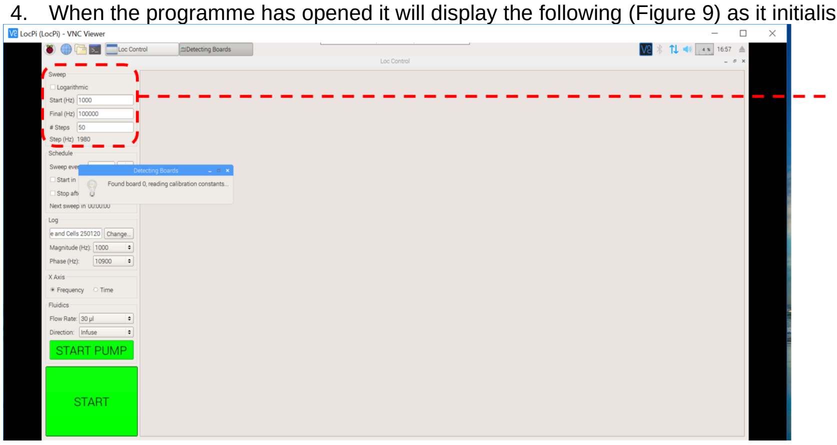

Sweep
☐ Logarithmic
Start (Hz) 1000
Final (Hz) 100000
Steps 50
Step (Hz) 1980

Schedule
Next sweep in 00:00:00

Detecting Boards
Found board 0, reading calibration constants...

Log
e and Cells 250120 Change...
Magnitude (Hz): 1000
Phase (Hz): 10900

X Axis
● Frequency ○ Time

Fluidics
Flow Rate: 30 µl
Direction: Infuse

Frequency:
Start 1000 Hz
Final 100000 Hz

Number of Steps: 48

This information should not change during an experiment. Also a logarithmic scale can be used by checking the box, otherwise the scale will be linear.

Figure 9: Initialisation screen when opening the programme.

5. Check that the values for the start (1000 Hz) and final frequencies (100000 Hz) in the sweep section are as highlighted in Figure 9. The step number should be 48 and the logarithmic box should be checked.

6. Following initialisation, the screen display will change as shown in Figure 10.

7. Here the port selection must match the port on the Raspberry Pi by checking the enabled box. Port 1, 2, 3 and 4 correspond to the sockets J1, J2, J3 and J4 on the Raspberry Pi PCB respectively.

8. The chips from which data will be acquired can be selected by checking the box next to the corresponding channel number.

9. The time between measurements is set to either 20 minutes when using a logarithmic scale or 10 minutes for a linear scale.

10. The frequencies that will be displayed on the screen (and also saved in the single frequencies files) can be selected here. These must be 1000 Hz for Magnitude of impedance and 10000 Hz for phase unless discussed otherwise.

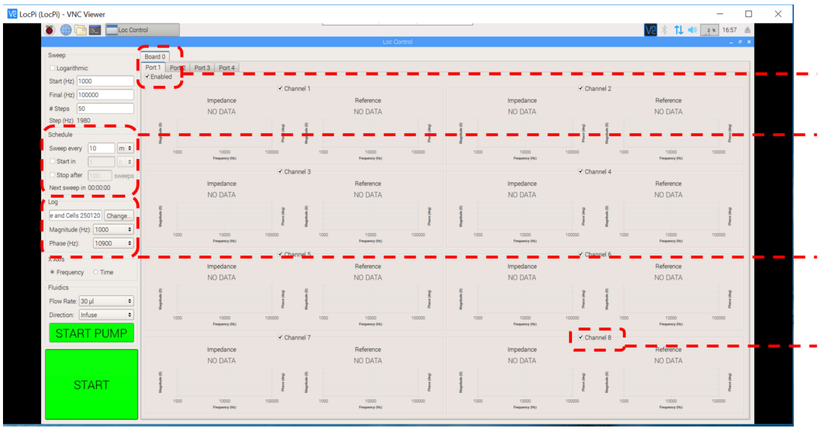

Sweep
☐ Logarithmic
Start (Hz) 1000
Final (Hz) 100000
Steps 50
Step (Hz) 1980

☑ Enabled

Schedule
Sweep every 10 m
☐ Start in 1 h
☐ Stop after 100 sweeps
Next sweep in 00:00:00

Log
e and Cells 250120 Change...
Magnitude (Hz): 1000
Phase (Hz): 10900

X Axis
● Frequency ○ Time

Fluidics
Flow Rate: 30 µl
Direction: Infuse

Port Selection:
Ensure that the port on the Raspberry Pi connected to the impedance PCB is the same as the port enabled on the programme.

Schedule:
Time in between sets of measurements 10-20 minutes used.

Also includes a timer indicating when the next sweep will begin.

Log:
Folder selection to choose where data will be saved.
Magnitude (1000Hz) and Phase (10000Hz) frequency selection.

Other Notes
Ensure that all used chips have been selected by checking the box next to 'Channel _'.

Figure 10: Programme display after initialisation. Different settings that can be changed and how.

11. A new folder must be created and named appropriately to allow data to be easily accessed in the future. The naming system used currently consists of either PBSDDMMYY if testing system with PBS on the benchtop or BaselineandCellsDDMMYY for the media baseline and cell experiments. A new folder can be generated following the pathway highlighted in Figure 11.

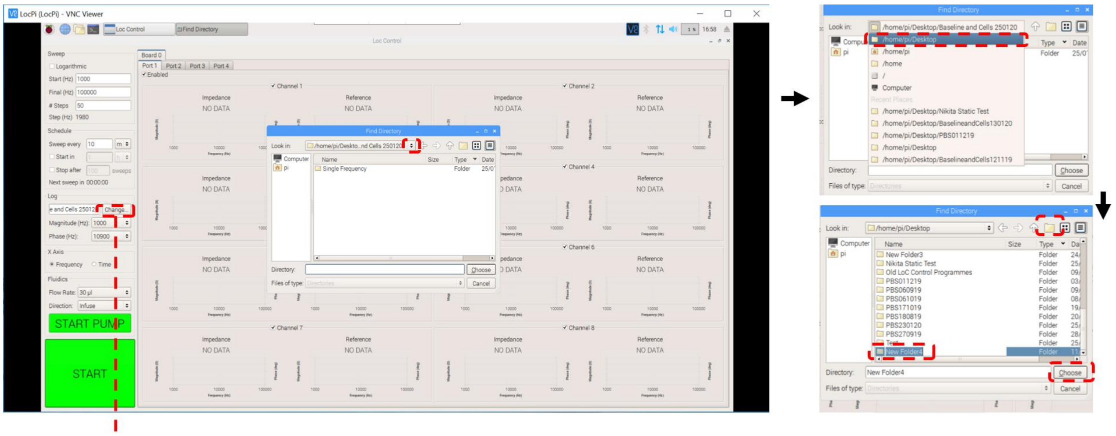

Changing the folder to which files are saved:

Click **'Change'** : this will open current file location as shown in window
Click drop down menu and select **'/home/pi/Desktop'**
Click **folder icon** on the top to create new folder
Rename Folder with either PBSDDMMYY or BaselineandCellsDDMMYY
Click **'Choose'**

Figure 11: How to create a new folder for a new experiment PBS testing or BaselineandCells.

12. To start the pump select the appropriate flowrate via the dropdown menu in the fluidics section as highlighted by Figure 12. Ensure that the flowrate is set to '30 µL' and direction to 'infuse' during experimentation (the 'fast' flowrate and 'withdraw' functions are only used during the setting up stages).

13. After this has been checked, click 'START PUMP' to begin infusion (the colour will then change to red and read 'STOP PUMP').

14. Ensure that the frequency setting has been chosen for the display (otherwise the programme may crash if left in the overtime setting for extended periods of time). This also allows the status of the system to be quickly analysed to check if chips are connected, if there are bubbles inside the Biochip or if cells are growing etc.

15. To begin data acquisition click the 'START' button. The 'Impedance' or 'Reference' names will flash when they are being measured and the current frequency sweep will be displayed on the screen. The axis will adjust during the course of measurements to allow the graphs to all be on the same scale.

16. The blue line indicates the magnitude of impedance (Ω) and the red line indicates the phase angle (°).

17. Additionally if desired double clicking on a graph will change the display to full screen mode and it will display the chip and characteristic being measured and automatically cycle between them. Double clicking again will bring you back to the display shown in Figure 12. It is best to leave the display showing all 8 chips to allow rapid identification of any issues.

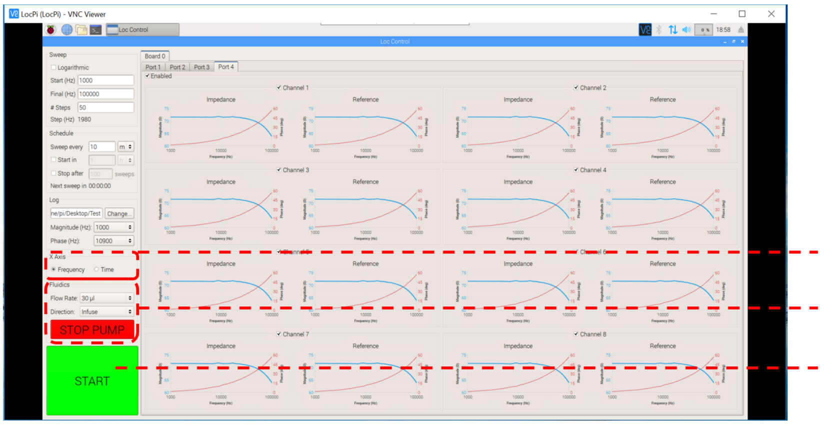

Data Visualisation:
To choose between current frequency sweep or over time display.

Pump Controls:
To choose the flowrate and direction of the pump.

Data Measurement Start/Stop:
To begin or end data acquisition, when the programme has been started, the button will change colour and read 'END'.

Figure 12: Starting and Stopping the pump and data acquisition. Also changing the display on the screen.

Switching Off to Change Syringes/Adding Cells.

<u>Changing Syringes</u>

This will occur swapping syringes filled with PBS to syringes filled with complete MEM Media or during primary cell experiments to replace with a new full syringe with complete MEM Media.

Note: If changes of syringes involve media this MUST be performed with aseptic technique inside a Class II MSC to limit infection and maintain sterility. It is better to fill new syringes with media and keep inside packaging before removing old syringes.

1. After the system has been cleaned as aforementioned on page 4. The system (Biochip, Manifold, Stand, Bubble Traps) and fluidic connectors (that will adjoin onto syringes) must be kept inside a Class II MSC.
2. Remove old micro tubes and keep for measurement of weight and further analysis.
3. Replace with new micro tubes accordingly, it is better to do this one at a time. Ensure that the micro tubes, lids and ends of tubing are sprayed with 70% Ethanol or IPA to maintain sterility.
4. The pump itself can remain outside the hood and can be withdrawn.
5. Stop the pump as highlighted in Figure 12.
6. Change flow rate to ‘Fast’ and direction to ‘Withdraw’ and wait until the back-plate of the pump is withdrawn enough to place a filled syringe.
7. The syringes and associated tubing are then removed from the stand, sprayed with 70% Ethanol or IPA (one at a time) and taken into the Class II MSC.
8. Remove the old syringe and discard into 2% Virkon solution.
9. Spray the connector and new syringe with 70% Ethanol or IPA and connect as tightly as possible. Spray the outside again and the syringe can go back into the pump outside of the Class II MSC.
10. This is repeated for all the syringes.
11. Spray syringes again with 70% Ethanol or IPA and place pump lid ontop.
12. Change the flowrate on the programme to ‘5000 µL’ and the direction to ‘infuse’, change the flow in the 3-way valves to waste and click start.
13. Keep a careful eye on the syringes and micro tubes, stop the pump when all micro tubes have liquid inside them.
14. After this change the micro tubes with pre-weighed micro tubes as directed in point 3. Spray the area with micro tubes again with 70% Ethanol or IPA.
15. Move the system back into the incubator and the pump back into the fridge.
16. Restart data acquisition by clicking ‘START’.
17. Change the 3-way valves flow to the system, the flow rate to ‘30 µL’ and direction to ‘infuse’ and click ‘START PUMP’.

<u>Adding cells</u>

This will occur when adding cells at the start of an experiment

1. Click ‘STOP’ to stop data acquisition.
2. Click ‘STOP PUMP’ to stop pump fluidic infusion.
3. Disconnect Ethernet cable from impedance PCB.
4. Remove system from inside incubator and place inside Class II MSC.
5. Follow cell culture protocol (separate document).
6. Place the system back inside incubator.
7. Reconnect Ethernet cable to impedance PCB.
8. Wait 1 hour for proper cell sedimentation onto the membrane.
9. Click ‘START’ to begin data acquisition.
10. Click ‘START PUMP’ to restart pump fluidic infusion.

Switching Off to Turn Off or Restart Computer

1. Stop data acquisition by clicking ‘STOP’.
2. Stop pump by clicking ‘STOP PUMP’.
3. Close programme by clicking cross in top right hand corner.
4. Click Raspberry Pi logo in top left hand corner -> select shutdown -> shutdown/ reboot.
5. Wait until lights turn off on the Raspberry Pi and turn off switch on main power supply.

Cell Culture (16HBE14o-)

Note: This must be performed inside a class II microbiological safety cabinet (MSC) and the system must be enclosed fluidically (no tubes, syringes or chambers open to air) from syringe to micro-tubes.

Solutions and Materials Required
90 mL x Minimal essential medium with supplements
1 mL Trypsin (%) per flask
5 mL HBSS
75 µL Trypan Blue
Haemocytometer
8 x 100 µL of cell suspension (150,000 cells per well)
8 X 2 mL Micro-Tubes
Box of 1 mL Pipette Tips
Box of 200 µL Pipette Tips
Box of 20 µL Pipette Tips
96 Well Plate PDMS Gas-Permeable Adhesive Seals Cut to Individual Sizes
70% Ethanol or IPA
Absorbent Tissue

Protocol
Growth

1. Wipe the outside of the assembled system with 70% ethanol or IPA and place only the stand and associated components inside the MSC.
2. When microfluidic device, in-house transwells and commercial transwells are ready collagen coat each as detailed below
   i. Collagen coat membrane filters by apically applying 100ul of collagen I solution (30µg/ml final = 1 in 100 dilution of 3 mg/ml stock) and incubating for 30min at 37C
   ii. Collagen coat new T75 flasks by applying 5ml of collagen I solution (30µg/ml final = 1 in 100 dilution of 3 mg/ml stock) and incubating for 30min at 37C
   iii. While collagen coating membranes and flasks, prepare cell solution
3. Take cells at 70-90% confluency and rinse T75cm^2 flask with 10ml HBSS for 10 minutes at 37C
4. Remove HBSS as completely as possible and add 1ml of 1X trypsin/EDTA solution and incubate for 5-7 minutes (until cells are non-adherent) at 37C. Firmly tap flask to dislodge cells.
5. Neutralise trypsin with media (containing 10% FBS). Run down base of flask to dislodge any remaining cells.
6. Transfer into a 15ml Falcon tube and centrifuge with appropriate balance at 1500rpm, 5min, room temp
7. Resuspend in 1ml media and count using the trypan blue exclusion method.
   i. Make-up an Eppendorf cell solution with 25 µL and 75 µL trypan blue (1 in 4 dilution).
   ii. Mix thoroughly and add 10 µL of solution to cytometer.
   iii. Count cells in top left, top right, bottom left and bottom right quadrants. Clumps = 1 cell. Exclude cells which have taken up the blue dye. Cells on left and top edge line of quadrant count, cells on bottom and right edge line of quadrant do not count. Ideally between 100 and 250. If less than 100, make up a new Eppendorf with increased cell concentration

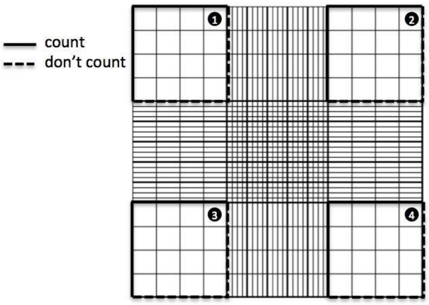

   iv. Divide total count from these four quadrants by 4 and multiply by dilution factor (4) and cytometer factor (10,000)
   v. E.g. (cell count / 4) x 4 x 10,000 = number of cells
8. Require 150,000 cells per Transwell/fluidic chip i.e. 0.15x10^6/well/100ul = 1.5 x10^6/ml
   i. Therefore, if needing enough for 8 chips, make up surplus i.e. 10 chips
   ii. 10 chips = (100ul * 10 = 1ml) and (0.15x10^6 x10 = 1.5x10^6)
   iii. To get 1.5x10^6 cells in 1ml from 5x10^6 stock – 1,500,000/5,000,000 = 0.3ml or 300ul of cell stock in 700ul media (1ml total)
9. Place 100ul of cell solution per transwell/fluidic chip (except no cell controls).

10. Leave in microfluidic device for 1h without flow at 37C before starting flow at 30µL/hr and impedance/phase measurements.
11. Measure Transwell TER post-seeding after 1 hour (=T_0)
12. Transwell apical and basolateral medium changed on days 2 and 4. For the lung on chip, the apical medium is NOT changed.

Challenge

Make up the following solutions for challenging the cells using the equation:

$$C_1V_1 = C_2V_2$$

$$V_1 = \frac{C_2V_2}{C_1}$$

1. **Poly I:C**

   *Stock Poly I:C = 1000 µg/mL (**C1**)*
   *Desired Poly I:C = 25 µg/mL, needs to be multiplied by 5 to account for 1:5 dilution in transwell/ cell chamber (100/20 = 5) = 125 µg/mL (**C2**)*
   *Desired Total Volume = 6 x 20 µL = 120 µL (make up 200 µL) (**V2**)*
   *Volume needed from stock = Unknown (**V1**)*

   Using equation C1 x V1 = C2 x V2
   Rearranges to V1 = (C2 x V2) / C1

   Therefore V1 = (125 x 200)/1000
   = 25 µ*L of Poly I:C from stock required*

   Need a total volume of 200 µ*L therefore*

   V2 – V1 = 175 µ*L of media required to dilute stock*

2. **Fluticasone**

   Stock Fluticasone = 10^7 nM (***C1***)
   *Desired Fluticasone = 100 nM, needs to be multiplied by 5 to account for 1:5 dilution in transwell/ cell chamber (100/20 = 5) = 500 nM (**C2**)*
   *Desired Total Volume = 6 x 20 µL = 120 µL (make up 200 µL) (**V2**)*
   *Volume needed from stock = Unknown (**V1**)*
   Requires 3 step serial dilution:

   i. Using equation C1 x V1 = C2 x V2
   Rearranges to V1 = (C2 x V2) / C1

   Therefore V1 = (10^5 nM x 750 µ*L*)/10^7 nM
   = 7.5 µ*L of Fluticasone from stock required diluted into 742.5* µ*L of media.*

   ii. Using previous dilution
   = (10^3 nM x 1000 µ*L*)/10^5 nM
   = 10 µ*L of diluted Fluticasone diluted into 990* µ*L of media.*

   iii. Using previous dilution
   = (500 nM x 500 µ*L*)/10^3 nM
   = 250 µ*L of diluted Fluticasone diluted into 250* µ*L of media.*

3. **Combination (Poly I:C and Fluticasone)**

   Perform separate poly I:C and Fluticasone dilutions

   Poly I:C dilution:
   *Stock Poly I:C = 1000 µg/mL (**C1**)*
   *Desired Poly I:C = 25 µg/mL, needs to be multiplied by 5 to account for 1:5 dilution in transwell/ cell chamber (100/20 = 5) = 125 µg/mL (**C2**)*
   *Desired Total Volume = 6 x 20 µL = 120 µL (make up 200 µL) (**V2**)*
   *Volume needed from stock = Unknown (**V1**)*

   Using equation C1 x V1 = C2 x V2
   Rearranges to V1 = (C2 x V2) / C1

   Therefore V1 = (250 x 100)/1000
   = 25 µ*L of Poly I:C from stock required diluted into 75* µ*L of media*

Fluticasone dilution:
Stock Fluticasone = 10^7 nM *(**C1**)*
*Desired Fluticasone = 100 nM, needs to be multiplied by 5 to account for 1:5 dilution in transwell/ cell chamber (100/20 = 5) = 500 nM (**C2**)*
*Desired Total Volume = 6 x 20 μL = 120 μL (make up 200 μL) (**V2**)*
*Volume needed from stock = Unknown (**V1**)*
Requires 3 step serial dilution:

i. Using equation C1 x V1 = C2 x V2
Rearranges to V1 = (C2 x V2) / C1

Therefore V1 = (10^5 nM x 750 μ*L*)/10^7 nM
= 7.5 μ*L of Fluticasone from stock required diluted into 742.5 μL of media.*

ii. Using previous dilution
= (10^3 nM x 1000 μ*L*)/10^5 nM
= 10 μ*L of diluted Fluticasone diluted into 990 μL of media.*

Combination solution:

Mix 100 μL of the last poly I:C dilution (250 μg/mL) with 100 μL of the last fluticasone dilution (1000 nM), reaching a final solution volume of 200 μL with a poly I:C concentration of 125 μg/mL and a fluticasone concentration of 500 nM.
When 20 μL of the final solution is added to the biochips apical compartment, the final challenge concentration is diluted in 1/5, meaning that cells will be challenged with 25 μg/mL of poly I:C and 100 nM of fluticasone.

4. For the LoC platform, challenges are conducted using a Hamilton syringe INSIDE the incubator to pierce the gas permeable membrane and deposit 20 µL of the challenge, ensuring that the tip does not pierce the membrane and cells. The hole is then covered with another gas permeable adhesive seal to maintain sterility. For the transwells a pipette is used inside a class II MSC to deposit challenge and then placed back inside incubator, and measurements are conducted for 6 hours (every hour following deposition) and 24 hours after using chopstick electrodes. Ensure that the electrodes are cleaned between measurements/wells.
5. Following completion of experiment, LoC basolateral collection reservoirs are weighed, and Biochips fixed using 4% PFA for 20 minutes which is removed and replaced with PBS for storage in a fridge. Transwells are also fixed this way. Basolateral collections and apical collections can be frozen for subsequent analysis. Ensure that samples are labelled clearly with date, chip number and day of experiment (e.g. Day 0, Day 5).
6. LoC System is cleaned using cleaning protocol.

PBEC Cell Culture LLI

Note: This must be performed inside a class II microbiological safety cabinet (MSC) and the system must be enclosed fluidically (no tubes, syringes or chambers open to air) from syringe to micro-tubes.
For the full protocol see Protocol cell culture 04 BEC culture protocol[10212].

Solutions and Materials Required

Equipment

- -80ºC Freezer
- Centrifuge
- Class II microbiological safety cabinet
- Humidified CO_2 Incubator
- Gilson pipettes
- Pipette boy
- Light microscope

Consumables

- 25ml polystyrene Universalt (Greiner, Cat No:201172
- 5 ml stripettes (Fisher, Cat No: 11869181)
- 10 ml stripettes (Fisher, Cat No: 11870181)
- 25 ml stripettes (Fisher, Cat No: 11839181)
- T25cm^2 Filter flasks (Fisher, Cat No: 156499)
- T75cm^2 filter flasks (Fisher, Cat No: 156472)
- 1.8ml cryotubes (Sarstedt, Cat No: 72.380.002)

Reagents

- RPMI 1640 medium without L-Glutamine (Life Technologies, Cat No:31870025)
- Fetal Bovine Serum (heat inactivated) (Fisher ,Cat No: 11573397)
- Penicillin-Streptomycin (5000IU/ml Penicillin, 5000ug/ml Streptomycin) (Life Technologies, Cat No: 15070063)
- Collagen I solution (PureCol) (Advanced BioMatrix, Cat No 5005-B)
- Hanks Balanced Salt Solution (HBSS) without Ca2+ or Mg2+ (Sigma-Aldrich Cat No: H9394-6X500ML)
- Trypsin, 0.5% (10x) with EDTA 4Na (Life Technologies, Cat No: R001100)
- SAGM BulletKit (contains SABM and SingleQuots) (Lonza, Cat No: CC-3118)
- DMEM w/o L-glutamine (Life Technologies, Cat No: 11960044)
- Non Essential Amino Acids (x100) w/o L-Glut (Life Technologies, Cat No: 11140035)
- Sodium Pyruvate (100mM) (Life Technologies, Cat No: 11360039)
- L-Glutamine 200mM (x100) (Life Technologies, Cat No: 25030024)
- Dimethyl sulfoxide (DMSO) (Sigma, Cat No: D2650)
- Airway Epithelial Cell Basal Medium (PromoCell, Cat No: C-21260)
- Airway Epithelial Growth medium Supplement Pack (PromoCell Cat No: C-39160)

Preparation of Reagents for BEC Culture

1. *RPMI + FCS + Pen/strep (wash buffer)*

Reagent	Vol/ml (ml)	Vol/50 ml (ml)
RPMI	0.6	39
FCS (20%)	0.2	10
Pen/strep (2%)	0.2	1

2. **Collagen I solution (1:100)**
   1. Prepare a 30 µg/ml collagen I solution by adding 0.5ml of 3mg/ml collagen I stock to 49.5 ml of sterile ddH_2O in a 50 ml conical tube.

3. **Complete DMEM (10%FBS) for neutralising trypsin in BEC cultures**

Reagent	Vol/50 ml (ml)	Vol/500 ml (ml)
DMEM	43	430
FBS (heat inactivated)	5	50

Non-essential amino acids	0.5	5
Sodium pyruvate	0.5	5
Penicillin/streptomycin (100X)	0.5	5
L-glutamine (100X)	0.5	5

- Make up a minimum of 50ml of DMEM and store in 50ml conicals

○ **Trypsin solution**

Reagent	Vol/10ml (ml)
HBSS	9
Trypsin (10X)	1

Preparation of PBEC medium, BEGM (Lonza)/Airway epithelial Medium (PromoCell)

The singlequot vials should not be freeze/thawed. Making up 2x BEGM enables the singlequots to be used for both monolayer and ALI cultures. We now do the following:

2.1 Preparing 2x PromoCell Airway medium

- The singlequot vials should not be freeze/thawed.
- PromoCell media is stable for a **maximum** of 1 month.
- Take 250 ml sterile bottle and add 245 ml of PromoCell basal medium
- After defrosting singlequot vials, briefly centrifuge (1200rpm, 1min) to collect contents at the bottom of the vial and transfer to the 250ml bottle
- Thoroughly mix the 250ml bottle using a 25 ml pipette by pipetting up and down several times

Reagent	Vol/250ml 2x BEGM (ml)
PromoCell Airway Epithelial Cell Basal Medium	245
Bovine Pituitary extract	2
hEGF	0.5
Insulin	0.5
Hydrocortisone	0.5
Transferrin	0.5
Triiodothyronine	0.5
Epinephrine	0.5

- Label the 250ml bottle **2x PromoCell -RA** and date and name and place in fridge in TC1

Unopened Basal medium bottles are stored in TC3 fridge and singlequots are stored in TC3 freezer. Once opened, Basal medium bottles should not be moved between TC labs. There should be an open bottle of basal media per TC lab.

2.2 Preparing 1x PromoCell (+RA) media for monolayer cultures

- Take 2x 50 ml conical tubes and aliquot 25 ml of BEBM medium per tube
- Add 25 ml of 2x PromoCell airway medium w/o RA to each tube (from TC1 fridge)
- Add 50 ul of retinoic acid (PromoCell singlequot from -20C) per tube
- Label the conical tube with **1x PromoCell (+RA)**, date and name and store at 4ºC in TC1

With the retinoic acid stocks from the singlequot bag try and use the freshly defrosted stock which you would use to prepare the 2xPromoCell w/o RA. Refreeze unused stocks of RA (only once) by aliquoting into 105ul eppendorfs, label with the expiry date and put in the black box in TC1 freezer.

Protocol for Transwells

1. Wipe the outside of the assembled system with 70% ethanol or IPA and place only the stand and associated components inside the MSC.

Passage 0→1

- After 24hr, check BEC culture for infection and replace the media* with fresh PBEC medium (T25cm^2 flask: 4ml) to remove contaminating non-adherent cells. (n.b. sometimes get a lot of red blood cells which need to be removed).
  * **Note: It's often worth transferring the media to a new flask rather than discarding it: often more cells will adhere.**
- Monitor BEC culture daily and replace media every 2 days until they have reached 70-80% confluence*.
  * **Note: if there are a lot of immune cells/debris, the epithelial cells may benefit from a gentle HBSS wash (~4ml) prior to new media after a few days in culture.**
- Once ~80% confluent cells are ready for passaging and/or freezing (only in passage 0).
- Prior to trypsinising cells, pre-coat T75cm^2 tissue culture flasks with 5ml collagen I (30 µg/ml) for 30min at 37ºC.
- Meanwhile, rinse PBECs twice with HBSS (T25cm^2 flask: 5ml) and add trypsin (T25cm^2 flask: 1ml) and place flasks at 37ºC for 3-5min (n.b. check cells regularly to ensure cells are not over trypsinised).
- Neutralise the trypsin with complete DMEM medium containing 10% FBS (T25cm^2 flask: 5ml) ensuring to rinse the flask and transfer to 25 ml conical tube (n.b. If cells are still not detached by 5 min repeat trypsinisation).
- Centrifuge cells at 1200 rpm (300 xg), 5 min, 20ºC
- Resuspend cells in 1 ml PBEC medium per T25cm^2 flask (n.b. if have 2 T25cm^2 flask, resuspend in 2ml) – **If required, cells can be cryopreserved at this stage:**

Passage 1→2

- When 70-80% confluent, cells are ready for plating as monolayers (see below) or for ALI cultures (see separate "ALI culture protocol").
- Follow same protocol as per passage 0→1, then plate cells on to Collagen 1-coated plates at the following densities

PBEC Cell Culture ALI

Note: This must be performed inside a class II microbiological safety cabinet (MSC) and the system must be enclosed fluidically (no tubes, syringes or chambers open to air) from syringe to micro-tubes.
For full protocol see Protocol cell culture 02 ALI culture protocol[10211].

Solutions and Materials Required

Equipment

- -20°C Freezer
- Centrifuge
- Class II microbiological safety cabinet
- Humidified CO_2 incubator
- Gilson pipettes
- Pipette boy
- Light microscope
- TER reader (Voltohmmeter EVOM): World precision instruments with chopstick electrodes

Consumables

- 20ml polystyrene Universals (Greiner, Cat No: 201172)
- 5 ml stripettes (Fisher, Cat No: 11869181)
- 10 ml stripettes (Fisher, Cat No: 11870181)
- 25 ml stripettes (Fisher, Cat No: 11839181)
- Extended Fine Tip Pastette: alpha Laboratories, Cat No: LW4232
- Syringe driven sterile filter unit (Millex-GP, 0.22 µm, polyethersulfone, 33 mm, radio-sterilized): Millipore, Cat No: SLGP033RS
- 6.5mm Transwell® with 0.4µm Pore Polyester Membrane Insert, Sterile: Fisher cat# 10482181 Corning, Cat No 3470

Reagents

- Collagen I solution (PureCol) (Advanced BioMatrix, Cat No 5005-B)
- Hanks Balanced Salt Solution (HBSS) w/o Ca^{2+} or Mg^{2+} (Sigma-Aldrich Cat No: H9394-6X500ML)
- Trypsin, 0.5% (10x) with EDTA 4Na (Life Technologies, Cat No: R001100) diluted 1:10 with HBSS, aliquoted in 10ml and stored at -20˚C
- Fetal Bovine Serum (heat inactivated) (Fisher ,Cat No: 11573397)
- RPMI 1640 medium without L-Glutamine (Life Technologies, Cat No:31870025)
- Dulbecco's Modified Eagle Medium (DMEM) high glucose (Life Technologies, Cat No: 11960044)
- Penicillin-Streptomycin (5000IU/ml Penicillin, 5000ug/ml Streptomycin) (Life Technologies, Cat No: 15070063)
- Non Essential Amino Acids (x100) w/o L-Glut: Life Technologies (Cat No: 11140035)
- Sodium Pyruvate MEM 100mM (Life Technologies, Cat No: 11360039)
- L-Glutamine 200mM (x100) (Life Technologies, Cat No: 25030024)
- Airway Epithelial Cell Basal Medium (PromoCell, Cat No: C-21260)
- Airway Epithelial Growth medium Supplement Pack (PromoCell Cat No: C-39160)
- Albumin from bovine serum (BSA) (Sigma, Cat No: A3059-100G)
- Dimethyl sulfoxide (DMSO) (Sigma, Cat No: D2650)
- Retinoic acid (RA) (Sigma, Cat No R2625)

Preparation of Reagents for ALI Medium

3. Collagen I solution (1:100)

Prepare a 30 µg/ml collagen I solution by adding 0.5ml of 3mg/ml collagen I stock to 49.5 ml of sterile ddH_2O in a 50 ml conical tube

4. BSA stock (500 mg/ml) for 2x ALI medium

Prepare a 500 mg/ml BSA stock by dissolving 5g BSA in 10 ml DMEM. Sterile filter using a low protein binding filter, make 100ul aliquots (0.5ml microtubes) and store at -20˚C in TC3 freezer.

5. Preparing 2x PBEC medium Lonza (BEGM)/PromoCell Airway Medium

3.1 2x BEGM medium

- The singlequot vials should not be freeze/thawed.
- BEGM is stable for a **maximum** of 1 month. If a lot of ALIs are in culture then prepare 250ml of 2xBEGM and 500ml DMEM, as per recipes below:
- Take 250 ml sterile bottle and add 244.5 ml of BEBM medium
- After defrosting singlequot vials/BSA, briefly centrifuge (1200rpm, 1min) to collect contents at the bottom of the vial and transfer to the 250ml bottle
- Thoroughly mix the 250ml bottle using a 25 ml pipette by pipetting up and down several times

Reagent	**Vol/250ml 2x BEGM (ml)**
BEBM	245
Bovine Pituitary extract (BEGM singlequot)	2
hEGF (BEGM sinlgequot)	0.5
Insulin (BEGM sinlgequot)	0.5
Hydrocortisone (BEGM sinlgequot)	0.5
Transferrin (BEGM sinlgequot)	0.5
Triiodothyronine (BEGM sinlgequot)	0.5
Epinephrine (BEGM sinlgequot)	0.5

- Label the 250ml bottle **2x BEGM -RA/GA** and date and name and place in fridge in TC4

If there are very few ALIs in culture, the 2x BEGM for PBEC culture can be used, so as to prevent wastage of expensive media. Please co-ordinate with TC1 PBEC users.

Unopened BEBM bottles are stored in TC3 fridge and singlequots are stored in TC3 freezer. Once opened, BEBM bottles should not be moved between TC labs. There should be an open bottle of BEBM per TC lab.

3.2 Preparing 2x PromoCell Airway medium

- The singlequot vials should not be freeze/thawed.
- PromoCell medium is stable for a **maximum** of 1 month. If a lot of ALIs are in culture then prepare 250ml of 2xBEGM and 500ml DMEM, as per recipes below:
- Take 250 ml sterile bottle and add 245 ml of PromoCell Basal medium
- After defrosting singlequot vials/BSA, briefly centrifuge (1200rpm, 1min) to collect contents at the bottom of the vial and transfer to the 250ml bottle
- Thoroughly mix the 250ml bottle using a 25 ml pipette by pipetting up and down several times

Reagent	**Vol/250ml 2x BEGM (ml)**
PromoCell Airway Epithelial Cell Basal Medium	245
Bovine Pituitary extract	2
hEGF	0.5
Insulin	0.5
Hydrocortisone	0.5
Transferrin	0.5
Triiodothyronine	0.5
Epinephrine	0.5

- Label the 250ml bottle **2x PromoCell -RA/GA** and date and name and place in fridge in TC4

If there are very few ALIs in culture, the 2x PromoCell medium for PBEC culture can be used, so as to prevent wastage of expensive media. Please co-ordinate with TC1 PBEC users.

Unopened Basal medium bottles are stored in TC3 fridge and singlequots are stored in TC3 freezer. Once opened, Basal medium bottles should not be moved between TC labs. There should be an open bottle of Basal medium per TC lab.

6. DMEM for 1x ALI medium

Reagent	Vol/50 ml (ml)	Vol/250 ml (ml)	Vol/500 ml (ml)
DMEM	48	240	480
Non-essential amino acids	0.5	2.5	5.0
Sodium pyruvate	0.5	2.5	5.0
Penicillin/streptomycin (100X)	0.5	2.5	5.0
L-glutamine (100X)	0.5	2.5	5.0
BSA (500 mg/ml)	0.1	0.5	1.0

- Make up a minimum of 50 ml of DMEM and store in 50ml conicals
- Note; we usually make up 500 ml at a time when a lot of ALIs are in culture

7. Retinoic acid (all-trans RA) $5x10^{-5}$ M (50 uM)

- Make the primary stock solution by dissolving 50 mg retinoic acid (MW 300) in 16.67 ml DMSO in a darkened room to exclude UV light to give a final concentration of 3 mg/ml (10mM). Make 25ul aliquots and store in a bag wrapped in tin foil at -80ºC freezer (LF1, Freezer 2, rack A) in main lab.
- To make a working stock solution: dilute 20 □l of the primary stock in 4ml DMSO to give a final concentration of 50 µM ($5x10^{-5}$ M) and store 60 □l aliquots ready for use at -20ºC in a light tight container in TC3 (large freezer in black box, top shelf). **Do not thaw and refreeze.**
- **Use 1ul per 1ml 1xBEGM, final working concentration in media = 50nM**

8. Preparing 1x ALI media

**** BEGM is expensive and can't be stored once retinoic acid has been added, so only make up what is required***

- Work out how much media is required (300ul/transwell + 10% for pipetting losses)
- Into a 25/50ml universal tube add half the total volume of ALI DMEM and half the total volume of 2xALI BEGM/2xPromoCell medium.
- Just before use, thaw a vial of retinoic acid (50uM) and add 1ul per ml of 1x ALI media.
  Retinoic acid is unstable and light sensitive: protect from light, do not thaw/refreeze and do not thaw ≥½day before use.

9. Starvation media for ALI culture

Reagent	Vol/50 ml (ml)
BEBM/ PromoCell Basal medium	49
ITS (100X)	0.5
BSA (100mg/ml stock)	0.05
Penicillin-Streptomycin	0.5

Protocol for Transwells

Wipe the outside of the assembled system with 70% ethanol or IPA and place only the stand and associated components inside the MSC.

PREPARING THE TRANSWELL TRAYS (DAY 0)

- Prepare Collagen I solution (1:100) from stock of 3 mg/ml = 30ug/ml) (Purecol) in sterile double distilled water and add 100ul/well into apical compartment of required Transwell inserts into 24-well plates
- Place in 37˚C incubator for 30min to polymerise the collagen
- Remove collagen with fine-tip sterile pastette

Use Passage 1→2 primary bronchial epithelial cells for air-liquid interface (ALI) cultures.

(2) Taking Transwells to Air-liquid Interface DAY 1

PREPARATION OF ALI MEDIA

- Calculate how much 1x ALI medium is needed for culture (0.3ml/transwell + 10% for pipetting losses), prepare in 50ml conical tube (see below) and warm in 37°C incubator for >20 mins.

> **NOTES:**
>
> - On day 1 the cultures should be 95-100% confluent. If they are sub-confluent feed as described above and they may become confluent over the following few days. Persistant sub-confluent cultures may indicate that the cells are becoming quiescent and are less likely to differentiate.
>
> - After the first few days a confluent cell layer may appear to form ‘holes’ that give a lace curtain appearance. This will not inhibit differentiation and these areas should regress over time.
>
> - The cells start to visibly produce mucus at around 7 days. Pipette off daily as necessary.
>
> - Ciliated cells should start to appear from day 14-19 but you may not be able to see them under an inverted microscope if there is mucus impeding their beat.
>
> - Cells are generally used for assays from day 19-21. However, leaving the cultures for longer (e.g. another week) generally increases the percentage of ciliated cells.

- Just before use, defrost an aliquot of retinoic acid (RA) (5×10^{-5}M) and protect from light by placing in hand or wrapping in foil.
- Add 1□l of 50µM RA stock for each ml of ALI medium, e.g. if 20 ml is required use 10ml DMEM + 10ml 2x ALI medium + 20□l RA (final RA concentration of 50nM).

    - Need to protect 1xALI from light as RA is UV-sensitive.
    - Add RA to culture media immediately prior to use and cover conical with aluminium foil.
    - Do not thaw/re-freeze RA.

PROTOCOL

- Check cells under the microscope to ensure there is a confluent monolayer of cells in transwell insert.

    - Note: if cells are <95% confluent, remove media apically and basally and replace with 500ul pre-warmed 1x PBEC media to the basal side and 200ul BEGM on the apical side (see BEC culture protocol for 1xPBEC media preparation). Check daily, replace apical and basal PBEC media every 48hrs, then take to ALI (see below) when >95% confluent.

- Prepare 1x ALI media as described above.
- Using a fine-tip sterile pastette/aspirator, remove first the basal then apical medium from the transwells, taking care not to scrape the cell layer.
- Add 300□l of 1x ALI media underneath the transwell in the basal compartment. Do not add any medium to the apical surface of the cells.
- Place back in 37˚C incubator.

(3) Continuous Feeding of ALI cultures (TC3, TC4) DAY 2-21 onwards

- Make up required volumes of 1x ALI medium without RA into 50ml conical tubes and leave media to warm in 37˚C incubator for ≥20min.
- Just before use, add required amount of RA (1µl/ml) into 1xALI media, mix and place tube in foil (it is essential that the RA is not exposed to UV light as this will degrade it).
- Using a fine-tip sterile pastette or vacuum aspirator, remove the basal medium from the transwells.
- Remove any medium from the apical compartment that leaks through the cell layer during the first few days and remove excess mucus that accumulates on the apical surface from approx. day 7 onwards, taking care not to scrape the cell layer.
- Add 300□l of 1x ALI media underneath the transwell in the basal compartment.
- Sign log book to keep a record of the ALIs that have been fed.

(4) Transepithelial Resistance Measurement DAY 7, 14, 21

On day 7, 14 and 21 read TERs to check barrier integrity, using protocol below:

- Aliquot ~5 ml of HBSS (-Ca^{2+}/-Mg^{2+})/plate into 5ml bijouxs and place in 37˚C incubator to warm up for **minimum** of 30 minutes.
- Meanwhile, sterilise TER chopsticks by placing in a 25ml conical tube with 70% isopropanol.
- Remove any excess mucus from apical compartment of the transwells
- Add 100ul of pre-warmed HBSS (-Ca^{2+}/-Mg^{2+}) to apical compartment and place plate and HBSS bijoux in incubator for 15 min.
- Place plate on plastic rack in the TC hood to maintain a temp. as close to 37˚C as possible.
- Remove chopstick electrodes from isopropanol, allow to evaporate, then dip electrodes in the HBSS.
- Position electrodes at a 90˚ angle to the base of the plate, with the longest electrode on the outside (basal) and shortest electrode on the inside (apical) side of the transwell insert.
- Once the reading has stabilised, make a note of the TER reading on lid of the plate.
- Once all TER readings on a plate have been acquired, remove basal medium and then remove HBSS from apical compartment with fine-tipped pastette/aspirator.
- Add freshly prepared 1x ALI into basal compartment.
- Record TER values onto sheet in folder then place plate back into incubator.
- Update M:drive file with TER measurements

NOTES:

- Basal resistance = approx. 150 Ω
- Resistance of differentiated cultures = approx. 400 – 3000.
- Ideally want >1000 prior to experiment.

A.2.2 Platform Fabrication and Assembly

A.2.2.1 Manifold

The manifold used to provide basolateral perfusion to microfluidic chips was micromilled from 10 mm thick PEEK sheets (RS-Components, 129-820) at the UoS ECS Workshop. Gripper ferrules (Dibafit Gripper Ferrules, 002310) were placed in the manifolds and used to connect with bubble traps (Darwin Microfluidics, LVF-KBT-S 44 μL internal volume), with each bubble trap connected to the syringe pump. PTFE tubing with 1.6 mm OD and 0.5 mm ID (Kinesis, 008T16-050-20) was used to make connections between components. Two magnets (Supermagnete, Q-10-05-03-N) were placed in the appropriate slots, which are used to place and align the microfluidic chip. O-rings (RS-Components, 196-4728) are located between manifold and microfluidic chip, providing fluidic seal.

A.2.2.2 Microfluidic Chip

The microfluidic chip is composed of PMMA, glass and a high porous membrane. The microfluidic channel was laser cut from 275 μm thick PMMA (TechSoft UK) and top part micromilled, by UoS ECS workshop, from 10 mm PMMA (Goodfellow). All layers were held together using double-sided adhesive (3M Adhesive Transfer Tape 467MP).

Patterning of electrodes in the glass chip was conducted in the cleanroom by Nikita Karra, Sumit Kalsi and Katie Chamberlain. The electrodes in the glass chip surface were made by sputtering (Orion AJA sputterer) 20 nm of titanium and 200 nm of platinum onto a 1.1 mm glass wafer. Once coated, the glass wafers underwent a photolithography process (S18183 resist) in which a custom-made film mask (Micro Lithography Services) was patterned into the photoresist. The wafer is then developed (MF319 developer solution) and the exposed platinum is etched. The remaining photoresist is cleaned with NPS, FNA and acetone. Ruthenium oxide coating requires the coating of the platinum patterned wafer with AZ2070 resist, being softbaked at 110 °C for 90 seconds and patterned with an UV exposure of 95 mJ/cm2 with a second film mask that only exposes the area of the electrodes that will be in contact with fluids. The wafer then underwent a post bake step at 110 ºC for 90 seconds and is developed in A726 developer for 2 minutes, followed by descumming process on the reactive ion etching (RIE) 80+ and the sputtering of 10 nm Titanium and 120 nm Ruthenium Oxide onto the surface using the AJA Orion Sputterer. Lift off is performed overnight with N-Methyl-2-Pyrrolidone (NMP) to remove excess metals. The wafer was then washed with acetone and IPA before scribing. Following metal deposition, chips were annealed at 420 ºC overnight.

A.2.3 Continuous Cell Culture

A.2.3.1 16HBE14o- Cells

The human bronchial epithelial cell line (16HBE14o-) was maintained in collagen I (30 μg/mL) (Advanced Biomatrix, 14170-138) coated flasks in minimal essential medium (MEM) with Glutamax (Gibco, 41090), 10% foetal bovine serum (FBS) (Sigma, F7524-500ML) and 1% penicillin/streptomycin (Sigma, 59202C-100ML) (complete MEM; cMEM) in an humidified incubator at 37 °C and 5 % CO2. Cells were harvested by first incubating with 10 mL of Hanks buffered saline solution (HBSS) (Life Technologies, 15400) for 10 minutes, followed by a second incubation of 5 minutes in 1 mL of 1x trypsin-EDTA in HBSS (Life Technologies, 15400-054). Once cells detached from the flask, 10 mL of cMEM were used to neutralise the existing trypsin-EDTA and the entire cell solution underwent centrifugation at 300 x *g* for 5 minutes at 20 ºC. After centrifugation, the cell pellet was resuspended in cMEM. Cells were counted using a haemocytometer and the cell density calculated via trypan blue exclusion method. A flask was coated with collagen I (30 μg/mL) for 30 minutes. Following coating, collagen was removed and 11 mL of cMEM cell media were inserted in the flask. A 1 mL solution containing 2×10^5 cells was introduced into the flask, before being placed in a high humidity incubator at 37 ºC and 5% CO_2. Cell media in each flask was replaced every 2 days and cells were passaged when cell confluency in the flask reached approximately 70%.

A.2.3.2 Caco-2 Cells

The human adenocarcinoma cell line (Caco-2) was maintained in collagen I (30 μg/mL) (Advanced Biomatrix, 14170-138) coated flasks in Dulbecco's modified eagle medium (DMEM) (FisherScientific, 11500416), 1x Glutamax (Gibco, 41090), 10% FBS (Sigma, F7524-500ML), 1% penicillin/streptomycin (Sigma, 59202C-100ML), 1% sodium pyruvate (FisherScientific, 12539059) and 1% non-essential amino acid solution (Sigma, M7145-100ML) (complete DMEM, cDMEM) in an incubator. Cells were harvested by first incubating with 10 mL of Hanks buffered saline solution (HBSS) (Life Technologies, 15400) for 10 minutes, followed by a second incubation of 5 minutes in 1 mL of 1x trypsin-EDTA in HBSS (Life Technologies, 15400). Once cells detached from the flask, 10 mL of cDMEM was used to neutralise the existing trypsin and the entire cell solution underwent centrifugation at 300 x *g* for 5 minutes at 20 ºC. After centrifugation, the cell pellet was resuspended in cDMEM. Cells were counted using a haemocytometer and solution cell concentration was calculated via trypan blue exclusion method. A flask was coated with collagen I (30 μg/mL) for 30 minutes. Following coating, collagen was removed and 11 mL of cDMEM cell media were inserted in the flask. A 1 mL solution containing 2 × 105 cells was introduced into the flask before being placed in a high humidity incubator at 37 °C and 5% CO2. Cell media in each flask was replaced every 2 days and cells were split when flask reached approximately 70% confluency.

A.2.4 TER Measurements in Transwells

TER measurements in Transwell supports were performed using Epithelial Voltohmmeter (EVOM) chopstick electrodes (World Precision Instruments) every day. Plates containing Transwell supports were removed from the incubator and placed inside an MSC Class II Biological Safety Cabinet. Each chopstick electrode was placed in the apical and basolateral compartments respectively. Resistance measurements were recorded and Transwells were placed inside the incubator. Resistance values were multiplied by the cell culture surface area of a Transwell support (0.33 cm^2) to obtain TER values in $\Omega.cm^2$.

A.2.5 Cell Fixing

Transwell supports and microfluidic chips with cells were fixed for subsequent immunofluorescent staining as follows. Cell media was removed from the apical and basolateral compartments, being replaced by a solution of 4% paraformaldehyde (PFA) in phosphate buffered saline (PBS) (Sigma-Aldrich, P4417) for 30 minutes at room temperature. After which, both compartments were washed with PBS 3 times for 5 minutes per wash. Both Transwells and microfluidic chips were stored with PBS in both compartments, inside appropriate well plates with the lids properly sealed with parafilm. Well plates were stored at 4 °C until required.

A.2.6 Cell Staining

Cell staining and confocal imaging was performed by Nikita Karra for the results shown in Chapter 4.

For immunofluorescent staining, the porous membranes were removed from the Transwell or microfluidic chip and transferred to a microscope slide. Membranes were submerged in blocking buffer to prevent sample drying. These were washed in PBS for 10 minutes and incubated in permeabilization buffer (0.1 % TX-100 in PBS) for 15 minutes at room temperature. The liquid was wicked away from the membrane with tissue and samples were incubated in blocking buffer (1 % bovine serum albumin (BSA), 0.1 % Tween 20 in PBS) for 1 hour. Following incubation, the membrane was gently dried once more and incubated in 50 μL of staining solution containing the AlexaFluor488-conjugated occludin monoclonal antibody (clone OC-3F10, Life Technologies), final concentration 5 µg/mL) and Acti-stain 555phalloidin (PHDH1-A, final concentration 70 nM) in blocking buffer overnight in a humidified chamber at 4 ℃. Staining solution was removed and membrane was washed 3 times for 5 minutes in 100 μL of PBS with 0.1 % Tween 20. After gently drying the membrane, DAPI staining solution (Merck, 10236276001; 2µg/mL in dH2O) was added and incubated for 15 minutes at room temperature. DAPI staining solution was removed and membranes were washed 4 times for 5 minutes with 100 μL of PBS with 0.1 % Tween 20, followed by 1 wash with dH_2O. The membrane was transferred to a clean microscope slide and mounted with a coverslip using Mowiol (Merck, 81381) mounting medium. These were stored in the dark at 4 ℃ until analysis.

Confocal microscopy images were obtained at 63X in xyz mode (Leixa TCS-SP8 laser scanning microscope) with wavelengths of 405 nm (DAPI), 561 nm (Actin) and 488 nm (Occludin). A z-projection stacks were obtained using a sequential scan between the top of the cell layer and the porous support.

A.2.7 Apical Stimulant Preparation

A.2.7.1 Triton X-100

A 5 % Triton X-100 (TX-100; Sigma-Aldrich, X-100) stock solution was prepared with cell media. 20 μL of the stock solution was added to the apical compartment of the microfluidic chip to give a final concentration of 1 % (20 μL with 5 % diluted in a total volume of 100 μL (1 in 5 dilution)).

A.2.7.2 Poly I:C

Stock solution of viral dsRNA in dH2O (Invivogen, tlrl-pic-5) with a concentration of 1 mg/mL was prepared (together with Nikita Karra) by mixing 50 mg of dsRNA with 50 mL of dH_2O (provided in the product package). The solution was mixed while in a water bath at 50 ℃ and 100 μL aliquots were stored in centrifuge tubes at -20 ℃ until further use.

For apical stimulation, aliquots were serial diluted in cell media from 1 mg/mL to 125 μg/mL in cell culture media (1 in 8 dilution) and 20 μL was added to the apical compartment of the chip, resulting in a final concentration of 25 μg/mL (20 μL with 25 μg/mL diluted in a total volume of 100 μL (1 in 5 dilution)).

A.3 Droplet Generating System

A.3.1 Peristaltic Controller

The PMMA layers for the pressure controller were assembled using 50 µm double-sided adhesive tape (3M Adhesive Transfer Tape 467MP). Each layer was machined using a laser cutter (Epilog Laser, 85% power and 15%speed) and holes for the inlet and outlet connectors were manually threaded. Solenoid 2-way valves (LFNA1250125H, The Lee Company) were attached to the PMMA with M1.6 screws and controlled with a microcontroller connected to a laptop. Pressure was controlled via an Arduino script and the outlets were connected to the PDMS droplet generator with PTFE tubing (1.6 mm OD). The two Arduino scripts below were used to prime (Continuous_Oil_Pumping) and generate droplets (Droplet_Generation). Scripts were loaded to an Arduino Teensy 3.2 using the Arduino IDE. Frequency of operation can be changed with the ”Delay” variable (which is set in ms), with $Frequency = (6 \times Delay \times 0.001)^{-1}$.

A.3.1.1 Continuous_Oil_Pumping

```
//the valves
int valve4 = 7;
int valve5 = 8;
int valve6 = 9;
int valve1 = 10;
int valve2 = 11;
int valve3 = 12;
int valve7 = 15;
int valve8 = 14;
int Delay =25;

void setup() {

  // setup the pins to input or output
  pinMode(valve1, OUTPUT);
  pinMode(valve2, OUTPUT);
  pinMode(valve3, OUTPUT);
  pinMode(valve4, OUTPUT);
  pinMode(valve5, OUTPUT);
  pinMode(valve6, OUTPUT);
  pinMode(valve7, OUTPUT);
  pinMode(valve8, OUTPUT);
        digitalWrite(valve1, 1);
        delay (100);
        digitalWrite(valve2, 1);
        digitalWrite(valve3, 1);
}

```

```
void loop() {
        delay(Delay);
        digitalWrite(valve1, 0);
        digitalWrite(valve2, 0);
        digitalWrite(valve3, 0);
        digitalWrite(valve7,0);

        digitalWrite(valve4, 1);
        delay(Delay);
        digitalWrite(valve5, 1);
        delay(Delay);

        digitalWrite(valve4, 0);
        digitalWrite(valve1, 1);
        delay(Delay);

        digitalWrite(valve6, 1);
        digitalWrite(valve5, 0);
        delay(Delay);
        digitalWrite(valve2, 1);
        delay(Delay);

        digitalWrite(valve6, 0);
        digitalWrite(valve1, 1);
        digitalWrite(valve3, 1);
}
```

Continuous_Oil_Pumping.ino

A.3.1.2 Droplet_Generation

```
//the valves
int valve4 = 7;
int valve5 = 8;
int valve6 = 9;
int valve1 = 10;
int valve2 = 11;
int valve3 = 12;
int valve7 = 15;
int valve8 = 14;
int Delay = 25;

void setup() {
  // setup the pins to input or output
  pinMode(valve1, OUTPUT);
  pinMode(valve2, OUTPUT);
  pinMode(valve3, OUTPUT);
  pinMode(valve4, OUTPUT);
  pinMode(valve5, OUTPUT);
  pinMode(valve6, OUTPUT);
```

```
  pinMode(valve7, OUTPUT);
  pinMode(valve8, OUTPUT);
}

void loop() {

    digitalWrite(valve7,0);
    digitalWrite(valve8,1);
    for (int i=0; i<=15;i ++){
        delay(Delay);
        digitalWrite(valve1, 0);
        digitalWrite(valve2, 0);
        digitalWrite(valve3, 0);
        digitalWrite(valve4, 0);
        digitalWrite(valve5, 0);
        digitalWrite(valve6, 0);
        digitalWrite(valve4, 1);
        delay(Delay);
        digitalWrite(valve5, 1);
        delay(Delay);
        digitalWrite(valve4, 0);
        digitalWrite(valve1, 1);
        delay(Delay);
        digitalWrite(valve6, 1);
        digitalWrite(valve5, 0);
        delay(Delay);
        digitalWrite(valve2, 1);
        delay(Delay);
        digitalWrite(valve6, 0);
        digitalWrite(valve1, 1);
        digitalWrite(valve3, 1);
    }
        digitalWrite(valve6, 1);
        digitalWrite(valve5, 1);
        digitalWrite(valve4, 1);
        digitalWrite(valve3, 0);
        digitalWrite(valve2, 0);
        digitalWrite(valve1, 0);
        digitalWrite(valve8,0);
        digitalWrite(valve7,1);
        delay (1200000);
        //Entire Cycle
}
```

Droplet_Generation.ino

A.3.2 Droplet Generator and Peristaltic Pump Fabrication

The droplet generator and peristaltic pump were designed using Solidworks and fabricated from PDMS. 3D printed moulds of Veroclear were printed using an Object Connex 350 3D printer, present at the UoS ECS workshop. Moulds were cleaned of any support material and placed in an oven at 65 ◦C to cure for a minimum of 24 hours (preferably over the weekend). Once cured, a solution of PDMS with a 1:10 ratio between elastomer and curing agent was poured into the moulds and placed in a desiccator for 1 hour. Following gas removal, moulds were placed in an oven at 65 ◦C for 12 hours, leading to the curing of PDMS and pattern transfer from the mould to PDMS. The actuation membrane was acquired through Silex and was 200 μm thick. Inlet and outlet holes were punctured into the PDMS layers where required using biopsy punchers with 1.5 mm OD. The three layers composing each device (top, bottom and actuation membrane) were bounded together using oxygen plasma.

A.3.3 COMSOL Diffusion and Fluidics Simulation

Diffusion simulations were performed using the Transport of Diluted Species and Laminar Flow physic modules in COMSOL Multiphysics.

A.3.3.1 Geometry

For the microfluidic chip. basolateral and apical compartments were created as cylinders above the electrodes with a radius of 2.5 mm and heights of 0.275 and 5 mm respectively. Microfluidic channel design was imported from Solidworks as .STL, with a height of 0.275. Inlet and outlet holes for the microfluidic chip were generated with cylinders with 0.5 mm radius and 0.275 mm height. Outlet tubing attached to the chip was created with a cylinder with a radius of 0.5 mm and 10 cm height. A cylinder representing the porous membrane was created between apical and basolateral compartments with a height of 10 μm

For the Transwell support, basolateral and apical compartments were generated as cylinders with radius of 0.78 and 0.35 cm and heights of 0.35 and 0.46 cm respectively. The porous membrane in-between compartments was a cylinder with radius of 0.35 cm and height of 10 μm.

A fine mesh was applied to the geometries.

A.3.3.2 Materials

All boundaries were set to Water, liquid.

A.3.3.3 Conditions

Additional transport mechanism of convection and mass transfer in porous domains were activated in the Transport of Diluted Species module.

For the biochip, a mass flow rate of $8.3E - 9$ Kg/s was set to the inlet and atmospheric pressure assigned to the outlet of the tubing. Every external facing surface was set to "no slip" and no flux boundary condition. The porous membrane was set as a porous matrix, with a porosity of 0.12566. An initial solute concentration was set to 1 mol/m^3 in the apical compartment, with all other domains being set to 0.

For the Transwell, the porous membrane was set as a porous matrix with a porosity of 0.00503. Every external facing surface was set to no flux condition. An initial concentration was assigned to the apical compartment of 1 mol/m^3, with all other domains being set to 0.

A time dependent study was performed for diffusion assessment during 48 hours, with 2 hour steps.

A.3.4 FITC-Dextran Solution

A stock solution with a concentration of 20 mg/mL of FITC-Dextran 10kDa (Merck, FD10S-100MG) was diluted to 10 mg/mL in cell media and 20 μL was added to the apical compartment of the microfluidic chip (final concentration of 2 mg/mL). If used in conjunction with Triton X-100, the stock solution of FITC-Dextran was diluted to 10 mg/mL in cell media with 5 % Triton X-100 instead.

A.3.5 Fluorescein Solution

Fluorescein (FITC) (Sigma-Aldrich, F7505) solution with a final concentration of 0.05 mg/mL was made by mixing 250 mg of FITC powder with 50 mL of dH_2O in a centrifuge tube. 100 μL of this solution was apically added to the microfluidic chips for solute diffusion studies.

A.3.6 ELISA Protocol

IL-8 detection in solution obtained from Transwell supports and microfluidic chips was performed via ELISAs using a Duoset ELISA kit (R&D Biosystems, DY208) and a Duoset ELISA ancillary kit (R&D Biosystems, DY008). Maxisorp 96-well plates were incubated with capture antibody (4 μg/mL in 1x PBS) at room temperature in the dark overnight. Following incubation, the plate was washed three times with wash buffer (0.05% Tween-20 in PBS, pH 7.2-7.4) and incubated with block buffer (1% BSA in PBS, pH 7.2-7.4, 0.2 μM filtered) for at least 1 hour at room temperature in the dark. Frozen samples from Transwells or microfluidic chips were thawed on ice and diluted in reagent diluent (0.1% BSA 0.05% Tween-20 in Tris Buffered Saline, pH 7.2-7.4, 0.2 μm sterile filtered) in a 1:25 ratio for all samples apart from Transwell controls basolateral solutions, which were diluted in a 1:10 ratio instead (ratios obtained through optimization experiments performed by Nikita Karra (PhD student) in separate experiments). Solutions required to do a standard curve were generated through serial dilutions, with a concentration gradient from 2000 pg/mL to 31.3 pg/mL and the reagent diluent as a blank control. Following block buffer incubation, the plate was washed three times with wash buffer, samples were introduced onto the plate and incubated for at least 2 hours at room temperature in dark. The plate was washed three times using wash buffer and incubated with detection antibody (10 ng/mL in reagent diluent) for 2 hours at room temperature in the dark. After incubation, the plate was washed three times and incubated with horseradish peroxidase (HRP) solution (1:40 in reagent diluent) for 20 minutes at room temperature in the dark. Following incubation, the plate was washed three times with wash buffer and incubated with 1x TMB (Thermo Fisher Scientific, 12750000) in the dark while applying gentle agitation. Stop solution (2 N H2SO4) was added to the plate when a colour change is noticeable between the top two and bottom two positions in the standard solutions. The plate was then read at 450 nm and 570 nm after 30 second agitation at 400 rpm (BMG Labtech, CLARIOstar). Concentrations of IL-8 in samples were calculated from the standard curve (Figure A.1) after blank subtraction (containing diluent instead of sample) using the software accompanying the plate reader.

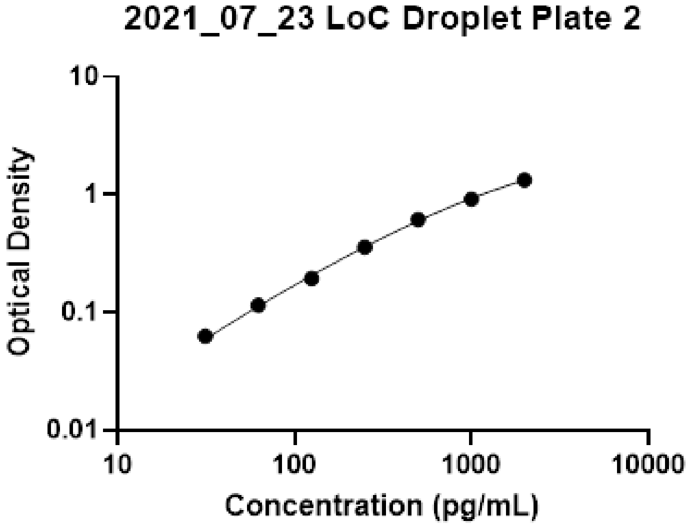

FIGURE A.1: IL-8 ELISA standard curve used for data extrapolation.

References

LFN Series 2-Way Solenoid Valves — The Lee Co. URL `https://www.theleeco.com/product/lfn-series-2-way-solenoid-valves/`.

Cezmi A. Akdis. Does the epithelial barrier hypothesis explain the increase in allergy, autoimmunity and other chronic conditions?, 2021. ISSN 14741741.

Frank Alexander, Sebastian Eggert, and Joachim Wiest. A novel lab-on-a-chip platform for spheroid metabolism monitoring. *Cytotechnology*, 70(1):375–386, 2018a. ISSN 15730778. .

Frank A. Alexander, Sebastian Eggert, and Joachim Wiest. Skin-on-a-chip: Transepithelial electrical resistance and extracellular acidification measurements through an automated air-liquid interface. *Genes*, 9(2):114, feb 2018b. ISSN 20734425. . URL `http://www.mdpi.com/2073-4425/9/2/114`.

Shaista Anwer and Katalin Szászi. Measuring Cell Growth and Junction Development in Epithelial Cells Using Electric Cell-Substrate Impedance Sensing (ECIS). *Bio-Protocol*, 10(16):1–13, 2020. ISSN 2331-8325. .

Athanasia Apostolou, Rohit A. Panchakshari, Antara Banerjee, Dimitris V. Manatakis, Maria D. Paraskevopoulou, Raymond Luc, Galeb Abu-Ali, Alexandra Dimitriou, Carolina Lucchesi, Gauri Kulkarni, Tengku Ibrahim Maulana, Magdalena Kasendra, Jordan S. Kerns, Bertram Bleck, Lorna Ewart, Elias S. Manolakos, Geraldine A. Hamilton, Cosmas Giallourakis, and Katia Karalis. A Novel Microphysiological Colon Platform to Decipher Mechanisms Driving Human Intestinal Permeability. *Cmgh*, 12(5):1719–1741, 2021. ISSN 2352345X. . URL `https://doi.org/10.1016/j.jcmgh.2021.07.004`.

Applied BioPhysics. No Title. URL `https://www.biophysics.com/whatIsECIS.php`.

R. Aris. A. On the dispersion of a solute in a fluid flowing through a tube. *Process Systems Engineering*, 1(C):109–120, 1999. ISSN 18745970. .

Yusuf B. Arlk, Marinke W. Van Der Helm, Mathieu Odijk, Loes I. Segerink, Robert Passier, Albert Van Den Berg, and Andries D. Van Der Meer. Barriers-on-chips: Measurement of barrier function of tissues in organs-on-chips. *Biomicrofluidics*, 12(4), 2018. ISSN 19321058. .

Nureddin Ashammakhi, Rohollah Nasiri, Natan Roberto de Barros, Peyton Tebon, Jai Thakor, Marcus Goudie, Amir Shamloo, Martin G Martin, and Ali Khademhosseni. Gut-on-a-chip: Current progress and future opportunities, 2020. ISSN 18785905. URL `https://doi.org/10.1016/j.biomaterials.2020.120196`.

Anthony K. Au, Hoyin Lai, Ben R. Utela, and Albert Folch. *Microvalves and micropumps for BioMEMS*, volume 2. 2011. ISBN 1206616903. .

H. Azizgolshani, J. R. Coppeta, E. M. Vedula, E. E. Marr, B. P. Cain, R. J. Luu, M. P. Lech, S. H. Kann, T. J. Mulhern, V. Tandon, K. Tan, N. J. Haroutunian, P. Keegan, M. Rogers, A. L. Gard, K. B. Baldwin, J. C. de Souza, B. C. Hoefler, S. S. Bale, L. B. Kratchman, A. Zorn, A. Patterson, E. S. Kim, T. A. Petrie, E. L. Wiellette, C. Williams, B. C. Isenberg, and J. L. Charest. High-throughput organ-on-chip platform with integrated programmable fluid flow and real-time sensing for complex tissue models in drug development workflows. *Lab on a Chip*, 21(8):1454–1474, 2021. ISSN 1473-0197. .

Peter J. Barnes, Sergio Bonini, Werner Seeger, Maria G. Belvisi, Brian Ward, and Anthony Holmes. Barriers to new drug development in respiratory disease. *European Respiratory Journal*, 45(5):1197–1207, 2015. ISSN 13993003. . URL `http://dx.doi.org/10.1183/09031936.00007915`.

D O N W Barrier. Function of Epithelia. pages 275–288, 1981.

Kathrin Benson, Sandra Cramer, and Hans Joachim Galla. Impedance-based cell monitoring: Barrier properties and beyond, 2013. ISSN 20458118.

Cornelia Blume, Riccardo Reale, Marie Held, Timothy M. Millar, Jane E. Collins, Donna E. Davies, Hywel Morgan, and Emily J. Swindle. Temporal monitoring of differentiated human airway epithelial cells using microfluidics. *PLoS ONE*, 10(10): 1–13, 2015. ISSN 19326203. .

Cornelia Blume, Riccardo Reale, Marie Held, Matthew Loxham, Timothy M. Millar, Jane E. Collins, Emily J. Swindle, Hywel Morgan, and Donna E. Davies. Cellular crosstalk between airway epithelial and endothelial cells regulates barrier functions during exposure to double-stranded RNA. *Immunity, Inflammation and Disease*, 5(1): 45–56, 2017. ISSN 20504527. . URL `http://doi.wiley.com/10.1002/iid3.139`.

Kieran Brune, James Frank, Andreas Schwingshackl, James Finigan, and Venkataramana K. Sidhaye. Pulmonary epithelial barrier function: Some new players and mechanisms. *American Journal of Physiology - Lung Cellular and Molecular Physiology*, 308(8):L731–L745, 2015. ISSN 15221504. .

Henrik Bruus. Theoretical microfluidics. *Choice Reviews Online*, 45(10):45–5602–45–5602, 2008. ISSN 0009-4978. .

Patrick J. Callaghan, Bryan Ferrick, Elizabeth Rybakovsky, Sunil Thomas, and James M. Mullin. Epithelial barrier function properties of the 16HBE14o- human bronchial epithelial cell culture model. *Bioscience Reports*, 40(10):1–16, oct 2020a. ISSN 15734935. . URL `https://pubmed.ncbi.nlm.nih.gov/32985670/`.

Patrick J. Callaghan, Bryan Ferrick, Elizabeth Rybakovsky, Sunil Thomas, and James M. Mullin. Epithelial barrier function properties of the 16HBE14o- human bronchial epithelial cell culture model. *Bioscience Reports*, 40(10), oct 2020b. ISSN 15734935. . URL `https://pubmed.ncbi.nlm.nih.gov/32985670/`.

Tommaso Casalini, Matteo Salvalaglio, Giuseppe Perale, Maurizio Masi, and Carlo Cavallotti. Diffusion and aggregation of sodium fluorescein in aqueous solutions. *Journal of Physical Chemistry B*, 115(44):12896–12904, 2011. ISSN 15205207. .

Diana F. Cedillo-Alcantar, Yong Duk Han, Jonghoon Choi, Jose L. Garcia-Cordero, and Alexander Revzin. Automated Droplet-Based Microfluidic Platform for Multiplexed Analysis of Biochemical Markers in Small Volumes. *Analytical Chemistry*, 91(8):5133–5141, 2019. ISSN 15206882. .

Handy Chandra, Spencer W. Allen, Shane W. Oberloier, Nupur Bihari, Jephias Gwamuri, and Joshua M. Pearce. Open-source automated mapping four-point probe. *Materials*, 10(2), 2017. ISSN 19961944. .

Wen L.K. Chen, Collin Edington, Emily Suter, Jiajie Yu, Jeremy J. Velazquez, Jason G. Velazquez, Michael Shockley, Emma M. Large, Raman Venkataramanan, David J. Hughes, Cynthia L. Stokes, David L. Trumper, Rebecca L. Carrier, Murat Cirit, Linda G. Griffith, and Douglas A. Lauffenburger. Integrated gut/liver microphysiological systems elucidates inflammatory inter-tissue crosstalk. *Biotechnology and Bioengineering*, 114(11):2648–2659, 2017. ISSN 10970290. .

Kenneth M. Chrobak, Daniel R. Potter, and Joe Tien. Formation of perfused, functional microvascular tubes in vitro. *Microvascular Research*, 71(3):185–196, 2006. ISSN 00262862. .

Jared M. Churko and Dale W. Laird. Gap Junctions. *Cellular Domains*, pages 339–347, 2011. .

Daniel R. Clayburgh, Le Shen, and Jerrold R. Turner. A porous defense: The leaky epithelial barrier in intestinal disease, 2004. ISSN 00236837.

A. L. Cozens, M. J. Yezzi, K. Kunzelmann, T. Ohrui, L. Chin, K. Eng, W. E. Finkbeiner, J. H. Widdicombe, and D. C. Gruenert. CFTR expression and chloride secretion in polarized immortal human bronchial epithelial cells. *American journal of respiratory cell and molecular biology*, 10(1):38–47, 1994. ISSN 10441549. .

Jared M. Diamond. The Epithelial Junction: Bridge, Gate, and Fence. *Physiologist*, 20: 10–18, 1977. ISSN 0031-9376.

Karel Domansky, Walker Inman, James Serdy, Ajit Dash, Matthew H.M. Lim, and Linda G. Griffith. Perfused multiwell plate for 3D liver tissue engineering. *Lab on a Chip*, 10(1):51–58, 2010. ISSN 14730189. .

K. L. Dorrington and C. A.R. Boyd. Active transport in the alveolar epithelium of the adult lung: vestigial or vital? *Respiration Physiology*, 100(3):177–183, 1995. ISSN 00345687. .

Ali Doryab, Ghassem Amoabediny, and Amir Salehi-Najafabadi. Advances in pulmonary therapy and drug development: Lung tissue engineering to lung-on-a-chip. *Biotechnology Advances*, 34(5):588–596, 2016. ISSN 07349750. . URL `http://dx.doi.org/10.1016/j.biotechadv.2016.02.006`.

Michael Dourson, Lorna Ewart, Suzanne C Fitzpatrick, Silvia B M Barros, Brinda Mahadevan, and A Wallace Hayes. The Future of Uncertainty Factors With In Vitro Studies Using Human Cells . *Toxicological Sciences*, (November):1–6, 2021. ISSN 1096-6080. .

Mays El-Dairi and Robert James House. Optic nerve hypoplasia, 2019.

Eric W. Esch, Anthony Bahinski, and Dongeun Huh. Organs-on-chips at the frontiers of drug discovery. *Nature Reviews Drug Discovery*, 14(4):248–260, apr 2015. ISSN 1474-1776. . URL `http://www.ncbi.nlm.nih.gov/pubmed/25792263http://www.pubmedcentral.nih.gov/articlerender.fcgi?artid=PMC4826389http://www.nature.com/doifinder/10.1038/nrd4539`.

Gareth W.H. Evans, Wahida T. Bhuiyan, Susan Pang, Brett Warren, Kyriacos Makris, Sharon Coleman, Sammer Ul Hassan, and Xize Niu. A portable droplet microfluidic device for cortisol measurements using a competitive heterogeneous assay. *Analyst*, 146(14):4535–4544, 2021. ISSN 13645528. .

Samantha C. Faber, Nicole A. McNabb, Pablo Ariel, Emily R. Aungst, and Shaun D. McCullough. Exposure Effects beyond the Epithelial Barrier: Transepithelial Induction of Oxidative Stress by Diesel Exhaust Particulates in Lung Fibroblasts in an Organotypic Human Airway Model. *Toxicological Sciences*, 177(1):140–155, 2020. ISSN 10960929. .

Jing Fan, Shuaijun Li, Ziqian Wu, and Zi Chen. *Diffusion and mixing in microfluidic devices*. Elsevier Inc., 2018. ISBN 9780128126592. . URL `http://dx.doi.org/10.1016/B978-0-12-812659-2.00003-X`.

João Fernandes, Nikita Karra, Joel Bowring, Riccardo Reale, Jonathan James, Cornelia Blume, Theresa J Pell, Wendy C Rowan, Donna E Davis, Emily J Swindle, and Hywel Morgan. Real-Time Monitoring of Epithelial Barrier Function by Impedance Spectroscopy in a Microfluidic Platform. *Lab on a Chip*, 1, 2022. ISSN 1473-0197. .

Erika Ferrari, Cecilia Palma, Simone Vesentini, Paola Occhetta, and Marco Rasponi. Integrating Biosensors in Organs-on-Chip Devices: A Perspective on Current Strategies to Monitor Microphysiological Systems. *Biosensors*, 10(9), 2020. ISSN 20796374. .

Adolf Fick. On liquid diffusion (Reprint of the original 1855 article). *Journal of Membrane Science*, 100(1):33–38, 1995. ISSN 03767388. URL `http://linkinghub.elsevier.com/retrieve/pii/037673889400230V`.

J. Fogh, W. C. Wright, and J. D. Loveless. Absence of HeLa cell contamination in 169 cell lines derived from human tumors. *Journal of the National Cancer Institute*, 58(2): 209–214, 1977. ISSN 00278874. .

Ben Forbes, Atiya Shah, Gary P. Martin, and Alison B. Lansley. The human bronchial epithelial cell line 16HBE14o- as a model system of the airways for studying drug transport. *International Journal of Pharmaceutics*, 257(1-2):161–167, 2003. ISSN 03785173. .

Silvio Garattini and Giuliano Grignaschi. Animal testing is still the best way to find new treatments for patients. *European Journal of Internal Medicine*, 39:32–35, 2017. ISSN 18790828. . URL `http://dx.doi.org/10.1016/j.ejim.2016.11.013`.

L A Geddes. Historical evolution of circuit models for the electrode-electrolyte interface, 1997. ISSN 00906964.

T. N. Gerasimenko, O. V. Kindeeva, V. a. Petrov, a. I. Khaustov, and E. V. Trushkin. Modelling and characterization of a pneumatically actuated peristaltic micropump. *Applied Mathematical Modelling*, 52:590–602, 2017. ISSN 0307904X. . URL `http://dx.doi.org/10.1016/j.apm.2017.08.008`.

Tatiana Gerasimenko, Sergey Nikulin, Galina Zakharova, Andrey Poloznikov, Vladimir Petrov, Ancha Baranova, and Alexander Tonevitsky. Impedance Spectroscopy as a Tool for Monitoring Performance in 3D Models of Epithelial Tissues. *Frontiers in Bioengineering and Biotechnology*, 7(January), jan 2020a. ISSN 22964185. . URL `https://www.frontiersin.org/article/10.3389/fbioe.2019.00474/full`.

Tatiana Gerasimenko, Sergey Nikulin, Galina Zakharova, Andrey Poloznikov, Vladimir Petrov, Ancha Baranova, and Alexander Tonevitsky. Impedance Spectroscopy as a Tool for Monitoring Performance in 3D Models of Epithelial Tissues. *Frontiers in Bioengineering and Biotechnology*, 7(January), 2020b. ISSN 22964185. .

Marlene Geyer and Karla Queiroz. Microfluidic Platforms for High-Throughput Pancreatic Ductal Adenocarcinoma Organoid Culture and Drug Screening. *Frontiers in Cell and Developmental Biology*, 9(December):1–9, 2021. .

Amir M. Ghaemmaghami, Matthew J. Hancock, Helen Harrington, Hirokazu Kaji, and Ali Khademhosseini. Biomimetic tissues on a chip for drug discovery. *Drug Discovery Today*, 17(3-4):173–181, 2012. ISSN 13596446. . URL `http://dx.doi.org/10.1016/j.drudis.2011.10.029`.

Melanie L. Graham and Mark J. Prescott. The multifactorial role of the 3Rs in shifting the harm-benefit analysis in animal models of disease. *European Journal of Pharmacology*, 759:19–29, 2015. ISSN 18790712. . URL `http://dx.doi.org/10.1016/j.ejphar.2015.03.040`.

Yuki Hagiwara, Harumi Kumagai, Niels Ouwerkerk, Linda Gijzen, Rumaisha Annida, Marleen Bokkers, Remko van Vught, Kouichi Yoshinari, Yoshifumi Katakawa, Kei Motonaga, and Tomokazu Tajiri. A Novel In Vitro Membrane Permeability Methodology Using Three-dimensional Caco-2 Tubules in a Microphysiological System Which Better Mimics In Vivo Physiological Conditions. *Journal of Pharmaceutical Sciences*, 111(1):214–224, 2022. ISSN 00223549. . URL `https://doi.org/10.1016/j.xphs.2021.11.016`.

James E Hall. Access resistance of a small circular pore, 1975. ISSN 15407748. URL `http://rupress.org/jgp/article-pdf/66/4/531/1245944/531.pdf`.

Andrea Hartsock and W. James Nelson. Adherens and tight junctions: Structure, function and connections to the actin cytoskeleton. *Biochimica et Biophysica Acta - Biomembranes*, 1778(3):660–669, 2008. ISSN 00052736. .

Sammer Ul Hassan, Adrian M. Nightingale, and Xize Niu. Optical flow cell for measuring size, velocity and composition of flowing droplets. *Micromachines*, 8(2):1–10, 2017. ISSN 2072666X. .

I. H. Heijink, M. R. Jonker, M. de Vries, A. J.M. van Oosterhout, E. Telenga, N. H.T. ten Hacken, D. S. Postma, and M. van den Berge. Budesonide and fluticasone propionate differentially affect the airway epithelial barrier. *Respiratory Research*, 17(1): 1–13, 2016. ISSN 1465993X. .

H. Helmholtz. Studien über electrische Grenzschichten. *Annalen der Physik*, 243(7): 337–382, 1879. ISSN 15213889. .

Olivier Y.F. F. Henry, Remi Villenave, Michael J. Cronce, William D. Leineweber, Maximilian a. Benz, and Donald E. Ingber. Organs-on-chips with integrated electrodes for trans-epithelial electrical resistance (TEER) measurements of human epithelial barrier function. *Lab Chip*, 17(13):2264–2271, 2017. ISSN 1473-0197. . URL `http://dx.doi.org/10.1039/C7LC00155Jhttp://xlink.rsc.org/?DOI=C7LC00155J`.

Klaus Peter Hoffmann, Roman Ruff, and Wigand Poppendieck. Long-term characterization of electrode materials for surface electrodes in biopotential recording. *Annual International Conference of the IEEE Engineering in Medicine and Biology - Proceedings*, pages 2239–2242, 2006. ISSN 05891019. .

Song Huang, Ludovic Wiszniewski, and Samuel Constant. The Use of In Vitro 3D Cell Models in Drug Development for Respiratory Diseases. *Drug Discovery and Development*, pages 169–190, 2011. .

David J. Hughes, Tomasz Kostrzewski, and Emma L. Sceats. Opportunities and challenges in the wider adoption of liver and interconnected microphysiological systems. *Experimental Biology and Medicine*, 242(16):1593–1604, 2017. ISSN 15353699. .

D. Huh, B. D. Matthews, a. Mammoto, M. Montoya-Zavala, H. Y. Hsin, and D. E. Ingber. Reconstituting Organ-Level Lung Functions on a Chip. *Science*, 328(5986):1662–1668, 2010. ISSN 0036-8075. . URL `http://www.sciencemag.org/cgi/doi/10.1126/science.1188302`.

Dongeun Huh, Geraldine A Hamilton, Donald E Ingber, and Biology Program. From Three-Dimensional Cell Culture to Organs-on-Chips Dongeun. *Trends Cell Biol.*, 21 (12):745–754, 2011. .

Mouhita Humayun, Chung-Wai Chow, and Edmond W. K. Young. Microfluidic lung airway-on-a-chip with arrayable suspended gels for studying epithelial and smooth muscle cell interactions. *Lab on a Chip*, 18:1298–1309, 2018. ISSN 1473-0197. . URL `http://xlink.rsc.org/?DOI=C7LC01357D`.

Walker Inman, Karel Domansky, James Serdy, Bryan Owens, David Trumper, and Linda G. Griffith. Design, modeling and fabrication of a constant flow pneumatic micropump. *Journal of Micromechanics and Microengineering*, 17(5):891–899, 2007. ISSN 09601317. .

Paul Ben Ishai, Mark S. Talary, Andreas Caduff, Evgeniya Levy, and Yuri Feldman. Electrode polarization in dielectric measurements: A review. *Measurement Science and Technology*, 24(10), 2013a. ISSN 13616501. .

Paul Ben Ishai, Mark S. Talary, Andreas Caduff, Evgeniya Levy, and Yuri Feldman. Electrode polarization in dielectric measurements: A review. *Measurement Science and Technology*, 24(10), 2013b. ISSN 13616501. .

Mohammad Yaghoub Abdollahzadeh Jamalabadi, Mohammadreza DaqiqShirazi, Ali Kosar, and Mostafa Safdari Shadloo. Effect of injection angle, density ratio, and viscosity on droplet formation in a microfluidic T-junction. *Theoretical and Applied Mechanics Letters*, 7(4):243–251, 2017. ISSN 20950349. . URL `http://dx.doi.org/10.1016/j.taml.2017.06.002`.

Abidemi Junaid, Vincent van Duinen, Wendy Stam, Sophie Dólleman, Wei Yang, Yolanda de Rijke, Hendrik Endeman, Cees van Kooten, Alireza Mashaghi, Hetty de Boer, Janine van Gils, Thomas Hankemeier, and Anton Jan van Zonneveld. A Microfluidics-Based Screening Tool to Assess the Impact of Blood Plasma Factors on Microvascular Integrity. *Advanced Biology*, 5(11), 2021. ISSN 27010198. .

N. Karra, E.J. Swindle, and H. Morgan. Drug delivery for traditional and emerging airway models. *Organs-on-a-Chip*, 1:100002, dec 2019. ISSN 26661020. . URL `https://doi.org/10.1016/j.ooc.2020.100002`.

Mark D. Kellogg. *Measurement of Biological Materials*. Elsevier Inc., 2017. ISBN 9780128021019. . URL `http://dx.doi.org/10.1016/B978-0-12-802101-9.00008-9`.

Robert T. Kennedy. Emerging trends in in vivo neurochemical monitoring by microdialysis. *Current Opinion in Chemical Biology*, 17(5):860–867, 2013. ISSN 13675931. . URL `http://dx.doi.org/10.1016/j.cbpa.2013.06.012`.

S. Jordan Kerns, Chaitra Belgur, Debora Petropolis, Marianne Kanellias, Riccardo Barrile, Johannes Sam, Tina Weinzierl, Tanja Fauti, Anne Freimoser-Grundschober, Jan Eckmann, Carina Hage, Martina Geiger, Patrick Ray Ng, William Tien-Street, Dimitris V. Manatakis, Virginie Micallef, Regine Gerard, Michael Bscheider, Ekaterina Breous-Nystrom, Anneliese Schneider, Anna Maria Giusti, Cristina Bertinetti-Lapatki, Heather Shannon Grant, Adrian B. Roth, Geraldine A. Hamilton, Thomas Singer, Katia Karalis, Annie Moisan, Peter Bruenker, Christian Klein, Marina Bacac, Nikolce Gjorevski, and Lauriane Cabon. Human immunocompetent organ-on-chip platforms allow safety profiling of tumor-targeted t-cell bispecific antibodies. *eLife*, 10:1–28, 2021. ISSN 2050084X. .

Hiroshi Kimura, Takatoki Yamamoto, Hitomi Sakai, Yasuyuki Sakai, and Teruo Fujii. An integrated microfluidic system for long-term perfusion culture and on-line monitoring of intestinal tissue models. *Lab on a Chip*, 8(5):741–746, 2008. ISSN 14730189. .

Andrew P. Kowalczyk and Kathleen J. Green. Structure, function, and regulation of desmosomes. *Progress in Molecular Biology and Translational Science*, 116:95–118, 2013. ISSN 18771173. .

Hoyin Lai and Albert Folch. Design and dynamic characterization of "single-stroke" peristaltic PDMS micropumps. *Lab Chip*, 11(2):336–342, 2011. ISSN 1473-0197. . URL `http://xlink.rsc.org/?DOI=C0LC00023J`.

A. V. Lakhin, V. Z. Tarantul, and L. V. Gening. Aptamers: Problems, solutions and prospects. *Acta Naturae*, 5(19):34–43, 2013. ISSN 20758251. .

G. Láng and K. E. Heusler. Remarks on the energetics of interfaces exhibiting constant phase element behaviour. *Journal of Electroanalytical Chemistry*, 457(1-2):257–260, 1998. ISSN 15726657. .

Edward L. LeCluyse, Rafal P. Witek, Melvin E. Andersen, and Mark J. Powers. Organotypic liver culture models: Meeting current challenges in toxicity testing. *Critical Reviews in Toxicology*, 42(6):501–548, 2012. ISSN 10408444. .

Junmin Lee, Shreya Mehrotra, Elaheh Zare-Eelanjegh, Raquel O. Rodrigues, Alireza Akbarinejad, David Ge, Luca Amato, Kiavash Kiaee, Yong Cong Fang, Aliza Rosenkranz, Wendy Keung, Biman B. Mandal, Ronald A. Li, Ting Zhang, Hea Yeon Lee, Mehmet Remzi Dokmeci, Yu Shrike Zhang, Ali Khademhosseini, and Su Ryon Shin. A Heart-Breast Cancer-on-a-Chip Platform for Disease Modeling and Monitoring of Cardiotoxicity Induced by Cancer Chemotherapy. *Small*, 17(15):1–17, 2021. ISSN 16136829. .

Chi Leng Leong, Sharon Coleman, Adrian M. Nightingale, Sammer Ul Hassan, David Voegeli, Martyn G. Boutelle, and Xize Niu. Lactate monitoring in droplet microfluidics: A cautionary tale in assay miniaturisation. *Analytical Methods*, 11(48):6119–6123, 2019. ISSN 17599679. .

Albert P. Li, Chris Bode, and Yumiko Sakai. A novel in vitro system, the integrated discrete multiple organ cell culture (IdMOC) system, for the evaluation of human drug toxicity: Comparative cytotoxicity of tamoxifen towards normal human cells from five major organs and MCF-7 adenocarcinoma breast. *Chemico-Biological Interactions*, 150(1):129–136, 2004. ISSN 00092797. .

Ban Ruo Li, Jia Wu, Hua Shan Li, Zhi Hui Jiang, Xiu Min Zhou, Cai Hua Xu, Ning Ding, Juan Min Zha, and Wei Qi He. In Vitro and In Vivo Approaches to Determine Intestinal Epithelial Cell Permeability. *Journal of visualized experiments : JoVE*, (140): 1–6, 2018. ISSN 1940087X. .

Georg Linz, Suzana Djeljadini, Lea Steinbeck, Gurbet Köse, Fabian Kiessling, and Matthias Wessling. Cell barrier characterization in transwell inserts by electrical impedance spectroscopy. *Biosensors and Bioelectronics*, 165(May):112345, 2020. ISSN 18734235. . URL `https://doi.org/10.1016/j.bios.2020.112345`.

Fengjiao Lyu, Lucas R. Blauch, and Sindy K.Y. Tang. *Quantifying phenotypes in single cells using droplet microfluidics*, volume 148. Elsevier Inc., 1 edition, 2018. ISBN 9780128142844. . URL `http://dx.doi.org/10.1016/bs.mcb.2018.09.006`.

Christian Maass, Cynthia L. Stokes, Linda G. Griffith, and Murat Cirit. Multi-functional scaling methodology for translational pharmacokinetic and pharmacodynamic applications using integrated microphysiological systems (MPS). *Integrative Biology (United Kingdom)*, 9(4):290–302, 2017. ISSN 17579708. .

Christian Maass, Matthew Dallas, Matthew E. Labarge, Michael Shockley, Jorge Valdez, Emily Geishecker, Cynthia L. Stokes, Linda G. Griffith, and Murat Cirit. Establishing quasi-steady state operations of microphysiological systems (MPS) using tissue-specific metabolic dependencies. *Scientific Reports*, 8(1):1–13, 2018. ISSN 20452322. . URL `http://dx.doi.org/10.1038/s41598-018-25971-y`.

Kuldeep Mahato, Suveen Kumar, Ananya Srivastava, Pawan K. Maurya, Renu Singh, and Pranjal Chandra. *Electrochemical immunosensors: Fundamentals and applications in clinical diagnostics*. Elsevier Inc., 2018. ISBN 9780128117620. . URL `http://dx.doi.org/10.1016/B978-0-12-811762-0.00014-1`.

Y. Mermoud, M. Felder, J. D. Stucki, a. O. Stucki, and O. T. Guenat. Microimpedance tomography system to monitor cell activity and membrane movements in a breathing lung-on-chip. *Sensors and Actuators, B: Chemical*, 255:3647–3653, 2018. ISSN 09254005. . URL `http://dx.doi.org/10.1016/j.snb.2017.09.192`.

Alyssa J. Miller and Jason R. Spence. In Vitro Models to Study Human Lung Development, Disease and Homeostasis. *Physiology*, 32(3):246–260, 2017. ISSN 1548-9213. . URL `http://physiologyonline.physiology.org/lookup/doi/10.1152/physiol.00041.2016`.

R. H.G. Mingels, S Kalsi, Y Cheong, and H Morgan. Iridium and Ruthenium oxide miniature pH sensors: Long-term performance. *Sensors and Actuators, B: Chemical*, 297, 2019. ISSN 09254005. . URL `https://doi.org/10.1016/j.snb.2019.126779`.

Emmanuelle Moens and Marc Veldhoen. Epithelial barrier biology: Good fences make good neighbours. *Immunology*, 135(1):1–8, 2012a. ISSN 00192805. .

Emmanuelle Moens and Marc Veldhoen. Epithelial barrier biology: Good fences make good neighbours. *Immunology*, 135(1):1–8, 2012b. ISSN 00192805. .

Kevin Mullane and Michael Williams. Animal models of asthma: Reprise or reboot? *Biochemical Pharmacology*, 87(1):131–139, 2014. ISSN 00062952. . URL `http://dx.doi.org/10.1016/j.bcp.2013.06.026`.

K. Nakahara, K. Yoshimura, Y. Okayama, and N. Miki. A peristaltic micropump using traveling waves of polymer membranes driven by a single actuator. *Proceedings of the IEEE International Conference on Micro Electro Mechanical Systems (MEMS)*, pages 1083–1086, 2011. ISSN 10846999. .

Divya D. Nalayanda, Christopher Puleo, William B. Fulton, Leilani M. Sharpe, Tza Huei Wang, and Fizan Abdullah. An open-access microfluidic model for lung-specific functional studies at an air-liquid interface. *Biomedical Microdevices*, 11(5): 1081–1089, 2009. ISSN 13872176. .

Janna C. Nawroth, Carolina Lucchesi, Deion Cheng, Abhishek Shukla, Justin Ngyuen, Tanvi Shroff, Antonio Varone, Katia Karalis, Hyun Hee Lee, Stephen Alves, Geraldine A. Hamilton, Michael Salmon, and Remi Villenave. A microengineered airway lung chip models key features of viral-induced exacerbation of asthma. *American Journal of Respiratory Cell and Molecular Biology*, 63(5):591–600, 2020. ISSN 15354989. .

Thao Nguyen, Su Hyun Jung, Min Seok Lee, Tae Eun Park, Suk Kyun Ahn, and Joo H Kang. Robust chemical bonding of PMMA microfluidic devices to porous PETE membranes for reliable cytotoxicity testing of drugs. *Lab on a Chip*, 19(21):3706–3713, 2019. ISSN 14730189. .

A. Nicolas, F. Schavemaker, K. Kosim, D. Kurek, M. Haarmans, M. Bulst, K. Lee, S. Wegner, T. Hankemeier, J. Joore, K. Domansky, H. L. Lanz, P. Vulto, and S. J. Trietsch. High throughput transepithelial electrical resistance (TEER) measurements on perfused membrane-free epithelia. *Lab on a Chip*, 21(9):1676–1685, 2021. ISSN 1473-0197. .

Adrian M. Nightingale, Gareth W. H. Evans, Peixiang Xu, Byung Jae Kim, Sammer-ul Hassan, and Xize Niu. Phased peristaltic micropumping for continuous sampling and hardcoded droplet generation. *Lab Chip*, 17(6):1149–1157, 2017. ISSN 1473-0197. . URL `http://xlink.rsc.org/?DOI=C6LC01479H`.

Adrian M. Nightingale, Chi Leng Leong, Rachel A. Burnish, Sammer ul Hassan, Yu Zhang, Geraldine F. Clough, Martyn G. Boutelle, David Voegeli, and Xize Niu. Monitoring biomolecule concentrations in tissue using a wearable droplet microfluidic-based sensor. *Nature Communications*, 10(1):1–12, 2019. ISSN 20411723. . URL `http://dx.doi.org/10.1038/s41467-019-10401-y`.

Xize Niu and Andrew J. DeMello. Building droplet-based microfluidic systems for biological analysis. *Biochemical Society Transactions*, 40(4):615–623, 2012. ISSN 0300-5127. . URL `http://biochemsoctrans.org/lookup/doi/10.1042/BST20120005`.

Xize Niu, Liyu Liu, Weijia Wen, and Ping Sheng. Microfluidic manipulation in lab-chips using electrorheological fluid. *Journal of Intelligent Material Systems and Structures*, 18 (12):1187–1190, 2007. ISSN 1045389X. .

Mathieu Odijk, Andries D. Van Der Meer, Daniel Levner, Hyun Jung Kim, Marinke W. Van Der Helm, Loes I. Segerink, Jean Phillipe Frimat, Geraldine A. Hamilton, Donald E. Ingber, and Albert Van Den Berg. Measuring direct current trans-epithelial electrical resistance in organ-on-a-chip microsystems. *Lab on a Chip*, 15(3):745–752, 2015. ISSN 14730189. .

Massimo Onor, Stefano Gufoni, Tommaso Lomonaco, Silvia Ghimenti, Pietro Salvo, Fiodor Sorrentino, and Emilia Bramanti. Potentiometric sensor for non invasive lactate determination in human sweat. *Analytica Chimica Acta*, 989:80–87, oct 2017. ISSN 18734324. . URL `http://www.sciencedirect.com/science/article/pii/S0003267017308541http://dx.doi.org/10.1016/j.aca.2017.07.050`.

Ali Ostadfar. *Fluid Mechanics and Biofluids Principles*. 2016. ISBN 9780128024089. .

Dick Papazian, Peter A. Würtzen, and Soren W.K. Hansen. Polarized Airway Epithelial Models for Immunological Co-Culture Studies, jul 2016. ISSN 14230097. URL `www.karger.com/iaa`.

Iosif Pediaditakis, Konstantia R. Kodella, Dimitris V. Manatakis, Christopher Y. Le, Chris D. Hinojosa, William Tien-Street, Elias S. Manolakos, Kostas Vekrellis, Geraldine A. Hamilton, Lorna Ewart, Lee L. Rubin, and Katia Karalis. Modeling alpha-synuclein pathology in a human brain-chip to assess blood-brain barrier disruption. *Nature Communications*, 12(1):1–17, 2021. ISSN 20411723. . URL `http://dx.doi.org/10.1038/s41467-021-26066-5`.

R. K. Rao, R. D. Baker, S. S. Baker, A. Gupta, and M. Holycross. Oxidant-induced disruption of intestinal epithelial barrier function: Role of protein tyrosine phosphorylation. *American Journal of Physiology - Gastrointestinal and Liver Physiology*, 273(4 36-4):812–823, 1997. ISSN 01931857. .

Riccardo Reale. Microfluidic Airway On-Chip. 2017.

Osborne Reynolds. An experimental investigation of the circumstances which determine whether the motion of water in parallel channels shall be direct or sinuous and of the Society, The Royal Transactions, Philosophical Society, Royalaw of resistance in parallel channels. *Society, The Royal Transactions, Philosophical Society, Royal*, 174 (1883):935–982, 1883.

Fariba Rezaee, Nida Meednu, Jason A. Emo, Bahman Saatian, Timothy J. Chapman, Nayden G. Naydenov, Anna De Benedetto, Lisa A. Beck, Andrei I. Ivanov, and Steve N. Georas. Polyinosinic:polycytidylic acid induces protein kinase D-dependent disassembly of apical junctions and barrier dysfunction in airway epithelial cells. *Journal of Allergy and Clinical Immunology*, 128(6):1216, 2011. ISSN 10976825. . URL `/pmc/articles/PMC3273326/?report=abstracthttps://www.ncbi.nlm.nih.gov/pmc/articles/PMC3273326/`.

Lewis H. Romer, Konstantin G. Birukov, and Joe G.N. Garcia. Focal Adhesions. *Circulation Research*, 98(5):606–616, 2006. ISSN 0009-7330. .

John Saliba, Arij Daou, Samar Damiati, Jessica Saliba, Marwan El-Sabban, and Rami Mhanna. Development of microplatforms to mimic the in vivo architecture of CNS and PNS physiology and their diseases. *Genes*, 9(6), 2018. ISSN 20734425. .

Robert P. Schleimer and Sergejs Berdnikovs. Etiology of epithelial barrier dysfunction in patients with type 2 inflammatory diseases. *Journal of Allergy and Clinical Immunology*, 139(6):1752–1761, 2017. ISSN 10976825. . URL `http://dx.doi.org/10.1016/j.jaci.2017.04.010`.

H. P. Schwan. Electrode Polarization Impedance and Measurements in Biological Materials. *Annals of the New York Academy of Sciences*, 148(1):191–209, 1968. ISSN 17496632. .

B. Shachar-Hill and A. E. Hill. Ion, fluid and charge transport across necturus intestinal epithelium in response to alanine. *Journal of Membrane Biology*, 158(2):109–118, 1997. ISSN 00222631. .

Su Ryon Shin, Tugba Kilic, Yu Shrike Zhang, Huseyin Avci, Ning Hu, Duckjin Kim, Cristina Branco, Julio Aleman, Solange Massa, Antonia Silvestri, Jian Kang, Anna Desalvo, Mohammed Abdullah Hussaini, Su Kyoung Chae, Alessandro Polini, Nupura Bhise, Mohammad Asif Hussain, Hea Yeon Lee, Mehmet R. Dokmeci, and Ali Khademhosseini. Label-Free and Regenerative Electrochemical Microfluidic Biosensors for Continual Monitoring of Cell Secretomes. *Advanced Science*, 4(5):1–14, 2017. ISSN 21983844. .

Longlong Si, Haiqing Bai, Melissa Rodas, Wuji Cao, Crystal Yuri Oh, Amanda Jiang, Rasmus Moller, Daisy Hoagland, Kohei Oishi, Shu Horiuchi, Skyler Uhl, Daniel Blanco-Melo, Randy A. Albrecht, Wen Chun Liu, Tristan Jordan, Benjamin E. Nilsson-Payant, Ilona Golynker, Justin Frere, James Logue, Robert Haupt, Marisa McGrath, Stuart Weston, Tian Zhang, Roberto Plebani, Mercy Soong, Atiq Nurani, Seong Min Kim, Danni Y. Zhu, Kambez H. Benam, Girija Goyal, Sarah E. Gilpin, Rachelle Prantil-Baun, Steven P. Gygi, Rani K. Powers, Kenneth E. Carlson, Matthew Frieman, Benjamin R. TenOever, and Donald E. Ingber. A human-airway-on-a-chip for the rapid identification of candidate antiviral therapeutics and prophylactics. *Nature Biomedical Engineering*, 5(8):815–829, 2021. ISSN 2157846X. . URL `http://dx.doi.org/10.1038/s41551-021-00718-9`.

Aleksander Skardal, Thomas Shupe, and Anthony Atala. Organoid-on-a-chip and body-on-a-chip systems for drug screening and disease modeling. *Drug Discovery Today*, 21(9):1399–1411, 2016. ISSN 18785832. . URL `http://dx.doi.org/10.1016/j.drudis.2016.07.003`.

Somayeh Sohrabi, Nour Kassir, and Mostafa Keshavarz Moraveji. Droplet microfluidics: Fundamentals and its advanced applications. *RSC Advances*, 10(46):27560–27574, 2020. ISSN 20462069. .

Joseph W. Song, Jungwook Paek, Kyu Tae Park, Jeongyun Seo, and Dongeun Huh. A bioinspired microfluidic model of liquid plug-induced mechanical airway injury. *Biomicrofluidics*, 12(4), 2018. ISSN 19321058. .

Balaji Srinivasan, Aditya Reddy Kolli, Mandy Brigitte Esch, Hasan Erbil Abaci, Michael L. Shuler, and James J. Hickman. TEER Measurement Techniques for In Vitro Barrier Model Systems. *Journal of Laboratory Automation*, 20(2):107–126, 2015. ISSN 22110690. .

Gopu Sriram, Massimo Alberti, Yuri Dancik, Bo Wu, Ruige Wu, Zhaoxu Feng, Srinivas Ramasamy, Paul Lorenz Bigliardi, Mei Bigliardi-Qi, and Zhiping Wang. Full-thickness human skin-on-chip with enhanced epidermal morphogenesis and barrier function. *Materials Today*, 21(4):326–340, may 2018. ISSN 18734103. .

Andreas O. Stucki, Janick D. Stucki, Sean R. R. Hall, Marcel Felder, Yves Mermoud, Ralph a. Schmid, Thomas Geiser, and Olivier T. Guenat. A lung-on-a-chip array with an integrated bio-inspired respiration mechanism. *Lab Chip*, 15(5):1302–1310, 2015. ISSN 1473-0197. . URL `http://xlink.rsc.org/?DOI=C4LC01252F`.

Janick D. Stucki, Nina Hobi, Artur Galimov, and Andreas O. Stucki. Medium throughput breathing human primary cell alveolus-on-chip model. *(in Revision)*, pages 1–13, 2018. ISSN 2045-2322. . URL `http://dx.doi.org/10.1038/s41598-018-32523-x`.

Tanja Šuligoj, Louise Kristine Vigsnæs, Pieter Van Den Abbeele, Athanasia Apostolou, Katia Karalis, George M Savva, Bruce Mcconnell, and Nathalie Juge. Gut Microbiota and Barrier Function. 2020.

Tao Sun, Hywel Morgan, and Nicolas G. Green. Analytical solutions of ac electrokinetics in interdigitated electrode arrays: Electric field, dielectrophoretic and traveling-wave dielectrophoretic forces. *Physical Review E - Statistical, Nonlinear, and Soft Matter Physics*, 76(4):1–18, 2007. ISSN 15393755. .

Tao Sun, Emily J. Swindle, Jane E. Collins, Judith a. Holloway, Donna E. Davies, and Hywel Morgan. On-chip epithelial barrier function assays using electrical impedance spectroscopy. *Lab on a Chip*, 10(12):1611, 2010a. ISSN 1473-0197. . URL `http://xlink.rsc.org/?DOI=c000699h`.

Tao Sun, Soichiro Tsuda, Klaus Peter Zauner, and Hywel Morgan. On-chip electrical impedance tomography for imaging biological cells. *Biosensors and Bioelectronics*, 25 (5):1109–1115, 2010b. ISSN 09565663. .

S P Sutera and R Skalak. the History of Poiseuille ' S. *Annual Review of Fluid Mechanics*, 25(25):1–19, 1993. URL `https://doi.org/10.1146/annurev.fl.25.010193.000245`.

R. S.N. Tavares, T. Phuong-Tao, I. Maschmeyer, S. S. Maria-Engler, M. Schäfer-Korting, A. Winter, C. Zoschke, R. Lauster, U. Marx, and L. R. Gaspar. Toxicity of topically applied drugs beyond skin irritation: Static skin model vs. Two organs-on-a-chip. *International Journal of Pharmaceutics*, 589:119788, nov 2020. ISSN 18733476. . URL `https://linkinghub.elsevier.com/retrieve/pii/S0378517320307730`.

Cormac T. Taylor, Des C. Winter, Maeve M. Skelly, Diarmuid P. O'Donoghue, Gerald C. O'Sullivan, Brian J. Harvey, and Alan W. Baird. Berberine inhibits ion transport in human colonic epithelia. *European Journal of Pharmacology*, 368(1):111–118, 1999. ISSN 00142999. .

Geoffrey Taylor. Dispersion of soluble matter in solvent flowing slowly through a tube. *Proceedings of the Royal Society of London. Series A. Mathematical and Physical Sciences*, 219(1137):186–203, 1953. ISSN 0080-4630. .

Shia-Yen Teh, Robert Lin, Lung-Hsin Hung, and Abraham P. Lee. Droplet microfluidics. *Lab on a Chip*, 8(2):198, 2008. ISSN 1473-0197. . URL `http://xlink.rsc.org/?DOI=b715524g`.

Charles K. Thodeti, Benjamin Matthews, Arvind Ravi, Akiko Mammoto, Kaustabh Ghosh, Abigail L. Bracha, and Donald E. Ingber. TRPV4 channels mediate cyclic strain-induced endothelial cell reorientation through integrin-to-integrin signaling. *Circulation Research*, 104(9):1123–1130, 2009. ISSN 00097330. .

V. Todorović, K. R. Kligys, R. L. Dusek, J. C.R. Jones, and K. J. Green. Desmosomes and Hemidesmosomes. In *Encyclopedia of Biological Chemistry: Second Edition*, pages 636–643. 2013. ISBN 9780123786319. .

Sebastiaan J. Trietsch, Guido D. Israëls, Jos Joore, Thomas Hankemeier, and Paul Vulto. Microfluidic titer plate for stratified 3D cell culture. *Lab on a Chip*, 13(18):3548–3554, 2013. ISSN 14730189. .

Nikolaos Tsamandouras, Wen Li Kelly Chen, Collin D. Edington, Cynthia L. Stokes, Linda G. Griffith, and Murat Cirit. Integrated Gut and Liver Microphysiological Systems for Quantitative In Vitro Pharmacokinetic Studies. *AAPS Journal*, 19(5):1499–1512, 2017. ISSN 15507416. .

Marinke W. van der Helm, Olivier Y.F. F. Henry, Amir Bein, Tiama Hamkins-Indik, Michael J. Cronce, William D. Leineweber, Mathieu Odijk, Andries D. van der Meer, Loes I. Segerink, Donald E. Ingber, Jan C. T. Eijkel, Michael J. Cronce, Mathieu Odijk, Amir Bein, William D. Leineweber, Andries D. van der Meer, Albert van den Berg, Marinke W. van der Helm, Donald E. Ingber, Tiama Hamkins-Indik, Loes I. Segerink, and Olivier Y.F. F. Henry. Non-invasive sensing of transepithelial barrier function and tissue differentiation in organs-on-chips using impedance spectroscopy. *Lab on a Chip*, 19(3):452–463, 2019. ISSN 14730189. .

Simon van der Schans, Frans De Loos, Cornelis Boersma, Maarten J. Postma, and Hans Büller. A novel perspective on pharmaceutical R&D costs: opportunities for reductions. *Expert Review of Pharmacoeconomics and Outcomes Research*, 00(00):1–9, 2021. ISSN 17448379. . URL `https://doi.org/10.1080/14737167.2022.1987219`.

Sandeep K. Vashist and John H.T. Luong. *Immunoassays: An overview*. Elsevier Inc., 2018. ISBN 9780128117620. . URL http://dx.doi.org/10.1016/B978-0-12-811762-0.00001-3.

Kitty Verhoeckx, Paul Cotter, Iván López-Expósito, Charlotte Kleiveland, Tor Lea, Alan Mackie, Teresa Requena, Dominika Swiatecka, and Harry Wichers. *The impact of food bioactives on health: In vitro and Ex Vivo models*. 2015. ISBN 9783319161044. .

Remi Villenave, Samantha Q. Wales, Tiama Hamkins-Indik, Efstathia Papafragkou, James C. Weaver, Thomas C. Ferrante, Anthony Bahinski, Christopher A. Elkins, Michael Kulka, and Donald E. Ingber. Human gut-on-a-chip supports polarized infection of coxsackie B1 virus in vitro. *PLoS ONE*, 12(2):1–17, 2017. ISSN 19326203. .

Qin Wang, Yue Xu, Shiliang Zuo, Hailong Yao, Tsung Yi Ho, Bing Li, Ulf Schlichtmann, and Yici Cai. Pressure-Aware Control Layer Optimization for Flow-Based Microfluidic Biochips. *IEEE Transactions on Biomedical Circuits and Systems*, 11(6):1488–1499, 2017. ISSN 19324545. .

E. Warburg. Ueber das Verhalten sogenannter unpolarisirbarer Elektroden gegen Wechselstrom. *Annalen der Physik und chemie*, 3:483–499, 1899.

E. Warburg. Ueber die Polarisationscapacität des Platins. *Annalen der Physik und chemie*, 311(2):125–135, 1901.

D. Weiss, M. Brischwein, H. Grothe, B. Wolf, and J. Wiest. Label-free monitoring of whole cell vitality. *Proceedings of the Annual International Conference of the IEEE Engineering in Medicine and Biology Society, EMBS*, pages 1607–1610, 2013. ISSN 1557170X. .

J. Wu and H. X. Ju. Clinical immunoassays and immunosensing. *Comprehensive Sampling and Sample Preparation*, 3:143–167, 2012. .

Maierdanjiang Wufuer, Geon Hui Lee, Woojune Hur, Byoungjun Jeon, Byung Jun Kim, Tae Hyun Choi, and Sang Hoon Lee. Skin-on-a-chip model simulating inflammation, edema and drug-based treatment. *Scientific Reports*, 6(1):1–12, nov 2016. ISSN 20452322. . URL www.nature.com/scientificreports/.

Rosalyn S. Yalow and Solomon A. Berson. Immunoassay of endogenous plasma insulin in man. *Obesity Research*, 4(6):583–600, 1960. ISSN 10717323. .

Jose Yeste, Xavi Illa, Mar Alvarez, and Rosa Villa. Engineering and monitoring cellular barrier models. *Journal of Biological Engineering*, 12(1):1–19, 2018. ISSN 17541611. .

Boyang Zhang and Milica Radisic. Organ-on-a-chip devices advance to market. *Lab Chip*, 17(14):2395–2420, 2017. ISSN 1473-0197. . URL http://xlink.rsc.org/?DOI=C6LC01554A.

Ning Zhang, Flurin Stauffer, Benjamin R. Simona, Feng Zhang, Zhao Ming Zhang, Ning Ping Huang, and János Vörös. Multifunctional 3D electrode platform for real-time in situ monitoring and stimulation of cardiac tissues. *Biosensors and Bioelectronics*, 112:149–155, 2018. ISSN 18734235. . URL `https://doi.org/10.1016/j.bios.2018.04.037`.

Yu Shrike Zhang, Julio Aleman, Su Ryon Shin, Tugba Kilic, Duckjin Kim, Seyed Ali Mousavi Shaegh, Solange Massa, Reza Riahi, Sukyoung Chae, Ning Hu, Huseyin Avci, Weijia Zhang, Antonia Silvestri, Amir Sanati Nezhad, Ahmad Manbohi, Fabio De Ferrari, Alessandro Polini, Giovanni Calzone, Noor Shaikh, Parissa Alerasool, Erica Budina, Jian Kang, Nupura Bhise, João Ribas, Adel Pourmand, Aleksander Skardal, Thomas Shupe, Colin E. Bishop, Mehmet Remzi Dokmeci, Anthony Atala, and Ali Khademhosseini. Multisensor-integrated organs-on-chips platform for automated and continual in situ monitoring of organoid behaviors. *Proceedings of the National Academy of Sciences*, 114(12):E2293–E2302, 2017. ISSN 0027-8424. . URL `http://www.pnas.org/lookup/doi/10.1073/pnas.1612906114`.

Yangzhi Zhu, Kalpana Mandal, Ana Lopez Hernandez, Satoru Kawakita, Wei Huang, Praveen Bandaru, Samad Ahadian, Han Jun Kim, Vadim Jucaud, Mehmet R. Dokmeci, and Ali Khademhosseini. State of the art in integrated biosensors for organ-on-a-chip applications. *Current Opinion in Biomedical Engineering*, 19:100309, 2021. ISSN 24684511. . URL `https://doi.org/10.1016/j.cobme.2021.100309`.

Ceniz Zihni, Clare Mills, Karl Matter, and Maria S. Balda. Tight junctions: From simple barriers to multifunctional molecular gates. *Nature Reviews Molecular Cell Biology*, 17 (9):564–580, 2016. ISSN 14710080. . URL `http://dx.doi.org/10.1038/nrm.2016.80`.